Luminescent perovskites: From materials to light-emitting devices

- Tesis doctoral -

VNIVERSITAT DE VALÈNCIA

Doctorado en Nanociencia y Nanotecnología

Laura Martínez Sarti

Directores:

Prof. Hendrik J. Bolink

Dr. Michele Sessolo

Noviembre 2019

Prof. Hendrik J. Bolink y **Dr. Michele Sessolo**, Investigadores de la Universidad de Valencia en el Instituto de Ciencia Molecular (ICMol), certifican que la memoria presentada por la estudiante de doctorado Laura Martínez Sarti, con el título "Luminescent perovskites: From materials to light-emitting devices", corresponde a su Tesis Doctoral y ha sido realizada bajo su dirección y tutoría, autorizando mediante este escrito la presentación de la misma.

En Valencia, a 14 de noviembre de 2019

Prof. Hendrik J. Bolink

(Director y tutor)

Dr. Michele Sessolo

(Director)

Index

Chapter 1.

Introduction

1.1. Overview

Light-emitting diodes (LEDs) are devices that emit light upon application of a voltage to the leads, causing electrons to recombine with holes within a semiconductor and releasing energy in the form of photons. This phenomenon is called electroluminescence, and the colour of the light is determined by the energy bandgap of the chosen semiconductor. LEDs are being widely adopted as alternative light-sources to incandescent light bulbs and fluorescent tubes.

LEDs' advantages over incandescent light sources include lower energy consumption, longer lifetime, improved physical robustness and smaller size. LEDs have become ubiquitous and are found in diverse applications in the aerospace and automotive industries, as well as in advertising, traffic signals, camera flashes, displays and lighting.

Current commercial high-quality LEDs are based on inorganic, direct bandgap semiconductors, fabricated at high temperatures and through complex deposition processes. Importantly, these inorganic LEDs are point light sources, which makes them difficult to implement in flexible displays or flat panel luminaires. Organic LEDs (OLEDs) are more suited to these applications, as they are flat devices comprising multilayers of "soft" organic semiconductors, which can be processed at low temperature and hence on virtually any substrate, including flexible. However, one of the main remaining hurdles is the fabrication of efficient blue OLEDs: the high energy of the electronic transitions required to obtain deep blue photons inevitably results in organic semiconductors which are electrochemically unstable. Researchers have recently found that perovskites, which are direct-bandgap semiconductors, could be alternative emitters to both inorganic and organic semiconductors for applications as colour displays and lighting, since they are inexpensive and easy to make and can be tuned to emit light in a variety of colours.

In accordance with the International Telecommunication Union (ITU) and the International Commission on Illumination (CIE) recommendations, the three primary emission peaks for displays and for the wide-gamut colorimetry are centred at 630 nm (red), 532 nm (green), and 467 nm (blue).[1] In this regard, colour-tunable perovskites are particularly promising for LEDs. In particular, metal halide perovskites, especially when nanostructured, could be suitable for optoelectronics devices as they can be processed from solution at low temperatures onto a wide range of flexible or rigid substrates. Perovskite nanostructures attain superior photoluminescence efficiency and narrow emission line width (considering the full width at half maximum, FWHM). Perovskites have an optical bandgap that can be easily modified from the ultraviolet (UV) to the near infrared (NIR) part of the electromagnetic spectrum, which is essential for a wide range of optoelectronic applications.

In order to be applied in LEDs, there are some obstacles which perovskite still have to overcome, such as the poor stability upon prolonged exposure to light, humidity and high

temperature.[2–4] Nevertheless, major progress is already being made in this field, and it seems that perovskites might indeed be applied to inexpensive, colour-tunable LEDs.

Among the metal halide perovskites, the most promising semiconducting materials are the lead halide perovskites. Perovskite solar cells and LEDs are demonstrating performances comparable to those of inorganic semiconductors.[5,6] In perovskite devices, only very thin layers (< 1 µm) of the active material, are needed to obtain high power conversion efficiencies. Although the total amount of toxic Pb per m^2 is very low, many studies are being carried out to reduce the amount of lead in order to make perovskites acceptable for LED production. In the last years, a lot of progress has been made in the development of effective encapsulations against moisture and oxygen,[7,8] and even in the recycling of perovskites at the end of the device lifetime.[9,10] In parallel, researchers are also focusing on the development of lead-free perovskites. Albeit other perovskites structures using alternative metals such as tin, germanium, palladium, bismuth or antimony have been reported,[11–14] lead halide semiconductors still outperform all other alternative materials.[15] Some of the favourable characteristics of lead halide perovskites are:

a. The low-cost of precursors, which use abundant elements that can be easily-recycled.
b. Simple reactivity, allowing processing of perovskite thin films at low temperature.
c. High absorption coefficient.
d. Possibility to achieve high photoluminescence quantum yield (PLQY).
e. Long charge carrier diffusion length (compared to organic semiconductors).

In view of these properties and of the successful implementation of perovskite compounds in high efficiency devices, the perovskites developed in this thesis are all based on lead.

1.2. Metal halide perovskites

Perovskites owe their name to the oxide mineral $CaTiO_3$ known as perovskite, which was named after the Russian mineralogist Lev Perovski.[16] However, perovskites include all materials which have the same type of crystal structure as the calcium titanium oxide, and even their derivatives. The general formula for 3D perovskites is AMX_3, where A and M are two cations of different sizes and natures, and X is an anion. Although the most common perovskite compounds are oxides, a subclass of these materials consists in ternary metal halides, where A is an organic or inorganic monovalent cation, M is usually a divalent metal and X is a halide. Investigations on lead halide perovskites were already ongoing decades ago, although mainly with the aim of studying the structural and magnetic properties.[17,18] Seminal work on the optical properties of hybrid lead halide perovskites was carried out by Ishihara et al.,[19,20] who described the excitonic properties of layered compounds. The first attempts to fabricate light-emitting devices using lead halide perovskites were reported at the end of the XX century.[21,22] However, electroluminescence could only be achieved at

liquid nitrogen temperatures, rendering the devices impractical for applications. It was not until 2014 that the first infrared and visible electroluminescence from lead halide perovskites at room temperature (RT) was demonstrated.[23]

Despite the promising initial results, the efficiency was very low and much further development was needed to consider the implementation of perovskites in the LED technology. To ensure high efficient LEDs, one of the requirements is the use of semiconductors with high PLQY. As for inorganic semiconductors, the main strategy towards the preparation of highly emissive perovskites consists in confining charge carriers within nanostructures, such as quantum dots (QDs). Initial strategies consisted in the use of a dielectric matrix such as poly(methyl methacrylate) (PMMA)[24] or casting the precursor solution onto a porous alumina scaffold (Figure 1.1),[25] to limit the growth of the lead halide perovskite crystals. In 2014, octadecylammonium bromide was used as a capping ligand to achieve the direct synthesis of nanoparticles with tailored size and hence controlled properties.[26]

Figure 1.1. Pictures of in situ synthesis of luminescent perovskite nanostructures under UV light. Perovskite precursor solution (left) is uniformly dropped onto a mesoporous alumina thin film. During spin-coating, the quick vaporization of the organic solvent triggers the crystallization of highly luminescent lead bromide perovskite nanostructures within the mesoporous alumina. Adapted from reference 25.

In the last 5 years, the understanding of the perovskite properties and crystallization has greatly advanced, leading to the development of efficient perovskite LEDs. At the moment of the preparation of this thesis, red and green-emitting devices with external quantum efficiencies (page 22 for term clarification) exceeding 20%,[27] and blue-emitting devices with external quantum efficiencies up to 9.5% have been demonstrated.[28]

1.2.1. Composition, crystal structure and size

Perovskites can crystallize in different structures. As mentioned above, the simplest structure is the three-dimensional (3D) AMX_3-type perovskite lattice, which has been widely studied due to the excellent photovoltaic properties in solar cells. Lower dimensional perovskites derive from the 3D crystal structure by slicing the inorganic lattice along different

crystallographic planes or isolating the basic component. In the AMX_3 structure, A is a small monovalent cation, usually methylammonium (MA^+, $CH_3NH_3^+$), formamidinium (FA^+, $CH(NH_2)_2^+$) or caesium (Cs^+); M is a divalent metal with stable octahedral coordination, Pb^{2+}, Sn^{2+} and Ge^{2+}; and X is a halide anion or a mixture of them (Cl^-, Br^- or I^-). The 3D perovskite structure consists of corner-sharing $[MX_6]^{4-}$ octahedra, with A cations occupying the cavities formed by eight adjacent lead halide octahedra (Figure 1.2). Perovskite compounds are mostly held together by ionic bonds.

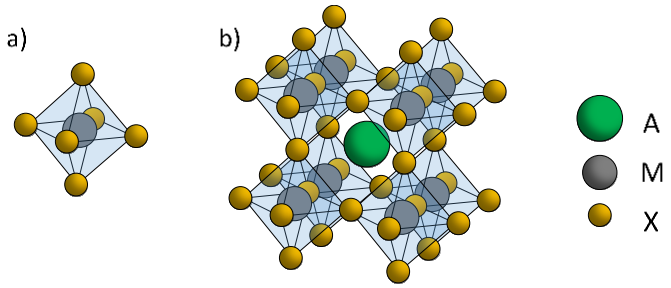

Figure 1.2. Schematics of a) a single lead halide octahedra and b) a unit cell comprising eight adjacent $[PbX_6]^{4-}$ octahedra intercalated with an A cation.

In stable 3D structures, the A cations must fit in the cavity delimited by the inorganic octahedra. To evaluate the structural stability of perovskite composition with different A, M and X components, two simple geometrical indicators are often used, the Goldschmidt tolerance factor (t) and the octahedral factor (μ). The Goldschmidt tolerance factor can be calculated simply on the basis of the ionic radii r_A, r_M and r_X, of A, M and X, respectively, following the expression 1.[29,30] The octahedral factor makes use of the radius ratio of the cation M over the anion X (expression 2) to predict if they can coordinate to form stable octahedral $[MX_6]^{4-}$ building blocks.[30]

(1) $$t = \frac{r_A + r_X}{\sqrt{2}(r_M + r_X)}$$ (2) $$\mu = \frac{r_M}{r_X}$$

In lead halide perovskites, a tolerance factor of $0.7 < t < 1.1$ and an octahedral factor ranging between 0.4 and 0.8, typically predict stable structures. According to these geometrical limitations, only few A cations (MA^+, FA^+ and Cs^+) can lead to the formation of stable 3D AMX_3 structures. If larger organic cations are used, the 3D lattice cannot accommodate them and lower dimensional perovskites crystal structures are formed instead.[31,32] To refer to the different types of perovskites, terms like “3D/2D/1D/0D” or concepts as “low-dimensional”

are often used. However, such terminology might lead to misconceptions as these terms are used to describe both the crystal size and the crystal structure (or inorganic framework) of perovskites. These parameters, size and crystal structure, can be used to classify perovskites as depicted in Figure 1.3.

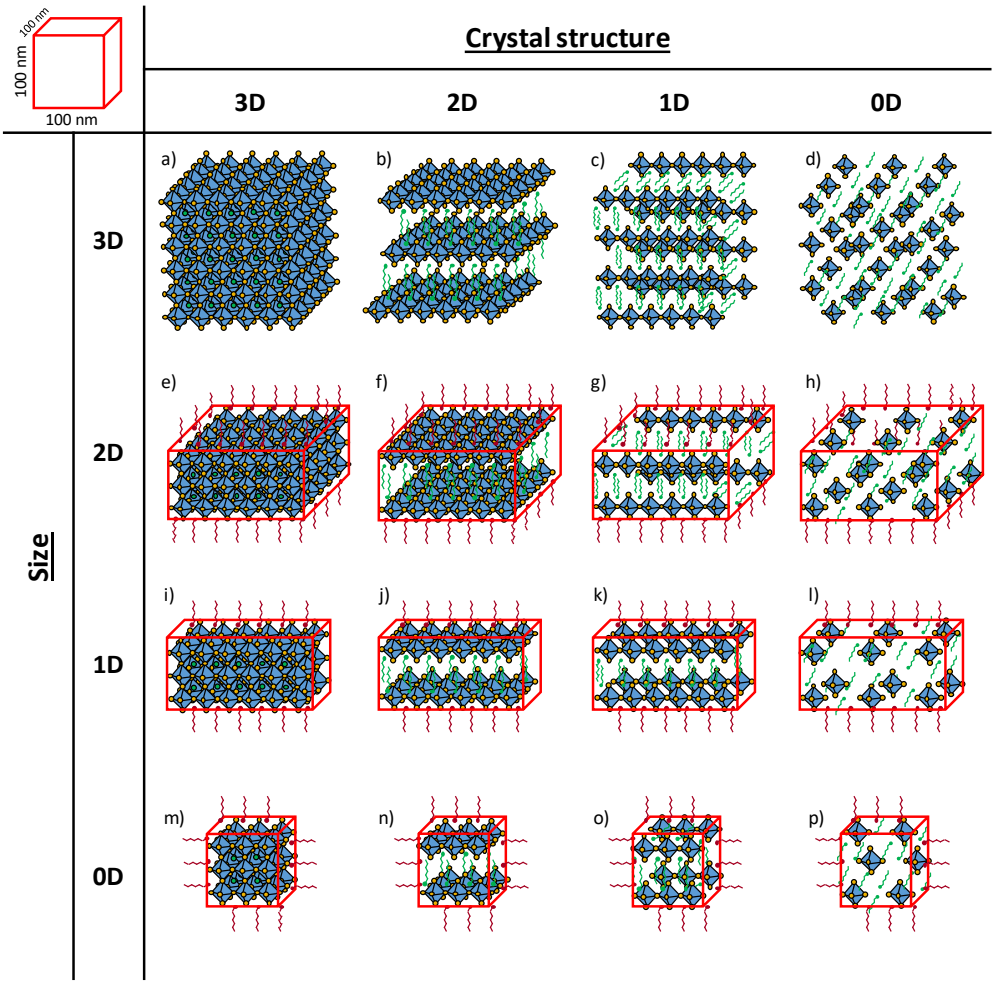

Figure 1.3. Scheme of different perovskites classified according to the size and the crystal structure. Some molecules have been excluded in the scheme to enhance clarity.

Crystal structure

Perovskites can be classified depending on the mutual spatial arrangement of the A cations and the $[MX_6]^{4-}$ framework, $[PbX_6]^{4-}$ in the case of lead halide perovskites. The overall structural motif strongly depends on the steric hindrance of the A cations used.[33,34] When the size of the organic cations cannot be accommodated within the cavities of the inorganic

lattice, as in the case of long-chain alkyl- or aryl- ammonium cations, the 3D structure (Figure 1.3a, e, i, m) collapses into lower dimensional crystal structures. If just large cations are present, the crystalline structure formed consists in layers of corner-sharing $[PbX_6]^{4-}$ octahedra alternated with layers of these large organic cations (LA). These two-dimensional (2D) structures are formulated by $(LA)_2PbX_4$ (Figure 1.3b, f, j, n). Additionally, using mixtures of large and small cations in the A site leads to an intermediate low-dimensional crystal structure, known as quasi-2D or Ruddlesden-Popper phase,[35,36] and with the generic formula $(LA)_2(A)_{n-1}Pb_nX_{3n+1}$. Perovskites with a quasi-2D structure consist in several layers (n) of corner sharing $[PbX_6]^{4-}$ octahedra intercalated with the small cations and separated by layers of the large ammonium cations (Figure 1.4q). The optical properties of the quasi-2D structures are strongly related to the n-value, i.e. the number of inorganic layers in between the large cations, which will be discussed further in the next section.

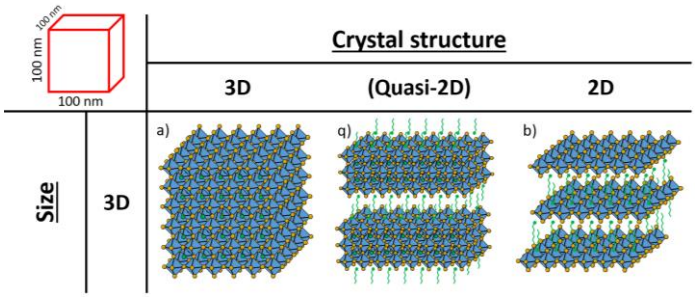

Figure 1.4. Scheme of the intermediate 2D-3D crystal structure classification, known as quasi-2D or Ruddlesden-Popper phase.

Lower dimensional crystals structures can also be obtained for perovskites. The lead halide framework can consist of $[PbX_6]^{4-}$ octahedra connected at the corners, edges or faces, forming a chain in a one-dimensional (1D) crystal structure (Figure 1.3c, g, k, o). The chemical formula is variable depending on the connectivity of the metal halide octahedra. Zero-dimensional (0D) inorganic frameworks consist of isolated $[PbX_6]^{4-}$ octahedra fully surrounded by "large" cations, with the generic formula A_4PbX_6 (Figure 1.3d, h, l, p). Following this classification, one can prepare bulk perovskites with different crystalline structures: As an example, perovskites with crystals larger than 100 nm in the three dimensions and with a 3D crystalline structure,[37] 2D quantum wells,[38–40] 1D quantum wires[41,42] and 0D molecules/clusters[43–45] (Figures 1.3a, b, c, d, respectively).

Size

Apart from the crystal structure dimensions, perovskites, and in general any material, can be classified according to their physical size. In this view, 3D defines bulk perovskites with crystals/grains measuring more than 100 nm in their three dimensions. Likewise, 2D, 1D and 0D correspond to materials with dimensions smaller than 100 nm in one, two and all three dimensions, respectively. The clearest nomenclature to refer to the different perovskite size would be *bulk* for the 3D (Figure 1.3a, b, c, d), *nanoplatelets* or *nanosheets* for 2D (Figure 1.3e, f, g, h), *nanowires* or *nanorods* for 1D (Figure 1.3i, j, k, l) and *nanoparticles* for 0D (Figure 1.3m, n, o, p). Thus, one can find in the literature examples of perovskite structures with different size but the same crystalline structure. As for example, bulk perovskite,[37] nanoplatelets,[46] nanowires,[47–49] and nanoparticles[26,50] with the same 3D AMX_3 crystalline structure (Figure 1.3a, e, i, m, respectively).

The formation of low-dimensional crystal structures or small crystal size perovskites is a consequence of restrictions in the growth of the material, which can be produced, among others, by the presence of long-chain ammonium cations (Different synthesis methods will be discussed in section 1.2.3). When these large molecules are present in the synthesis, the formation of either size reduced particles or low-dimensional crystal structures, depends on factors such as chemical nature and ratio of these molecules, and can lead often to a mixture of species. In perovskite nanoparticles synthesis, the coordinating long chain ammonium cations are commonly referred to as ligands.

1.2.2. Optoelectronic and structural properties

Metal halide perovskite exhibit favourable optical properties, such as high absorption coefficient, high PLQY and narrow photoluminescent (PL) spectrum, which can be tuned from the near UV to NIR by varying their constituent elements, size or crystal structure. Several works have demonstrated that a change of the halide component modifies the optical properties.[51–53] Mixed halide perovskites can also be easily prepared, showing intermediate optical properties as compared to pure halide materials (Figure 1.5a).[52,53] Most of the characteristics shown by the material can be rationalized on the basis of its electronic structure. A schematic energy diagram is reported in Figure 1.5b.[54]

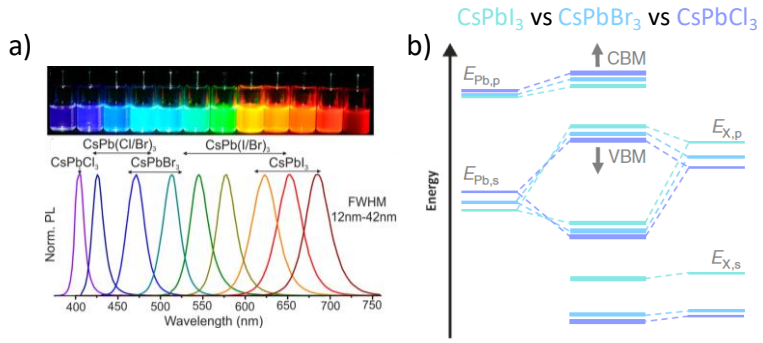

Figure 1.5. a) Colour tuning by partial or total halide substitution (Reproduced from reference 52). b) Scheme of the formation of electronic bands in a lead iodide perovskite through the hybridization of lead and iodide orbitals (Reproduced from reference 54).

The conduction band of halide perovskites forms from the antibonding orbitals of the hybridization of Pb *p* orbitals and *s* orbitals of the halide, and it is mostly *p*-like due to the high density of states from the lead contribution. The valence band, on the other hand, forms from the antibonding states of the hybridization of Pb *s* and halide *p*-orbitals.[54–57] An exchange of the halide leads to significant changes in the bandgap. As the conduction band is mostly influenced by the energy of the Pb *p* atomic orbitals, the halide exchange affects mainly the valence band. The *p* orbitals contributing to the valence band formation change from the 5*p* to 4*p* and to 3*p* as the halide is changed from I to Br and to Cl. The downward shift of the X *p* level is the dominating factor in determining the position of the valence band, which results in an increase in the bandgap going from I to Br to Cl. On the other hand, the A site cation does not directly participate in the bonding and only influences the electronic structure indirectly via changing the volume of the AMX_3 lattice or by introducing distortion in the ideal perovskite structure. Increasing the size of the A cation, for example going from Cs to MA and FA, generally increases the volume or distortion of the lattice, which leads to a decrease in the M levels. This reduction is due to the moderation of the confinement effect, i.e. an electron on a Pb atom is less confined and its energy decreases. Varying the A cation leads to relatively mild changes in volume and structure and, consequently, the bandgap is only slightly affected.[54]

In addition to the composition, the optical properties of lead halide perovskites are strongly determined both by the particle size and by the dimensionality of the crystal structure (depicted in Figure 1.3). If the spatial confinement of charge carriers is in the same order of magnitude of the exciton Bohr radius, perovskites exhibit quantum confinement effects. In particular, the bandgap increases as the spatial confinement increases. The most straightforward way to achieve quantum confinement in perovskites is the reduction of the particle size, as in traditional semiconducting QDs.[58] This corresponds to moving from top to bottom in Figure 1.3. Alternatively, perovskites can show confinement effects when

diminishing the dimensionality of the crystal structure (moving from left to right in Figure 1.3 and Figure 1.4),[59] for example from AMX_3 (3D) to $(LA)_2PbX_4$ (2D) or for small n-values in quasi-2D perovskites $(LA)_2(A)_{n-1}Pb_nX_{3n+1}$. In the latter low-dimensional perovskites, composed by alternating inorganic semiconducting and organic insulating sheets, electrons and holes are confined within the inorganic layers, causing quantum confinement effects.

A key feature of metal halide perovskites is the high tolerance to structural defects. Defects induce localized electronic states which can act as electronic traps, where charge carriers can be captured and lost. Due to the nature of the band structure of lead halide perovskites, defect states tend to be either shallow or localized within the electronic bands, and hence are essentially benign.[60] This unique feature allows to obtain highly luminescent perovskites without the use of sophisticated processing techniques.[61] In fact, perovskite nanocrystals (NCs) typically show very high PLQY, with values close to unity already reported.[62] The spatial confinement of the charges, together with a passivation of the surface of the material, effectively enhances the PL efficiencies by eliminating virtually all non-radiative decay pathways (further details in section 1.3.1). Even though the high defect tolerance is a common feature to all metal halide perovskites, the PLQY generally does decrease for larger bandgaps. Most likely, the wider the bandgaps, the more important the impact of defects becomes. Shallow traps or defect electronic states that fall within the electronic bands in narrow bandgap perovskites become deeper when the bandgaps are increased, being able to act as non-radiative recombination centres. Another consequence of the high defect tolerance of lead halide perovskites is their good charge transport properties when compared to organic semiconductors, showing long charge diffusion lengths, ambipolar charge transport and a high carrier mobility.[63–66]

1.2.3. Nanocrystals colloidal synthesis methods

The formation of the perovskite thin films for the preparation of LEDs, often takes place during the deposition step from its precursors onto a substrate (see section 1.3.3 for further details). However, in the case of low-dimensional structures, it generally requires first the synthesis of colloidal suspensions and then the deposition onto a substrate. The synthetic methods of lead halide perovskite nanocrystals can be classified into two main groups, solution-based and solid-based methods, depending on the state of the precursor materials. Solution-based synthesis is the classical approach for QDs preparation, and require solvents to dissolve, mix and allow the reaction of the perovskite precursors to form the colloidal nanocrystals. Solid-based synthesis methods use the precursors in a solid state and no solvent or very small quantities of solvent are used during the synthesis. In Figure 1.6, it is possible to find a classification of the most relevant synthesis methods.

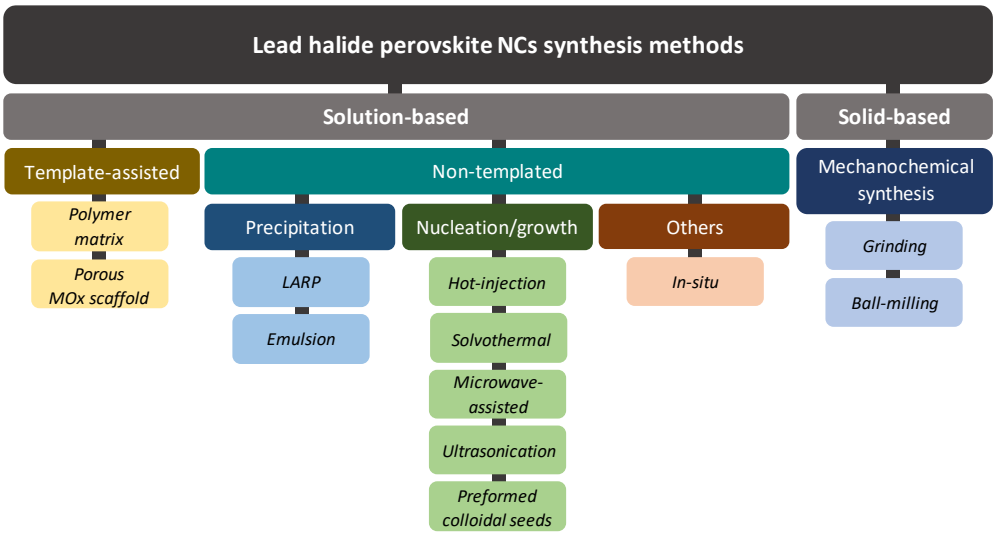

Figure 1.6. Classification of several reported and relevant synthesis methods of perovskite nanostructures.

Solution-based synthesis methods for perovskite nanocrystals

As previously stated, the preparation of nanocrystals requires limiting the growth of the material at the nanoscale. The growth limitation can be achieved either using an inert, preformed material (template) to spatially confine the perovskite crystals at the nanometre scale, or by a direct synthesis without the need of an external structure. *Template-assisted* methods make use of a polymer matrix, as PMMA,[24] or a porous metal oxide scaffold.[25] The main drawback of these techniques is the poor electrical conductivity of the resulting layers as the confinement takes place within a dielectric matrix.

Perovskite nanocrystals can also be synthesized directly, without the need of an external structure acting as a template. This can be achieved either by nucleation and growth of the crystals from a change in the reaction conditions, or by an induced supersaturation of a solution which leads to the precipitation and crystallization of the perovskite nanocrystals.

In the latter case, the most studied and used synthesis method is the *ligand-assisted reprecipitation process*, also known as *LARP technique*. This method consists in the fast injection or dropwise addition of a solution, where the precursors salts are dissolved in a polar (named “good”) solvent, into a second miscible solvent in which the solubility of the precursors is low (“bad” non-polar solvent). The addition takes place in the presence of surfactants (ligands), typically long-chain alkylammonium molecules, and an organic acid, at RT. The mixture of the two solvents induces an instantaneous precipitation and crystallization of the material, while the ligands limit the growth of the crystals leading to the formation of nanocrystals. The presence of the amines helps to regulate the kinetics of the crystallization

and hence the NCs size, while the organic acids help to supress the NCs aggregation.[67] The key parameters to control the size and the shape of the resulting NCs from this strategy are i) the precursors/ligands ratio, ii) the type of ligands (chain length and chemical nature), iii) the reaction temperature and time and iv) the type of bad solvent. Even if long-chain alkylammonium molecules are the most common confinement agents used for the one-pot synthesis of perovskite nanocrystals, some examples have been published using other species such as inorganic salts (KPF_6), where K^+ is believed to stabilize the colloidal nanoparticles (NPs).[68]

Another relevant technique is the *emulsion method*, which can be considered as a variation of the LARP technique. In this method, the precursors are dissolved in a good polar solvent and then mixed with a non-miscible solvent, where the ligands are dissolved, to form an emulsion. When a demulsifier (usually a solvent miscible with both other solvents) is added to the mixture, it induces the crystallization.[69]

There are several techniques in which the perovskite nanocrystals are synthesized by nucleation and growth as a consequence of changes in the reaction conditions. Among them, the *hot injection method* is the most relevant, as it has been extensively used for the synthesis of metal chalcogenide and pnictide nanocrystals and it was later adapted for the formation of perovskite nanocrystals.[52] The method consists in the fast injection of one of the precursors into a solution with a high temperature where the other precursors and the ligands are dissolved in a high boiling point solvent. The size and shape of the resulting NCs are controlled by the ratio of the surfactant to the precursors, the temperature, the reaction time and the concentration of the precursors. With this method it is possible to obtain small NCs with a narrow size distribution.

In an attempt to simplify the synthesis conditions, several groups have reported the synthesis of perovskite nanocrystals by mixing all the precursors with the ligands and using uniform temperature in an autoclave (*solvothermal*), *ultrasonication* or *microwave irradiation*.[70–72]

Alternatively, the growth of the perovskite nanocrystals can also be carried out starting the nucleation from preformed nanocrystals or colloidal seeds, as pre-synthesized PbI_2.[73]

All the above described methods are used to prepare nanocrystals which are then casted onto substrates to form thin films for the preparation of LEDs. Conversely, the direct formation of nanocrystals in a film can also be carried out. In this technique, named as *"in situ" preparation*, the perovskite precursors are dissolved in a good solvent, and the crystal growth is limited by large organoammonium halides introduced during the film formation. The large cations are dissolved in a bad solvent for the perovskite, which is dripped on top of the forming film while the crystallization of the perovskite is taking place during spin-coating.[74]

Solid-state synthesis methods

Metal halide perovskite NCs can also be synthesized with dry procedures or with minimal quantities of solvent. The *grinding method* consists in mixing the precursors powders with the large organic ligands (or a mixture of amine and organic acid) and a small quantity of solvent in a mortar, and manually grinding them in air and at RT.[75] This method is classified as top-down, as the mechanical impact reduces the material size and then the chemical reaction takes place. High-energy *ball milling* is another type of mechanochemical synthesis. In this method, the mixture of the perovskite precursors, with a small quantity of solvent and the ligands, are mixed in a grinding jar with balls of a specific size. The grinding jars are placed in a ball mill which, through rotary motion of the bowl, produces the elastic deformation of the material, the plastic deformation and ultimately the fracture and the chemical reaction, giving place to the perovskite nanocrystals formation.[76]

1.3. Perovskite light-emitting diodes

Due to the good transport properties shown by perovskites, as the high carrier mobility of both electrons and holes (> 1 $cm^2/V{\cdot}s$), these materials can act as charge transporting layers in LEDs.[77] However, this section is focused on perovskite LEDs, where the electroluminescence takes place in the semiconducting perovskite.

1.3.1. Working principles

In semiconductors, electrons and holes can be either photo-generated or electrically injected. The process by which charge carriers recombine and emit photons is known as *radiative recombination*. If the process takes place without the emission of photons, it is named *non-radiative recombination*. In order to have efficient luminescence, non-radiative recombination should be minimized, typically reducing the concentration of defects. Although metal halide perovskites have high defect-tolerance, trap states are still present in perovskite thin films. Importantly, the nature and density of defect states in perovskites are highly sensitive to the material processing conditions.[78] In this view, the synthesis (section 1.2.3) as well as the deposition method (section 1.3.3) are of great importance to obtain high quality semiconducting materials.

In a perovskite LED, a perovskite film is sandwiched between semiconducting layers that selectively inject and transport electrons and holes from the electrodes into the active material. Once the charge carriers (electrons and holes) meet in the perovskite, they can either recombine as free carriers or via the formation of excitons, releasing photons in a process known as electroluminescence. An approximate model to describe the working mechanism of a perovskite diode is the p-i-n junction, where the perovskite acts as the

intrinsic material in between oppositely doped layers.[79] When the external electrodes of a LED are short-circuited, the Fermi levels of the metal contacts align, and the potential (built-in potential, V_{bi}) drops over the intrinsic region. The current density vs. voltage (J-V) characteristics are typically characterized by three regimes. The first is the ohmic regime, where the leakage current due to defects and shunts is observed (Figure 1.7, part 1). When a small positive voltage, lower than the V_{bi}, is applied to the diode, electrons and holes diffuse towards the intrinsic region, in the so-called diffusion current regime (Figure 1.7, part 2). If voltages higher than V_{bi} are applied, the electrons and holes move under the effect of the applied voltage (drift current, Figure 1.7, part 3) and the current is either injection-limited or space-charged limited. The low mobility of the organic materials translates in an accumulation of charges that limits the current at high voltages. However, the mobility of the perovskite is higher compared to organic semiconductors, reducing the space-charge limitation.

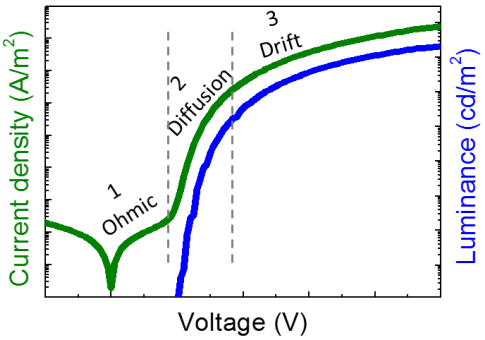

Figure 1.7. Diode regimes in a forward current density-voltage curve.

To describe the performance of a LED, there are several representative figures of merit as luminance (cd/m^2), current density (A/m^2), current efficiency (cd/A), power efficiency (lm/W) or external quantum efficiency (EQE_{EL}, %).

Luminance: It represents the intensity of light emitted (expressed in candelas, cd) by the device per unit of surface in a given direction, taking into account the human eye sensitivity curve. It is expressed in cd/m^2 in the International System of Units.

Current density (J): It corresponds to the electrical current per unit area of the device. Its units are A/m^2.

Current efficiency: It is the ratio of the luminance with the correspondent current density. It is expressed in cd/A.

Power or luminous efficiency (PCE): It is the ratio of luminous flux to electrical power consumed by the source. It is a measure of how well a light source produces visible light. Its units are lm/W.

External quantum efficiency (EQE_{EL}): It defines the number of emitted photons over the number of injected electrons. It is expressed as a %.

1.3.2. Devices architectures

The structure of perovskite LEDs is analogous to that of OLEDs (Figure 1.8a). They are multilayer devices where the processes of charge injection, transport and recombination are carried out by different materials, optimized for each particular process. In perovskite LEDs, the emissive layer, a metal halide perovskite film with the desired bandgap, is sandwiched between charge selective layers. Charge selective layers have the task of transporting and injecting holes and electrons into the perovskite. These layers are intrinsic semiconductors, either organics or metal oxides, and are named as hole transport layer (HTL) and electron transport layer (ETL), respectively. Their energy levels typically allow to selectively transport one type of carrier (holes or electrons) and block the opposite charges. Hence charge recombination takes place within the perovskite film, enhancing the probability of radiative recombination. To match the work function (WF) of the electrodes, injection layers are often used, which consist in doped semiconductor to enhanced their carrier density. These layers are known as hole injection layer (HIL) and electron injection layer (EIL). Poly(3,4-ethylenedioxythiophene) doped with polystyrene sulfonate (PEDOT:PSS) is a conducting polymer broadly employed as HIL, ensuring an ohmic contact with the electrode. In order to efficiently inject electrons, doped organics or n-type metal oxides (as TiO_2, SnO_2 or ZnO) EIL are widely used. Finally, the device is sandwiched between two electrodes, the anode (positively biased, for hole injection) and the cathode (negatively biased, for electron injection), which are either metals or transparent conductive oxides (TCOs). TCOs are particularly important to enable the light to exit the device, the most common being indium tin-doped oxide (ITO) or fluorine-doped tin oxide (FTO). Substrates are usually glass or plastic flexible foils (as polyethylene terephthalate, PET) on which the rest of the layers are deposited. If the light exits the device through this component, it is important to use a transparent material with a matching refractive index. There are two types of device architectures depending on the polarity of the transparent electrode. Depending on whether the TCO is used as the anode (typically ITO on glass) or the cathode, the device is named p-i-n or n-i-p, respectively.[80]

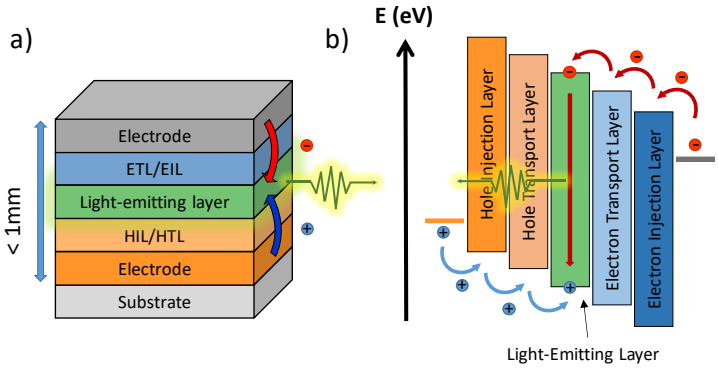

Figure 1.8. a) Scheme of a LED and b) corresponding flat band energy diagram highlighting the relevant processes.

Depending on the perovskite type, and in particular on the absolute position of the electronic band edges, charge selective materials have to be carefully chosen, with HOMO (highest occupied molecular orbital) and/or LUMO (lowest unoccupied molecular orbital) levels to minimize the energy difference with the perovskite bands. In the same way, electrodes must have the adequate WF to match the energy level of the transport/injection layers.

Independently of the materials used and the polarity of their charge carriers, p-i-n and n-i-p devices share the same working principles. Briefly, when a voltage higher than V_{bi} is applied in a perovskite LED at their electrodes, electrons and holes are injected into the device and transported to the active material trough the EIL/HIL and ETL/HTL, respectively (Figure 1.8a). Once they reach the perovskite film, if they recombine radiatively, the process leads to light-emission. Figure 1.8b shows a flat band energy diagram and highlights the different processes leading to electroluminescence taking place in a LED (lines represents the WF of the electrodes, while coloured rectangles the bandgap of the semiconductors, with the top and bottom lines corresponding to the HOMO and LUMO or the valence and conduction bands).

1.3.3. Deposition techniques

The possibility to obtain high quality (both optically and electronically) semiconducting thin films with simple deposition methods is one of the main features of perovskites.[81–83] Perovskite thin films and devices can be processed from solution or with vacuum methods. The processing technique should allow control over crystallinity, thickness and purity, as these determine the charge transport and optical properties, and hence the device performance.

Solution-based deposition methods are potentially inexpensive and compatible with roll-to-roll fabrication, which is suitable for large-scale production. The perovskite precursors are typically dissolved in polar solvents such as N,N-dimethylformamide (DMF), dimethyl sulfoxide (DMSO), γ-butyrolactone (GBL) or N-methyl pyrrolidone (NMP). The solution-processing method most commonly adopted in research laboratories is known as spin-coating. This procedure consists in the application of a small amount of precursor solution on the centre of a substrate, which is then rotated at high speed in order to spread the solution by centrifugal force, coating the substrate. A post-annealing process is usually required for a quantitative conversion of the precursors into a polycrystalline perovskite film. Other common deposition methods are dip-, spray-, blade- and slot-die coating. As in all these procedures the film formation relies on the crystallization following the solvent evaporation, it is important to control the reaction kinetics considering several parameters. The main parameters are the nature of the solvent and its vapour pressure, the substrate and its surface polarity, the concentration of the solution, the atmosphere, the temperature and the specific technique parameters such as the rotation speed, total spin time and acceleration in the case of spin-coating. All these parameters must be taken into account to obtain an optimum film morphology. As mentioned in section 1.2.3, small crystal size perovskites, such as nanoparticles or nanoplatelets, are generally synthesized and suspended in solution prior to deposition. Even though the perovskite crystals are already formed in the suspension, the choice of the deposition technique also plays an important role in obtaining uniform and homogeneous films, which are needed for a good device performance. Suspensions of pre-synthesized nanoparticles or nanoplatelets are deposited using solution-based techniques as described above.

On the other hand, vacuum deposition methods have the advantage of a higher control over the perovskite film thickness, uniformity and quality. Vacuum methods are also intrinsically additive, so that multilayer devices can be easily obtained without the need to use orthogonal solvents. The precursors are placed in temperature controlled thermal sources (ceramic crucibles or metallic boats) inside a high vacuum chamber. The substrates, protected by a mechanical shutter, are placed above the thermal sources. Then, the material is heated to its evaporation/sublimation temperature and condense on the substrate. In the case of perovskites, this method can be carried out from the pure compound or by simultaneous co-deposition of the precursors. The latter method has been used for both 2D and 3D hybrid perovskites.[80,84–86]

1.4. Motivation and thesis overview

To contribute to the next generation lighting systems, high current efficiency, stability and simple preparation procedures with reduced economic and energetic costs are essential characteristics for perovskites LEDs. The preparation of high quality emissive materials with high purity, high PL efficiency and colour tuning is crucial to achieve highly-efficient devices.

The results collected in this thesis aim to contribute to the progress in perovskite optoelectronics by the development of efficient and inexpensive light-emitting materials and devices.

In the different chapters several perovskite types are described and studied, from nanosized perovskites (Chapter 2, 3 and 4) to bulk perovskites (Chapter 5), all with a 3D crystal structure. Additionally, other types of crystal structures are studied, such as nanoplatelets with 2D (Chapter 3) and even quasi-2D structures (Chapter 2). Photoluminescence and electroluminescence with colours ranging from red to green and blue are described.

Chapter 2 focuses on obtaining stable and very PL efficient red-emitting hybrid quasi-2D perovskite NCs with a narrow linewidth. The work experiments with a controllable shift of the bandgap, accomplished by varying the chain length of the alkylammonium ligands employed in its synthesis.

Chapter 3 describes the novel use of a bifunctional ligand for the synthesis of highly photoluminescent green-emitting $MAPbBr_3$ NPs. Additionally, the ligand allows the nanostructures to effectively anchor on a variety of conducting polymers and inorganic semiconducting surfaces, which can be used for the preparation of solution-based multilayer LEDs.

Chapter 4 is about green-emitting LEDs with a remarkably high combination of EQE, luminance, power and current efficiency. The outstanding performance is described to be due to an energy cascade from hierarchical self-assembled structures. These structures, low-dimensional octylammonium lead bromide microplatelets (MPLs) and 3D $FAPbBr_3$ NCs, form ultra-smooth films with a very high PLQY.

Chapter 5 describes a mechanochemical synthesis of stable mix-cation/mix-halide lead perovskites powders ($MA_{1-y}Cs_yPb(Br_nCl_{1-n})_3$) with emission spanning the green to blue region of the visible spectrum. Upon addition of amantadine hydrochloride, a strong enhancement in the PLQY can be obtained with only minor structural changes.

Chapter 2.

Low-dimensional iodide perovskite nanocrystals enable efficient red emission

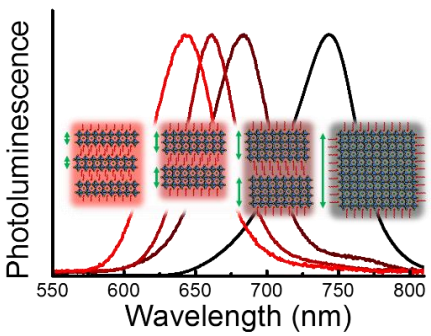

2.1. Motivation, work description and achievement

Obtaining stable and efficient red PL emission from perovskite NCs is not trivial and has been a challenge for several years. Iodide-based perovskites are the halide perovskites with the smallest bandgap, hence, they have been employed as a suitable option to obtain small bandgaps emissions. However, bulk $MAPbI_3$ and $FAPbI_3$ are not suitable for the preparation of red light-emitting systems, as they emit at a wavelength higher than 770 nm, in the NIR region. Additionally, the chemical instability of $MAPbI_3$ and the phase instability of $FAPbI_3$ and $CsPbI_3$, make it difficult to obtain efficient and stable iodide-based perovskite NCs.[87–90] Recently, some progress has been made in the stabilization of such systems.[90–92] Despite this, pure red emission (approx. 630-650 nm) has not yet been achieved. An alternative to achieve red emission from these perovskites is the use of mixed Br/I halide based perovskites.[93] Nevertheless, they are not always appropriate as they can suffer from phase segregation.[94] Stable perovskites having a pure red emission with a high PL efficiency are still missing.

This chapter describes the development of red-emitting NCs with a PLQY exceeding 90% and stable for over 500 hours using a simple ligand-assisted reprecipitation method at RT. The possibility of tuning the bandgap in a reproducible and controllable way by varying the chain length of the alkylammonium ligands is investigated. The chain length modification aims to reduce the dimensionality of the nanostructures and obtain, through this, efficient red-emitting hybrid quasi-2D perovskite NCs. An antisolvent washing step is crucial to purify the samples and obtain single-peak PL with a narrow linewidth.

2.2. Experimental details and methodology

A simple synthesis protocol was carried out for the preparation of iodide-based 3D perovskite NCs, using $MA_{0.8}Cs_{0.2}PbI_3$ as the starting stoichiometry. The introduction of a small quantity of Cs cations into this hybrid material is known to enhance the stability and reproducibility of the perovskite.[95–97]

The mixed cation MA-Cs perovskite NCs were prepared by a direct non-template synthesis based on a previously published protocol with slightly modified conditions and starting materials.[98] $PbBr_2$, 1-octadecene (ODE), oleylamine (or lately decylamine, octylamine and hexylamine) and oleic acid (OA) were mixed together, obtaining a solution named here "*Pb solution*". Simultaneously, methylammonium iodide (MAI) and CsI were added to a solution with 1-butanol (1-BuOH), ODE and OA (called "*MACs solution"*). Both solutions were heated under continuous stirring to ensure complete dissolution. After cooling them down, the *Pb solution* was injected drop by drop into the *MACs solution* under vigorous stirring at RT. A dark red precipitate was immediately observed, suggesting the formation of the NCs. The as-prepared dispersion was subsequently washed and the NCs were separated by a

centrifugation step. This process was done twice to obtain high purity NCs. The bright red luminescent supernatant was used for the characterization without further purification.

Some samples were modified by the addition of large quantities of an additional solvent during the purification step. For these modified samples, the synthesis was performed as described above but with the addition of 3 mL of 1-BuOH to the NCs dispersion prior to the first centrifugation step. The following steps were kept unvaried, and the precipitated was collected and redispersed in toluene.

The PL characteristics were studied using a Xe lamp coupled to a monochromator as the excitation source and an integrated sphere coupled to a spectrometer (Hamamatsu C9920-02 with a Hamamatsu PMA-11 optical detector), in order to quantitatively determine the PLQY. Samples were excited at 530 nm and pure toluene was used as the reference. Samples had an absorbance of approximately 0.4 - 0.5, which allows for an accurate quantitative PLQY determination. UV-visible spectra of the colloidal dispersions were recorded using quartz cuvettes and a UV-visible spectrophotometer Agilent 8453E. Transmission electron microscopy (TEM) images were obtained with a JEOL JEM1010 transmission electron microscope operated at 100 kV. X-ray diffraction was measured with a Panalytical Empyrean diffractometer equipped with a copper anode (CuKα) operated at 45 kV and 30 mA and a Pixel 1D detector in scanning line mode. Single scans were acquired in the 2θ = 5° to 35° range in Bragg-Brentano geometry in air.

2.3. Results and discussion

The synthesis successfully led to the formation of luminescent NCs, however, two different spectral features were observed (Figure 2.1a), suggesting the presence of several emitting species in the colloidal solution. The absorbance spectrum showed an absorption onset at 740 nm and a sharp absorption feature at 617 nm. The PL analysis highlighted an intense peak centred at 747 nm and a secondary weaker peak centred at 625 nm. These data are consistent with the simultaneous formation of 3D (narrow bandgap PL signal at 747 nm) and quasi-2D perovskite NCs (wide bandgap luminescence), the latter due to the interaction with the oleylamine.[99,100] Pure 2D crystals (quasi-2D with n = 1) lead iodide perovskites were excluded as these would show a luminescence peak around 525 nm, that is not observed.[101,102] While the length of the oleylamine backbone and its non-planar configuration (caused by the vinyl bond) might seem incompatible with the formation of low-dimensional structures, 2D and quasi-2D perovskites with oleylamine have been reported.[103,104] As the PL energy is affected by the n-value in the quasi-2D crystal structures (i.e. n is the number of metal halide octahedra sheets separated by the long-chain cations), based on our PL characterization it is reasonable to assume a value of n = 4 for the emission centred at 625 nm.[101] An X-ray diffraction (XRD) analysis on drop-casted NCs films revealed broad diffraction peaks centred at 2θ = 14.0° and 2θ = 28.3°, consistent with the formation

of 3D perovskite, and sharp peaks at low angles (i.e., larger interatomic distances), confirming the presence of quasi-2D crystals (Figure 2.1b).

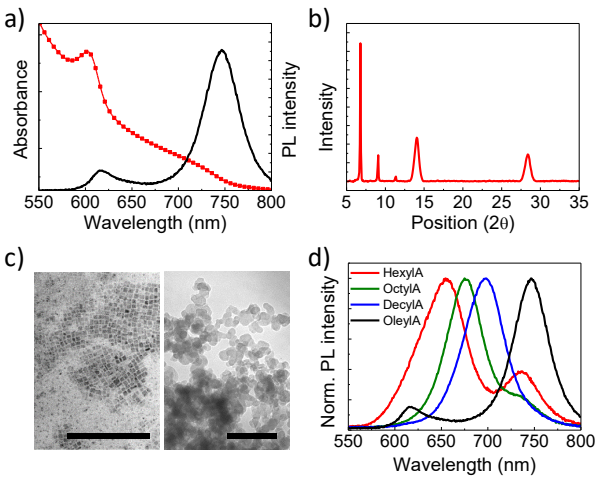

Figure 2.1. a) Absorbance (red) and PL spectra (black), b) X-ray diffraction pattern and c) TEM images (scale bar is 200 nm) of the perovskite nanostructures obtained in the presence of oleylamine. The TEM images highlight the formation of 3D (left) and quasi-2D (right) structures. d) Comparison of the PL spectra collected for NCs synthesized using alkylammonium ligands with increasing alkyl-chain length.

TEM characterization (Figure 2.1c) revealed the presence of cubic-shaped perovskite nanocrystals with a typical dimension of 10 nm, consistent with the broad peaks in XRD as well as with the low-energy optical transitions ascribed to 3D NCs. Additionally, TEM analysis also showed large nanosheets without a well-defined morphology, similar to previous observations of quasi-2D oleylammonium lead halide perovskites,[103] confirming the coexistence of 3D and quasi-2D iodide nanocrystals.

It has been reported that the dimensionality of the NCs can be modulated by varying the alkyl chain length and/or the concentration of the ligands, and consequently, tune the luminescence properties.[99,105] With this idea, we studied the luminescent characteristics of the NCs when replacing oleylA by smaller saturated alkylamines with decreasing chain lengths, decylamine (decylA), octylamine (octylA) and hexylamine (hexylA). All other synthesis conditions were kept unvaried. While the iodide perovskite NCs with oleylA ligands emit mainly in the NIR, a decrease of the alkyl chain length of the ligand led to a progressive blue-shift of the PL maximum. In particular, we obtained colloidal dispersions in toluene (Figure 2.1d) with emission in the red part of the spectrum (PL maxima centred at 697 nm, 676 nm and 655 nm for decylA, octylA and hexylA, respectively). This behaviour has been attributed to the faster diffusion of shorter chain ammonium ions.[105–107] Thus, the favoured intercalation of shorter amines results in the formation of quasi-2D structures with thinner

metal halide octahedra sheets (i.e., lower n-values), leading to exciton confinement and hence an increased bandgap. At the same time, shorter amines led to a reduction of the spacing between the lead halide-based layers in the quasi-2D structure. Moreover, the use of shorter amines resulted in an enhancement of the PLQY as compared to the oleylA suspension (28%), reaching values of 90%, 85% and 68% for decylA, octylA and hexylA, respectively. A hypothesis for such significant increase is a favoured quasi-2D crystal formation, with less defects when rigid and linear molecules are used. However, as in the original synthesis with oleylA, most PL spectra present broad and multi-component peaks, which points to the coexistence of different emitting species (most likely a dispersion in the n-values).

The use of additional solvents during the purification step can lead to materials with enhanced optical properties.[108] In our case, the addition of 1-BuOH in large quantities during the first centrifugation step resulted in NCs that exhibit a small blue-shift of the main PL signals and, more importantly, more symmetric PL spectra (Figure 2.2a), suggesting a smaller distribution of emitting species. Based on the literature, these PL bands have been ascribed to quasi-2D lead iodide NCs with n = ∞ (3D), n = 7, n = 6, and n = 5, respectively.[101] The decrease in the length of the alkylammonium ligand from oleylA to decylA resulted in a PL shift of about 147 meV, 58 meV from decylA to octylA and 55 meV from octylA to hexylA (Figure 2.2b). The PLQY value was found to increase only for the hexylA sample (82%), while NCs with oleylA, decylA and octylA showed similar PLQYs.

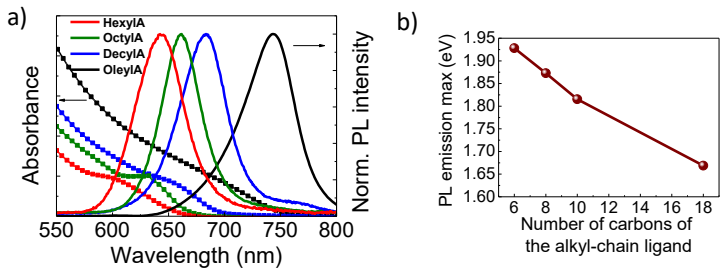

Figure 2.2. a) Absorbance (square symbols with lines) and PL (lines) spectra for purified samples (with 1-BuOH) and with different alkylammonium ligands. b) PL peak maxima as a function of the number of carbon atoms in the alkyl chain of the ligands.

The diffraction patterns of the further purified samples also showed the characteristic sharp peaks at low angles (Figure 2.3a), indicative of the formation of low-dimensional perovskite crystals. The XRD signals were found to shift as a function of the alkyl chain length. Indeed, the interlayer spacing increased linearly with increasing the alkyl chain length, in agreement with previous reports.[109,110] The formation of quasi-2D crystals with different periodicities is

consistent with the progressive blue-shift of the optical characteristics presented in Figure 2.2a, as a result of quantum confinement.[99,111]

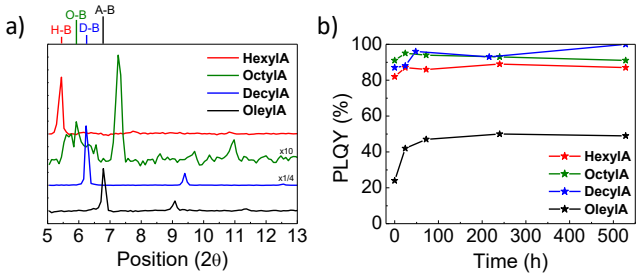

Figure 2.3. a) X-ray diffraction patterns of the samples with the different long-chain cations. b) PLQY for the same series of materials measured over time.

Additionally, the modified NCs demonstrated excellent stability when kept dispersed in toluene in ambient conditions, with their PLQY slightly increasing in the first 50 hours after synthesis and then remaining constant for up to 500 hours (Figure 2.3b). Although the reason for the initial PLQY increase is not clear, it is likely a consequence of passivation upon air exposure, as observed by others in lead halide perovskites.[112]

2.4. Published work

The work was carried out in collaboration with PNEL, the research group of Prof. Tae-Woo Lee in the Seoul National University in South Korea. The research topic was initiated during a secondment in Seoul in 2018, in close collaboration with Dr. Young Hoon Kim and Seung Hyeon Jo. The work continued in the Institute of Molecular Science at the Universidad de Valencia.

The publication is reproduced by permission of The Royal Society of Chemistry. DOI: 10.1039/C9NR04520A, Nanoscale, 2019, 11, 12793-12797.

Nanoscale

COMMUNICATION

View Article Online
View Journal | View Issue

Cite this: *Nanoscale*, 2019, **11**, 12793

Received 27th May 2019,
Accepted 14th June 2019

DOI: 10.1039/c9nr04520a

rsc.li/nanoscale

Low-dimensional iodide perovskite nanocrystals enable efficient red emission†

Laura Martínez-Sarti, [a] Seung Hyeon Jo,[b] Young-Hoon Kim,[b] Michele Sessolo, [a] Francisco Palazon, *[a] Tae-Woo Lee [b] and Henk J. Bolink [a]

We report herein a simple ligand-assisted reprecipitation method at room temperature to synthesize mixed-cation hybrid organic–inorganic perovskite nanocrystals with low structural dimensionality. The emission wavelength of iodide-based perovskites is thus tuned from the near-infrared to the red part of the visible spectrum. While this is mostly achieved in the literature by addition of bromide, we demonstrate here a controllable blueshift of the band gap by varying the chain length of the alkylammonium ligands. Furthermore, an antisolvent washing step was found to be crucial to purify the samples and obtain single-peak photoluminescence with a narrow linewidth. The so-formed nanocrystals exhibit high and stable photoluminescence quantum yields exceeding 90% over 500 hours, making these materials ideal for light-emitting applications.

Metal halide perovskites have emerged in the last few years as promising materials for applications in optoelectronic devices such as solar cells,[1–3] light-emitting diodes (LEDs)[4–8] or X-ray detectors.[9,10] The reason behind the interest in perovskite nanocrystals (NCs) is based on their high photoluminescence quantum yield (PLQY), related to the spatial charge carrier confinement and passivation of surface states by organic capping ligands, as well as their narrower emission lines and higher stabilities as compared to their bulk counterparts.[11–15] Considering the simple methods that have been developed for their synthesis, perovskite NCs have become ideal materials for electroluminescent phosphor applications.

Although seminal reports have focused on hybrid methylammonium lead halide perovskites,[16] several recent studies have shown that the introduction of inorganic Cs^+ cations in small quantities (≤20%) into these hybrid materials leads to beneficial effects including an enhanced stability and reproducibility.[17–19] It is well known that the shape, size and optical properties of perovskite NCs are strongly affected by the ligands.[20–27] When the size of nanocrystals is less than or equal to the exciton Bohr diameter, they exhibit quantum confinement, and the optical absorption and photoluminescence (PL) are blue-shifted compared to their bulk counterparts. It has been reported that the dimensionality of the NCs can be modulated by varying the alkyl chain length and/or the concentration of the surface ligands, and consequently, tuning the emission features.[21,24] Fundamentally, this is linked to the fact that the ammonium head group of alkylammonium ligands can occupy the A-site in the $APbX_3$ perovskite structure. As a result, using long ammonium (LA) molecules in combination with a small A-cation such as methylammonium ($CH_3NH_3^+$, MA), formamidinium ($CH(NH_2)_2^+$, FA) or Cs^+ may lead to the so-called Ruddlesden–Popper quasi-2D phase,[28,29] with the generic formula $(LA)_2(A)_{n-1}Pb_nI_{3n+1}$, where perovskite slabs of n layers are separated by a bilayer of the large ammonium cation. These quasi-2D structures show quantum confinement effects strongly related to the n-value,[21,30] which in turn can be tuned by the amount and length of the alkyl chain used in the synthesis. More precisely, the thickness of a single lead iodide perovskite monolayer is approximately 6.3 Å, corresponding to twice the length of the Pb–I bond, or in other words to the height of a PbI_6 octahedron (octahedral tilting and slight differences in Pb–I bond lengths are ignored in this approximation).[29] In contrast, the reported values for the exciton Bohr diameter of $MAPbI_3$ are around 2.2 nm [31] to 4.6 nm.[32] Therefore, quasi-2D $(LA)_2(MA)_{n-1}Pb_nI_{3n+1}$ start showing quantum-confinement effects when the n value is roughly below 10 (corresponding to a layer thickness of around 6.3 nm, hence comparable to the exciton Bohr diameter). Above a value of *ca.* 10, n can be considered large enough so that the quasi-2D crystal is equivalent to a 3D $MAPbI_3$ structure ($n = \infty$).[29]

[a]*Instituto de Ciencia Molecular (ICMol), Universidad de Valencia, Catedrático José Beltrán, 2, 46980 Paterna, Spain. E-mail: francisco.palazon@uv.es*
[b]*Department of Materials Science and Engineering, Institute of Engineering Research, Research Institute of Advanced Materials, Nano Systems Institute (NSI), BK21 PLUS SNU Materials Division for Educating Creative Global Leaders, Seoul National University, 1 Gwanak-ro, Gwanak-gu, Seoul 08826, Republic of Korea*
†Electronic supplementary information (ESI) available. See DOI: 10.1039/c9nr04520a

As has recently been shown, these quantum-confined quasi-2D perovskites (with $n < 10$) are ideal materials for efficient perovskite LEDs.[5]

In this work, we describe a simple ligand-assisted reprecipitation (LARP) method at room temperature (RT) to prepare efficient red-emitting low-dimensional NCs and study the change in the optical properties as a function of different synthesis conditions. In particular, we will discuss the variation of the band gap from the near-infrared (NIR) to the visible range as a function of the alkylammonium molecule length. Mixed-cation MA-Cs perovskite NCs were prepared by a direct, non-template method synthesis based on a previously published protocol[33] with slightly modified conditions and starting materials. Briefly, a solution of PbI_2 (dissolved in 1-octadecene (ODE) with oleylamine (oleylA) and oleic acid (OA) ligands) was injected at RT into a solution of MAI and CsI (0.8 : 0.2 ratio; dissolved in a mixture of 1-butanol (1-BuOH) and ODE with OA), leading to the formation of perovskite NCs, which were subsequently washed by centrifugation steps (see the Experimental section of the ESI† for more details). The optical characteristics of the obtained NCs are presented in Fig. 1a. An absorption onset of around 740 nm with the corresponding photoluminescence peak centred at 747 nm (FWHM of 45 nm), together with a sharp absorption feature at 617 nm and its Stokes shifted PL peak centred at 625 nm (FWHM of about 30 nm), can be observed. It is worth noting that when the synthesis is carried out at 0 °C instead of RT, no significant spectral differences are observed, whereas at high temperature a rather clear yellow solution with a very low PL is obtained (Fig. S1, ESI†). Hence, all further syntheses were carried out at RT. The two aforementioned features observed in the optical characterization of the sample (Fig. 1a) are consistent with 3D (narrow bandgap) and quasi-2D (wide bandgap due to quantum confinement) iodide perovskite NCs.[21,34] We note that this is not the first report on quantum confined perovskite structures using oleylamine. Almeida *et al.* have shown that oleylammonium cations can induce anisotropic growth,[35] while others have claimed that oleylammonium (despite the length of its backbone and its non-planar configuration caused by the vinyl bond) may lead to quasi-2D structures.[36,37] In order to further prove this hypothesis, we conducted XRD analysis (Fig. 1b) on drop-cast NC films. The broad diffraction peaks centred at $2\Theta = 14.0°$ and $2\Theta = 28.3°$ are consistent with the formation of 3D iodide perovskite NCs. In addition, sharp peaks at low angles (*i.e.*, larger interatomic distances) are clearly visible, confirming the presence of quasi-2D crystals consisting of perovskite sheets separated by long-chain oleylammonium cations. In principle, it is possible to determine the n value of quasi-2D Ruddlesden–Popper crystals with the chemical formula $(LA)_2(A)_{n-1}Pb_nI_{3n+1}$ by XRD. Nonetheless, this requires high quality data up to very low diffraction angles,[29,38] which we were not able to acquire here. Moreover, the XRD peaks' positions and spacing do not depend only on the n value but also on the length of the LA molecule, so that our data cannot be directly compared with those of Ruddlesden–Popper crystals obtained with other LA molecules such as butylammonium.[29] However, based on PL characterization, it is reasonable to assume a value of $n = 4$ for the emission centered at 625 nm.[39] It is worth noting that pure 2D ($n = 1$) lead iodide perovskites exhibit an emission peak around 525 nm.[39,40] Hence the formation of pure 2D crystals can be excluded. TEM characterization (Fig. 1c) revealed the presence of cubic-shaped perovskite nanocrystals with a typical dimension of 10 nm. This is consistent with the broad peaks in XRD as well as the low-energy optical transitions previously discussed for 3D NCs. Additionally, TEM analysis also showed large nanosheets without a well-defined morphology, similar to the previous observations of quasi-2D oleylammonium lead halide perovskites,[36] confirming the coexistence of both 3D and quasi-2D iodide nanocrystals.

While the iodide perovskite NCs discussed so far emit preferentially in the NIR, the PL can be blue-shifted through a reduction of the material structural dimensionality, *i.e.* the number of lead halide layers separated by alkylammonium in the quasi-2D structure. Several reports have shown that the inorganic layer thickness can be tuned by the amount and length of the alkylammonium ligands.[23,30,41–43] From this point we controlled the PL maximum by replacing oleylA ligands by smaller saturated alkylamines with decreasing chain lengths: decylamine (decylA), octylamine (octylA) and hexylamine (hexylA). All other synthesis conditions, in particular the concentration of alkylamine (thus also the amine/acid ratio), were unvaried. In all cases, the synthesis led to the formation of nanocrystals. The colloidal dispersions in toluene exhibited PL with maxima centred at 697 nm, 676 nm and 655 nm for decylA, octylA and hexylA, respectively (Fig. 1d). Hence a decrease of the alkyl chain length of the ligand led to

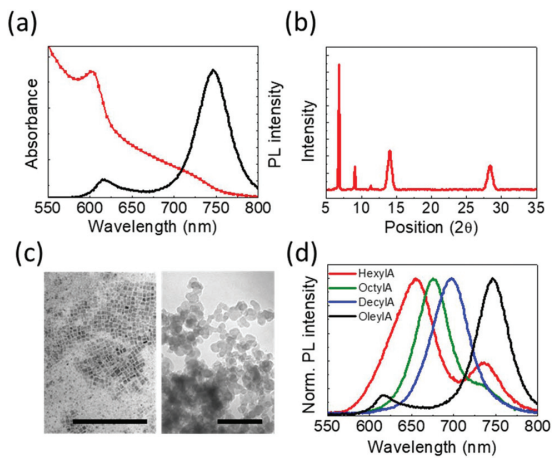

Fig. 1 (a) Absorbance (red line) and PL spectra (black line), (b) X-ray diffraction pattern and (c) TEM images (the scale bar is 200 nm) of the mixed Cs-MA perovskite nanostructures obtained using oleylamine as the ligand. The images illustrate the formation of 3D (left) and quasi-2D structures (right). (d) Comparison of the PL spectra registered for NCs obtained with different alkyl chain length ligands.

a progressive blue-shift of the PL maximum. This trend was also observed by other groups,[20,24,44] and some attributed it to the faster diffusion of shorter chain ammonium ions which results in faster on–off exchange rates. It is important to note that shorter amines not only lead to a reduction of the space between the 3D "slabs" in the quasi-2D structure, directly linked to the alkyl chain length. The easier intercalation of the shorter amines results in the stabilization of thinner 3D layers (*i.e.*, lower *n*-values) leading to exciton confinement and hence a PL blue-shift. Additionally, the use of shorter amines results in an enhancement of the PLQY compared to the oleylA sample (28%), reaching values of 90%, 85% and 68% for decylA, octylA and hexylA, respectively. However, as in the original synthesis with oleylA, most PL spectra present broad and multiple peaks, which points out the coexistence of different species (different *n*-values).

In order to purify the samples, we tested the addition of 1-BuOH in large quantities during the first centrifugation step (see the Experimental section of the ESI† for more details). The use of additional solvents during the purification step has been reported to change the optical properties of the synthesized product.[45] Upon this treatment, the resulting NC dispersions showed a main PL peak centred at 743 nm, 683 nm, 662 nm and 643 nm for the oleylA, decylA, octylA and hexylA ligand, respectively (Fig. 2a). Based on the literature, these PL bands can be ascribed to quasi-2D lead iodide NCs with $n = \infty$ (3D), $n = 7$, $n = 6$, and $n = 5$, respectively.[39] As can be seen by comparing Fig. 2a and 1d, this modified washing step leads to more symmetric PL spectra that suggest a smaller distribution of species in the suspension. Representative TEM images of samples synthesized with short amines and washed with butanol are presented in Fig. S2.† Additionally, we observed a small blue-shift of the main PL signal between the pristine samples and the samples washed with 1-BuOH (Fig. S3, ESI†). Also worth noting is the steady change of the PL maximum of the treated samples as a function of the size of the alkyl chain ligand, represented in Fig. 2b. Decreasing the length of the capping ligand from oleylA to decylA results in a PL emission shift of about 147 meV, which further shifts by 58 meV and 55 meV from decylA to octylA and from octylA to hexylA, respectively. The associated PLQYs for the further purified NCs were 24%, 87%, 91% and 82% for oleylA, decylA, octylA and hexylA, respectively. Remarkably, the use of 1-BuOH during the purification process induced a PLQY enhancement in the hexylA sample, while oleylA, decylA and octylA PLQYs remained almost unvaried.

On these further purified samples, we also observed the characteristic sharp peaks at low angles in the diffraction patterns (Fig. 3a) (see Fig. S4† for complete X-ray diffraction patterns). As expected from the change in the alkyl chain length, these peaks are also shifted. Indeed, the interlayer spacing increases linearly with increasing the alkyl chain length, in agreement with previous reports.[43,46] The formation of quasi-2D crystals with different periodicities as a function of alkyl

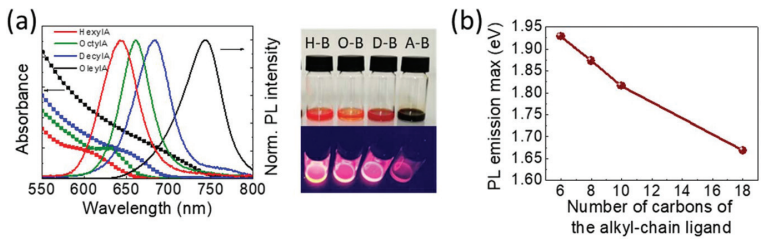

Fig. 2 (a) Absorbance (square symbols with lines) and PL (lines) for further purified samples (with 1-BuOH) obtained using different ligands during the synthesis. On the right, photographs of colloidal solutions under ambient light (top) and under UV excitation (λ = 365 nm) (bottom) for hexylA (H-B), octylA (O-B), decylA (D-B) and oleylA (A-B). (b) Energy at the PL maximum as a function of the number of carbon atoms in the capping ligand.

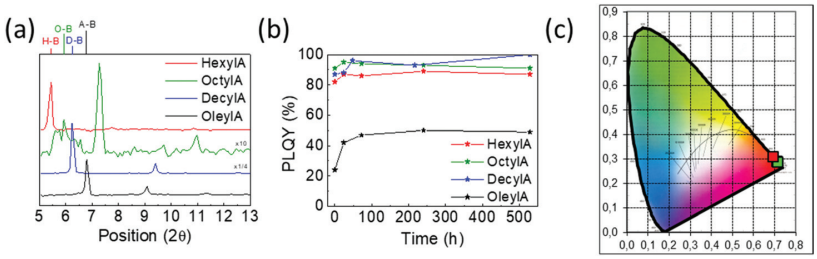

Fig. 3 (a) X-ray diffraction patterns of mixed Cs-MA NCs obtained with different alkylamines. (b) PLQY for suspensions of the same compounds monitored over time. (c) Corresponding CIE coordinates for the different samples.

chain length, as evidenced by XRD, is consistent with the progressive blue-shift of the optical characteristics presented in Fig. 2a, as a result of quantum confinement.[21,47]

In order to evaluate the stability of the materials, the nanocrystals were kept dispersed in toluene, under ambient air. The only noticeable change in spectral features is a slight narrowing of the emission from the oleylA sample after the first day (see Fig. S5†). PLQY values were measured over time (Fig. 3b). All samples exhibit a slight increase in PLQY in the first 50 hours. The exact reason for this effect is not clear, although it may be ascribed to passivation upon air exposure, as observed by others in lead iodide perovskites.[48] In all cases, after this initial increase, the PLQY remained constant up to 500 hours, demonstrating an excellent stability for iodide perovskite nanocrystals.[49] Furthermore, we note that replacing long-chain unsaturated oleylamine by shorter saturated alkylamines leads to a significant increase in absolute PLQY, with values that are close to unity. We speculate that this may be linked to a better quasi-2D crystal formation with less defects when rigid and straight spacer molecules are used. Corresponding CIE coordinates for the different samples are plotted in Fig. 3c.

Conclusions

In summary, we have presented a simple method to prepare efficient red-emitting hybrid quasi-2D perovskite nanocrystals of the type $(LA)_2(A)_{n-1}Pb_nI_{3n+1}$, where LA is an alkylamine and A a mixture of MA and Cs^+. We have discussed the effects of the synthesis conditions on the material structural and optical properties. In particular, we have shown that the PL can be tuned from the near-infrared to the visible region by the alkyl chain length and that the addition of butanol in the first washing step leads to an improved purity of the sample with a higher PLQY, exceeding 90%. The high PLQY is maintained for more than 500 h, making these materials especially promising for applications in light-emitting diodes and phosphors.

Conflicts of interest

There are no conflicts to declare.

Acknowledgements

The research leading to these results has received funding from the European Union Programme for Research and Innovation Horizon 2020 (2014–2020) under the Marie Skłodowska-Curie Grant Agreement PerovSAMs No. 747599 and the Spanish Ministry of Economy and Competitiveness (MINECO) *via* the Unidad de Excelencia María de Maeztu MDM-2015-0538, MAT2017-88821-R, ERA NET PCIN-2017-014, PCIN-2015-255, predoctoral grant to L. M.-S., and RyC contract to M. S. This work was also supported by the National Research Foundation of Korea (NRF) grant funded by the Korea government (MSIT) (NRF-2016R1A3B1908431). We also acknowledge the SCSIE Burjassot where the TEM analysis was performed.

Notes and references

1 L. Zhang, X. Zhou, X. Zhong, C. Cheng, Y. Tian and B. Xu, *Nano Energy*, 2019, **57**, 248–255.
2 F. Fu, T. Feurer, T. P. Weiss, S. Pisoni, E. Avancini, C. Andres, S. Buecheler and A. N. Tiwari, *Nat. Energy*, 2016, **2**(1), 16190.
3 W. S. Yang, B.-W. Park, E. H. Jung, N. J. Jeon, Y. C. Kim, D. U. Lee, S. S. Shin, J. Seo, E. K. Kim, J. H. Noh and S. Il Seok, *Science*, 2017, **356**, 1376–1379.
4 Y. H. Kim, H. Cho, J. H. Heo, T.-S. Kim, N. Myoung, C. L. Lee, S. H. Im and T.-W. Lee, *Adv. Mater.*, 2015, **27**, 1248–1254.
5 X. Yang, X. Zhang, J. Deng, Z. Chu, Q. Jiang, J. Meng, P. Wang, L. Zhang, Z. Yin and J. You, *Nat. Commun.*, 2018, **9**(1), 570.
6 Q. A. Akkerman, L. Martínez-Sarti, L. Goldoni, M. Imran, D. Baranov, H. J. Bolink, F. Palazon and L. Manna, *Chem. Mater.*, 2018, **30**, 6915–6921.
7 H. Cho, S.-H. Jeong, M.-H. Park, Y.-H. Kim, C. Wolf, C.-L. Lee, J. H. Heo, A. Sadhanala, N. Myoung, S. Yoo, S. H. Im, R. H. Friend and T.-W. Lee, *Science*, 2015, **350**, 1222.
8 K. Lin, J. Xing, L. N. Quan, F. P. G. de Arquer, X. Gong, J. Lu, L. Xie, W. Zhao, D. Zhang, C. Yan, W. Li, X. Liu, Y. Lu, J. Kirman, E. H. Sargent, Q. Xiong and Z. Wei, *Nature*, 2018, **562**, 245–248.
9 H. Wei, Y. Fang, P. Mulligan, W. Chuirazzi, H. H. Fang, C. Wang, B. R. Ecker, Y. Gao, M. A. Loi, L. Cao and J. Huang, *Nat. Photonics*, 2016, **10**, 333–339.
10 J. A. Steele, W. Pan, C. Martin, M. Keshavarz, E. Debroye, H. Yuan, S. Banerjee, E. Fron, D. Jonckheere, C. W. Kim, W. Baekelant, G. Niu, J. Tang, J. Vanacken, M. Van der Auweraer, J. Hofkens and M. B. J. Roeffaers, *Adv. Mater.*, 2018, **30**(46), 1804450.
11 H. Huang, L. Polavarapu, J. A. Sichert, A. S. Susha, A. S. Urban and A. L. Rogach, *NPG Asia Mater.*, 2016, **8**, e328–e328.
12 F. Zhang, H. Zhong, C. Chen, X. G. Wu, X. Hu, H. Huang, J. Han, B. Zou and Y. Dong, *ACS Nano*, 2015, **9**, 4533–4542.
13 Y. H. Kim, G. H. Lee, Y. T. Kim, C. Wolf, H. J. Yun, W. Kwon, C. G. Park and T. W. Lee, *Nano Energy*, 2017, **38**, 51–58.
14 A. Dutta, S. K. Dutta, S. Das Adhikari and N. Pradhan, *Angew. Chem., Int. Ed.*, 2018, **57**, 9083–9087.
15 Y. H. Kim, C. Wolf, Y. T. Kim, H. Cho, W. Kwon, S. Do, A. Sadhanala, C. G. Park, S. W. Rhee, S. H. Im, R. H. Friend and T.-W. Lee, *ACS Nano*, 2017, **11**, 6586–6593.
16 L. C. Schmidt, A. Pertegás, S. González-Carrero, O. Malinkiewicz, S. Agouram, G. Mínguez Espallargas, H. J. Bolink, R. E. Galian and J. Pérez-Prieto, *J. Am. Chem. Soc.*, 2014, **136**, 850–853.

17 J. W. Lee, D. H. Kim, H. S. Kim, S. W. Seo, S. M. Cho and N. G. Park, *Adv. Energy Mater.*, 2015, **5**(20), 1501310.
18 G. Niu, W. Li, J. Li, X. Liang and L. Wang, *RSC Adv.*, 2017, **7**, 17473–17479.
19 X. Liu, Z. Yang, C. C. Chueh, A. Rajagopal, S. T. Williams, Y. Sun and A. K. Y. Jen, *J. Mater. Chem. A*, 2016, **4**, 17939–17945.
20 A. Pan, B. He, X. Fan, Z. Liu, J. J. Urban, A. P. Alivisatos, L. He and Y. Liu, *ACS Nano*, 2016, **10**, 7943–7954.
21 J. Cho, Y. H. Choi, T. E. O'Loughlin, L. De Jesus and S. Banerjee, *Chem. Mater.*, 2016, **28**, 6909–6916.
22 H. Huang, J. Raith, S. V. Kershaw, S. Kalytchuk, O. Tomanec, L. Jing, A. S. Susha, R. Zboril and A. L. Rogach, *Nat. Commun.*, 2017, **8**(1), 996.
23 I. Levchuk, P. Herre, M. Brandl, A. Osvet, R. Hock, W. Peukert, P. Schweizer, E. Spiecker, M. Batentschuk and C. J. Brabec, *Chem. Commun.*, 2017, **53**, 244–247.
24 S. Sun, D. Yuan, Y. Xu, A. Wang and Z. Deng, *ACS Nano*, 2016, **10**, 3648–3657.
25 J. Shamsi, Z. Dang, P. Bianchini, C. Canale, F. Di Stasio, R. Brescia, M. Prato and L. Manna, *J. Am. Chem. Soc.*, 2016, **138**, 7240–7243.
26 Z. Xiao, R. A. Kerner, N. Tran, L. Zhao, G. D. Scholes and B. P. Rand, *Adv. Funct. Mater.*, 2019, **1807284**, 1807284.
27 M. E. Kamminga, H. H. Fang, M. R. Filip, F. Giustino, J. Baas, G. R. Blake, M. A. Loi and T. T. M. Palstra, *Chem. Mater.*, 2016, **28**, 4554–4562.
28 Z. Wang, Q. Lin, F. P. Chmiel, N. Sakai, L. M. Herz and H. J. Snaith, *Nat. Energy*, 2017, **2**, 1–10.
29 C. C. Stoumpos, D. H. Cao, D. J. Clark, J. Young, J. M. Rondinelli, J. I. Jang, J. T. Hupp and M. G. Kanatzidis, *Chem. Mater.*, 2016, **28**, 2852–2867.
30 Y. Bekenstein, B. A. Koscher, S. W. Eaton, P. Yang and A. P. Alivisatos, *J. Am. Chem. Soc.*, 2015, **137**, 16008–16011.
31 K. Tanaka, T. Takahashi, T. Ban, T. Kondo, K. Uchida and N. Miura, *Solid State Commun.*, 2003, **127**, 619–623.
32 Z. Yang, A. Surrente, K. Galkowski, N. Bruyant, D. K. Maude, A. A. Haghighirad, H. J. Snaith, P. Plochocka and R. J. Nicholas, *J. Phys. Chem. Lett.*, 2017, **8**, 1851–1855.
33 X. Liang, R. W. Baker, K. Wu, W. Deng, D. Ferdani, P. S. Kubiak, F. Marken, L. Torrente-Murciano and P. J. Cameron, *React. Chem. Eng.*, 2018, **3**, 640–644.
34 D. H. Cao, C. C. Stoumpos, O. K. Farha, J. T. Hupp and M. G. Kanatzidis, *J. Am. Chem. Soc.*, 2015, **137**, 7843–7850.
35 G. Almeida, L. Goldoni, Q. Akkerman, Z. Dang, A. H. Khan, S. Marras, I. Moreels and L. Manna, *ACS Nano*, 2018, **12**, 1704–1711.
36 X. X. Zhang, C. Wang, Y. Zhang, X. X. Zhang, S. Wang, M. Lu, H. Cui, S. V. Kershaw, W. W. Yu and A. L. Rogach, *ACS Energy Lett.*, 2019, **4**, 242–248.
37 S. Ahmad, C. Hanmandlu, P. K. Kanaujia and G. V. Prakash, *Opt. Mater. Express*, 2014, **4**, 1313–1323.
38 M. C. Weidman, M. Seitz, S. D. Stranks and W. A. Tisdale, *ACS Nano*, 2016, **10**, 7830–7839.
39 Y. H. Chang, J. C. Lin, Y. C. Chen, T. R. Kuo and D. Y. Wang, *Nanoscale Res. Lett.*, 2018, **13**, 247.
40 J. V. Milić, J. H. Im, D. J. Kubicki, A. Ummadisingu, J. Y. Seo, Y. Li, M. A. Ruiz-Preciado, M. I. Dar, S. M. Zakeeruddin, L. Emsley and M. Grätzel, *Adv. Energy Mater.*, 2019, **1900284**, 1–12.
41 D. N. Congreve, M. C. Weidman, M. Seitz, W. Paritmongkol, N. S. Dahod and W. A. Tisdale, *ACS Photonics*, 2017, **4**, 476–481.
42 Z. Yuan, Y. Shu, Y. Xin and B. Ma, *Chem. Commun.*, 2016, **52**, 3887–3890.
43 Y. Takeoka, K. Asai, M. Rikukawa and K. Sanui, *Bull. Chem. Soc. Jpn.*, 2006, **79**, 1607–1613.
44 N. Pradhan, D. Reifsnyder, R. Xie, J. Aldana and X. Peng, *J. Am. Chem. Soc.*, 2007, **129**, 9500–9509.
45 L. Yuan, R. Patterson, X. Wen, Z. Zhang, G. Conibeer and S. Huang, *J. Colloid Interface Sci.*, 2017, **504**, 586–592.
46 S. Gonzalez-Carrero, G. M. Espallargas, R. E. Galian and J. Pérez-Prieto, *J. Mater. Chem. A*, 2015, **3**, 14039–14045.
47 J. Yan, W. Qiu, G. Wu, P. Heremans and H. Chen, *J. Mater. Chem. A*, 2018, **6**, 11063–11077.
48 Y. Tian, M. Peter, E. Unger, M. Abdellah, K. Zheng, T. Pullerits, A. Yartsev, V. Sundström and I. G. Scheblykin, *Phys. Chem. Chem. Phys.*, 2015, **17**, 24978–24987.
49 B. Luo, S. B. Naghadeh and J. Z. Zhang, *ChemNanoMat*, 2017, **3**, 456–465.

Electronic Supplementary Information

Low-dimensional Iodide Perovskite Nanocrystals Enables Efficient Red Emission

Laura Martínez-Sarti,[1] Seung Hyeon Jo,[2] Young-Hoon Kim,[2] Michele Sessolo,[1] Francisco Palazon,[1,*] Tae-Woo Lee[2] and Henk J. Bolink.[1]

[1] Instituto de Ciencia Molecular (ICMol), Universidad de Valencia, Catedrático José Beltrán, 2, 46980 Paterna, Spain

[2] Department of Materials Science and Engineering, Institute of Engineering Research, Research Institute of Advanced Materials, Nano Systems Institute (NSI), BK21 PLUS SNU Materials Division for Educating Creative Global Leaders, Seoul National University, 1 Gwanak-ro, Gwanak-gu, Seoul 08826, Republic of Korea

Experimental section

Synthesis of the MA-Cs mix cation NCs

For the MA-Cs nanocrystals (NCs) synthesis, 0.8 mmol of $PbBr_2$, 8 mL of 1-octadecene (ODE), 1.2 mL of oleylamine (or 0.73 mL of decylamine, 0.6 mL of octylamine or 0.48 mL of hexylamine) and 1.2 mL of oleic acid (OA) were mixed together, and the solution was labelled as *Pb solution*. Simultaneously, 0.64 mmol of methylammonium iodide (MAI) and 0.16 mmol of CsI (for a 0.8:0.2 MA-Cs ratio) were added to a solution with 8 mL of 1-butanol (1-BuOH), 4 mL of ODE and 1 mL of OA, labelling the results as *MACs solution*. Both solutions were heated at 130 ºC under continuous stirring for approximately 1 hour. Subsequently, and after cooling them down, 1 mL of *Pb solution* was injected drop by drop into 1 mL of *MACs solution* under vigorous stirring at room temperature. A dark red precipitate was immediately observed, indicating the formation of the NCs. Then, the dispersion was centrifuged at 12 krpm for 10 minutes, followed by a redispersion of the obtained precipitate in toluene. When a homogeneous dispersion was obtained, the result was centrifuged a second time at 3750 rpm for 10 minutes. The bright red luminescent supernatant was then studied and used as-obtained.

For the further purified samples, the synthesis was performed as described with the difference of adding 3 mL of 1-BuOH to the NCs dispersion prior to the first centrifugation step. The following steps were kept the same, taking the precipitate and redispersing it in toluene.

Optical characterization

The photoluminescence (PL) characteristics were studied using a Xe lamp coupled to a monochromator as the excitation source and an integrated sphere coupled to a spectrometer (Hamamatsu C9920-02 with a Hamamatsu PMA-11 optical detector) in order to quantitatively determine the PLQYs. Samples were excited at 530 nm and neat toluene was used as reference. Most samples had a 0.4 - 0.5 of absorption for an accurate quantitative PLQY value. UV-visible spectra of the colloidal dispersions were recorded using quartz cuvettes in a UV-visible spectrophotometer Agilent 8453E.

Transmission electron microscopy

TEM images were obtained with a JEOL JEM1010 transmission electron microscope operated at 100 kV.

X-ray diffraction

X-ray diffraction was measured with a Panalytical Empyrean diffractometer equipped with CuKα anode operated at 45 kV and 30 mA and a Pixel 1D detector in scanning line mode. Single scans were acquired in the 2Θ = 5° to 35° range in Bragg-Brentano geometry in air.

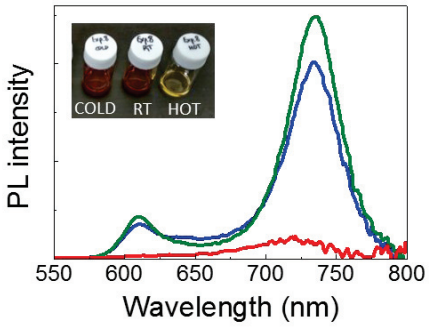

Fig. S1 PL emission out of samples synthesized at 0 ºC (blue), room temperature (green) and 134 ºC (red). Inset shows a photograph under visible white light of the three colloidal dispersions.

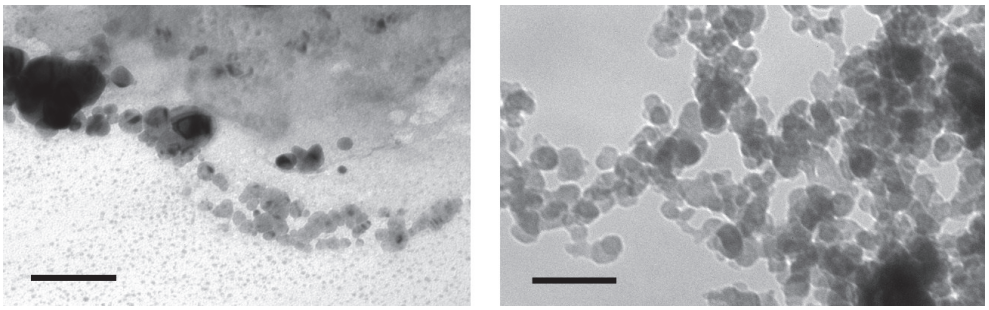

Fig. S2 TEM images of samples synthesized with hexylamine (left) and decylamine (right) after washing with butanol. Scale bars are 100 nm.

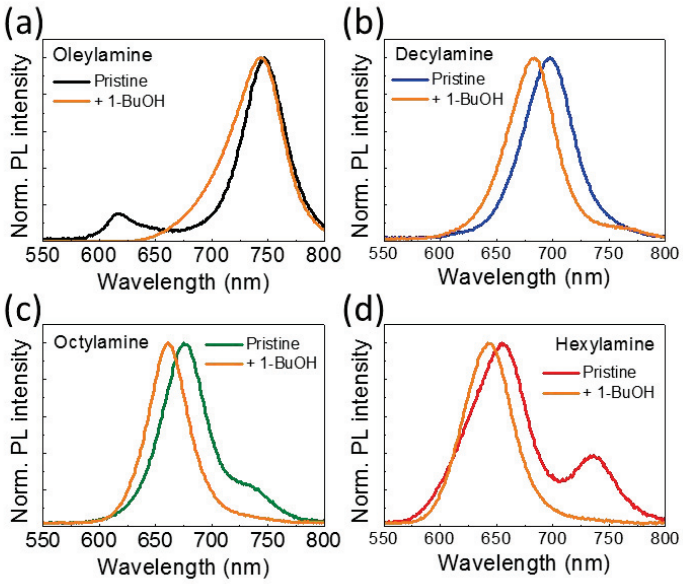

Fig. S3 PL spectra comparison between pristine and further purified NCs (orange lines) for samples with (a) oleylamine, (b) decylamine, (c) octylamine and (d) hexylamine.

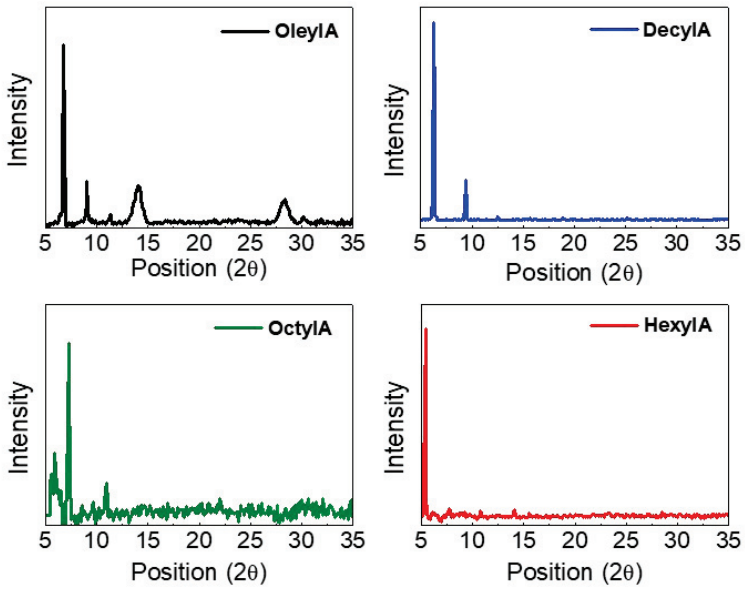

Fig. S4 X-ray diffraction pattern of the different further purified samples plotted from 5° to 35°. All samples show sharp peaks at low angles ascribed to quasi-2D nanocrystals. Only oleylA sample shows additional broad peaks corresponding to 3D NCs.

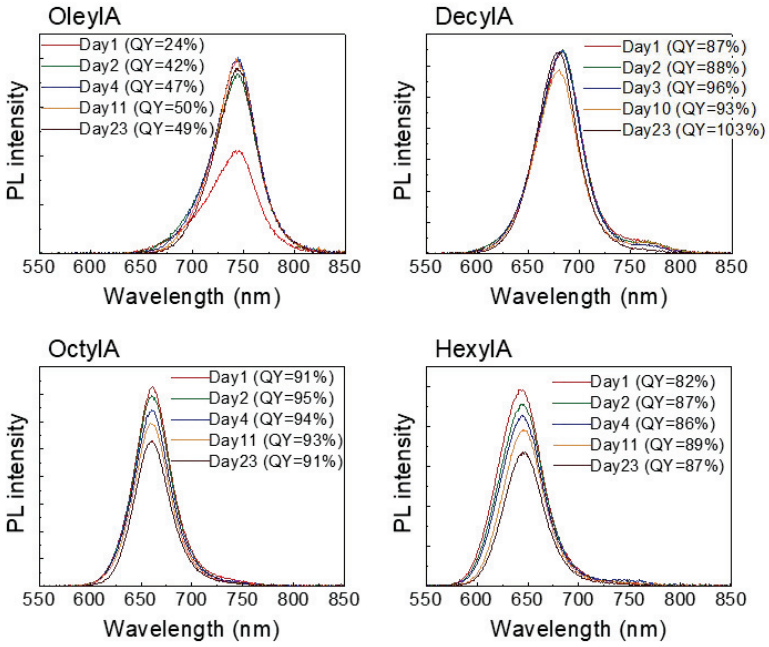

Fig. S5 PL spectra of different samples upon ageing.

Chapter 3.

Efficient photoluminescent thin films consisting of anchored hybrid perovskite nanoparticles

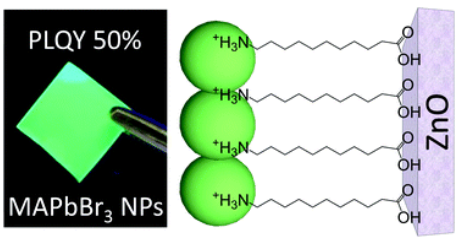

3.1. Motivation, work description and achievement

As described in the thesis introduction, the preparation of LEDs by solution deposition techniques offers several advantages, such as inexpensive manufacturing, reduced complexity and the possibility of large-scale production. In multilayer LEDs, however, several layers have to be coated one on top of each other, which can lead to partial redissolution or intermixing between the adjacent layers. To reduce this problem, one possibility is the addition of a cross-linker to the solution of the compound to be coated, in order to make the film resistant to further solution-processing. Unfortunately, cross-linkers are not chemically compatible with all materials and can introduce trap states due to unreacted initiator or crosslinking moieties.

In this thesis a different and novel approach is attempted, which relies on the fixation of the light emitting species to a previously deposited layer. For this, a bifunctional ligand (11-aminoundecanoic acid hydrobromide) is used for the synthesis of highly photoluminescent $MAPbBr_3$ NPs. Dispersions of NPs with a diameter below 10 nm and a PLQY of about 80% were readily obtained at RT and in atmospheric conditions. The bifunctional ligand, in addition to coordinate to the NPs, allows them to anchor on a variety of conducting polymers and inorganic semiconducting surfaces. In this thesis it was evaluated on ZnO and PEDOT:PSS thin films, resulting in bright films with a PLQY exceeding 50%. The effective anchoring of semiconducting NPs to different type of surfaces opens new paths for the preparation of simple and inexpensive solution-based multilayer LEDs.

3.2. Experimental details and methodology

The 11-aminoundecanoic acid was initially converted to its ammonium salt ($Br^-NH_3^+$-C_{10}-COOH) by reaction with an excess of HBr, to enhance its solubility in DMF. The $MAPbBr_3$ NPs were obtained with ligand-assisted reprecipitation (LARP) synthesis procedure, taking advantage of the interplay between a polar solvent (DMF, able to solubilize the perovskite precursors) and a non-polar one (toluene) as described in previously published protocols.[26,113]

$PbBr_2$ and oleic acid were dissolved in DMF and referred to as *solution A*. Subsequently, a volume of this solution was added into *solution B*, a DMF solution of MABr with varying amounts of $Br^-NH_3^+$-C_{10}-COOH. Then, this precursor solution (A+B) was rapidly injected into toluene under vigorous stirring either at RT or at a temperature of 60 °C. A yellow-green suspension was immediately obtained, consequence of the formation of the NPs. The solution was centrifuged to remove larger aggregates, and a bright luminescent supernatant suspension was obtained.

ZnO films were prepared from ZnO NPs suspensions (40 wt% in ethanol from Sigma-Aldrich, with an average particle size of 35 nm) diluted in ethanol, by spin-coating using a GYRSET®

(closed cover coating technology) followed by annealing on a hot plate. In order to anchor the $MAPbBr_3$ NPs onto the ZnO films, the ZnO coated substrates were immersed into the NPs suspension for 12 hours and subsequently rinsed with toluene.

The PL characteristics were studied using a Xe lamp coupled to a monochromator as the excitation source and an integrated sphere coupled to a spectrometer (Hamamatsu C9920-02 with a Hamamatsu PMA-11 optical detector) in order to quantitatively determine the PLQY. UV-visible absorption spectra of the films were collected using an optical fibre based Avantes Avaspec2048 spectrophotometer. UV-visible spectra of the dispersions were recorded using a quartz cuvettes spectrometer in a UV-visible spectrophotometer Agilent 8453E. TEM and high resolution TEM (HR-TEM) were performed with a Field Emission Gun (FEG) TECNAI G2 F20 microscope operated at 200 kV. LEDs were characterized under inert atmosphere inside a nitrogen filled glovebox. The current density and luminance versus voltage characteristics were measured using a Keithley 2400 Source-Meter and a photodiode coupled to a Keithley 6485 pico-ammeter, using a Minolta LS100 camera to calibrate the photocurrent. The AFM images were collected with a Digital Instrument Veeco Nanoscope IVa AFM microscope in tapping mode, using silicon tips with natural resonance frequency of 320 kHz and with an equivalent constant force of 42 N m^{-1}.

3.3. Results and discussion

The synthesis of nanocrystals with the desired properties requires, among other parameters, the careful choice of the ligand, i.e. the surfactant molecule that will bond to the crystal surface and limit its size at the nanoscale. As these materials have a large surface-to-volume ratio, the surface is the dominant player in most physical and chemical processes.[114] In our group and in collaboration with the group of Prof. Mhaisalkar in Singapore, we developed the synthesis of $MAPbBr_3$ NPs using 11-aminoundecanoic acid hydrobromide ($Br^-NH_3^+$-C_{10}-COOH) as a ligand, in contrast to more commonly used long-chain ammonium cations or amines, such as oleylammonium halide or octylammonium halide, among many others.[67,105,115] This particular ligand has two different functionalities; on the one hand, the ammonium cation efficiently tether to the surface of the perovskite NPs, while the carboxyl group at the other extreme allows the anchoring of the NPs on functional surfaces, such as metal oxides.[116]

While developing the NPs synthesis, we observed that the optical properties were strongly dependent on the quantity of ligand employed. In this regard, when a molar ratio of NH_3^+-C_{10}-COOH/MA = 2 was used during the synthesis, a blue emitting NPs suspension was obtained, in contrast with the green luminescent NPs obtained with a NH_3^+-C_{10}-COOH/MA = 0.5 molar ratio (Figure 3.1, Table 1).

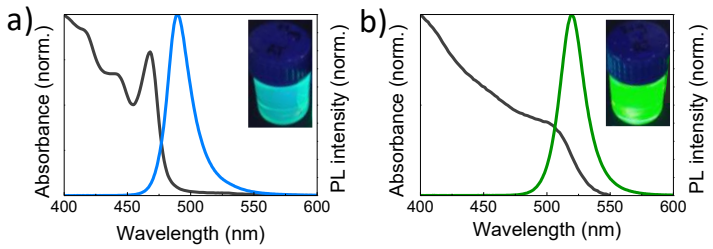

Figure 3.1. Absorption (gray) and PL spectra (blue and green) of $MAPbBr_3$ NPs colloids in toluene for $Br^-NH_3^+$-C_{10}-COOH/MA molar ratios of a) 2 and b) 0.5. Insets: photographs of each colloidal suspension under UV light excitation (λ = 365 nm).

NH_3^+-C_{10}-COOH/MA molar ratio	Maximum PL emission	FWHM	PLQY (excited at 380 nm)
2	490 nm	22 nm	25%
0.5	521 nm	20 nm	80%

Table 3.1. Photoluminescent characteristics of NPs obtained from the synthesis with different ligand contents.

We concluded that this was due to an equilibrium between the formation of three-dimensional $MAPbBr_3$ NPs and layered perovskite structures (2D) formed with the NH_3^+-C_{10}-COOH long-chain ammonium ligand.[32,117–119] Thereby, when a high ligand content is used in the synthesis (NH_3^+-C_{10}-COOH/MA = 2), mainly 2D perovskite nanostructures are obtained, showing the characteristic intense and sharp excitonic peak in the low energy part of the absorption spectra. On the other hand, by reducing the amount of ligand (NH_3^+-C_{10}-COOH/MA = 0.5), the typical $MAPbBr_3$ absorption and emission spectra can be observed, as a footprint of 3D NPs formation. Additionally, even if other works have shown that the temperature of the non-polar solvent is of special importance to define the NPs size and emission wavelength,[113] we achieved a rather temperature independent synthesis using the $Br^-NH_3^+$-C_{10}-COOH as a ligand, as the synthesis carried out at RT and 60 ºC led to similar results (Figure 3.2).

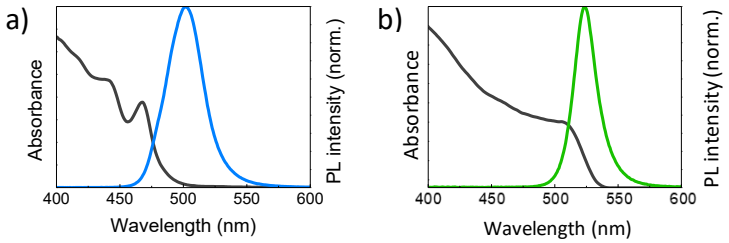

Figure 3.2. Absorption (grey) and PL spectra (blue and green) of $MAPbBr_3$ NPs colloidal solutions in toluene at 60 °C for $Br^-NH_3^+$-C_{10}-COOH/MA molar ratios of a) 2 and b) 0.5.

This hypothesis was confirmed by studying the material morphology by TEM. The images of the NPs suspensions prepared at RT show the presence of the perovskite NPs with a diameter in the 6-12 nm range (Figure 3.3a). With increased $Br^-NH_3^+$-C_{10}-COOH content, the morphology changes showing wide 2D sheets (50-200 nm) in combination with spherical nanocrystals (Figure 3.3b).

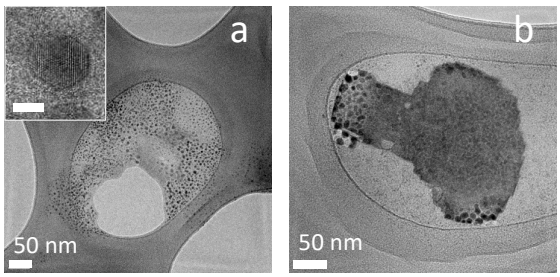

Figure 3.3. a) TEM image of the $MAPbBr_3$ NPs prepared using a molar ratio $Br^-NH_3^+$-C_{10}-COOH/MABr = 0.5 at RT (Figure 3.1a). Inset: High-resolution TEM image of an isolated NP (scale bar 4 nm). b) TEM image of the perovskite nanostructures obtained at RT in the presence of an excess of $Br^-NH_3^+$-C_{10}-COOH (Figure 3.1b).

This mixture of nanostructures has been previously described, and it is believed to originate from the competition among the formation of 3D and 2D-type perovskites.[26,120] More recently, it has been shown that under electron beam irradiation hybrid and all-inorganic lead halide perovskite nanocrystals can rapidly degrade leading to high contrast Pb° particles. This phenomenon would also explain the observation of spherical nanocrystals in the structures obtained with a high ligand content.[121]

The ligand used in the synthesis has a carboxyl group that, in principle, allows the anchoring of the NPs on functional surfaces. Thus, to examine the adhesion properties of the NPs, the suspension of the $MAPbBr_3$ NPs was used to sensitize ZnO films coated onto ITO/glass substrates. The ZnO is a n-type semiconductor widely used as electron injection layer in OLEDs.[122] When the ZnO coated substrates were immersed into the NPs suspension for 12 hours and then rinsed with toluene, the ZnO/$MAPbBr_3$ NPs films exhibited bright photoluminescence under UV light excitation (Figure 3.4a, Table 2). Importantly, the PLQY of these films was as high as 52% when excited at 380 nm, among the highest reported at that time for perovskite NPs thin films, which normally suffer from a PLQY decrease going from dispersion to the solid state. In fact, it has been widely shown that, when the NPs are deposited into thin films, the PLQY drops substantially and the maximum emission shifts. As it is paramount to obtain thin films of the luminescent material to enable their incorporation into devices such as light-emitting diodes, the observed decrease in PLQY is troublesome and needs to be avoided. Both, bathochromic (red-) and hypsochromic shifts (blue-shift) have been reported.[123–125] The explanation of these effects seems to be related with the unavoidable aggregation of the material and it is attributed to the different boundary conditions that the samples experiment in different environments. This is similar to the aggregation/concentration effect observed in many organic semiconductor crystals.[124] The hypothesis for the good optical properties in our system is that the anchoring of the NPs to the ZnO surface could inhibit their aggregation.

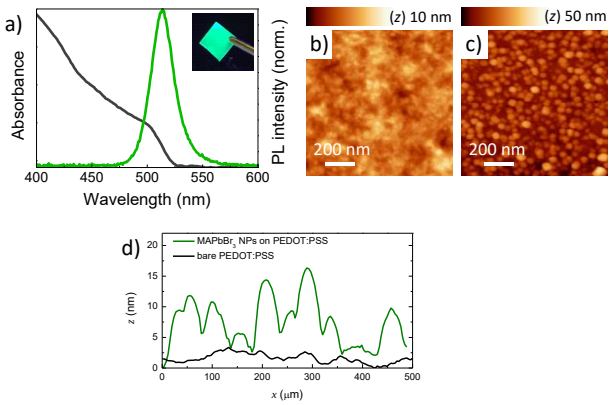

Figure 3.4. a) Absorption (grey) and PL (green) spectra of the $MAPbBr_3$ NPs anchored to a ZnO film. Inset: photograph of a ZnO/NPs film under UV light excitation (λ = 365 nm). AFM topographies of a PEDOT:PSS film without (b) and with (c) the anchored perovskite NPs. Note the different vertical scale used for the images. d) Comparison of the surface profile of the same two samples.

Surface	Maximum PL emission	FWHM	PLQY (excited at 380 nm)
ZnO	514 nm	25 nm	52%
PEDOT:PSS	513 nm	28 nm	50%

Table 3.2. Photoluminescent characteristics of NPs anchored on different surfaces.

Time-resolved PL measurements showed a reduced average lifetime (11 ns) for the ZnO films functionalized with the NPs in comparison with the NPs colloidal suspensions (65 ns) (Figure 3.5). In other similar reports showing $MAPbBr_3/TiO_2$ systems, the effect was ascribed to an efficient electron injection from the perovskite to the metal oxide conduction band,[126] which could also partially explain the PLQY reduction observed for the anchored $MAPbBr_3$ NPs. It was later shown that perovskite NPs coated onto ZnO suffered from severe non-radiative recombination at the perovskite grain boundaries or at the interface between the two layers.[37] This drawback was circumvented by modifying the ZnO surface with polyvinylpyrrolidone (PVP, a hydrophilic and insulating polymer), which can passivate the ZnO surface defects and/or improve the morphology leading to a dramatic increase in PL intensity.

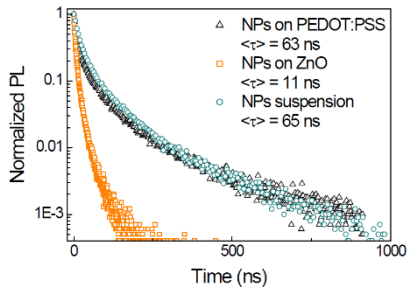

Figure 3.5. Time-resolved PL measurements taken at the peak emission wavelength (521 nm) of the $MAPbBr_3$ NPs colloidal solution and the NPs anchored on ZnO and PEDOT:PSS thin films, with a pump wavelength of 405 nm.

Importantly, with the use of the 11-aminoundecanoic acid hydrobromide, the $ZnO/MAPbBr_3$ NPs films maintained their luminescence after washing with toluene, implying that the NPs were effectively anchored to the surface, and hence, other functional layers (i.e. organic charge transport materials) can be coated on top of the perovskite NPs. The perovskite NPs did also adhere on a conducting polymer PEDOT:PSS coated substrate and, in spite of the

very different chemical nature compared to ZnO, led to analogous results to what was observed for the ZnO/NPs systems (Table 2).

Atomic force microscopy (AFM) was used to investigate the morphology of the anchored NPs films. The roughness of the solution-processed ZnO films, however, impeded to identify the perovskite NPs on the semiconductor surface. On the other hand, the substantially more flat and homogeneous surface of the PEDOT:PSS surface allowed a direct visualization of the perovskite NPs. Analysed by AFM, the surface of the PEDOT:PSS film is flat and homogeneous (Figure 3.4b), with an associated root-mean-square roughness of only 1.2 nm, calculated over a 2 x 2 μm^2 area. The same surface, when coated with the perovskite NPs, is composed by densely packed particles (Figure 3.4c). Measuring the surface profile (taking into account the deconvolution of the surface and the AFM tip), the estimated diameter of the NPs varies from 5 to 15 nm, in accordance with the TEM analysis. From this morphological analysis and considering the unchanged optical properties of the NPs when anchored to ZnO or PEDOT:PSS, we concluded that the $MAPbBr_3$ NPs are also grafted on the semiconducting ZnO surface, where they form homogeneous and compact films, suitable for the fabrication of optoelectronic devices. Hence, multilayer LEDs with n-i-p configuration were prepared. The ZnO sensitized with $MAPbBr_3$ NPs was deposited on ITO coated glass substrates, and a 100 nm thick CBP film (4,4'-Bis(N-carbazolyl)-1,1'-biphenyl, acting as the HTL) was spin-coated on top. The device was finished by vacuum deposition of a thin (10 nm) layer of MoO_3 (facilitating hole injection from the anode to the CBP) and a 100 nm thick gold anode on top. The flat band energy diagram for this set of materials is depicted in Figure 3.6a.

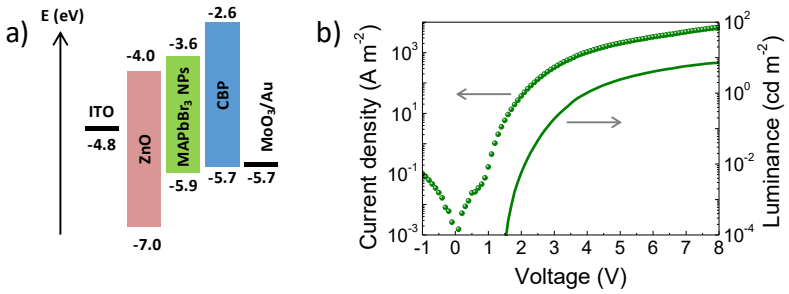

Figure 3.6. a) Flat band energy diagrams of the materials used in the NPs LEDs. b) Current density (symbols) and luminance (line) versus applied bias for the same device.

In the device performance (Figure 3.6b), the current density to voltage behaviour shows a typical diode characteristic (low leakage, exponential forward current injection), highlighting the good quality of the device and layers used. The LED turns on at about 1.5 V applied bias, reaching a luminance of 8 cd m^{-2} at 8 V. Unfortunately, the current density at the same

applied bias is very high (8000 A m^{-2}), limiting the overall current efficiency to about 10^{-3} cd A^{-1}. This can be a consequence of the extremely thin perovskite NPs layer used, limiting the attainable electroluminescence, or an uneven particle distribution causing insufficient coverage. The ZnO layer used is not completely flat and can hence cause an uneven distribution of the applied field or direct electron-hole recombination at the ZnO surface. It is known that the nanocrystalline morphology of the oxide film plays an important role in determining the electroluminescence process.[127] Considering that indeed LEDs employing a monolayer of luminescent NPs have been demonstrated,[128] a more homogeneous and especially flat surface would be desirable when using $MAPbBr_3$ NPs. Unfortunately, an inverted device (p-i-n) employing PEDOT:PSS/$MAPbBr_3$ NPs in combination with an electron transport layer showed no electroluminescence at all. This is not surprising since PEDOT:PSS/$MAPbBr_3$ is not a blocking interface, and direct charge recombination at the conducting polymer is favoured.

3.4. Published work

The work was carried out in collaboration with ERI@N, a research section of the Nanyang Technological University in Singapore headed by Prof. Subodh Mhaisalkar. The research topic was initiated during a stay there in 2015, in close collaboration with Dr. Koh Teck Ming, and continued in the Institute of Molecular Science at Universidad de Valencia after coming back.

The publication is reproduced by permission of The Royal Society of Chemistry. DOI: 10.1039/C6CC05549D, Chem. Commun., 2016, 52, 11351-11354.

ChemComm

COMMUNICATION

View Article Online
View Journal | View Issue

Cite this: *Chem. Commun.*, 2016, **52**, 11351

Received 5th July 2016,
Accepted 19th August 2016

DOI: 10.1039/c6cc05549d

www.rsc.org/chemcomm

Efficient photoluminescent thin films consisting of anchored hybrid perovskite nanoparticles†

Laura Martínez-Sarti,[a] Teck Ming Koh,[b] Maria-Grazia La-Placa,[a] Pablo P. Boix,[b] Michele Sessolo,[a] Subodh G. Mhaisalkar*[bc] and Henk J. Bolink*[a]

Methylammonium lead bromide nanoparticles are synthetized with a new ligand (11-aminoundecanoic acid hydrobromide) by a non-template method. Upon dispersion in toluene they show a remarkable photoluminescence quantum yield of 80%. In addition, the bifunctional ligand allows anchoring of the nanoparticles on a variety of conducting and semiconducting surfaces, showing bright photoluminescence with a quantum yield exceeding 50%. This opens a path for the simple and inexpensive preparation of multilayer light-emitting devices.

Recently, organic inorganic (hybrid) lead halide perovskites have been widely studied for photovoltaic applications, where power conversion efficiencies exceeding 22.1% have been demonstrated.[1,2] Beyond solar cells, these materials are interesting candidates for low-threshold lasers and light-emitting diodes (LEDs).[1,3–7] Their application in LEDs requires a precise control over their morphology, since this determines their optical and electronic properties.[8,9] In particular, materials with high photoluminescence quantum yield (PLQY) are desirable for the preparation of efficient LEDs. One of the most suitable strategies for controlling the morphology and enhancing the photoluminescence of perovskites is the preparation of nanostructured materials. In nanostructured perovskites, the spatial confinement of the charge carriers together with a passivation of the surface states result in a substantial increase of the luminescence yield when compared to bulk perovskites.[10] The recent breakthroughs in the PLQY of narrow-band emitting perovskite nanoparticles (NPs) (full width at half-maximum, FWHM, ~20 nm) make these materials promising candidates for light-emitting applications.[11,12] Perovskite NPs can be prepared by a direct, non-template method that makes use of organic ligands to disperse the material in the form of colloidal NPs.[13] These organic capping ligands are usually medium or long chain alkyl ammonium halides that limit the growth of the material in the three dimensions. Schmidt *et al.* reported, for the first time, the synthesis of 6 nm sized methylammonium lead bromide ($MAPbBr_3$) colloidal perovskite NPs using octadecylammonium as the capping ligand.[13] Thin films obtained by spin-coating the NP dispersion showed intense photoluminescence (PL) with an associated quantum yield of about 20%. Through modified synthetic conditions, the same group later showed that surface states could be further passivated by insertion of a complementary weak Lewis base, and PLQYs up to 82% in solution were achieved.[14] Recently, color tunable mixed halide perovskite NPs with PLQY in solution up to 93% have been demonstrated.[11] Interestingly, the NP size was found to be strongly dependent on the synthesis temperature, giving an additional degree of freedom in the material design while, at the same time, underlining the difficulties in achieving reproducible preparation of monodisperse hybrid perovskite NPs. The elimination of polar solvents such as dimethylformamide (DMF) during synthesis has been shown to substantially improve the nucleation and growth of $MAPbBr_3$ NPs.[15] In general, however, the PLQY decreases substantially when the nanoparticles are processed into thin films, due to unavoidable aggregation of the material.[10] In spite of such reduction of the PLQY, these films have been recently used to prepare LEDs.[16–19] Encouraging brightness and external quantum efficiencies have been shown, further demonstrating the potential of this type of material in lighting and display applications.

In this work, we describe the preparation of highly photoluminescent $MAPbBr_3$ NP thin-films, through a temperature-independent synthesis which makes use of a bifunctional ligand (11-aminoundecanoic acid hydrobromide, $Br^-NH_3^+$-C_{10}-COOH). This molecule efficiently coordinates the NPs and, at the same time, allows selective anchoring of the NPs onto various electroactive surfaces. This approach was then used to construct multilayer green emitting LEDs.

The 11-aminoundecanoic acid was converted into its ammonium bromide salt ($Br^-NH_3^+$-C_{10}-COOH) to enhance its solubility in DMF.

[a] *Instituto de Ciencia Molecular (ICMol), Universidad de Valencia, Catedrático José Beltrán, 2, 46980 Paterna, Spain. E-mail: henk.bolink@uv.es*
[b] *Energy Research Institute@NTU (ERI@N), Research Techno Plaza, X-Frontier Block, Level 5, 50 Nanyang Drive, 637553 Singapore, Singapore*
[c] *School of Materials Science and Engineering, Nanyang Technological University, 50 Nanyang Avenue, 639798 Singapore, Singapore. E-mail: Subodh@ntu.edu.sg*

† Electronic supplementary information (ESI) available. See DOI: 10.1039/c6cc05549d

The NPs were obtained by taking advantage of the interplay between a polar solvent (DMF, able to solubilize the perovskite precursors) and a non-polar one (toluene), as described in previously published protocols.[11,13] The perovskite precursors (MABr and $PbBr_2$) were dissolved in DMF (ratio 1 : 1, 0.04 M), together with oleic acid (to avoid the NP aggregation) and varying amounts of $Br^-NH_3^+$-C_{10}-COOH. A small volume of this solution was injected into toluene under vigorous stirring. The resulting solution was centrifuged in order to remove larger aggregates, and a bright luminescent supernatant suspension was obtained.

By modifying the ligand amount, a strong variation in the optical properties of the suspension was observed. In particular, when a $Br^-NH_3^+$-C_{10}-COOH/MA molar ratio of 2 was used during the synthesis, a blue light emitting NP suspension was obtained (Fig. 1a). This dispersion showed a maximum PL emission at 490 nm, an FWHM of 22 nm, and a PLQY of 25%. The influence of the long chain ammonium ligand $Br^-NH_3^+$-C_{10}-COOH on the color of the resulting suspension is a result of the equilibrium between the formation of three dimensional $MAPbBr_3$ NPs and two dimensional structures where the ligand itself participates in the formation of layered perovskites.[10,20–22] In particular, with an excess of $Br^-NH_3^+$-C_{10}-COOH, mainly 2D perovskite nanostructures are obtained. In these materials, the long chain cations alternate inorganic sheets of octahedral lead bromide, resulting in a multi-well, dielectric-semiconductor structure characterized by an increased exciton binding energy.[20] The formation of such structures leads to an intense and sharp peak in the low energy part of the absorption spectra, as is clearly visible in the case of our suspensions prepared with high ligand content (Fig. 1a). On the other hand, by reducing the amount of ligand used to a $Br^-NH_3^+$-C_{10}-COOH/MABr molar ratio of 0.5, the typical $MAPbBr_3$ absorption and emission spectra can be observed, as a footprint of 3D NP formation (Fig. 1b). This dispersion showed narrow and intense photoluminescence (centered at 521 nm, with an FWHM of about 20 nm) with an associated PLQY as high as 80%. As mentioned before, the temperature of the non-polar solvent (here toluene) was reported to be of special importance, defining the size and hence the emission wavelength of the NPs.[11]

Interestingly, the synthesis in the presence of $Br^-NH_3^+$-C_{10}-COOH was found to be rather temperature independent. In fact, when the synthesis is carried out at 60 °C, the absorption and luminescence spectra of the obtained NP suspension are similar to those prepared at room temperature (Fig. S1, ESI†).

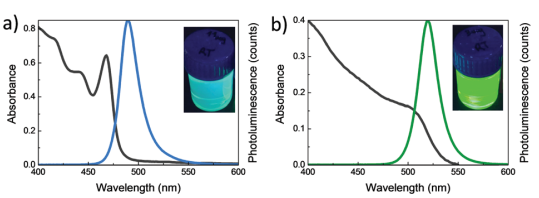

Fig. 1 Absorption (gray) and PL (blue and green) spectra of $MAPbBr_3$ NP colloidal solutions in toluene for $Br^-NH_3^+$-C_{10}-COOH/MA molar ratios of (a) 2 and (b) 0.5. Insets: Photographs of colloidal solutions under UV excitation (λ = 365 nm).

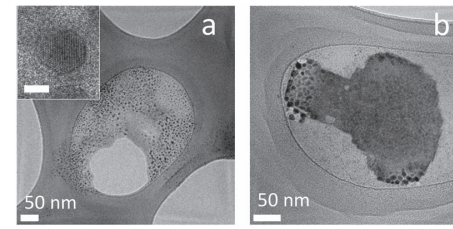

Fig. 2 (a) TEM image of the $MAPbBr_3$ NPs prepared using a $Br^-NH_3^+$-C_{10}-COOH/MABr molar ratio of 0.5 at 25 °C (Fig. 1a). Inset: High resolution TEM image of an isolated NP (scale bar 4 nm). (b) TEM image of the perovskite nanostructures obtained in the presence of an excess of $Br^-NH_3^+$-C_{10}-COOH at 25 °C (Fig. 1b).

We investigated the morphology of the NP suspensions prepared at 25 °C by transmission electron microscopy (TEM). The electron microscopy confirmed the presence of the perovskite NPs (Fig. 2a) with a diameter in the 3–10 nm range (4.5 nm in average, see Fig. S5, ESI,† for details). With increased $Br^-NH_3^+$-C_{10}-COOH content, the morphology changes showing wide 2D sheets (50–200 nm) embedded with spherical nanocrystals (Fig. 2b). This mixture of nanostructures has been described in several reports, and results from the competition among the formation of 3D and 2D-type perovskites, as described before.[13,23] The choice of the cationic ligand $Br^-NH_3^+$-C_{10}-COOH was made in order to enable efficient coordination to the perovskite NPs and, thanks to the carboxyl group, allow for the anchoring of the NPs on functional surfaces, such as metal oxides.[24] Moreover, the carboxyl group reduces the QD aggregation, enhancing the stability of the NP suspension, by analogy with the function of the oleic acid additive.[11] Hence, we tested the adhesion of the NPs onto thin films of ZnO, an n-type semiconductor widely used as an electron injection layer in OLEDs.[25] 150 nm thick ZnO layers were prepared by spin-coating and high temperature annealing (400 °C) of a commercial ZnO NP suspension on indium tin oxide (ITO) coated glass substrates. These ZnO coated substrates were immersed in the NP suspension for 12 hours and then rinsed with toluene before characterization. The ZnO/$MAPbBr_3$ NP films exhibited bright photoluminescence under UV excitation (λ = 365 nm) (Fig. 3a, inset), with a maximum PL emission at 514 nm and an FWHM of 25 nm (Fig. 3a). Importantly, the associated PLQY of the thin films was as high as 52% when excited at 380 nm. Despite the decrease of the PLQY from dispersion to the solid state, this value is among the highest reported for perovskite NP thin films, most likely thanks to the anchoring of the NPs which strongly inhibits their aggregation. Time-resolved PL measurements were performed both on the colloidal solution and on the ZnO films functionalized with the NPs (Fig. S4, ESI†). In accordance with previous reports, the average lifetime for the NP suspension was found to be 65 ns, with a long tail extending towards the microsecond timescale.[11,14] On the other hand, the excited state lifetime was found to be substantially reduced (11 ns) when the $MAPbBr_3$ NPs were anchored to the ZnO surface. The same effect has been

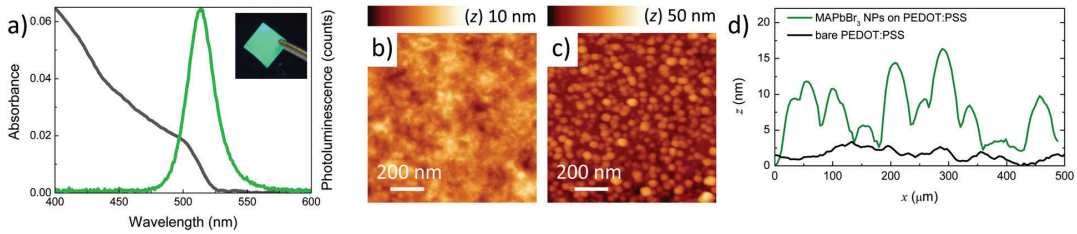

Fig. 3 (a) Absorption (gray) and PL (green) spectra of the $MAPbBr_3$ NPs anchored to a ZnO substrate. Inset: Photograph of a ZnO/NP film under UV excitation (λ = 365 nm). AFM topographies of a PEDOT:PSS film without (b) and with (c) the anchored perovskite NPs. Note the different vertical scales used for the images. (d) Comparison of the surface profiles of the same two samples.

previously observed in $MAPbBr_3/TiO_2$ bilayers and was ascribed to an efficient electron injection from the perovskite to the metal oxide conduction band.[26] Considering the very similar energy band alignment of TiO_2 and ZnO, the same mechanism is likely to take place at the $MAPbBr_3$ NP/ZnO interface, resulting in the shorter excited state lifetime observed here. The efficient charge transfer could also partially explain the PLQY reduction observed for the anchored $MAPbBr_3$ NPs. Importantly, the ZnO/$MAPbBr_3$ NP films maintained their luminescence after washing with toluene, implying that the NPs were effectively anchored to the surface. This is very important since other functional layers (*i.e.* organic charge transport materials) can be coated on top of the perovskite NPs, allowing for the preparation of multilayer LEDs.

In order to investigate the morphology of the NPs anchored on the ZnO NP film, atomic force microscopy (AFM) was used. The rather rough ZnO surface (Fig. S2, ESI†), however, made it difficult to discern the perovskite NPs. Hence, we looked for a substantially more flat surface compared to the solution processed ZnO that would allow a direct visualization of the perovskite NPs. We selected poly(3,4-ethylenedioxythiophene) doped with poly(styrene sulphonate) (PEDOT:PSS) as a test platform to anchor the $MAPbBr_3$ NPs. In spite of the very different chemical nature of PEDOT:PSS compared to ZnO, the perovskite NPs did also adhere on the conducting polymer coated substrate, and the films exhibited a maximum PL emission at 513 nm and a PLQY of 50%, analogous to what was observed for the ZnO/NP systems (Fig. S3, ESI†). The adhesion of the perovskite NPs on PEDOT:PSS is most likely promoted by the large amount of ionic groups (and in particular of cationic polythiopene derivatives) present in the conducting polymer, leading to a favorable electrostatic interaction between the carboxyl groups of the ligands and the surface. The morphology of the PEDOT:PSS/NP thin films was analyzed by AFM. The surface of the PEDOT:PSS film is flat and homogeneous (Fig. 3b), with an associated root-mean-square roughness of only 1.2 nm, calculated over a 2 × 2 μm area. The same surface, when coated with the perovskite NPs, is composed of densely packed particles (Fig. 3c), whose dimensionality can be estimated by measuring the surface profile (Fig. 3d). Structures with height varying from about 5 to 15 nm can be observed, indicating a low roughness and hence limited aggregation of the NPs on the surface (considering the particle size distribution obtained from TEM analysis). The lateral size of the particles, as observed from the AFM profiles, appears much larger as it is a deconvolution of the surface and the AFM tip. From this morphological analysis and considering the unchanged optical properties of the NPs when anchored to ZnO or PEDOT:PSS, we conclude that the $MAPbBr_3$ NPs are grafted onto the semiconducting ZnO surface, where they form homogeneous and compact films, suitable for the fabrication of optoelectronic devices. Hence, multilayer LEDs with an n–i–p configuration (an n-type layer deposited on the transparent substrate) were prepared. ZnO sensitized with $MAPbBr_3$ NPs was deposited on ITO coated glass substrates, and a 100 nm thick CBP film (4,4′-bis(*N*-carbazolyl)-1,1′-biphenyl, acting as the hole transport layer, HTL) was spin-coated on top from its chlorobenzene solution (20 mg mL^{-1}). The device was finished by vacuum deposition of a thin (10 nm) layer of MoO_3 (facilitating hole injection from the anode to the CBP) and a 100 nm thick gold anode on top. The flat band energy diagram for the materials used in the device is depicted in Fig. 4a.

The current density and luminance *versus* voltage characteristics for a device using $MAPbBr_3$ NPs as the emitting material is reported in Fig. 4b. The current density to voltage behavior shows a typical diode characteristic (low leakage, exponential forward current injection), highlighting the good quality of the device and layers used. The LED turns on at about 1.5 V applied bias, reaching a luminance of 8 cd m^{-2} at 8 V. Unfortunately, the current density at the same applied bias is very high (8×10^3 A m^{-2}), limiting the overall current efficiency to about 10^{-3} cd A^{-1}. This can be a consequence of the extremely thin perovskite NP layer used (virtually a monolayer), limiting the attainable electroluminescence. An uneven particle distribution causing insufficient coverage could also reduce the overall current efficiency. On the other hand, the ZnO layer used is not completely flat and can hence cause an uneven distribution of the applied field or direct electron–hole recombination at the ZnO surface. It is known that the nanocrystalline morphology of the oxide film plays an important role in determining the electroluminescence process.[27] Considering that indeed LEDs employing a monolayer of luminescent NPs have been demonstrated,[28] a more homogeneous and especially flat surface would be desirable when using $MAPbBr_3$ NPs. Unfortunately, an inverted device (p–i–n) employing PEDOT:PSS/$MAPbBr_3$ NPs in combination with an electron transport layer showed no electroluminescence at all. This is not surprising since PEDOT:PSS/$MAPbBr_3$ is not a

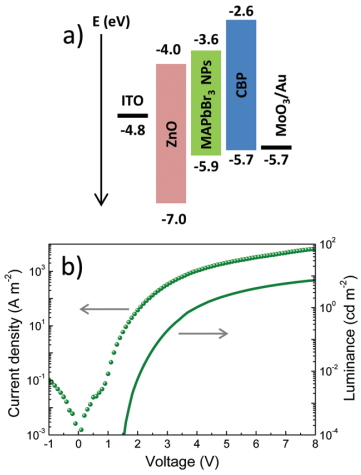

Fig. 4 (a) Flat band energy diagrams of the materials used in the NP LEDs. (b) Current density (symbols) and luminance (line) *versus* applied bias for the same device.

blocking interface, and direct charge recombination at the conducting polymer is favored.

In summary, a temperature-independent synthesis of $MAPbBr_3$ nanoparticles (NPs) employing the ammonium salt of 11-aminoundecanoic acid ($Br^-NH_3^+$-C_{10}-COOH) as a ligand has been developed. Dispersions of NPs with a diameter below 10 nm and a PLQY of about 80% can be readily obtained at room-temperature and under atmospheric conditions. Thanks to the use of the $Br^-NH_3^+$-C_{10}-COOH bifunctional ligand, the NPs can be anchored on a variety of electroactive surfaces, such as inorganic semiconductors or conducting polymers. The NPs anchored to ZnO and PEDOT:PSS thin films showed a remarkable photoluminescence quantum yield of approximately 50%. The NP-sensitized ZnO films can be directly integrated into light-emitting devices, leading to modest but homogeneous light-emission. The anchoring of perovskite NPs on several flat and semiconducting surfaces is being investigated, with the potential of opening new paths for the preparation of simple and inexpensive multilayer light-emitting devices.

We acknowledge financial support from the European Union H2020 project INFORM (grant 675867), the Spanish Ministry of Economy and Competitiveness (MINECO) *via* the Unidad de Excelencia María de Maeztu MDM-2015-0538, MAT2014-55200 and PCIN-2015-255 and the Generalitat Valenciana (Prometeo/2012/053). M. S. thanks the MINECO for a post-doctoral (JdC) contract. T. M. Koh, P. P. Boix and S. G. Mhaisalkar would like to acknowledge the funding from the Singapore NRF through the Competitive Research Program: NRF-CRP14-2014-03 as well as from the NTU-A*STAR Silicon Technologies Centre of Excellence under program grant no. 112 3510 0003.

References

1 S. D. Stranks and H. J. Snaith, *Nat. Nanotechnol.*, 2015, **10**, 391–402.
2 Q. Wang, H. Chen, G. Liu and L. Wang, *Sci. Bull.*, 2015, **60**, 405–418.
3 G. Xing, N. Mathews, S. S. Lim, N. Yantara, X. Liu, D. Sabba, M. Grätzel, S. Mhaisalkar and T. C. Sum, *Nat. Mater.*, 2014, **13**, 476–480.
4 N. Yantara, S. Bhaumik, F. Yan, D. Sabba, H. A. Dewi, N. Mathews, P. P. Boix, H. V. Demir and S. Mhaisalkar, *J. Phys. Chem. Lett.*, 2015, **6**, 4360–4364.
5 B. R. Sutherland and E. H. Sargent, *Nat. Photonics*, 2016, **10**, 295–302.
6 P. Docampo and T. Bein, *Acc. Chem. Res.*, 2016, **49**, 339–346.
7 S. A. Veldhuis, P. P. Boix, N. Yantara, M. Li, T. C. Sum, N. Mathews and S. G. Mhaisalkar, *Adv. Mater.*, 2016, **28**, 6804–6834.
8 N. K. Kumawat, A. Dey, K. L. Narasimhan and D. Kabra, *ACS Photonics*, 2015, **2**, 349–354.
9 J. C. Yu, D. B. Kim, E. D. Jung, B. R. Lee and M. H. Song, *Nanoscale*, 2016, **8**, 7036–7042.
10 S. González-Carrero, R. E. Galian and J. Pérez-Prieto, *Part. Part. Syst. Charact.*, 2015, **32**, 709–720.
11 H. Huang, A. S. Susha, S. V. Kershaw, T. F. Hung and A. L. Rogach, *Adv. Sci.*, 2015, **2**, 1500194.
12 L. Protesescu, S. Yakunin, M. I. Bodnarchuk, F. Krieg, R. Caputo, C. H. Hendon, R. X. Yang, A. Walsh and M. V. Kovalenko, *Nano Lett.*, 2015, **15**, 3692–3696.
13 L. C. Schmidt, A. Pertegás, S. González-Carrero, O. Malinkiewicz, S. Agouram, G. Mínguez Espallargas, H. J. Bolink, R. E. Galian and J. Pérez-Prieto, *J. Am. Chem. Soc.*, 2014, **136**, 850–853.
14 S. Gonzalez-Carrero, R. E. Galian and J. Pérez-Prieto, *J. Mater. Chem. A*, 2015, **3**, 9187–9193.
15 O. Vybornyi, S. Yakunin and M. V. Kovalenko, *Nanoscale*, 2016, **8**, 6278–6283.
16 M. F. Aygüler, M. D. Weber, B. M. D. Puscher, D. D. Medina, P. Docampo and R. D. Costa, *J. Phys. Chem. C*, 2015, **119**, 12047–12054.
17 H. Huang, F. Zhao, L. Liu, F. Zhang, X.-g. Wu, L. Shi, B. Zou, Q. Pei and H. Zhong, *ACS Appl. Mater. Interfaces*, 2015, **7**, 28128–28133.
18 W. Deng, X. Xu, X. Zhang, Y. Zhang, X. Jin, L. Wang, S. T. Lee and J. Jie, *Adv. Funct. Mater.*, 2016, **26**, 4797–4802.
19 Y. Ling, Z. Yuan, Y. Tian, X. Wang, J. C. Wang, Y. Xin, K. Hanson, B. Ma and H. Gao, *Adv. Mater.*, 2016, **28**, 305–311.
20 D. B. Mitzi, K. Chondroudis and C. R. Kagan, *IBM J. Res. Dev.*, 2001, **45**, 29–45.
21 D. Sapori, M. Kepenekian, L. Pedesseau, C. Katan and J. Even, *Nanoscale*, 2016, **8**, 6369–6378.
22 S. Bhaumik, S. A. Veldhuis, Y. F. Ng, M. Li, S. K. Muduli, T. C. Sum, B. Damodaran, S. Mhaisalkar and N. Mathews, *Chem. Commun.*, 2016, **52**, 7118–7121.
23 P. Tyagi, S. M. Arveson and W. A. Tisdale, *J. Phys. Chem. Lett.*, 2015, **6**, 1911–1916.
24 E. Galoppini, *Coord. Chem. Rev.*, 2004, **248**, 1283–1297.
25 M. Sessolo and H. J. Bolink, *Adv. Mater.*, 2011, **23**, 1829–1845.
26 H. B. Kim, I. Im, Y. Yoon, S. D. Sung, E. Kim, J. Kim and W. I. Lee, *J. Mater. Chem. A*, 2015, **3**, 9264–9270.
27 Y. Athanassov, F. P. Rotzinger, P. Péchy and M. Grätzel, *J. Phys. Chem. B*, 1997, **101**, 2558–2563.
28 S. Coe, W.-K. Woo, M. Bawendi and V. Bulovic, *Nature*, 2002, **420**, 800–803.

Supporting Information

Efficient photoluminescent thin films consisting of anchored hybrid perovskite nanoparticles

Laura Martínez-Sarti, Teck Ming Koh, Maria-Grazia La-Placa, Pablo P. Boix, Michele Sessolo, Subodh G. Mhaisalkar and Henk J. Bolink

[a] Instituto de Ciencia Molecular (ICMol), Universidad de Valencia, Catedrático José Beltrán, 2, 46980 Paterna, Spain.
[b] Energy Research Institute @ NTU (ERI@N), Research Techno Plaza, X-Frontier Block, Level 5, 50 Nanyang Drive, 637553 Singapore.
[c] School of Materials Science and Engineering, Nanyang Technological University, 50 Nanyang Avenue, 639798 Singapore.

Synthesis of the $MAPbBr_3$ NPs and sensitized ZnO films

For the $MAPbBr_3$ NPs fabrication, the 11-aminoundecanoic acid was initially converted into its ammonium salt with an excess of HBr, to enhance its solubility in DMF. $PbBr_2$ (0.04 M) and 474 µL of oleic acid were dissolved in 2.5 mL of DMF (solution A). Subsequently, 596 µL of this solution were added into 0.5 mL of another DMF solution B containing MABr (0.04 M) and varying amounts of $Br^-NH_3^+$-C_{10}-COOH. 0.5 mL of this precursor solution (A+B) was quickly injected into toluene (5 mL) under vigorous stirring at room temperature (RT) or previously heated at 60 ºC. A yellow-green solution was immediately observed, consequence of the formation of the NPs. The solution was centrifuged at 12.5 krpm for 10 minutes to remove larger aggregates, and a bright luminescent supernatant solution was obtained.

For coating the ZnO films, 0.5 mL of a solution of 40 wt% in ethanol from Sigma-Aldrich (average particle size of 35 nm) were diluted in 3 mL of ethanol, and then spin-coated using a GYRSET® (closed cover coating technology). The layers were then annealed at 450 ºC during 30 min.

For the ZnO/$MAPbBr_3$ NPs films preparation, the ZnO coated substrates were immersed into the NPs suspension for 12 hours and subsequently rinsed with toluene.

Characterization

The photoluminescence (PL) characteristics were studied using a Xe lamp coupled to a monochromator as the excitation source and an integrated sphere coupled to a spectrometer (Hamamatsu C9920-02 with a Hamamatsu PMA-11 optical detector) in order to quantitatively determine the PLQY. UV-visible absorption spectra of the films were collected using a fiber-optics based Avantes Avaspec2048 spectrophotometer. UV-visible spectra of the dispersions were recorded using a quartz cuvettes spectrometer in a UV-visible spectrophotometer Agilent 8453E. TEM and high resolution TEM (HR-TEM) were performed with a Field Emission Gun (FEG) TECNAI G2 F20 microscope operated at 200 kV. LEDs were characterized under inert conditions inside a glovebox. The current density and luminance versus voltage characteristics were measured using a Keithley 2400 Source-Meter and a photodiode coupled to a Keithley 6485 pico-ammeter, using a Minolta LS100 camera to calibrate the photocurrent. The AFM images were collected with a Digital Instrument Veeco Nanoscope IVa AFM microscope in tapping mode, using silicon tips with natural resonance frequency of 320 kHz and with an equivalent constant force of 42 N m^{-1}.

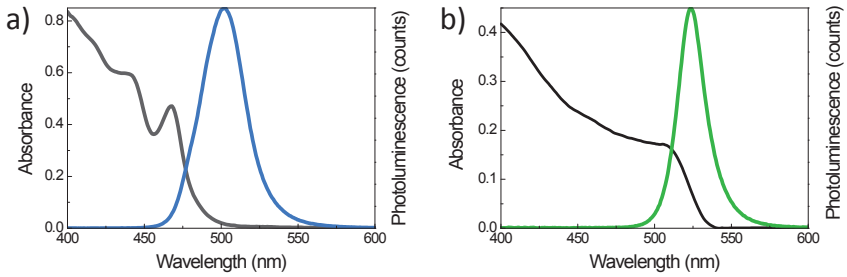

Fig. S1 Absorption (gray) and PL spectra (blue and green) of $MAPbBr_3$ NPs colloidal solutions in toluene at 60 ºC for $Br^-NH_3^+$-C_{10}-COOH/MA molar ratio of (a) 2 and (b) 0.5.

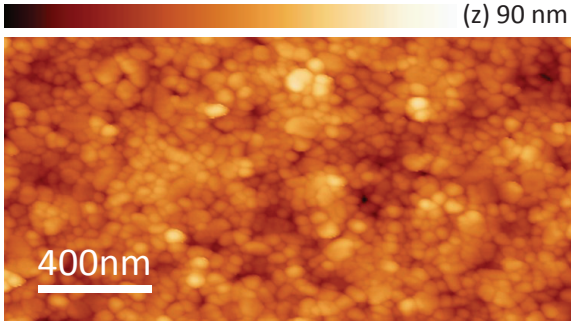

Fig. S2 AFM topography of a solution-processed ZnO film.

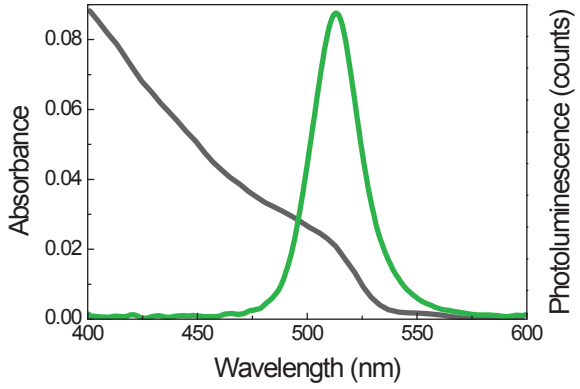

Fig. S3 Absorbance (gray) and photoluminescence (green) spectra of the $MAPbBr_3$ NPs anchored to a PEDOT:PSS substrate.

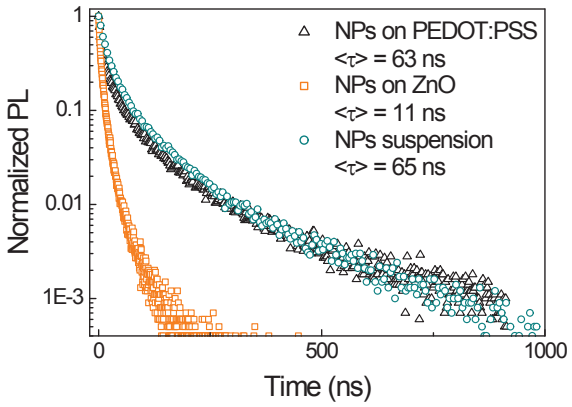

Fig. S4 Time-resolved PL measurements taken at the peak emission wavelength (521 nm) of the $MAPbBr_3$ NPs colloidal solution and the NPs anchored on ZnO and PEDOT:PSS thin films, with a pump wavelength of 405 nm.

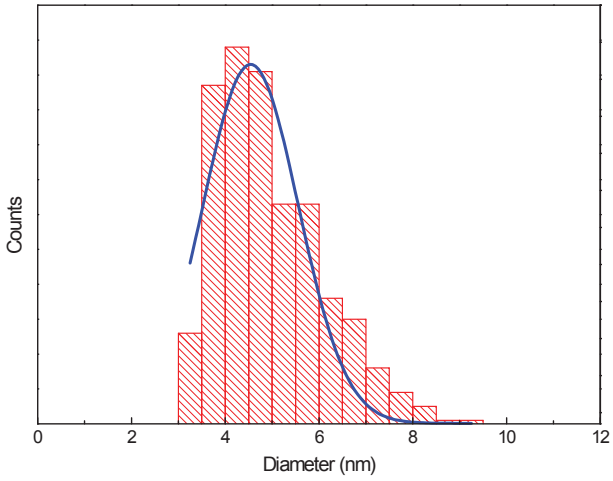

Fig. S5 Particle size histograms calculated from the TEM image in Fig. 2a, plotted from analysis of >500 particles. Mean and standard deviation for the distribution are 4.6 and 2.4 nm, respectively.

Chapter 4.

Self-assembled hierarchical nanostructured perovskites enable highly efficient LEDs via an energy cascade

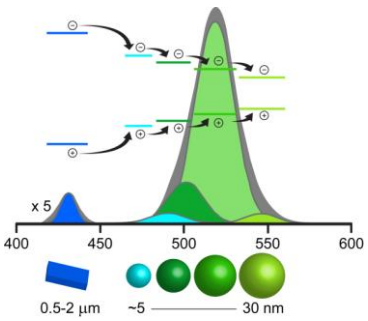

4.1. Motivation, work description and achievement

As highlighted in the introduction, metal halide perovskites exhibit properties which are interesting for applications in large area illumination and displays. However, the rather complex and often difficult to reproduce preparation methods, required to obtain highly luminescent materials, currently limit further progress towards applications.

This chapter describes the development and characterization of luminescent films consisting of self-assembled low-dimensional octylammonium lead bromide microplatelets (MPLs) and 3D $FAPbBr_3$ NCs. These hierarchical self-assemblies lead to layers with very high PLQY (over 80%) and show an energy cascade transfer mechanism which lead to LEDs with unprecedented electroluminescent efficiencies at that time (highest combination of EQE, luminance, power and current efficiency in green-emitting perovskite LEDs).

4.2. Experimental details and methodology

The ligand-assisted reprecipitation method (LARP) was used to synthesize the $FAPbBr_3$ NCs at RT. A precursor solution was prepared by mixing 0.2 mmol of FABr and 0.1 mmol of $PbBr_2$ in DMF. This was then added dropwise into a vigorously stirred toluene solution containing oleic acid, n-butanol and varying quantities of n-octylamine to achieve OA:$PbBr_2$ ratios from 3:1 to 10:1. Immediately after injection, a yellowish solution was formed, indicating the formation of the NCs. After reaction completion, the colloidal NCs solution was washed using two centrifugation steps. In the first, the NCs solution was centrifuged at 13400 rpm (revolutions per minute), after which the precipitate was redispersed in toluene. Then, the redispersed NCs were centrifugated at 4400 rpm. The resultant supernatant phase was used as NCs ink (estimated concentration of approximately 8-10 mg mL^{-1}) for the LED fabrication.

For the device fabrication, prepatterned ITO-coated glass substrates were used. The hole transporting layer, PEDOT:PSS (Clevios™ P VP AI 4083; filtered with 0.45 µm pore size PVDF filters), was spin-coated and annealed on top of the ITO to obtain a 30 nm thick layer. Then, the substrates were transferred into a nitrogen-filled glovebox where the NCs inks were drop-casted on top of the PEDOT:PSS layer and left for 5 min to slowly evaporate the solvent (and initiate self-assembly), prior to spin-coating at low speed, to obtain approximately 40 nm thick films. Later, 45 nm thick electron transport layer (either POT2T, 2,4,6-Tris[3-(diphenylphosphinyl)phenyl]-1,3,5-triazine, or B3PYMPM, 4,6-Bis(3,5-di(pyridin-3-yl)phenyl)-2-methylpyrimidine) were thermally evaporated in a high vacuum chamber. Finally, Ba (7 nm) and Al (80 nm) were subsequently thermally evaporated through a metal shadow mask. For the flexible devices fabrication, a similar protocol was followed but using ITO/PET flexible substrates. In this case, a thicker PEDOT:PSS layers was deposited (ca. 80 nm) to reduce the surface roughness (i.e. due to the rougher ITO layer on the flexible PET substrate).

LEDs were characterized under inert conditions in a nitrogen-filled glovebox. The current density and luminance versus voltage characteristics were measured using a Keithley 2400 Source-Meter and a photodiode coupled to a Keithley 6485 pico-ammeter, using a Minolta LS100 camera to calibrate the photocurrent.

The PL characteristics were studied using a Xe lamp coupled to a monochromator as the excitation source and an integrated sphere coupled to a spectrometer (Hamamatsu C9920-02 with a Hamamatsu PMA-11 optical detector) in order to quantitatively determine the PLQY. UV-visible spectra of the dispersions were recorded using a quartz cuvettes spectrometer in a UV-visible spectrophotometer Agilent 8453E. UV-visible absorption spectra of the films were collected using an optical fibre based Avantes Avaspec2048 spectrophotometer.

X-ray diffraction was collected using a Bruker D8 advance diffractometer with a 0D LynxEYE™ detector. Scans from 2θ = 5-35° were recorded from the spin-coated nanosized crystals inks samples on top of PEDOT:PSS.

Scanning transmission electron microscopy was performed with a Tecnai G2 F20 with a Schottky field emitter operated at 200kV. Selected samples were drop-casted on a carbon-copper grid, and mounted on a FEI Double Tilt Analytical Holder for examination. Tecnai G2 F20 STEM with an X-Twin lens objective lenses and field emission gun (Schottky field emitter) operates at a beam current of > 100 nA, providing high probe current (0.5 nA or more in 1 nm probe). The system is equipped with a fully embedded digital scan system; bright-field and annular dark-field modes are provided by ultra-high resolution high angle annular dark-field (HAADF) detector.

Cathodoluminescence microscopy measurements were performed in a scanning electron microscope equipped with a cathodoluminescence detection system, Attolight CL Allalin 4027 Chronos. A focused electron beam (electron energy 5 keV; beam current ~11 nA; dwell time 10-200 ms) scanned the samples while recording the light emission spectrum synchronously to produce hyperspectral images. The emitted light was collected by an achromatic reflective objective with a high numerical aperture (NA = 0.72) and sent to a UV-VIS spectrometer (Horiba iHR320) equipped with a thermoelectrically cooled silicon CCD array (Andor Newton).

The instantaneous PL spectra were obtained from the PL decay kinetics in the 420-570 nm range with a 2-5 nm step, using a Hamamatsu fluorometer Quantaurus-Tau.

4.3. Results and discussion

The LARP synthesis lead to the formation of $FAPbBr_3$ NCs together with large octylammonium lead bromide quasi-2D MPLs. Interestingly, the ratio between the MPLs and the NCs could be conveniently modulated by varying the OA:$PbBr_2$ ratio. This was evidenced by the absorption

spectra, where the peak intensity at 440 nm (which corresponds to the excitonic absorption of the MPLs) consistently changes with the OA content due to the increased presence of $(OA)_2(FA)_{n-1}PbnBr_{3n+1}$ MPLs with respect to $FAPbBr_3$ NCs (Figure 4.1a). In the same way, the PL spectra showed a pronounced emission at ~440 nm (from the MPLs) for the 10:1 composition, which was markedly reduced in the PL spectra of materials with a 5:1 ratio (Figure 4.1b). Based on the PL characterization and literature data, it is reasonable to assume the formation of low-dimensional perovskites with a very low n-value (see page 14 and Figure 1.4), near one unit cell thick, corresponding to almost pure 2D perovskite crystal structures.[59]

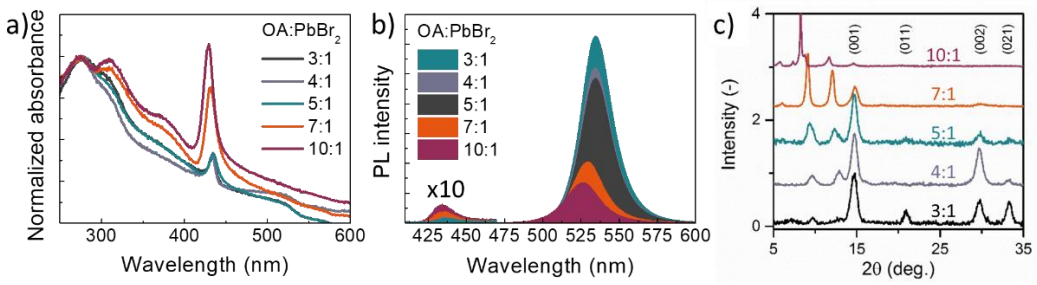

Figure 4.1. a) Absorption spectra, b) PL spectra (λ_{exc} = 405 nm) and c) X-ray diffraction patterns for perovskite samples with the different OA:$PbBr_2$ ratios.

XRD analysis on the films revealed the predominance of broad diffraction peaks centred at 2θ = 14.0° and 2θ = 28.3° in the lower OA:$PbBr_2$ ratios samples, consistent with the formation of 3D NCs. Additionally, sharp peaks were observed at 2θ = 8-12° (i.e., larger interatomic distances) when a higher OA:$PbBr_2$ ratio was used, confirming the preferred formation of low-dimensional crystals (Figure 4.1c).

In order to investigate the size and morphology of the particles, TEM analysis was carried out. High resolution TEM showed that the films were composed by NCs with diameter varying from 5 to 30 nm (average at about 10 nm) (Figure 4.2a), and MPLs with an edge length from about 0.5 to 2 µm (Figure 4.2b).

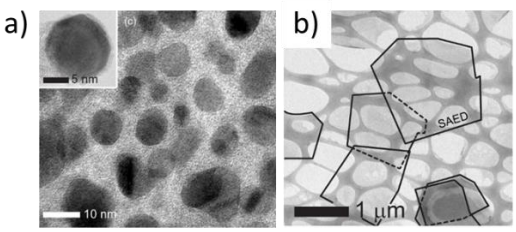

Figure 4.2. TEM images of drop-casted solution with OA:$PbBr_2$ ratio of 5:1 on carbon-Cu grid. a) Overview image of multiple NCs. The inset shows a crystalline $FAPbBr_3$ nanocrystal with diameter of approximately 10 nm. b) $(OA)_2(FA)_{n-1}Pb_nBr_{3n+1}$ MPLs (darker areas, outlined with solid lines) formed during the synthesis.

When deposited onto substrates, the dispersions led to very smooth (RMS ± 1 nm) self-assembled hierarchical composite films, which played a critical role to achieve high quality films and devices. Similar results were obtained for OA:$PbBr_2$ ratios < 7:1. The films exhibited remarkably high PLQYs for all the OA:$PbBr_2$ ratios, with values ranging between 75% and 89%.

Additionally, the microsized MPLs were observed to preferentially grow on top of the 3D NCs, as observed by cathodoluminescence (CL) microscopy (Figure 4.3a), which allows to visualize the emission from the NCs and the MPLs locally. In the images, a striking enhancement of green emission (at 525 nm) was observed for NCs located in the vicinity of MPLs. When the emission was filtered to exclude the green signal, the 440 nm emission from the MPLs could clearly be discerned. This self-assembly is induced by complete wetting of the substrate's surface, prior to spin-coating. During the process, the MPLs arguably accumulate at the liquid-air interface due to their large ligand-to-surface ratio, yielding very smooth mesoscopic composites films consisting of rectangular (or polygonal) MPLs intimately in contact with NCs of graded particle sizes. The effect of the waiting time between dropping the ink solution and the subsequent spin-coating was investigated by scanning electron microscopy (SEM) top surface images. Figure 4.3b shows that longer waiting times result in a larger concentration of MPLs (dark areas) on top of the NCs thin-film.

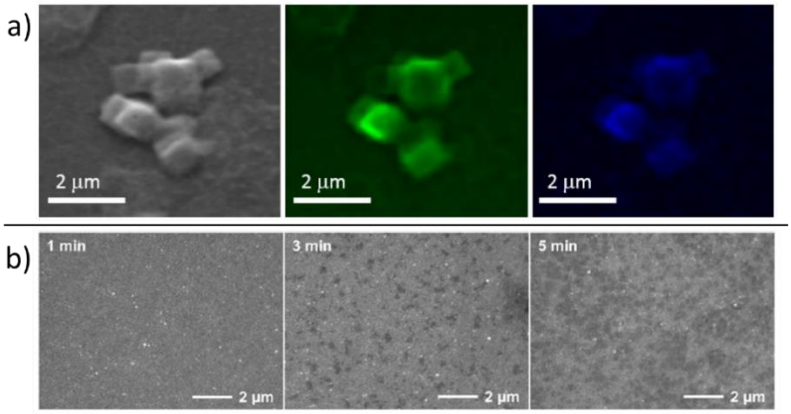

Figure 4.3. a) Cathodoluminescence images of a spin-coated NC film (OA:$PbBr_2$ = 5:1) on a silicon substrate. The CL images in the middle and right panels are obtained by mapping with emission wavelength at 525 nm and 440 nm, respectively. b) SEM top surface images displaying the effect of longer waiting times between dropping the NC ink and the subsequent spin-coating. Longer waiting times results in a large concentration of MPLs (dark areas) on top of the NCs thin-film.

Optimized devices from the 2D-3D self-assembled films displayed uniform and bright green emission, a fair temporal stability (comparable to the best efficiency perovskite LEDs to date),[129–131] and stable colour emission. The LEDs yielded record high current efficiency in excess of 57.6 cd A^{-1} with an external quantum efficiency above 13% (Figure 4.4b). The excellent quality of the diodes with the different OA:$PbBr_2$ ratios is demonstrated by the low leakage current (< 1 µA cm^{-2}) and the sharp rise of both the current density and luminance at 2.2-2.4 V applied bias (Figure 4.4a). Additionally, due to the low turn-on voltage for electroluminescence (~2.2 V), the LEDs had power efficiency exceeding 58 lm/W, obtained without any light-outcoupling structures.

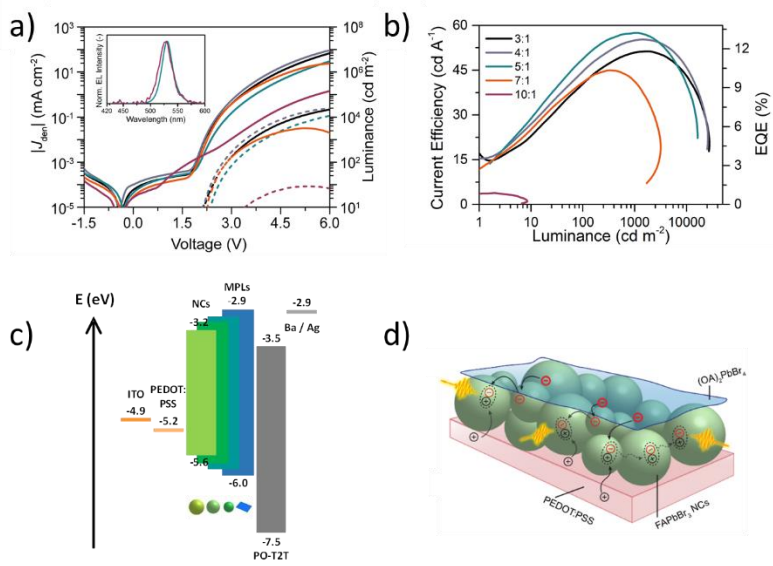

Figure 4.4. a) Current density and luminance vs voltage characteristics and b) current efficiency and EQE versus luminance of the NCs LEDs obtained with perovskite at increasing OA:$PbBr_2$ molar ratio. The inset of Figure a shows the EL spectra of the corresponding devices. c) Flat band energy diagrams of the materials used in the NPs LEDs. d) Schematic illustration of energy transfer under LED device operation in the deposited NCs thin-film on top of PEDOT:PSS.

The reason behind the highly efficient devices was ascribed to the 2D MPLs functioning as a transporting layer and as an intermediary to balance the electron and hole injection, while passivating the NCs. To further confirm the hypothesis, instantaneous PL spectra were obtained on the basis of measured PL decay kinetics in the range 420-570 nm. The emission associated with the MPLs (ca. 440 nm), showed an ultrafast build-up (beyond the time resolution of the setup) and a rapid decay, while the emission associated with the NCs (ca. 525 nm) reached the maximum after 500 ps, with a subsequent red-shift of the emission peak. The behaviour can be rationalized considering the build-up of charges and an energy cascade from the MPLs to the NCs (Figure 4.5).

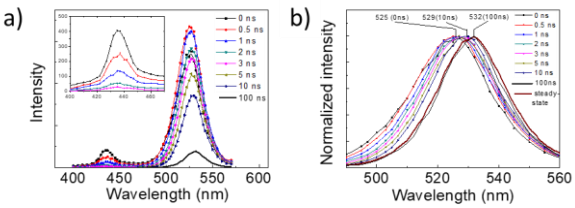

Figure 4.5. a) Instantaneous PL spectra reconstructed from PL decay kinetics at different wavelengths. b) Normalized low energy component of the PL spectra.

After the energy transfer from the MPLs, the charge carriers in the higher bandgap NCs (smaller sized) rapidly cascade into the lowest bandgap NCs (larger sized), within the size distribution. As a consequence of the charge carriers cascade, the photoexcited states tend to concentrate in the largest NCs, enhancing the bimolecular radiative recombination ratio. Interestingly, the use of a suitable ETL was essential to achieve charge balance and hence high electroluminescence efficiency. The molecule 2,4,6-tris[3-(diphenylphosphinyl)phenyl]-1,3,5-triazine (PO-T2T) was selected due to its high electron mobility,[132] enabling a low turn-on voltage, and the deep HOMO level,[133] which ensures good hole-blocking at the perovskite/ETL interface (Figure 4.4c and d). The LED performance depends on the OA:$PbBr_2$ ratio and, in correlation with PLQY, drops for films with high ratios. As the amount of octylamine increases, the fraction of 2D MPLs also grows, and the device efficiency decreases owing to poor charge injection/transport and increased film roughness. The excellent device properties were also observed in flexible devices and large-area devices.

4.4. Published work

The work was carried out in close collaboration with ERI@N, a research section of the Nanyang Technological University in Singapore headed by Prof. Subodh Mhaisalkar.

The publication is reproduced by permission of The Royal Society of Chemistry. DOI: 10.1039/C8EE00293B, Energy Environ. Sci., 2018, 11, 1770-1778.

Energy & Environmental Science

PAPER

View Article Online
View Journal | View Issue

Cite this: *Energy Environ. Sci.*, 2018, **11**, 1770

Self-assembled hierarchical nanostructured perovskites enable highly efficient LEDs *via* an energy cascade†

Xin Yu Chin,[a] Ajay Perumal,[b] Annalisa Bruno,[a] Natalia Yantara,[a] Sjoerd A. Veldhuis,[a] Laura Martínez-Sarti,[c] Bevita Chandran,[d] Vladimir Chirvony,[c] Alencious Shu-Zee Lo,[e] Jinkyu So,[e] Cesare Soci,[e] Michael Grätzel,[f] Henk J. Bolink,[c] Nripan Mathews *[ad] and Subodh G. Mhaisalkar *[ad]

Received 29th January 2018,
Accepted 12th March 2018

DOI: 10.1039/c8ee00293b

rsc.li/ees

Metal halide perovskites have established themselves as extraordinary optoelectronic materials, exhibiting promise for applications in large area illumination and displays. However, low luminescence, low efficiencies of the light-emitting diodes (LEDs), and complex preparation methods currently limit further progress towards applications. Here, we report on a new and unique mesoscopic film architecture featuring the self-assembly of 3D formamidinium lead bromide ($FAPbBr_3$) nanocrystals of graded size, coupled with microplatelets of octylammonium lead bromide perovskites, which enables an energy cascade, yielding very high-performance light-emitting diodes with emission in the green spectral region. These hierarchically structured perovskite films exhibit photoluminescence quantum yields of over 80% and LEDs associated with record high efficiencies in excess of 57.6 cd A^{-1} with an external quantum efficiency above 13%. Additionally, due to low turn-on voltages (~2.2 V) the LEDs have power efficiencies exceeding 58 lumens per watt, obtained without any light-outcoupling structures.

Broader context

Solution-processable halide perovskites have emerged as extraordinary optoelectronic materials for cost-effective and efficient photovoltaic applications and light-emitting diodes (LEDs). Despite major recent advances, the LED device efficiency is still lagging behind established technologies such as organic LEDs (OLEDs). The highest efficiencies reported to date are achieved by employing difficult-to-control anti-solvent engineering techniques to induce rapid crystallisation from solution; limiting the crystal growth while enhancing the radiative recombination properties. We propose to decouple the synthesis of nanocrystals from the film processing, allowing better control over the crystallite sizes and film morphology and an enhanced fabrication reproducibility. This can facilitate an improved scalability to larger area devices and high-throughput device printing methods. At the same time the hierarchically structured perovskite films obtained with this method have shown an external quantum efficiency exceeding 13% on small area devices and over 12% on large scale devices. These are amongst the highest reported values at the moment. This work thus presents an innovative and easy to scale method to fabricate bright and extremely efficient halide perovskite LEDs for potential applications in large area illumination and displays.

[a] *Energy Research Institute at Nanyang Technological University (ERI@N), 50 Nanyang Drive, Research Techno Plaza, X-Frontier Block, Level 5, Singapore 637553, Singapore. E-mail: nripan@ntu.edu.sg, subodh@ntu.edu.sg*
[b] *Department of Physics, Indian Institute of Science Education and Research (IISER), Berhampur, Odisha, 760010, India*
[c] *Instituto de Ciencia Molecular, Universidad de Valencia, C/Cat. J. Beltran 2, 46980 Paterna, Spain*
[d] *School of Materials Science and Engineering, Nanyang Technological University, Singapore, 639798, Singapore*
[e] *Centre of Disruptive Photonics Technologies, Division of Physics and Applied Physics, School of Physical and Mathematical Sciences, Nanyang Technological University, Singapore, 637371, Singapore*
[f] *Laboratory of Photonics and Interfaces, Department of Chemistry and Chemical Engineering, Swiss Federal Institute of Technology, Station 6, Lausanne 1015, Switzerland*

† Electronic supplementary information (ESI) available. See DOI: 10.1039/c8ee00293b

Metal halide perovskites have emerged as the only solution-processable photovoltaic technology to outperform multicrystalline silicon, by virtue of its intrinsic properties such as large absorption coefficient, balanced charge carrier transport, highly crystalline film formation, weak exciton binding energies, and slow bimolecular recombination.[1] Since 2014, perovskites have made strides in light-emitting applications with the first demonstration of amplified spontaneous emission and LEDs.[2,3] LEDs comprising various perovskite compositions have been reported, with a vast majority describing LEDs with low efficiency and luminance.[4–6] Central to the below-par efficiency have been low photoluminescence quantum yields (PLQYs) in the films resulting from the low exciton binding energies in 3D perovskites

(*e.g.* $CH_3NH_3PbBr_3$) and consequently slow electron–hole bimolecular recombination rates, especially at low carrier injection regimes where typical LEDs operate. High carrier density regimes where the PLQY could be higher, typically lead to material degradation.[3,7–10]

In the typical LED operational regime, the charge carrier concentrations ($\sim 10^{15}$ cm^{-3}) are comparable to the trap densities in 3D perovskites, which in combination with the large diffusion lengths (and charge carrier delocalization) leads to strong trap-mediated non-radiative recombination effects.[8,11] Strategies to counter these limitations include ultrathin emitter layers, nanostructured materials, grain size control through additives and process control (which localize the injected carriers), and the formation of low-dimensionality layered-perovskites (primarily modulating the excitonic effects). While the first PeLEDs were only demonstrated in 2014, the field evolved rapidly beyond 10% EQE, largely due to fast adaption of sequential advances in the field of QLEDs and organic LEDs; in which record EQEs in excess of 27% and 31% are demonstrated, respectively.[12,13] A solvent engineering approach led to $MAPbBr_3$ nanograins ($\sim$100 nm grains) with a maximum external quantum efficiency (EQE) of 8.5% and efficiencies of $\sim$43 cd A^{-1}, with the enhanced performance attributed to increased radiative recombination rates in nanoparticles or small crystal domains.[4] Long-chain ammonium halide surfactants provide surface passivation and limit the grain sizes to under 10 nm, resulting in an enhanced EQE of 10.4%.[8] In quasi-2D or Ruddlesden–Popper perovskites with a PLQY of $\sim$70%, improved LED performances, and an EQE of 11.7%,[14] have been attributed to an energy funnelling mechanism related to the presence of domains exhibiting a range of energetic excited states, enabling spatial concentration and confinement of excitons and high electroluminescence. These quasi-2D systems show promising performance and could still be improved by increasing the concentration of the emitting 3D perovskite domains in the thin films. Fabrication processes described thus far, involve precise control over surfactant addition and sensitive post-processing procedures, unfavourable to concerted commercialisation efforts. Decoupling the synthesis of perovskite nanocrystals (NCs) from the thin film processing step would allow for better control over crystal size and film thickness, thus improving fabrication reproducibility and advancing opportunities for scaling up device fabrication. Typically, long-chained capping ligands are employed during the NC synthesis to restrict the growth of the NCs and ensure colloidal stability of the solution.[15,16] Despite providing good surface passivation, these long chain ligands limit the electrical

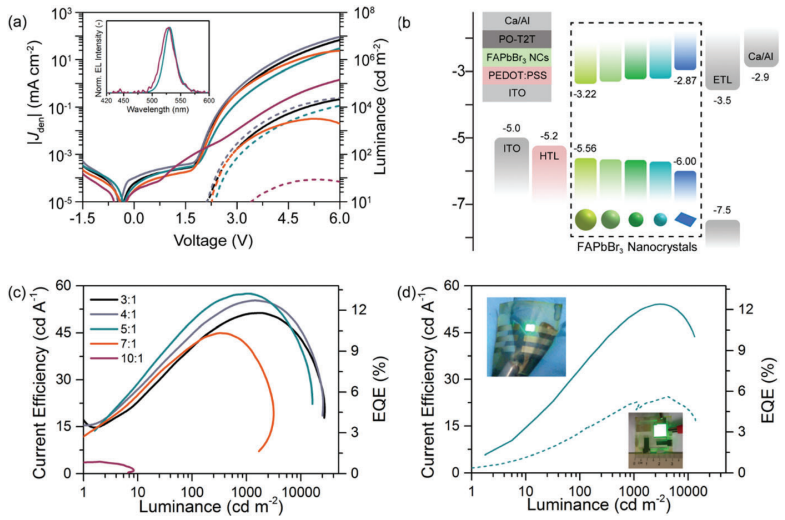

Fig. 1 Device characteristics of LEDs. (a) Current–voltage–luminance characteristics of NC LEDs. The inset shows the electroluminescence spectra of the respective devices. The EL peak is positioned around 528–532 nm with a FWHM of *ca.* 25–26 nm, corresponding to CIE 1931 colour coordinate (0.20, 0.76). Black, grey, dark cyan, orange, and purple curves show NCs with molar ratios of 3 : 1, 4 : 1, 5 : 1, 7 : 1, and 10 : 1 of OA : $PbBr_2$, respectively. (b) Schematic band diagram of the NC LEDs used in this work. (c) Characteristic current efficiency/EQE *versus* luminance (device area: 3 mm^2). (d) Current efficiency/EQE *versus* luminance of flexible (3 mm^2) and large area (95.2 mm^2) LED devices, with 4 : 1 NCs.

Table 1 The maximum luminance, current efficiency, luminous power efficiency, and EQE of the LED devices (as depicted in Fig. 1)

OA : $PbBr_2$ [—]	No. of devices [—]	Luminance [cd m^{-2}]	Current efficiency [cd A^{-1}]	Luminous power efficiency [lm W^{-1}]	EQE [%]
3 : 1	20	36 349 (32 030)	51.3 (33.0)	46.8 (28.2)	12.0 (7.8)
4 : 1	49	56 143 (33 054)	55.5 (52.7)	58.1 (51.3)	12.9 (12.3)
5 : 1	34	34 480 (21 354)	57.6 (52.5)	51.7 (46.1)	13.4 (12.1)
7 : 1	23	3325 (2359)	45.0 (41.0)	45.7 (40.3)	10.5 (9.6)
10 : 1	14	8.4 (6.4)	5.4 (2.9)	4.8 (2.6)	1.5 (0.8)

injection into the perovskite layer due to their insulating nature. A methodology that would allow for precise nanoparticle synthetic control and assembly to form highly efficient emitter layers is a requisite for a breakthrough in device performance.

Herein, we present high-performance devices fabricated from a synthetic protocol comprising judicious control over the addition of ligands to formamidinium bromide (FABr) and $PbBr_2$, to form a hierarchical self-assembly of 2D octylammonium lead bromide microplatelets ($(OA)_2(FA)_{n-1}Pb_nBr_{3n+1}$ MPLs) and $FAPbBr_3$ NCs (see Materials and methods for details). The self-assembled mesoscopic thin films comprising large plate-like ($\sim$0.5–2 μm edge length) domains of $(OA)_2(FA)_{n-1}Pb_nBr_{3n+1}$ and $FAPbBr_3$ NCs were sandwiched between suitable electron and hole transporting layers yielding the highest combination of EQE, luminance, power and current efficiency values (13.4% EQE, $\sim$56k cd m^{-2}, 58.1 lm W^{-1}, 57.6 cd A^{-1}) demonstrated to date in green-emitting perovskite LEDs.

The excellent quality of the diodes with the different OA : $PbBr_2$ ratios (Fig. 1, Fig. S1 and Table S1, ESI†) is evidenced by the low leakage current (<1 μA cm^{-2}) and the sharp turn-on of both the current density and luminance around 2.2–2.4 V. Device performance statistics (of 20–50 devices under each synthetic condition) show excellent reproducibility within the range of 4 : 1 and 7 : 1 OA : $PbBr_2$ ratios (Table 1, Fig. 2, Fig. S2, S3 and Tables S2, S3, ESI†). This validates the benefit of preparing and isolating the perovskite components prior to the integration into thin film devices. The correct choice of electron transport layer was essential to achieve charge balance and thus high efficiencies (Fig. S4, S5 and Table S4, ESI†). Indeed, the use of PO-T2T (2,4,6-tris[3-(diphenylphosphinyl)phenyl]-1,3,5-triazine), as opposed to B3PYMPM (4,6-bis(3,5-di(pyridin-3-yl)-phenyl)-2-methylpyrimidine), as an electron transporting layer of the LED devices lowered the turn-on voltage and improved the luminance, luminous power efficiency, current efficiency, and EQE. We attribute the overall improvement to the better hole-blocking properties of PO-T2T, enabled by the deeper HOMO level of PO-T2T (−7.5 eV)[17] compared to −6.9 eV of B3PYMPM[18] (Fig. S7, ESI†), while the reduction in the turn-on voltage is likely related to the superior electron mobility of PO-T2T ($\sim 10^{-3}$ cm^2 V^{-1} s^{-1})[19] *versus* B3PYMPM ($\sim 10^{-4}$ cm^2 V^{-1} s^{-1}).[20] These optimised devices displayed uniform and bright green emission (Fig. S6, ESI†), a fair temporal stability (Fig. S7, ESI,† comparable to the best efficiency PeLEDs[7,11,21]), and stable colour emission (Fig. S8, ESI†). Moreover, an excellent repeatability of device metrics (*i.e.* luminance and efficiency) was also achieved across a wide range of measurement scan rates (in the range 0.1–2 V s^{-1}), indicating minimal defects across the active layers and interfaces. These excellent properties allowed the conversion into flexible devices (3 mm^2, 12.4% EQE, $>$13k cd m^{-2}) and large-area devices (up to 95.2 mm^2, 5.7% EQE, $>$13k cd m^{-2}) as presented in Fig. 1d, Fig. S10, S11 and Tables S5–S8 (ESI†).

To elucidate the transport properties of the perovskite active layers, we collected current–voltage characteristics of single-carrier devices. In the case of the electron-only devices (device stack: ITO/PEIE/Perovskite/PO-T2T/Ca/Al, Fig. 3a), PEIE-treated

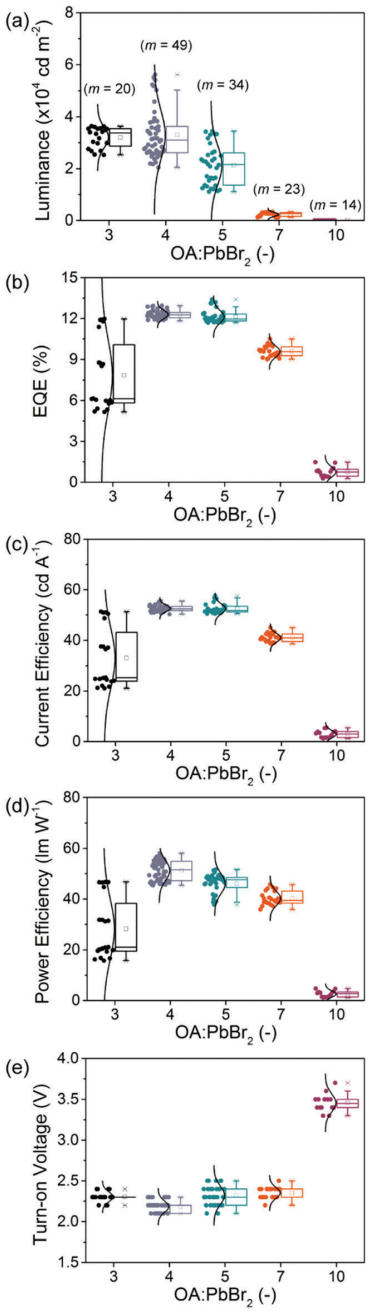

Fig. 2 Device statistics of LEDs. (a) Luminance, (b) EQE, (c) current efficiency, (d) power efficiency, and (e) turn-on voltage values shown as box plots for LED devices (*m* is the number of devices measured) based on different OA : $PbBr_2$ ratios. Each measured device is represented by filled circles with a normal distribution. The squares and crosses represent the median values and outliers, whereas the error bars represent the minimum and maximum values. Lower and upper bars within the box, represent the first and third quartile (Q1 and Q3), respectively.

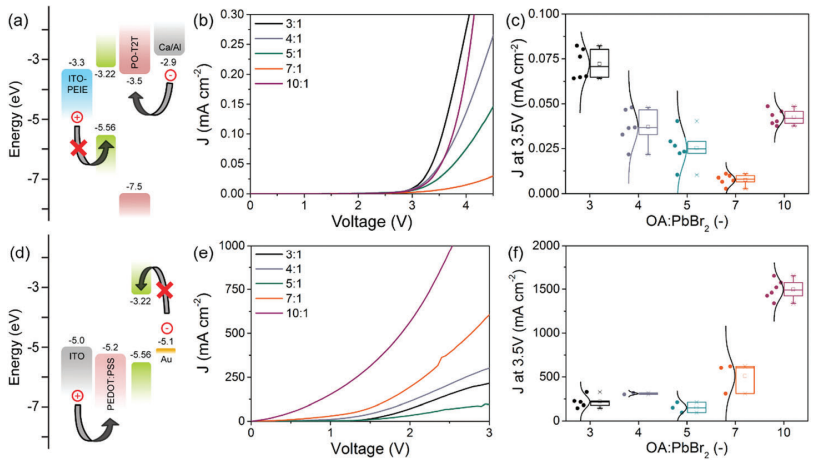

Fig. 3 Single carrier devices fabricated with different OA : $PbBr_2$ ratios. (a and d) Band diagrams, (b and e) representative *J–V* curves, and (c and f) box plots of the current density for electron-only (at 3.5 V) and hole-only (at 3.5 V) devices, respectively.

ITO substrates (work function 3.3 eV) were used instead of ITO/PEDOT:PSS, to block the hole injection into the perovskite layer. Conversely, for the hole-only devices (device stack: ITO/PEDOT:PSS/Perovskite/Au, Fig. 3d) we employed a Au contact, rather than PO-T2T/Ca/Al, to create a barrier for electron injection into the perovskite layer. The current density–voltage characteristics and current at 3.5 V for electron-only devices are summarized in Fig. 3b and c, which show that upon increasing the OA : $PbBr_2$ ratios (up to 7 : 1), the electron-transport in the devices decreases. On the other hand, hole injection (Fig. 3e and f) appears independent of the OA : $PbBr_2$ ratios up to 7 : 1. When OA : $PbBr_2$ is 10 : 1, significantly enhanced electron- and hole-transport was observed for all tested devices, presumably caused by pin holes in the resulting perovskite thin films (*i.e.* electrical shunt paths), as observed in the topographical images (see Fig. S15, ESI†). We note that no EL is observed in the single-carrier devices at higher operating voltages (*ca.* 3–4 V), suggesting that the diodes are operating with negligible minority carriers in the investigated operating regime. The balance between electron- and hole-injection into the emitter film is altered by the reduction of electron transport at increased OA : $PbBr_2$, which affects the device efficiency. The highest device efficiencies were achieved using 4 : 1 and 5 : 1, inferring more balanced carrier injection in these devices.

Although the efficiencies of the devices are high, the devices suffer an efficiency droop at higher current density, *i.e.* drop of efficiency at high luminance or in the high current density regime. The drop of efficiency in perovskite LEDs has previously been observed and attributed to the heat degradation of the materials driven at a large current density, where luminescence stability is observed to be improved while operating the LED with short duration voltage pulses.[3] It should also be noted that an efficiency droop is also commonly observed in nitride-based LEDs, where heat degradation,[22] enhanced Auger recombination,[23] carrier overflow at high carrier population,[24–26] and a carrier delocalization effect[27] have been argued to be the possible mechanism behind the unwanted phenomenon. The exact mechanism of the efficiency droop for PeLEDs is at present not completely understood and more investigations are required to resolve this issue.

As evidenced by field-emission scanning electron microscopy (FESEM), transmission electron microscopy (TEM), and cathodoluminescence (CL) studies, preferential deposition of the micron-sized 2D MPLs is observed on top of the 3D NCs, while the ratio between the 2D MPLs and 3D NCs can be conveniently modulated by varying the OA : $PbBr_2$ ratio. This self-assembly is induced by complete wetting of the substrate's surface, prior to spin-coating. Here, the 2D MPLs arguably accumulate at the liquid–air interface due to their large ligand-to-surface ratio (*i.e.* similar to Langmuir–Blodgett), and the yielded films are very smooth (RMS ± 1 nm) mesoscopic composites (Fig. 4a, b and Fig. S12–S15, ESI†) consisting of rectangular (or polygonal) MPLs intimately in contact with NCs of graded particle sizes (~5–30 nm). Morphological images of the films prove the formation of uniform and compact films. Only for thin films fabricated with OA : $PbBr_2$ 10 : 1 agglomerated structures were formed, indicating appropriate usage of surface ligands at lower ligand-to-precursor ratios. In SEM top view images (Fig. S12, ESI†) an increasing number of micrometer-sized dark patches were observed on the film's surface at increasing OA : $PbBr_2$ ratios. This can be related to the existence of $(OA)_2(FA)_{n-1}Pb_nBr_{3n+1}$ MPLs as revealed by the CL mapping (Fig. S22, ESI†). In addition, the number of MPLs on the surface could be maximised by increasing the delay times between dropping of the NC ink and the spin coating step (Fig. S13, ESI†). The current distribution throughout the film was observed using conducting AFM at 1 V bias (Fig. S15, ESI†). Uniform current was observed across the 3 : 1, 4 : 1, 5 : 1, and 7 : 1 films. This indicates that the existence of 2D MPLs does not significantly hinder the current flow at these compositions. In the case of the 10 : 1 film,

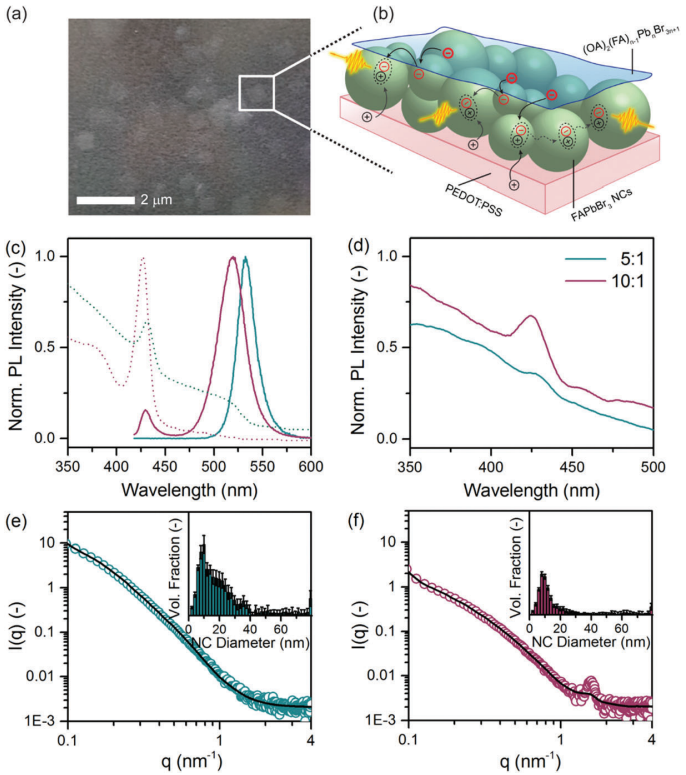

Fig. 4 Optical and structural characterisation of mixed $FAPbBr_3$ NCs and $(OA)_2(FA)_{n-1}Pb_nBr_{3n+1}$ MPLs. (a) The top-view FE-SEM image. (b) Schematic illustration of energy transfer under LED device operation in the deposited NCs thin film on top of PEDOT:PSS. (c) Absorption and steady-state photoluminescence (λ_{ex} = 405 nm) spectra showing excitonic absorption and photoluminescence from $(OA)_2(FA)_{n-1}Pb_nBr_{3n+1}$, for OA : $PbBr_2$ is 5 : 1 (dark cyan) and 10 : 1 (purple). (d) Excitation spectra (λ_{em} = 533 and 519 nm, for 5 : 1 and 10 : 1, respectively). (e and f) Small-angle X-ray scattering (SAXS) curves of NC inks, showing a Bragg reflection of the 2D MPLs. Insets: Particle size distribution extracted from the scattering curves.

patches of higher resistance area were noticed, which could be related to the existence of 2D MPL agglomerates, in agreement with the topographical images of the film (Fig. S12, ESI†).

Detailed characterisation by means of absorption and photoluminescence spectroscopy and small-angle X-ray scattering (SAXS), and X-ray diffraction (Fig. 4c–f and Fig. S16–S19, ESI†) indicate the presence of 2D $(OA)_2(FA)_{n-1}Pb_nBr_{3n+1}$ MPLs and 3D $FAPbBr_3$ NCs with a narrow size distribution of preferred orientation parallel to the substrate's surface. The steady state optical absorption spectra (Fig. 4c and Fig. S16, ESI†) of NC thin films with 5 : 1 and 10 : 1 OA : $PbBr_2$ ratios indicate the presence of two main features, a peak at 440 nm (*ca.* 2.82 eV) that corresponds to the excitonic absorption of the 2D MPLs and the band absorption of 3D $FAPbBr_3$ NCs at 520–530 nm (*ca.* 2.38–2.34 eV). The peak intensity consistently changes with the OA content due to the increased presence of $(OA)_2(FA)_{n-1}Pb_nBr_{3n+1}$ MPLs with respect to $FAPbBr_3$ NCs. The PL spectra show a pronounced emission from the MPLs at ~440 nm (for the 10 : 1 composition), however this emission is markedly absent from the 5 : 1 PL spectra. Excitation spectra (λ_{em} = 533 and 519 nm, for 5 : 1 and 10 : 1, respectively) provide the first intimation of an energy cascade from the higher bandgap $(OA)_2(FA)_{n-1}Pb_nBr_{3n+1}$ MPLs to the lower bandgap $FAPbBr_3$ NCs through a PL contribution around 425–430 nm (Fig. S17c, ESI†).

The presence of composite 2D and 3D perovskite structures was further confirmed by SAXS and XRD patterns with Bragg reflections of 2D $(OA)_2(FA)_{n-1}Pb_nBr_{3n+1}$ MPLs at $q \sim 1.60$ nm^{-1} (d-spacing of ~3.93 nm) and 2θ = 8–12°, respectively, at OA : $PbBr_2$ = 10 : 1; and predominance of the 3D $FAPbBr_3$ NCs at lower OA : $PbBr_2$ ratios.

Particle size distributions extracted from the SAXS scattering curves elucidate that the films are made up of NCs with a median diameter around 10 nm; with a narrower distribution for samples with OA : $PbBr_2$ ratios of 5 : 1 and with a much wider distribution at higher ratios (refer to Fig. S18, ESI† for details). Rocking curves of (001) reflection of $(OA)_2(FA)_{n-1}Pb_nBr_{3n+1}$ (2θ: ~9.6°) and (002) reflection of $FAPbBr_3$ (2θ: ~29.8°), display the occurrence of a peak, indicating a preferred orientation of both phases through self-assembly (refer to Fig. S17, ESI† for details).

Grazing-incidence small-angle X-ray scattering (GISAXS) was employed to probe the microstructural changes of the surface layer as a function of the delay time between drop casting of the NC inks and the subsequent spin-coating step (Fig. S18 and S19, ESI†).

While the lateral sizes of the MPLs are greater than observable in the measured q-range, Bragg-like reflections are only observed in samples prepared with OA : $PbBr_2$ = 10 : 1 at 2.23 and 2.50 nm^{-1} (Fig. S19d–f; also for OA : $PbBr_2$ = 7 : 1 in Fig. S18d, ESI†). The corresponding interlayer distances of *ca.* 28.2 and 25.1 Å, respectively, do not match the observed lattice spacing for pure $(OA)_2PbBr_4$,[28] but rather signify a persistent average distance between a multiple of stacked MPLs parallel to the substrate's surface. The further appearance of a 'bump' at $q \sim 1.85$ nm^{-1} (*i.e.* ~34 Å spacing) after 5 min delay further implies that this self-assembly into hierarchically stacked structures is a dynamic process. This is corroborated by the XRD measurements showing that the diffraction peak at $2\theta \sim 9.6^\circ$ moves to lower angles (Fig. S17a, ESI†). The absence of Bragg-like features in samples prepared with OA : $PbBr_2$ < 5 : 1 (Fig. S18f–h and S19a–c, ESI†) can be explained by the limited scattering volume of the MPLs (*i.e.* due to their low concentration on the surface). However, from the data obtained from SEM (Fig. S12 and S13, ESI†) and XRD (Fig. S17, ESI†) we infer that these MPLs are present.

Through a combination of transient optical spectroscopic techniques, we elucidate the energy cascade mechanism taking place from high bandgap 2D $(OA)_2(FA)_{n-1}Pb_nBr_{3n+1}$ MPLs into progressively lower bandgap $FAPbBr_3$ NCs, giving rise to high luminescence efficiency in $FAPbBr_3$ NC LEDs. Indeed, when charge carriers are injected (or photons are absorbed) into the 2D MPLs, since the energy transfer is fast enough to overcome non-radiative recombination, the excitons are preferentially transferred to the energetically favoured lower bandgap 3D $FAPbBr_3$ NCs, as in other multi-domain systems.[7,18–20,29] As a consequence, the photoexcited states tend to concentrate in the lower bandgap NCs, where the higher exciton concentrations would enhance the bimolecular radiative recombination.

The TA change following a λ = 375 nm pulsed excitation reveals two strong bleaching features at 440 and 520 nm for the 5 : 1 sample, in agreement with the absorption spectra (Fig. 5a, central and upper panels). The TA spectrum for the 10 : 1 panel is dominated by the photobleaching peak at 440 nm, indicating that the excitons are predominantly formed in the $(OA)_2(FA)_{n-1}Pb_nBr_{3n+1}$ MPLs. A secondary, albeit less intense peak at 520 nm, is detected and displays a rapid peak shift from 500 to 525 nm within 1 ps. The relative intensities of these two peaks are in agreement with the peaks in the absorption spectra for both samples. The 440 nm component is much shorter lived with respect to the 520 nm peak; the latter still observable even after 1000 ps (Fig. 5a and b lower panel).

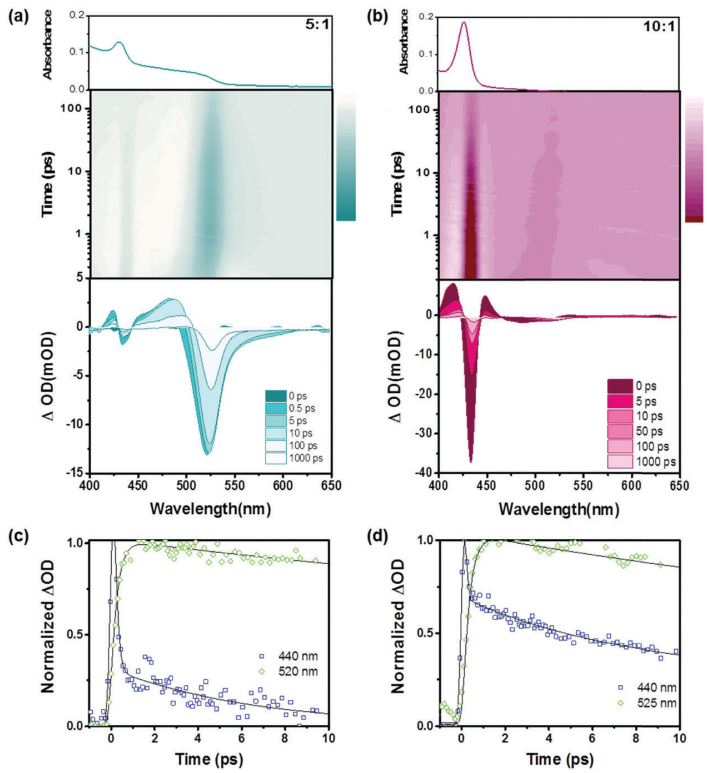

Fig. 5 Transient absorption (TA) spectra of $FAPbBr_3$ NCs. (a and b) UV-Visible absorption spectra (top) panel. TA mapping with excitation at λ = 375 nm, 150 fs, and 1 μJ cm^{-2} fluency in the 0–200 ps range (central panel) and the relative TA spectra up to 1000 ps (lower panel) for $FAPbBr_3$ NCs prepared with 3 : 1 (a), 4 : 1 (b) and 7 : 1 (c) OA : $PbBr_2$. Normalised kinetics of the TA signal at 440 nm and 520 nm for $FAPbBr_3$ NCs prepared with 5 : 1 (c) and 10 : 1 (d) OA : $PbBr_2$.

The kinetics of the TA signal at 440 nm and 525 nm for the 5 : 1 and 10 : 1 samples (Fig. 5c and d) provide strong evidence of an energy cascade between the $(OA)_2(FA)_{n-1}Pb_nBr_{3n+1}$ MPLs and $FAPbBr_3$ NCs. The 440 nm TA kinetics display very fast rising times, indistinguishable from the response function even after deconvolution (~150 fs), compatible with photon absorption taking place in the $(OA)_2(FA)_{n-1}Pb_nBr_{3n+1}$ MPLs. In contrast, the 520 nm kinetics display much slower (~400 fs) rise times, indicating a slower build-up of the absorption signal in $FAPbBr_3$ NCs, due to an energy cascade from the higher bandgap 2D MPLs to the lower bandgap $FAPbBr_3$ NCs.[11] The hierarchical architecture thus produces a vectoral energy flow within the self-assembled mesoscopic structure that enables the diodes to operate as very efficient light emitters. Subsequently, the $FAPbBr_3$ exciton population grows from the energy transfer, while its decay is dominated by radiative recombination. For all $OA : PbBr_2$ ratios, the decay kinetics at 525 nm are slower than that for 440 nm (refer to Fig. S20, S21; and Table S9, ESI† for details).

To visualize the emission from $FAPbBr_3$ NCs and $(OA)_2(FA)_{n-1}Pb_nBr_{3n+1}$ MPLs locally, CL mapping was used (Fig. 6a and Fig. S22, ESI†). Here, a striking enhancement of green emission (at 525 nm) was observed for $FAPbBr_3$ NCs existing in the vicinity of 2D MPLs. Only when the emission was filtered to exclude the green signal could the 440 nm emission from the MPLs be discerned (its relative intensity was very low due to fast energy transfer) (Fig. S23, ESI†). PL lifetimes probed between 440 and 540 nm (λ_{ex} = 405 nm) showed a significant spread consistent with graded NC sizes (*ca.* 5–30 nm) (Fig. 6b). Moreover, when excitons form in the higher bandgap (*i.e.* smaller NCs) and rapidly cascade into the lowest bandgap larger NCs within the size distribution, a variation in the relative weight of the components (of their corresponding PL life-times) is expected. At shorter probing wavelengths, the measured bi-exponential decay is dominated by a fast component related to intraband relaxation pathways inducing carrier cascading, whereas the largest $FAPbBr_3$ NCs (*i.e.* probed at longer wavelengths) show

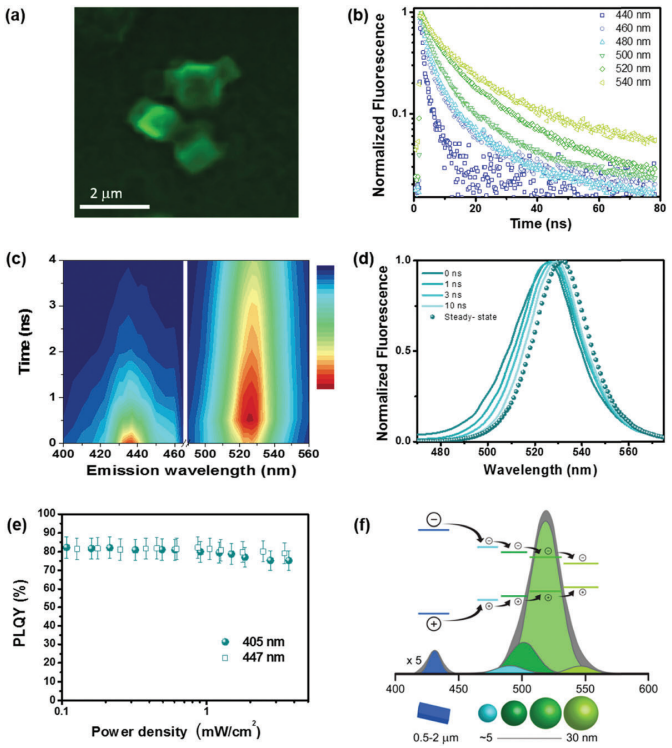

Fig. 6 Emission properties of hierarchically structured films prepared with $OA : PbBr_2$ = 5 : 1. (a) Cathodoluminescence image of a spin-coated film on a silicon substrate. Images are taken using an electron beam of 5 keV energy, current of ~11 nA, and exposure time of 10 ms. The image is obtained by mapping with an emission wavelength at 525 nm. (b) Time-resolved fluorescence decays collected at different emission wavelengths from 440 nm to 540 nm (blue square and slight green left-pointing triangle, respectively) at λ_{ex} = 405 nm. (c) Transient PL spectra at a time interval from 0–4 ns. (d) Normalised transient PL spectra at different time delays after excitation and the steady-state PL spectrum. (e) PLQY *versus* power density after CW laser excitation at λ = 405 and 447 nm. (f) Conceptual diagram representing the energy cascade from 2D MPLs to $FAPbBr_3$ NCs of graded size, where the deconvolution of the steady-state PL spectrum clearly displays the different PL contribution at varying NC sizes. Note: Deconvolution of the PL spectrum into 4 Gaussians is only used to illustrate the energy cascading from the smallest to largest NCs (*i.e.* largest to smallest bandgap). It does not represent the distribution of discrete energy levels originating from a continuous distribution of NCs of *ca.* 5–30 nm diameter, as extracted from the SAXS curves (Fig. S18, ESI†).

considerably longer lifetimes, where bimolecular recombination is the predominant process. (Tables S10–S14, ESI†). Additionally, from transient photoluminescence spectra (Fig. 6c) we can discern the ultrafast build-up of the emission at 440 nm and its rapid decay (within hundreds of picoseconds), which corroborates well with our previous TA observations (Fig. 5a and b). Conversely, the emission associated with the NCs (*ca.* 525 nm) only reached maximum emission after 500 ps, which confirms that the delayed build-up is owing to the energy cascade. This effect was further highlighted by the progressive red-shift of the emission peak within 10 ns (from 525 to 530 nm) (Fig. 6d), and a steady-state emission at 532 nm. The concurrent dynamic changes in the spectral shape and decreasing FWHM are thus likely caused by the lower contribution of the smallest NCs (*i.e.* blue-shifted part of the spectra), and associated with the energy cascade from the higher-to-lower bandgap. Consequently, this results in the narrowing of the transient emission spectra at longer decay times, eventually culminating in an even narrower steady-state emission (Fig. 6d).

PLQY of the composite films in the low power density regime (up to 6 mW cm^{-2}) recorded values of 80% consistently for both λ_{ex} = 405 nm (*i.e.* 2D MPLs and 3D NCs are excited) and λ_{ex} = 447 nm (*i.e.* 2D MPLs are not excited) (Fig. 6e; refer to Fig. S24 (ESI†) for additional details of PLQY as a function of λ_{ex}, power density, and OA : $PbBr_2$ ratios). The invariance of PLQY as a function of power density indicates that owing to the energy cascade mechanism, the carrier densities in the NCs have increased to a point whereby the trap states are overwhelmed and the chances of non-radiative recombination effectively suppressed; thus delivering a near unity value in photoluminescence yields. Concomitantly, the similar high PLQY values obtained at different excitation wavelengths further confirm that efficient energy transfer allows all absorbed photons (by the 2D MPLs) to be transferred as excitons in the graded $FAPbBr_3$ NCs.

The concept of multiple contributions from differently-sized NCs (as extracted from the scattering curves; *ca.* 5–30 nm) on the overall PL emission, is illustrated by deconvolution of the PL spectrum (Fig. 6f). This is confirmed by the considerable spread of characteristic lifetimes within the emission peak (Fig. 6b). The LED performance depends on the OA : $PbBr_2$ ratio, and in correlation with PLQY, drops for films with ratios above 5 : 1. As the amount of octylamine increases (to 10 : 1), the fraction of 2D MPLs increases, and the device efficiency decreases owing to factors including poor charge injection/transport and increased roughness of the films (Fig. 2 and Fig. S12, S15, ESI†). Emitters based on OA : $PbBr_2$ ratios of 3 : 1, 4 : 1 and 5 : 1 display good LED performances in line with the high PLQY observed for these films.

Conclusions

We developed 2D–3D self-assembled hierarchical composite films, comprising large $(OA)_2(FA)_{n-1}Pb_nBr_{3n+1}$ microplatelets (0.5–2 μm) attached to $FAPbBr_3$ nanocrystals (*ca.* 5–30 nm). Ultra-smooth thin films (RMS ± 1 nm, for OA : $PbBr_2$ < 7 : 1) were achieved by spin-coating inks containing the preformed NCs and MPLs, and play a critical role in the realisation of these high performance films and devices. Under electrically driven conditions the 2D MPLs function as a transporting layer and as an intermediary to balance the electron and hole injection, while passivating the NCs. The excitons form in the higher bandgap (smaller) NCs and rapidly cascade into the lowest bandgap (largest) NCs within the size distribution. In the largest nanocrystals, the carrier densities increase substantially thereby reducing the chances of non-radiative recombination, delivering extremely high values of PLQY, EQE, luminance, power and current efficiencies. These hierarchical self-assemblies were transferred to different substrates, shown to be scalable to larger active diode areas, and present high feasibility of further development and continued improvements in performance. The levels of expansive high-performance luminescence metrics are unparalleled in the field of PeLEDs and compare rather favourably with state of the art multilayer green emitting OLEDs.[30]

Author contributions

X. Y. C, A. P., N. M., and S. G. M conceived the idea for the manuscript and designed the experiments. A. B., A. S. Z. L, and J. S. conducted the spectroscopic characterisation. X. Y. C, S. V., N. Y., A. P., B. C., and L. M. S prepared the samples and performed sample characterisation. V. C. performed the PLQY studies. A. B., S. V., N. Y., N. M., S. G. M., H. J. B., M. G., and C. S. analysed the data and wrote the manuscript. All authors discussed the results and commented on the manuscript at all stages. N. M. and S. G. M. led the project.

Conflicts of interest

There are no conflicts of interest to declare.

Acknowledgements

This research was supported by the National Research Foundation, Prime Minister's Office, Singapore under its Competitive Research Programme (CRP Award No. NRF-CRP14-2014-03) and through the Singapore–Berkeley Research Initiative for Sustainable Energy (SinBeRISE) CREATE Program. C. S and J. K. S. acknowledge support from the Singapore Ministry of Education (MOE2011-T3-1-005). H. J. B. acknowledges financial support from the European Union H2020 project SOLEDLIGHT (grant 643791), and the Spanish Ministry of Economy and Competitiveness (MINECO) *via* the Unidad de Excelencia María de Maeztu MDM-2015-0538 and MAT-2017-88821-R. L. M. S. acknowledges a predoctoral contract (FPI) from MINECO. M. G. acknowledges funding from the Swiss National Science foundation.

References

1 M. A. Green, A. Ho-Baillie and H. J. Snaith, *Nat. Photonics*, 2014, **8**, 506–514.
2 G. Xing, N. Mathews, S. S. Lim, N. Yantara, X. Liu, D. Sabba, M. Grätzel, S. Mhaisalkar and T. C. Sum, *Nat. Mater.*, 2014, **13**, 476–480.

3 Z.-K. Tan, R. S. Moghaddam, M. L. Lai, P. Docampo, R. Higler, F. Deschler, M. Price, A. Sadhanala, L. M. Pazos, D. Credgington, F. Hanusch, T. Bein, H. J. Snaith and R. H. Friend, *Nat. Nanotechnol.*, 2014, **9**, 687–692.
4 H. Cho, S.-H. Jeong, M.-H. Park, Y.-H. Kim, C. Wolf, C.-L. Lee, J. H. Heo, A. Sadhanala, N. Myoung, S. Yoo, S. H. Im, R. H. Friend and T.-W. Lee, *Science*, 2015, **350**, 1222–1225.
5 M. Saliba, T. Matsui, K. Domanski, J.-Y. Seo, A. Ummadisingu, S. M. Zakeeruddin, J.-P. Correa-Baena, W. R. Tress, A. Abate, A. Hagfeldt and M. Grätzel, *Science*, 2016, **354**, 206–209.
6 X. Y. Chin, D. Cortecchia, J. Yin, A. Bruno and C. Soci, *Nat. Commun.*, 2015, **6**, 7383.
7 M. Yuan, L. N. Quan, R. Comin, G. Walters, R. Sabatini, O. Voznyy, S. Hoogland, Y. Zhao, E. M. Beauregard, P. Kanjanaboos, Z. Lu, D. H. Kim and E. H. Sargent, *Nat. Nanotechnol.*, 2016, **11**, 872–877.
8 Z. Xiao, R. A. Kerner, L. Zhao, N. L. Tran, K. M. Lee, T.-W. Koh, G. D. Scholes and B. P. Rand, *Nat. Photonics*, 2017, **11**, 108–115.
9 H. Zhu, Y. Fu, F. Meng, X. Wu, Z. Gong, Q. Ding, M. V. Gustafsson, M. T. Trinh, S. Jin and X. Zhu, *Nat. Mater.*, 2015, **14**, 636–642.
10 S. A. Veldhuis, P. P. Boix, N. Yantara, M. Li, T. C. Sum, N. Mathews and S. G. Mhaisalkar, *Adv. Mater.*, 2016, **28**, 6804–6834.
11 N. Wang, L. Cheng, R. Ge, S. Zhang, Y. Miao, W. Zou, C. Yi, Y. Sun, Y. Cao, R. Yang, Y. Wei, Q. Guo, Y. Ke, M. Yu, Y. Jin, Y. Liu, Q. Ding, D. Di, L. Yang, G. Xing, H. Tian, C. Jin, F. Gao, R. H. Friend, J. Wang and W. Huang, *Nat. Photonics*, 2016, **10**, 699–704.
12 H. Zhang, S. Chen and X. W. Sun, *ACS Nano*, 2018, **12**, 697–704.
13 C.-Y. Kuei, W.-L. Tsai, B. Tong, M. Jiao, W.-K. Lee, Y. Chi, C.-C. Wu, S.-H. Liu, G.-H. Lee and P.-T. Chou, *Adv. Mater.*, 2016, **28**, 2795–2800.
14 J. Li, X. Shan, S. G. R. Bade, T. Geske, Q. Jiang, X. Yang and Z. Yu, *J. Phys. Chem. Lett.*, 2016, **7**, 4059–4066.
15 G. Xing, B. Wu, X. Wu, M. Li, B. Du, Q. Wei, J. Guo, E. K. L. Yeow, T. C. Sum and W. Huang, *Nat. Commun.*, 2017, **8**, 14558.
16 F. Zhang, H. Zhong, C. Chen, X.-g. Wu, X. Hu, H. Huang, J. Han, B. Zou and Y. Dong, *ACS Nano*, 2015, **9**, 4533–4542.
17 J.-H. Lee, S.-H. Cheng, S.-J. Yoo, H. Shin, J.-H. Chang, C.-I. Wu, K.-T. Wong and J.-J. Kim, *Adv. Funct. Mater.*, 2015, **25**, 361–366.
18 H. Sasabe, T. Chiba, S. J. Su, Y. J. Pu, K. Nakayama and J. Kido, *Chem. Commun.*, 2008, 5821–5823.
19 W. Y. Hung, G. C. Fang, S. W. Lin, S. H. Cheng, K. T. Wong, T. Y. Kuo and P. T. Chou, *Sci. Rep.*, 2014, **4**, 5161.
20 H. Sasabe, D. Tanaka, D. Yokoyama, T. Chiba, Y.-J. Pu, K.-i. Nakayama, M. Yokoyama and J. Kido, *Adv. Funct. Mater.*, 2011, **21**, 336–342.
21 L. N. Quan, Y. Zhao, F. P. Garcia de Arquer, R. Sabatini, G. Walters, O. Voznyy, R. Comin, Y. Li, J. Z. Fan, H. Tan, J. Pan, M. Yuan, O. M. Bakr, Z. Lu, D. H. Kim and E. H. Sargent, *Nano Lett.*, 2017, **17**, 3701–3709.
22 A. Laubsch, M. Sabathil, W. Bergbauer, M. Strassburg, H. Lugauer, M. Peter, S. Lutgen, N. Linder, K. Streubel, J. Hader, J. V. Moloney, B. Pasenow and S. W. Koch, *Phys. Status Solidi C*, 2009, **6**, S913–S916.
23 Y. C. Shen, G. O. Mueller, S. Watanabe, N. F. Gardner, A. Munkholm and M. R. Krames, *Appl. Phys. Lett.*, 2007, **91**, 141101.
24 M.-H. Kim, M. F. Schubert, Q. Dai, J. K. Kim, E. F. Schubert, J. Piprek and Y. Park, *Appl. Phys. Lett.*, 2007, **91**, 183507.
25 Y. Yang, X. A. Cao and C. H. Yan, *Appl. Phys. Lett.*, 2009, **94**, 041117.
26 K. J. Vampola, M. Iza, S. Keller, S. P. DenBaars and S. Nakamura, *Appl. Phys. Lett.*, 2009, **94**, 061116.
27 Y. Yang, X. A. Cao and C. Yan, *IEEE Trans. Electron Devices*, 2008, **55**, 1771–1775.
28 S. Gonzalez-Carrero, G. M. Espallargas, R. E. Galian and J. Perez-Prieto, *J. Mater. Chem. A*, 2015, **3**, 14039–14045.
29 L. C. Schmidt, A. Pertegás, S. González-Carrero, O. Malinkiewicz, S. Agouram, G. Mínguez Espallargas, H. J. Bolink, R. E. Galian and J. Pérez-Prieto, *J. Am. Chem. Soc.*, 2014, **136**, 850–853.
30 Y. Seino, S. Inomata, H. Sasabe, Y. J. Pu and J. Kido, *Adv. Mater.*, 2016, **28**, 2638–2643.

Supporting Information

Self-assembled Hierarchical Nanostructured Perovskites Enable Highly Efficient LEDs via Energy Cascade

Xin Yu Chin,[a] Ajay Perumal,[b] Annalisa Bruno,[a] Natalia Yantara,[a] Sjoerd A. Veldhuis,[a] Laura Martínez-Sarti,[c] Bevita Chandran,[d] Vladimir Chirvony,[c] Alencious Shu-Zee Lo,[e] Jinkyu So,[e] Cesare Soci,[e] Michael Grätzel,[f] Henk J. Bolink,[c] Nripan Mathews,[*ad] Subodh G. Mhaisalkar[*ad]

[a] *Energy Research Institute at Nanyang Technological University (ERI@N), 50 Nanyang Drive, Research Techno Plaza, X-Frontier Block, Level 5, Singapore 637553, Singapore.*

[b] *Department of Physics, Indian Institute of Science Education and Research (IISER) Berhampur, Odisha, 760010, India.*

[c] *Instituto de Ciencia Molecular, Universidad de Valencia C/ Cat. J. Beltran 2, 46980 Paterna, Spain.*

[d] *School of Materials Science and Engineering, Nanyang Technological University, 639798 Singapore.*

[e] *Centre of Disruptive Photonics Technologies, Division of Physics and Applied Physics, School of Physical and Mathematical Sciences, Nanyang Technological University, 637371 Singapore.*

[f] *Laboratory of Photonics and Interfaces, Department of Chemistry and Chemical Engineering, Swiss Federal Institute of Technology, Station 6, Lausanne 1015, Switzerland.*

Experimental details

Nanocrystal (NC) synthesis & NC ink formation: Ligand-assisted reprecipitation (LARP) method was used to synthesize the $FAPbBr_3$ nanocrystals at room temperature. Precursor solutions were prepared by mixing 0.2 mmol of FABr (formamidinium bromideDyesol) and 0.1 mmol of $PbBr_2$ (99.999% trace metal basis, Sigma Aldrich) in 0.5 mL of DMF (anhydrous *N,N*-dimethylformamide, 99.8%, Sigma Aldrich). For each synthesis, 150 µL of the prepared 0.5 mL precursor solution was added dropwise into a vigorously stirred solution containing 5 mL toluene, 15-50 µL *n*-octylamine (OA:$PbBr_2$ 3:1 to 10:1; needed to passivate the as-formed NCs and concurrent formation of 2D layered perovskites), 0.3 mL oleic acid, and 2 mL *n*-butanol. Immediately after injection, a yellowish solution was formed, indicating the formation of $FAPbBr_3$ NCs. After reaction completion, the colloidal NC solution was washed using two centrifugation steps. In the first step, the NC solution was centrifuged at 14,680 rpm (g-force ~21,000), after which the supernatant phase was discarded and the precipitate redispersed in 1 mL of toluene. In the second centrifugation step, the redispersed NCs were centrifugated at 3,750 rpm (g-force ~1,300). The resultant supernatant phase was used as NC ink (estimated concentration ~8-10 mg mL^{-1}) for the LED device fabrication. Very similar results were obtained in Valencia when slightly different centrifuge settings were used, namely; 13,400 rpm and 4,400 rpm for the first and second step, respectively. It should be noted that a lower quantity of octylamine (< 15 µL) yield a much lower concentration of NC, since octylamiene is also a ligand component of NC to achieve colloidal suspension properties. The entire synthetic protocol is conducted in a fume hood under ambient conditions, whereas the thin film formation (i.e. spin-coating of the NC ink) was performed under inert atmosphere (Ar or N_2; with H_2O and O_2 levels <0.1 ppm). Noted that the entire synthesis procedure is conducted in chemical fumehood, while the spincoating of the NC ink is performed in an inert atmospheric glovebox.

Device fabrication: Pre-etched indium-tin oxide (ITO; sheet resistance ~8 Ω cm^{-1}; Wuhan Jinge Solar Energy Technology Co., Ltd) glass substrates were used as-purchased, and sequentially washed in detergent solution, acetone, ethanol, and 2-propanol in an ultrasonication bath. Subsequently, the substrates were dried and treated for 20 min with UV-ozone. The hole transporting layer, PEDOT:PSS (Clevios 4083; filtered with 0.45 µm PVDF filter) was then spin-

coated for 1 min at 4000 rpm and thermally annealed for 10 min at 130 °C to remove any residual solvent. The substrates were transferred into an argon-filled glovebox for the spin-coating of active emission materials. The NC inks (20 µL of NC ink was used per square centimeter of substrate area) were dropcasted on top of the PEDOT:PSS layer and left for 5 min to slowly evaporate (and initiate self-assembly), prior to spin-coating for 1 min at 1000 rpm, to obtain thin film of ~40 nm thick (see cross-sectional SEM images, Fig. S12). 45 nm of electron transporting layer (either POT2T, 2,4,6-Tris[3-(diphenylphosphinyl)phenyl]-1,3,5-triazine, or B3PYMPM, 4,6-Bis(3,5-di(pyridin-3-yl)phenyl)-2-methylpyrimidine) is thermally evaporated under high vacuum (10^{-6} torr). Lastly, the cathode materials Ca (7 nm) and Al (80 nm) were subsequently thermally evaporated through a metal shadow mask, to define the device active area of 3 mm^2. Flexible devices (with active area 3 mm^2) were fabricated on ITO/PET substrates following a similar protocol, although thicker PEDOT:PSS layers (ca. 80 nm) were deposited. A filtered PEDOT:PSS solution was spin-coated at 1000 rpm for 60 s, followed by thermal annealing at 120 °C for 10 min to reduce the surface roughness (i.e. due to the rough ITO layer on the flexible PET substrate). The ITO/PET substrates were etched with Zn powder and diluted hydrochloric acid, and subsequent sonication in soap water, acetone, ethanol, and 2-propanol for 10 min. The deposition of subsequent emissive layer, electron transporting layer, and cathode were the same as the standard devices fabricated on ITO/glass substrates. Large area devices are prepared similarly to the standard 3 mm^2 devices fabricated on ITO/glass substrates.

LED device characterization: All LED devices were encapsulated with epoxy resin before taken out from argon-filled glovebox for electroluminescence characterization. A Keithley 2612B was used to obtain the current-voltage characteristics of the LED devices using a scan rate of 1 V s^{-1} (step size 0.1 V, step interval 0.1 s), unless stated otherwise. The light emission was collected by an integrating sphere (OceanOptics FOIS-1) coupled to a calibrated spectrophotometer (OceanOptics QEPro). An OceanOptics HL-3 Plus vis-NIR light source, calibrated using a procedure and documentation patterned after the ISO 17025, IEC Guide 115 and JCGM100:2008 (GUM) protocols, is used to calibrate the absolute irradiance measurement of the spectrometer. As LED devices are placed on outside of the integrating sphere, only forward

emission is captured while the edge emission contribution is loss outside the integrating sphere. This method has also been widely used to measure the external quantum efficiency of organic light emitting diode.[1, 2] A schematic of the experimental setup is available in Fig. S25.

LED device stability: Before the stability test, the current-voltage-luminance characteristics of each device was recorded by sweeping voltages up to 2.9 V only to minimize the bias-stress degradation on the device. A constant current density was applied according to the current-voltage-luminance characteristics. For initial luminance L_0 ~100 cd m^{-2}, the luminance of the device decayed to half of the initial luminance after ~800 s (approx. 13 min).

X-ray diffraction: The crystal phase and lattice parameters of the thin films of synthesized NCs were determined using a Bruker D8 advance diffractometer with a 0D LynxEYE™ detector. Scans from 2θ = 5-35° were recorded (step sizes of 0.05° and 10 s per step) of thin films spin-coated on cleaned glass substrates coated with PEDOT:PSS (see device fabrication protocol). Rocking curves of the (001) and (002) reflections of 2D $(OA)_2(FA)_{n-1}Pb_nBr_{3n+1}$ (2θ ~9.6°) and 3D $FAPbBr_3$ (2θ ~29.8°) were recorded from ω = 2-6° and ω = 13-17°, respectively, with step sizes of 0.05° and 10 s per step.

Scanning transmission electron microscopy: Measurements were performed with a Tecnai G2 F20 with a Schottky field emitter operated at 200kV. Selected samples were diluted in toluene, dropcasted on a carbon-copper grid, and mounted on a FEI Double Tilt Analytical Holder for examination. Tecnai G2 F20 STEM with an X-Twin lens objective lenses and field emission gun (Schottky field emitter) operates at a beam current of > 100 nA, providing high probe current (0.5 nA or more in 1 nm probe). The system is equipped with a fully embedded digital scan system; bright-field and annular dark-field modes are provided by ultra-high resolution high-angle annular dark-field (HAADF) detector.

Field-emission scanning electron microscopy: The morphological images of the films were recorded using field-emission scanning electron microscope (FE-SEM, JEOL, J7600F).

Cathodoluminescence microscopy: The measurements were performed in a scanning electron microscope equipped with a cathodoluminescence detection system, Attolight CL Allalin 4027 Chronos. A focused electron beam (electron energy 5 keV; beam current ~11 nA; dwell time 10-200 ms) scanned the samples while recording the light emission spectrum synchronously to produce hyperspectral images. The emitted light was collected by an achromatic reflective objective with a high numerical aperture (NA = 0.72) and sent to a UV-VIS spectrometer (Horiba iHR320) equipped with a thermoelectrically cooled silicon CCD array (Andor Newton).

Small angle x-ray scattering: The Xenocs Nano-inXider, equipped with a Dectris Pilatus3 hybrid pixel detector was employed to record the combined small- and wide-angle X-ray scattering (SAXS/WAXS) patterns of NC inks. This allowed to measure an effective scattering vector magnitude in the range of $0.1 < q < 4$ nm^{-1} in SAXS, and up to $2\theta = 60°$ in WAXS. NC inks with OA:$PbBr_2$ ratios 3:1, 4:1, 5:1, 7:1, and 10:1 were measured in sealed glass capillaries (inner diameter 0.95 mm, length 100 mm) under vacuum at room temperature, with 15 min acquisition time. Thin film surfaces were investigated using grazing incidence small-angle X-ray scattering (GISAXS) recorded under a shallow angle of 0.2°. Size distributions (without prior assumption of particle shape) were obtained from our scattering curves using the Monte Carlo based software package McSAS,[3] using a convergence criterion of 2, with 10 calculating repetitions and 500 contributions.

Photoluminescence: The photoluminescence (PL) spectra of the $FAPbBr_3$ NC films were measured using a Horiba Fluoromax-4 (slit width 0.4 nm and 0.1 s integration time), respectively. For the excitation spectra, the maximum PL emission peak was used (slit width 0.1-0.2 nm and 0.3-0.5 s integration time).

Absorbance: The absorbance spectra of the composite NC films were measured using a Shimadzu UV-2550 spectrophotometer with an integrating sphere attachment (20 nm slit width is used to collect transmitted photon).

Time-resolved photoluminescence (TR-PL): The micro-PL setup is based on fiber coupled microscope system, where the excitation path and the emission collection from the side, using a VIS-NIR microscope objective (10x, NA= 0.65). The samples were excited with 5-MHz-repetition-rate, picosecond-pulse light sources at 405 nm (Picoquant P-C-405B) light-emitting diode. The beam spot size was about 10 µm. Time-resolved decay curves were collected using an Acton monochromator (SpectraPro 2300), fiber coupled to the microscope, to filter the desired wavelength, and detected by Micro Photon Devices single-photon avalanche photodiode (LDH-P-670). The signal was then acquired by a time-correlated single photon counting card (Pico Harp TSCPC module and Picosecond Event Timer 300). The temporal

resolution is ~50 ps. The decay curves were fitted with a double exponential function. The resulting decay components and the relative weights are reported in Table S10-S14.

Photoluminescence quantum yield (PLQY): PLQY dependencies on the excitation fluence were measured with a 2-inch integrating sphere (Thorlabs model IS200). Investigated samples were placed inside the sphere and excited using a semiconductor continuous-wave laser beam (200 mW full power) emitting at 405 and 447 nm. An optical fiber was attached to the sphere to direct the light to an Ocean Optics spectrometer. The excitation beam intensity was attenuated by means of calibrated neutral interference filters (Thorlabs).

Transient absorption: Visible pump visible probe transient absorption measurement was conducted using a Continuum IntegraC regenerative/multipass femtosecond amplifier system capable of generating <100 fs, 1 KHz and 2.5 mJ ultrashort pulse at 800 nm. Pump wavelength of 375 nm is generated by frequency doubled the 750 nm VIS2 output of a Continuum Pallitra OPA pumped with 1 mJ of the laser output. Two dielectric mirrors designed for 3rd harmonic of Nd:YAG laser are used as filter to remove fundamental 700 nm and any other residue output from the OPA. White light continuum is generated by focusing part of the amplifier output onto a constantly rotating CaF_2 with appropriate beam size and power control. To prevent oversaturation of the CCD spectrometer, a 700 nm shortwave pass filter is used to remove the excessive 800 nm generation beam. As a result, a stable smooth broadband white light continuum spanning 370-650 nm is generated. On the sample, the probe white light is focused via a parabolic mirror to a spot size of ~20 µm. A f = 250 mm UV fused silica (UVFS) lens is used to focus the pump beam onto the sample at its beam waist of ~100 µm diameter. To prevent sample degradation due to humidity and oxidation, the sample is taped onto a UVFS cuvette that has been filled with nitrogen. Longpass filters with cut-off wavelength of 375 nm were used to prevent scattered pump beam to enter the CCD spectrometer.

Global fitting: Global fitting is performed using the freely available Glotaran frontend[4] of the R-based TIMP global and target analysis software package.[5] The average of approx. -5 to -1 ps regime data are used for the baseline correction to remove the contribution of long lived

fluorescence signal around the photobleaching peak and coherent artifacts were removed numerically using the built-in instrument response function (IRF) model. Dispersion of the white-light probe and IRF were removed by numerical fitting using the default ParMu model for dispersion and Gaussian IRF.

***Photoelectron spectroscopy in air (PESA)*:** Measurements on spin-coated NC thin films were conducted using a Riken Keiki AC-2 spectrometer with a power setting of 800 nW (power number of 0.5).

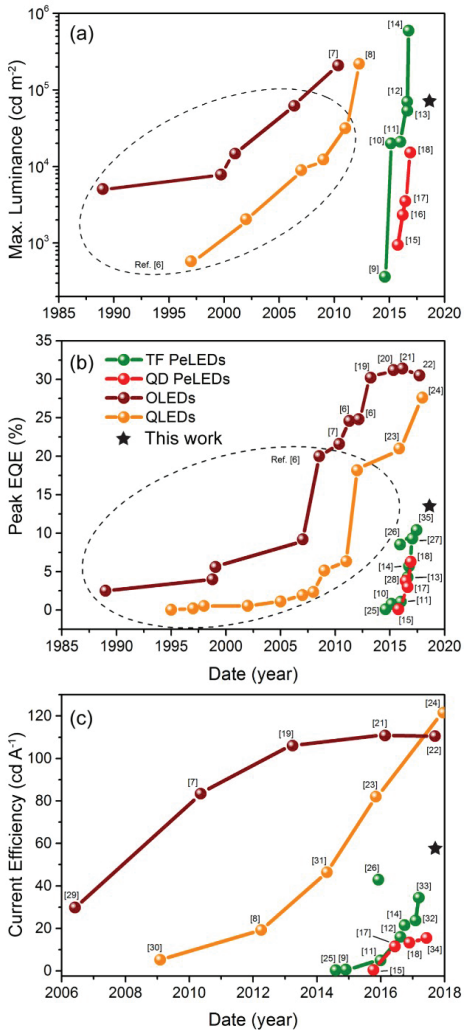

Fig. S1 Overview of best reported LED devices values for organic (OLED), semiconductor quantum dots (QLEDs), and perovskite (PeLED).[6-35] (a) Maximum luminance, (b) peak external quantum efficiency, and (c) current efficiency. Note: TF and QD refer to thin film and quantum dot (or nanoparticle) films. All perovskite device data is based on green-emitting materials. The star symbol represents the device performance demonstrated in this work. Most reported data points for QLEDs and OLEDs (within the dashed ovals) are derived from a recent review article by Shirasaki et al.[6] They represent the highest achieved device efficiencies and luminance (i.e. with or without out-coupling structures, inverted or normal structures). The data points in (a-c) for OLEDs are taken from references [6, 7, 19-22, 29]; data points in (a-c) for QLEDs are taken from references [6, 8, 23, 24, 30, 31]; data point for TF PeLEDs are taken from references [9-14, 25-27, 32, 33, 35]; and data point for QD PeLEDs are taken from references [15-18, 28, 34], respectively.

Fig. S2-S11: Device Fabrication, band alignment, stability, flexible/large area devices

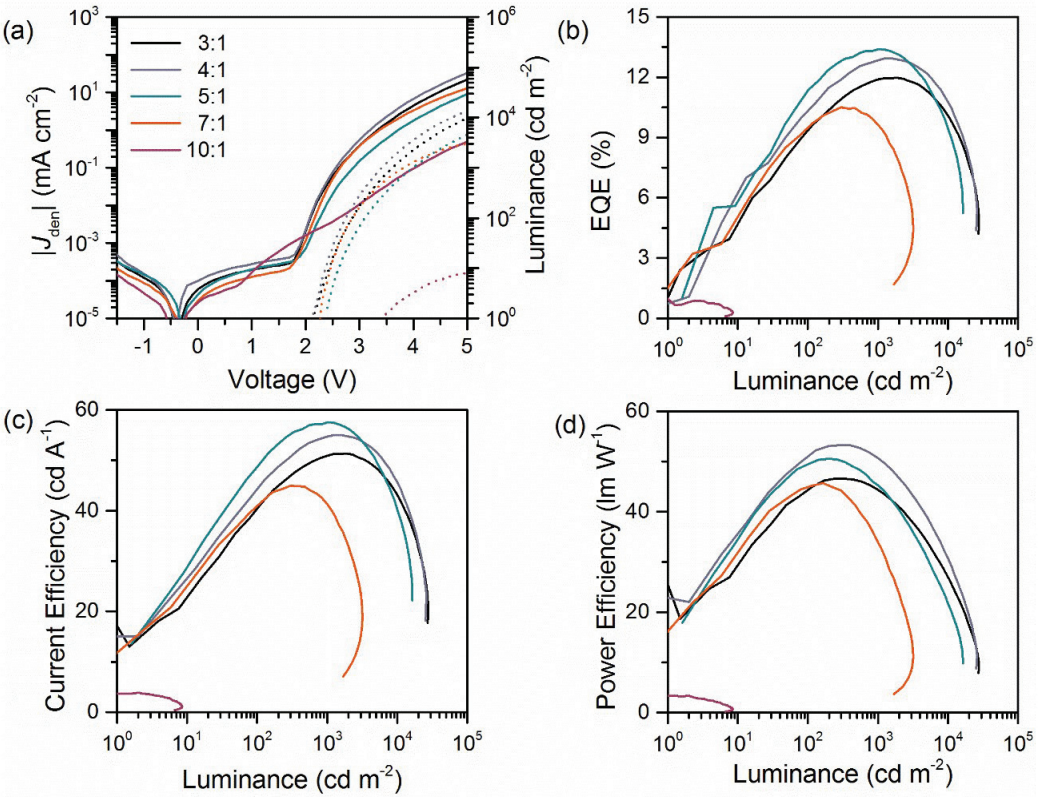

Fig. S2 LED device characteristics prepared with different OA:$PbBr_2$ ratios. (a) Current density-voltage-luminance characteristics, and (b) EQE, (c) current efficiency, and (d) luminous power efficiency versus luminance. The active device area is 3 mm^2. At low voltages (-1 V < *V* < 1 V), the measured current is smaller than 1 nA as a consequence of small device area (3 mm^2). The total current in this range are therefore inclusive of both charging and leakage currents from the coaxial cable, hence the slight shift of the zero current crossing towards negative voltages. The device parameters are summarized in Table 1 and S2.

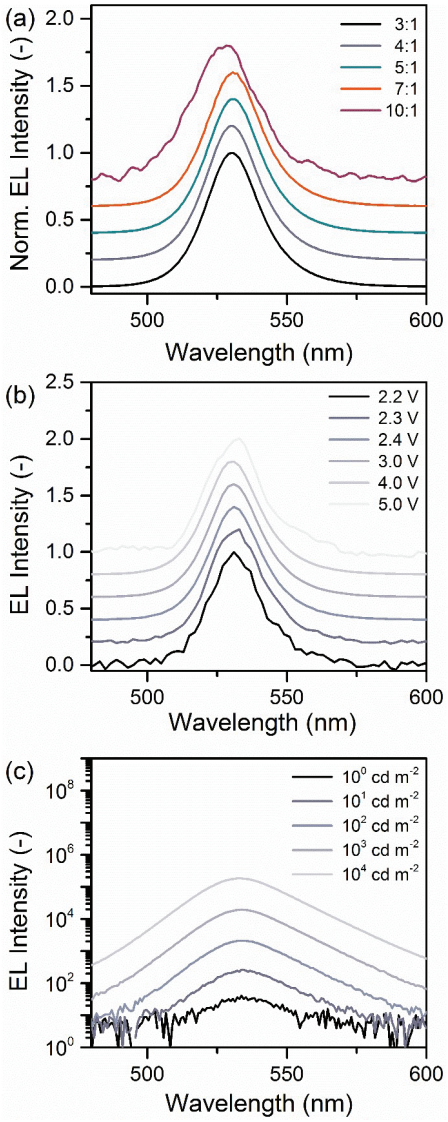

Fig. S3 Electroluminescence characteristics for (a) samples prepared with different OA:$PbBr_2$ ratios, (b) at different bias, and (c) at different luminance intensity. Devices in (b) and (c) are prepared with OA:$PbBr_2$ ratio 4:1. The active device area is 3 mm^2. (a) EL spectra collected at maximum luminance for different OA:$PbBr_2$ ratios are similar, except the slight blue-shift (3-5 nm) observed ratio 10:1. (b) Normalized EL spectra, collected at sub-energy-gap (2.2 V) and above energy gap bias (2.3-5 V), suggest that there is no sub-gap, trap-related EL emission at sub-energy-gap external voltage bias. (c) EL spectra at different luminance levels scale proportionally to the emission intensity, suggesting that the emissive species at different luminance are equal.

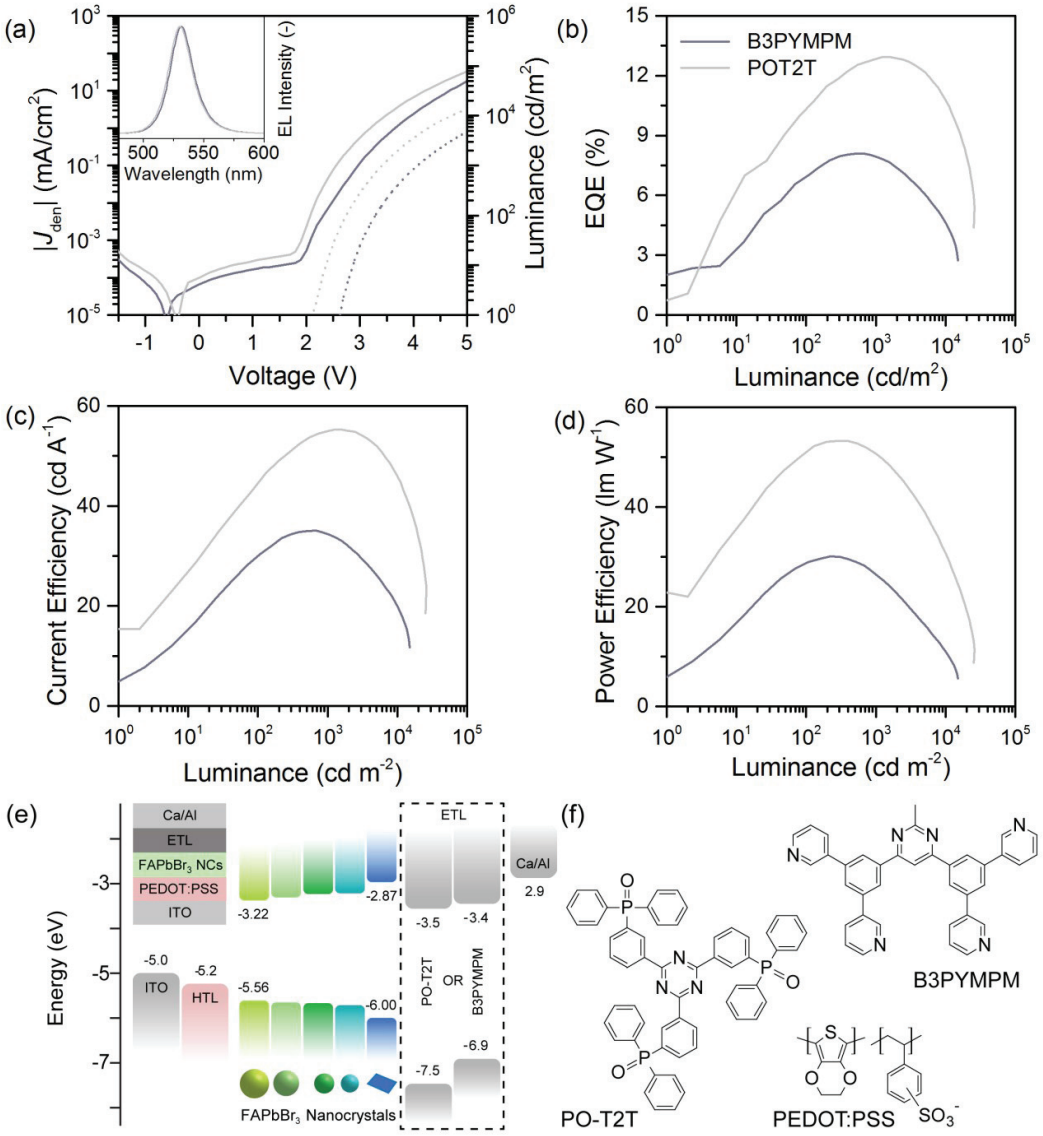

Fig. S4 LED characteristics with different electron transporting layers. (a) Current density-voltage-luminance characteristics of LED devices. The inset shows the electroluminescence spectra at maximum luminance. (b) Current efficiency, (c) EQE, and (d), luminous power efficiency as a function of luminance. (e) Band alignment of the device architecture and (f) the molecular structures of hole and electron transporting materials used in this work. The emissive layer is the perovskite nanocrystals synthesized with OA:$PbBr_2$ of 4:1. The device parameters are summarized in Table S4.

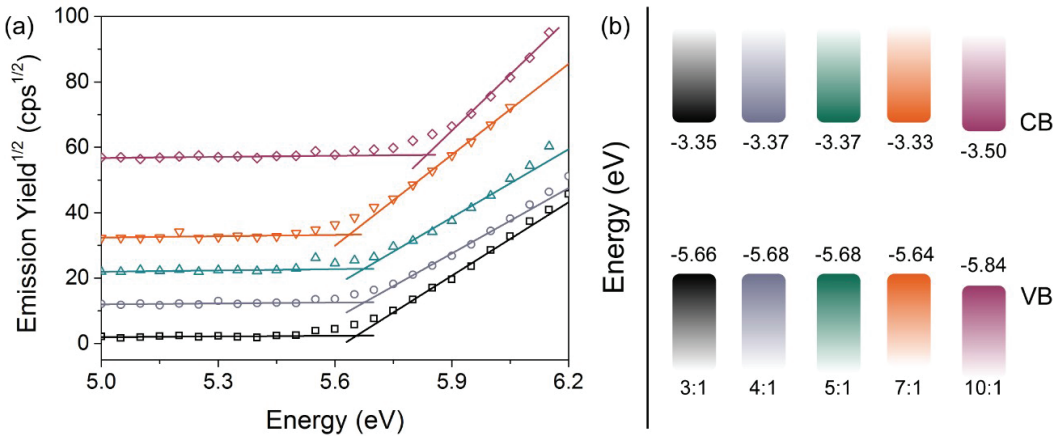

Fig. S5 Valence (VB) and conduction band (CB) level determination of $FAPbBr_3$ and $(OA)_2(FA)_{n-1}Pb_nBr_{3n+1}$ composite films using photoelectron spectroscopy in air. Here, the CB was calculated through addition of the optical bandgap and the VB. (a) PESA curves and respective fit curves, and (b) schematic representation of the band levels of samples prepared with different OA:$PbBr_2$ ratios.

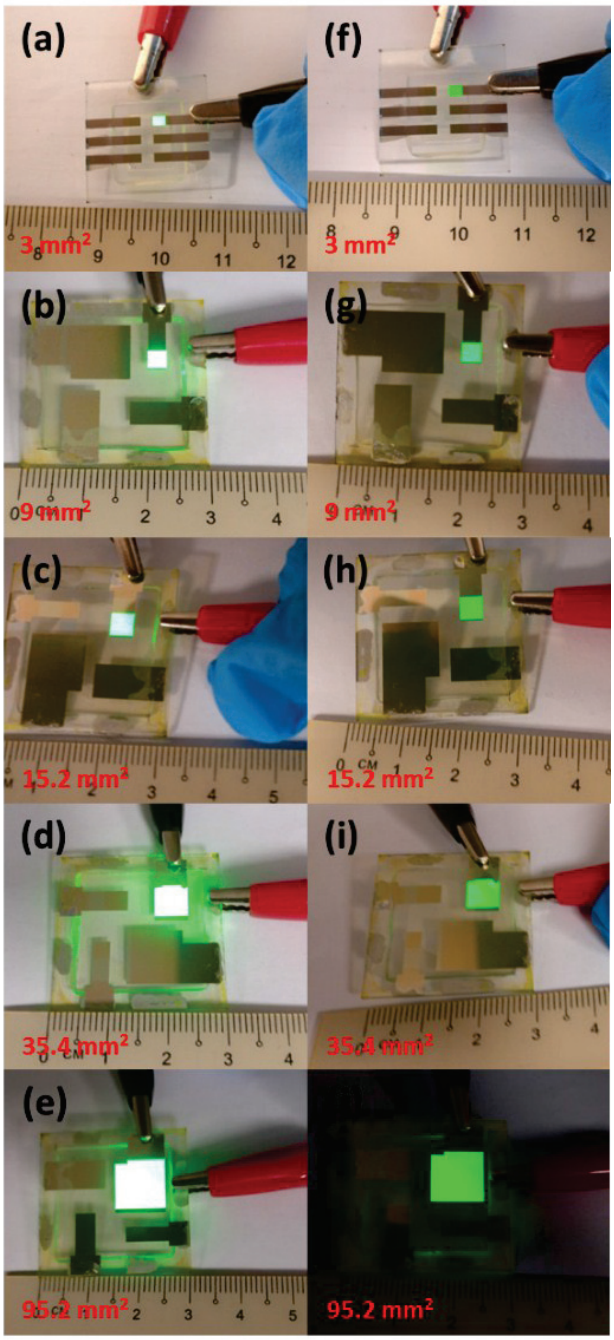

Fig. S6 Bright and uniform LED devices. (a-e) Bright luminescence of LED devices with different active area operating at 4.5 V. (f-j) Uniform emission from LED devices with different active area operating at 2.7 V.

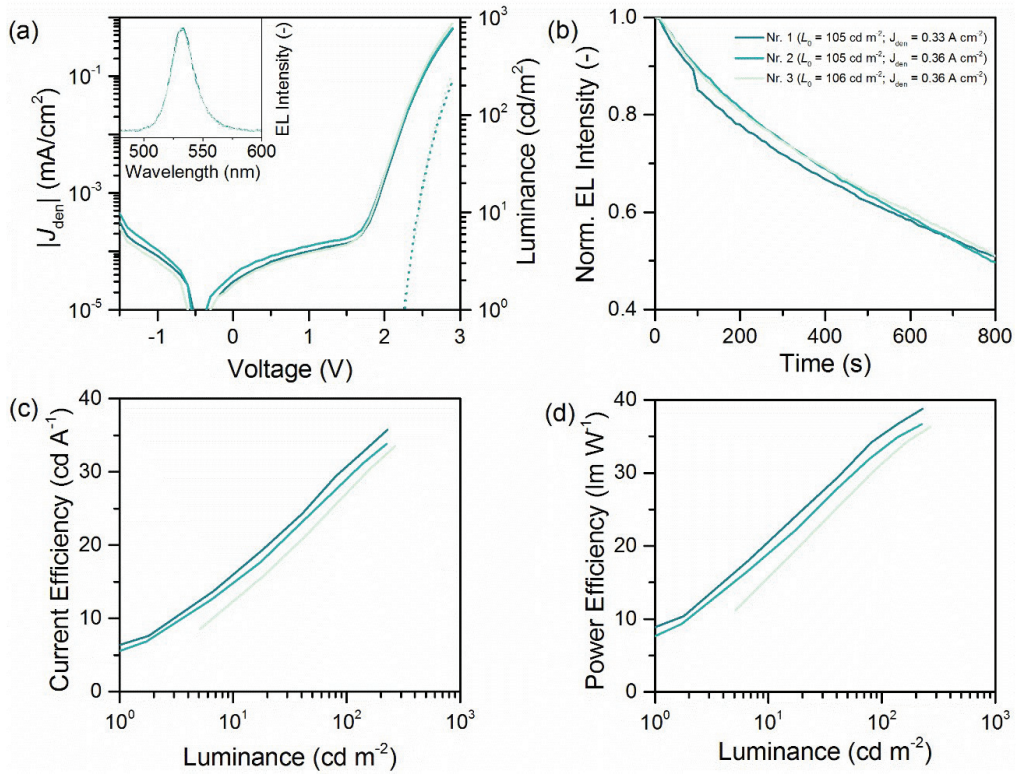

Fig. S7 LED device stability of three different devices under constant current bias. (a) Current-voltage-luminance characteristics. The inset shows the electroluminescence spectra at maximum luminance. (b) Constant current stability. The legend indicates the initial luminance L_0 and the current density applied to each device during the stability test. (c) Current efficiency and (d) luminous power density as a function of luminance of LED devices used for the constant current stability test. The device parameters are summarized in Table S3. The devices were measured by sweeping voltage biases up to 2.9 V before the constant current stability test. The emissive layer is the perovskite nanocrystals synthesized with OA:$PbBr_2$ of 5:1.

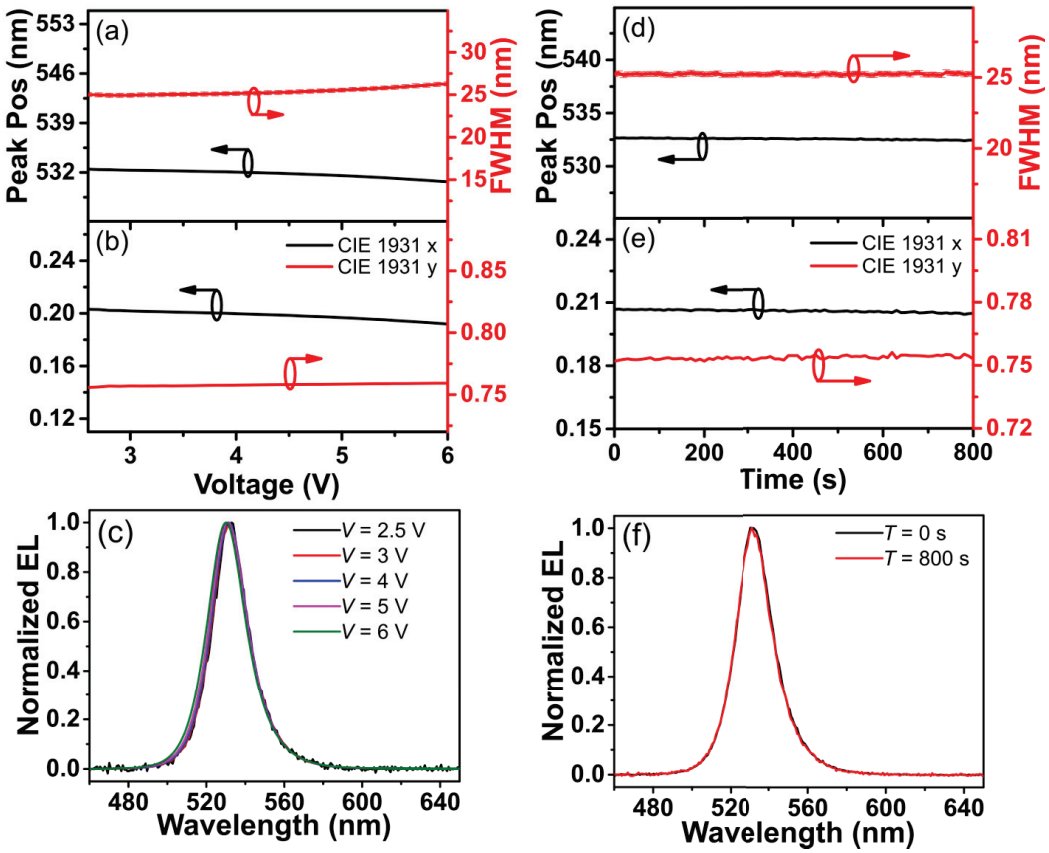

Fig. S8 Color stability of LED devices. (a) Peak position and FWHM, (b) CIE coordinate of electroluminescence spectra as a function of biased voltage. (c) Normalized electroluminescence spectra at selected bias voltages. (d) Peak position and FWHM, (e) CIE coordinate of electroluminescence spectra as a function of time of constant current measurement. (f) Normalized electroluminescence spectra at 0 s and 800 s of constant current measurement. The emissive layer is the perovskite nanocrystals synthesized with OA:$PbBr_2$ of 5:1.

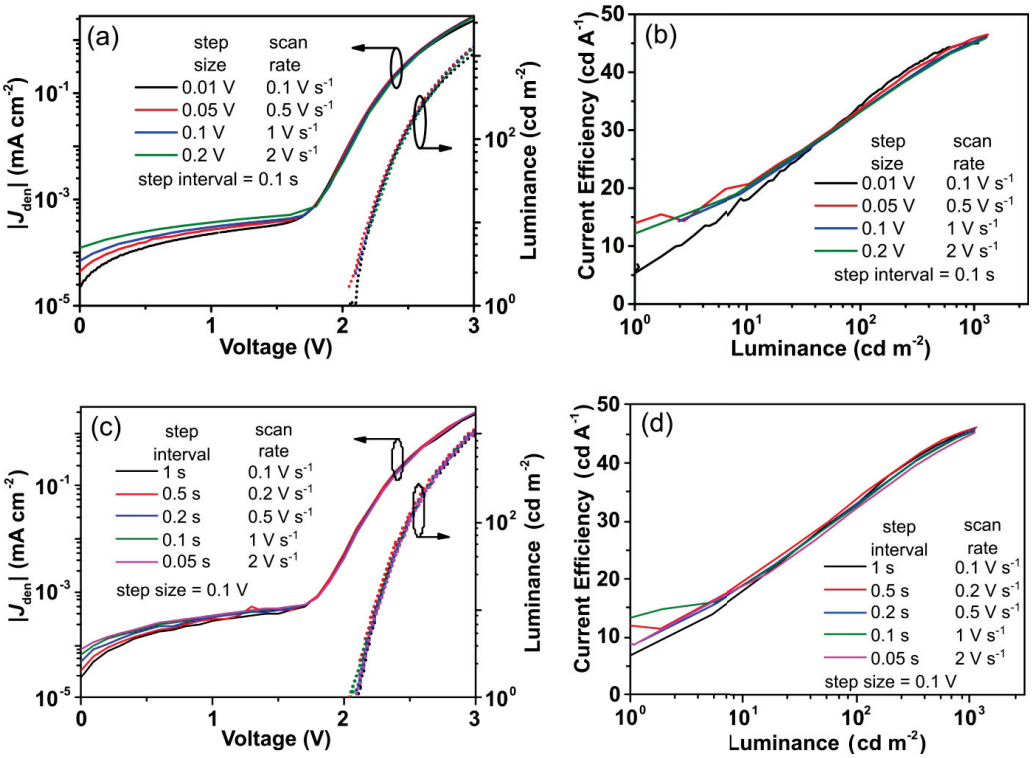

Fig. S9 LED characteristics as a function of scan rate. (a) Current-voltage-luminance characteristics and (b) current efficiency as a function of luminance of LED devices with different scan rate (fixed step interval, varying step size). (c) Current-voltage-luminance characteristics and (d) current efficiency as a function of luminance of LED devices with different scan rate (fixed step size, varying step interval). The emissive layer is the perovskite nanocrystals synthesized with OA:$PbBr_2$ of 5:1. The J-V-L and current efficiency vs luminance curves are nearly identical for all investigated scan rates. The collection duration required for lowest scan rate (0.1 V s^{-1}) are very well within the stability of the devices, which is shown to be around 14 minutes (Fig. S7(b)).

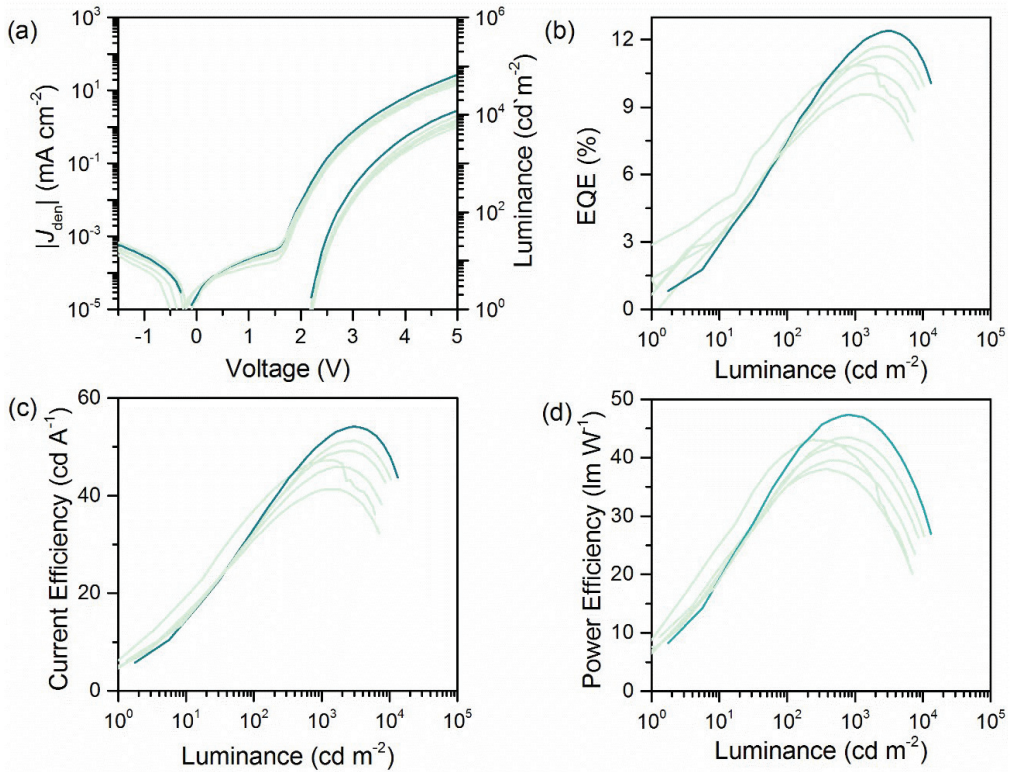

Fig. S10 Flexible LED device characteristics. (a) Current density-voltage-luminance characteristics, and (b) EQE, (c) current efficiency, and (d) luminous power efficiency versus luminance. The active device area is 3 mm^2. The emissive layer is the perovskite nanocrystals synthesized with OA:$PbBr_2$ of 4:1. The device parameters are summarized in Table S5 and S6.

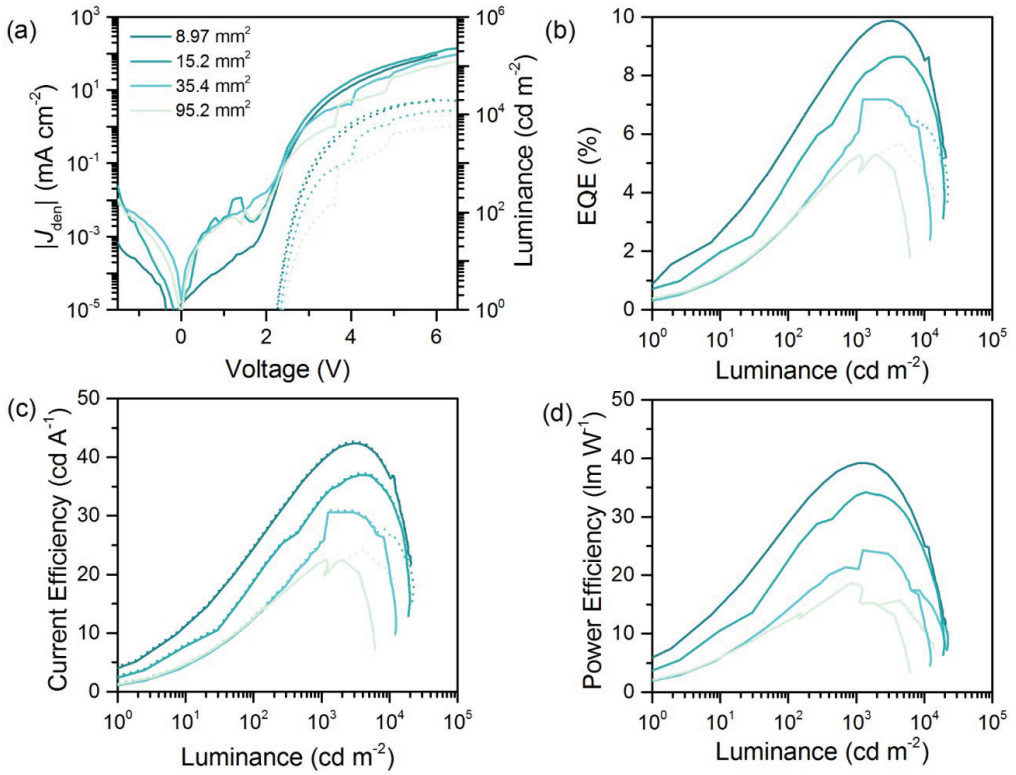

Fig. S11 Large area LED device characteristics. (a) Current density-voltage-luminance characteristics, and (b) EQE, (c) current efficiency, and (d) luminous power efficiency versus luminance. The solid lines represent the as-measured device characteristics, while the dotted lines represent the characteristics after correcting for the saturation of the spectrometer. The corrections are performed by scaling the luminance values linearly according to the spectral regions which did not saturate the spectrometer; under the assumption that the spectral shape remains unchanged at any given injection density. Note: the largest area device (95.2 mm^2) is larger than the opening of the integrating sphere (78.5 mm^2). The reported values are not corrected for the loss of photons (i.e. the photons not collected by the integrating sphere). The emissive layer is the perovskite nanocrystals synthesized with OA:$PbBr_2$ of 4:1. The device parameters are summarized in Table S7 and S8.

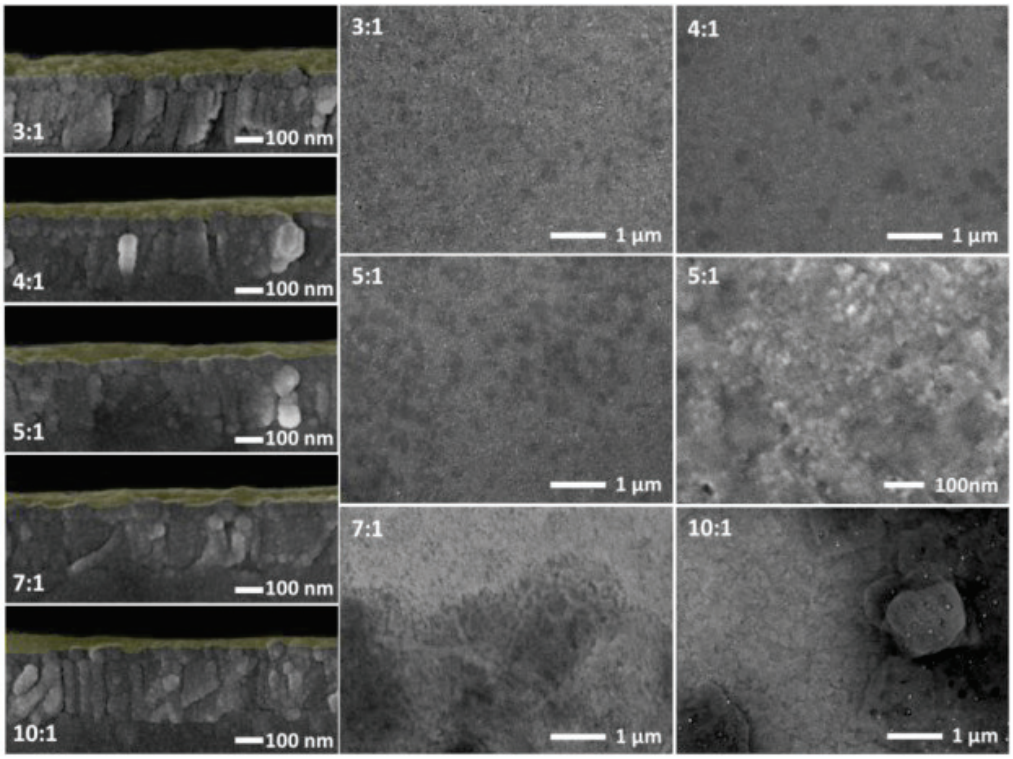

Fig. S12 Morphological investigation by FE-SEM of $FAPbBr_3$ and $(OA)_2(FA)_{n-1}Pb_nBr_{3n+1}$ composite films prepared with different OA:$PbBr_2$ ratios. Left panel: cross-sectional microscopy images of $FAPbBr_3$ nanoparticle films (colored). Right panels: top-view images showing an increased number of 2D MPLs (dark areas) for samples prepared with OA:$PbBr_2$ ratios up to 7:1. Increased ligand concentration resulted in the formation of mostly MPLs.

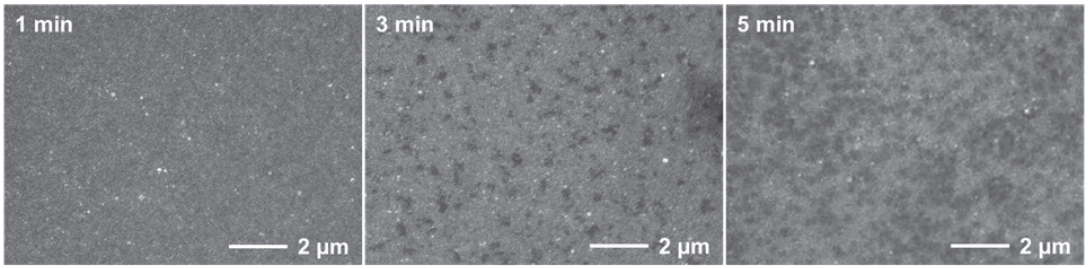

Fig. S13 SEM top surface images displaying the effect of longer waiting times between dropping the NC ink and the subsequent spin-coating. Longer waiting times results in a large concentration of MPLs (dark areas) on top of the NC thin film.

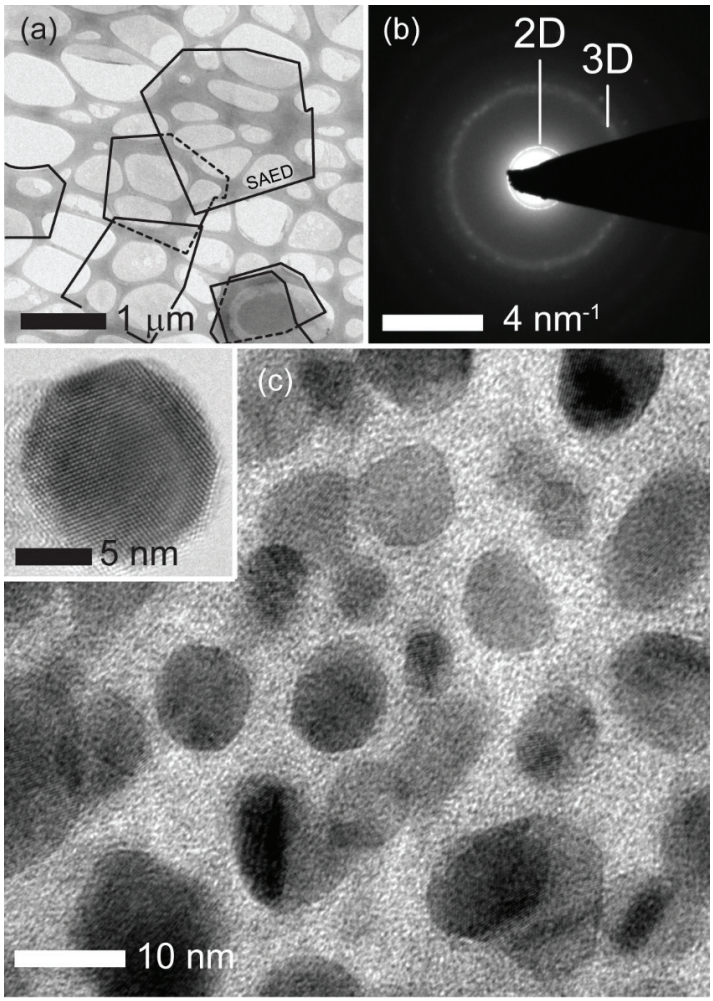

Fig. S14 STEM investigation of mixed-phase $FAPbBr_3$ and $(OA)_2(FA)_{n-1}Pb_nBr_{3n+1}$ NC inks dropcasted on a carbon-Cu grid with OA:$PbBr_2$ is 5:1. (a) The darker areas outlined with solid lines are $(OA)_2(FA)_{n-1}Pb_nBr_{3n+1}$ MPLs formed during the synthesis. (b) Selected-area electron diffraction pattern of marked area, exhibiting diffraction signals of both 2D and 3D phases. (c) Overview image of multiple NCs. The inset shows a crystalline $FAPbBr_3$ nanocrystal of approximately 10 nm diameter.

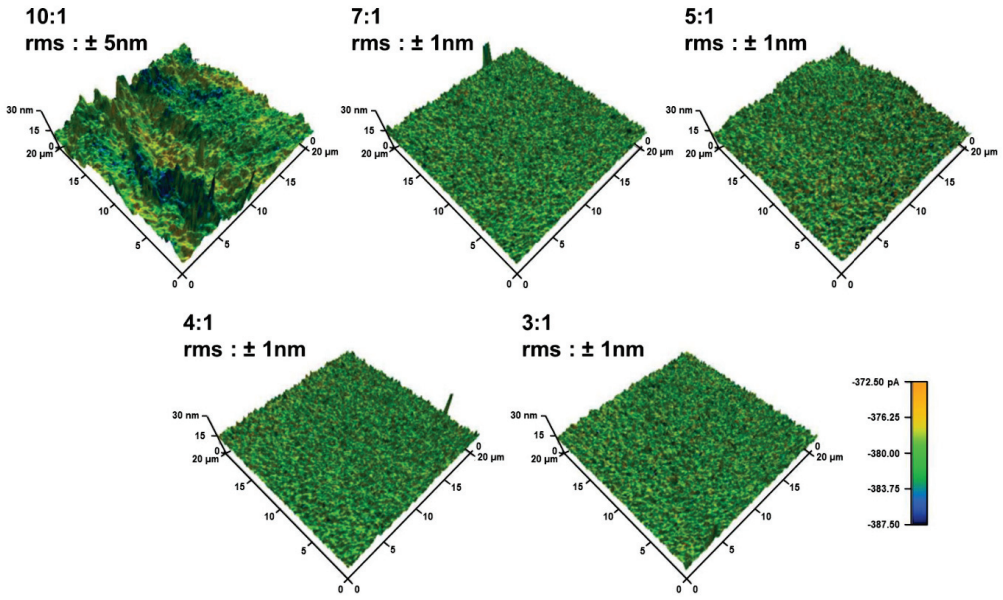

Fig. S15 Conducting AFM images of films synthesized using various amount of octylamine and $PbBr_2$ ratio. Current mapping was overlaid at the 3D surfaces of the film as color contour.

Fig. S16-S19: Optical and structural investigation of NC inks and composite thin films

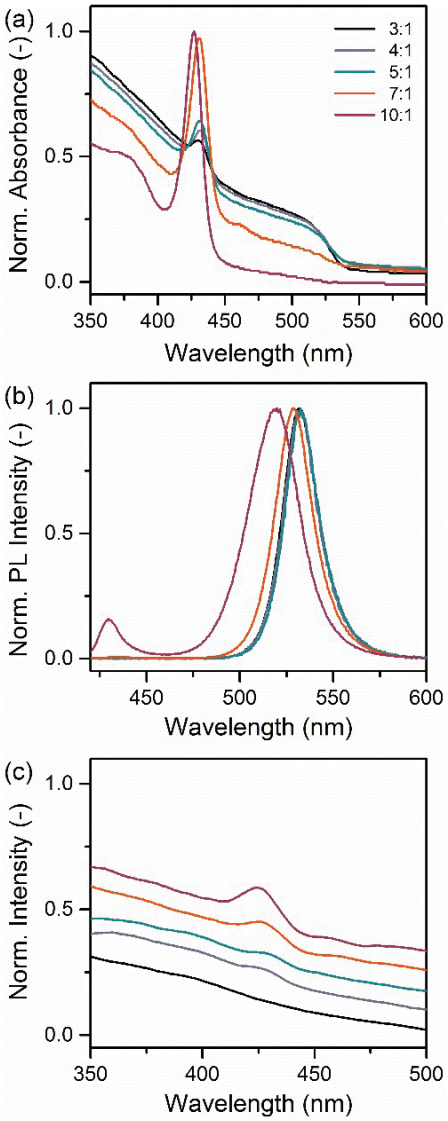

Fig. S16 Absorption, steady-state PL, and excitation spectra of thin film of mixed-phase NC inks synthesized with different OA:$PbBr_2$ ranging 3:1 (black) to 10:1 (purple).

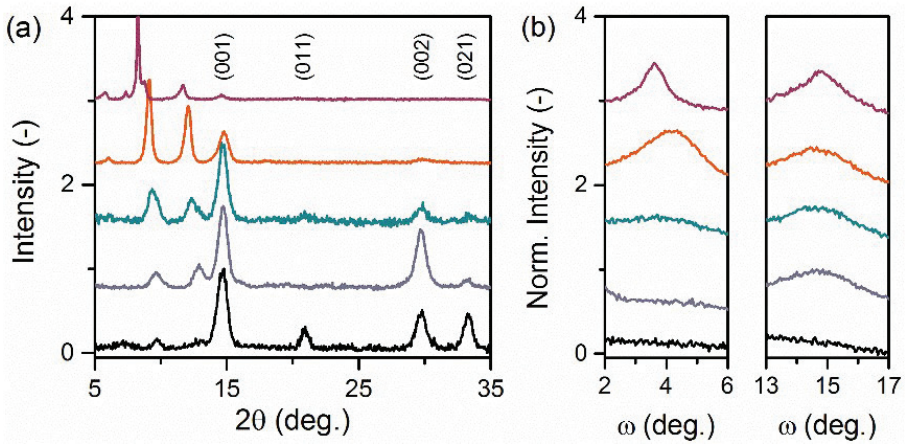

Fig. S17 (a) X-ray diffraction patterns and (b) rocking curves of self-assembled mixed-phase $FAPbBr_3$ and $(OA)_2(FA)_{n-1}Pb_nBr_{3n+1}$ thin films prepared with OA:$PbBr_2$ ranging 3:1 (black) to 10:1 (purple). Left panel: rocking curves of (001) reflection of $(OA)_2(FA)_{n-1}Pb_nBr_{3n+1}$ at 2θ ~9.6°. Right panel: rocking curves of (002) reflection of $FAPbBr_3$ at 2θ ~29.8°.

Small-angle X-ray scattering (SAXS). With SAXS, local electron density inhomogeneities are recorded at very small angles, which allows to extract structural information on length scales typically < 200 nm.[36] These density fluctuations may arise from a homogeneous suspension of nanocrystals (with electron density ρ) in a solvent matrix of different electron density, ρ_0 (or similarly from porosity within a particle). Conventionally, $I(q)$ is plotted versus the magnitude of the scattering vector, q, and is related to the scattering angle (2ϑ) and the wavelength (λ) of the incident beam via:

$$q = \frac{4\pi}{\lambda}\sin\theta$$ Equation 1

In the case of dispersed NCs, the recorded scattering intensity $I(q)$ is proportional to the square of electron density difference, $(\Delta\rho)^2$, between the particles and the solvent matrix. Here, the scattered intensity may arise from the internal electron interference of individual nanocrystals (intraparticular), or from the electrons in an assembly of particles (interparticular), and can be written as a function of a form factor, $P(q)$, and/or a structure factor, $S(q)$, respectively. The total scattered intensity is then:

$$\mathrm{I}(q) = N \cdot (\Delta p)^2 \cdot P(q) \cdot S(q)$$ Equation 2

where N is the number density of particles, and $(\Delta\rho)^2$ the scattering contrast. For dilute systems, the distance between individual particles is substantial and no interparticular interference is expected, *i.e.* $S(q) = 1$. The scattering intensity is then only proportional to the shape (form) of the particles. For smooth, solid spheres, P can be written as:

$$P(q, r_0) = \left[3 \cdot \frac{\sin(q \cdot r_0) - q \cdot r_0 \cdot \cos(q \cdot r_0)}{(q \cdot r_0)^3} \right]^2$$

Equation 3

Here, r_0 is the radius of the smallest scattering particles. The contribution of these smallest scatterer is visible at high q values ($q \cdot r_0 >> 1$), when the slope decreases asymptotically according to $I(q) \propto q^{-4}$ (Porod's law).[37] At low q values, the scattered intensity is predominantly determined by the scattering of large particles or aggregates, and is described by the Guinier approximation:[38]

$$I(q) = I_0 \cdot \exp\left[-\frac{(q \cdot R_g)^2}{3} \right] \quad (\text{for } q \to 0)$$

Equation 4

The radius of gyration, R_g, is defined as the root-mean square center-of-mass distances within a particle or an assembly of particles. It can be determined from the slope in a plot of q^2 vs ln $I(q)$; valid for $q \cdot R_g << 1$.

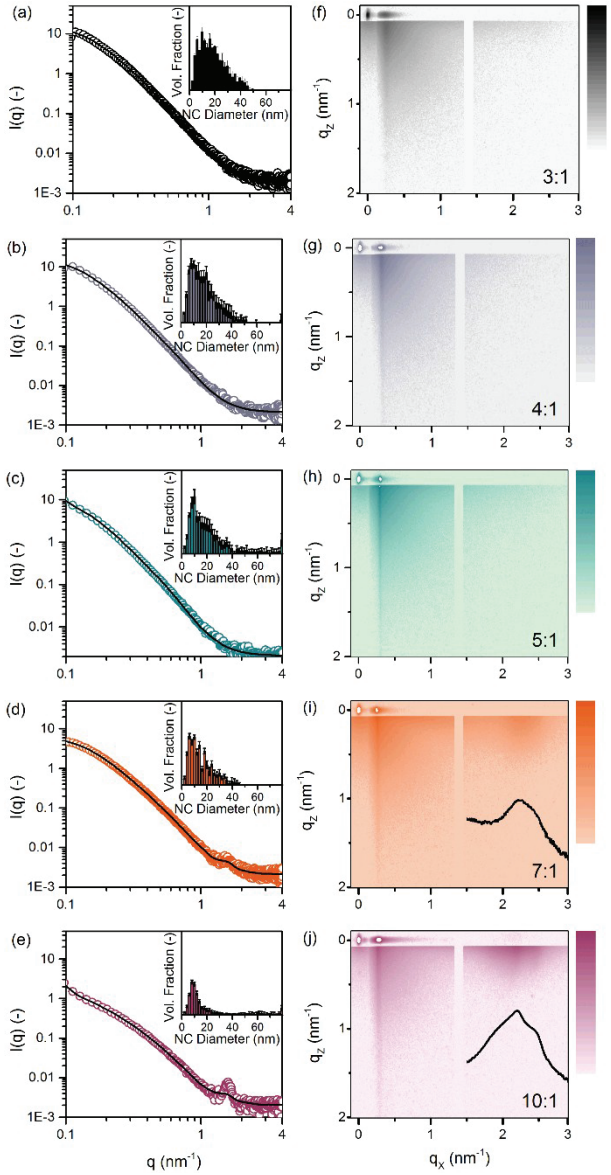

Fig. S18 Scattering curves of mixed $FAPbBr_3$ and $(OA)_2(FA)_{n-1}Pb_nBr_{3n+1}$ NC inks (a-e) and their self-assembled thin films (f-j) prepared with OA:$PbBr_2$ ranging 3:1 (black) and 10:1 (purple), respectively. (a-e) Small-angle x-ray scattering (SAXS) curves of NC inks, showing a Bragg reflection of 2D MPLs (at q ~1.60 nm^{-1} (equivalent to a d-spacing of approx. 3.93 nm) at OA:$PbBr_2$ ratios > 7:1. Insets: particle size distributions extracted from the scattering curves. (f-j) Grazing-incidence small-angle x-ray scattering (GISAXS) plots of the thin film top-surfaces, exhibiting perpendicular alignment of 2D $(OA)_2(FA)_{n-1}Pb_nBr_{3n+1}$ platelets (at q_X >1.5 nm^{-1}) with respect to the substrate's surface. The black curves in (i,j) represent the integrated peak area for $1.5 < q_X < 3$ nm^{-1}.

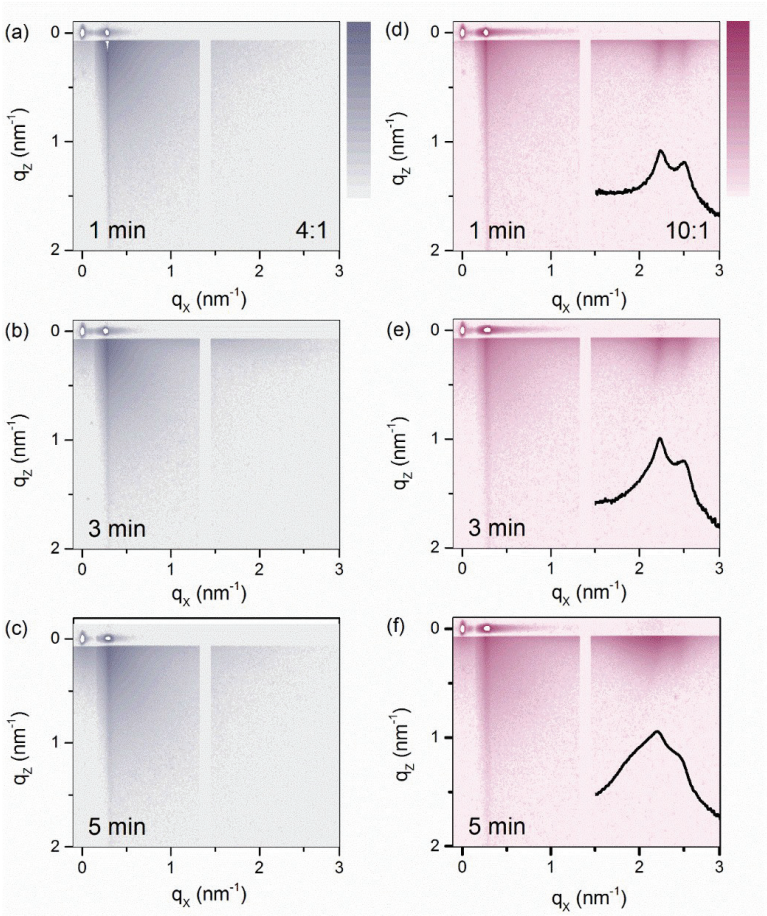

Fig. S19 Grazing-incidence small-angle x-ray scattering (GISAXS) plots of self-assembled mixed-phase $FAPbBr_3$ and $(OA)_2(FA)_{n-1}Pb_nBr_{3n+1}$ thin films prepared with OA:$PbBr_2$ 4:1 (a-c) and 10:1 (d-f), respectively. The NC inks were dropcasted on top of the ITO/PEDOT:PSS substrate layers and left for 1 to 5 min to initiate NC self-assembly, prior to spin-coating for 1 min at 1000 rpm. The 2D $(OA)_2(FA)_{n-1}Pb_nBr_{3n+1}$ platelets exhibit parallel alignment with respect to the substrate's surface, as observed by the peak formation at q_X >1.5 nm^{-1}. From the changes in the integrated peak shape and position, represented by the black curves in (d-f), it is evident that the $(OA)_2(FA)_{n-1}Pb_nBr_{3n+1}$ platelets self-assemble at longer waiting times.

Fig. S20-S21: Transient absorption characteristics

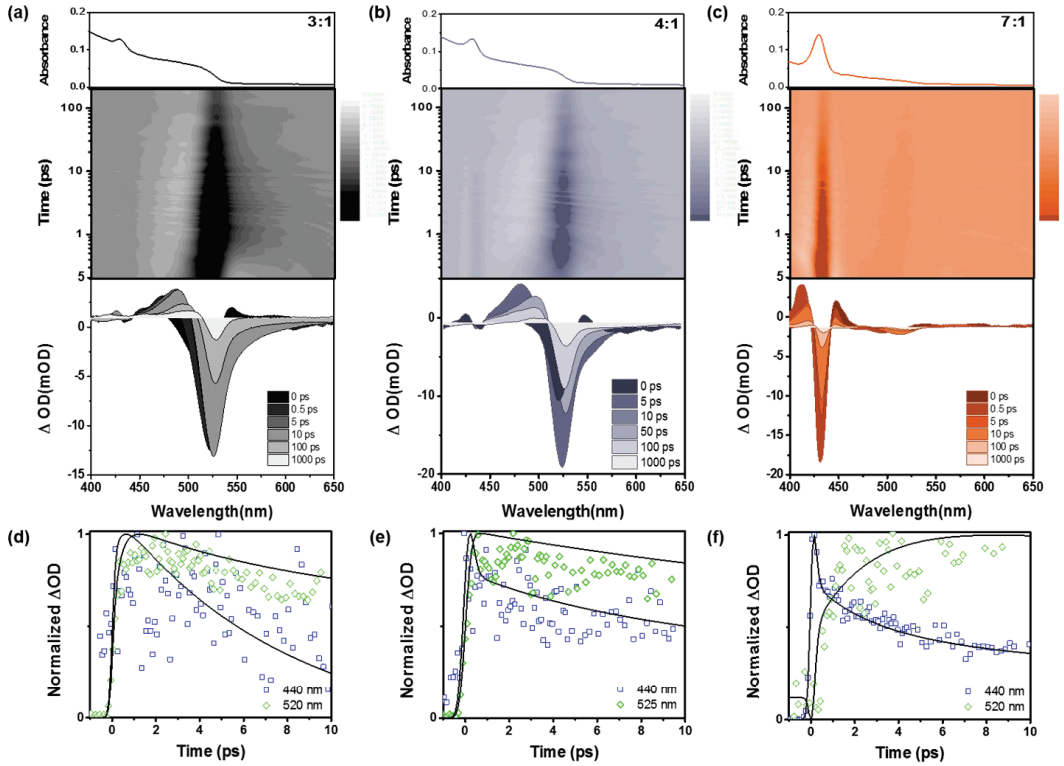

Fig. S20 Transient absorption (TA) spectra of $FAPbBr_3$ NCs. (a-c) UV-Visible absorption spectra (top) panel. TA mapping with excitation at λ=375 nm, 150 fs, and 1 μJ cm^{-2} fluency in the 0-200 ps range (central panel) and the relative TA spectra up to 1000 ps (lower panel) for $FAPbBr_3$ NCs prepared with 3:1 (a), 4:1 (b) and 7:1 (c) of OA: $PbBr_2$.. Normalized kinetics of the TA signal at 440 nm and 520 nm for $FAPbBr_3$ NCs prepared with 3:1 (d), 4:1 (e), and 7:1 (d) of OA:$PbBr_2$.

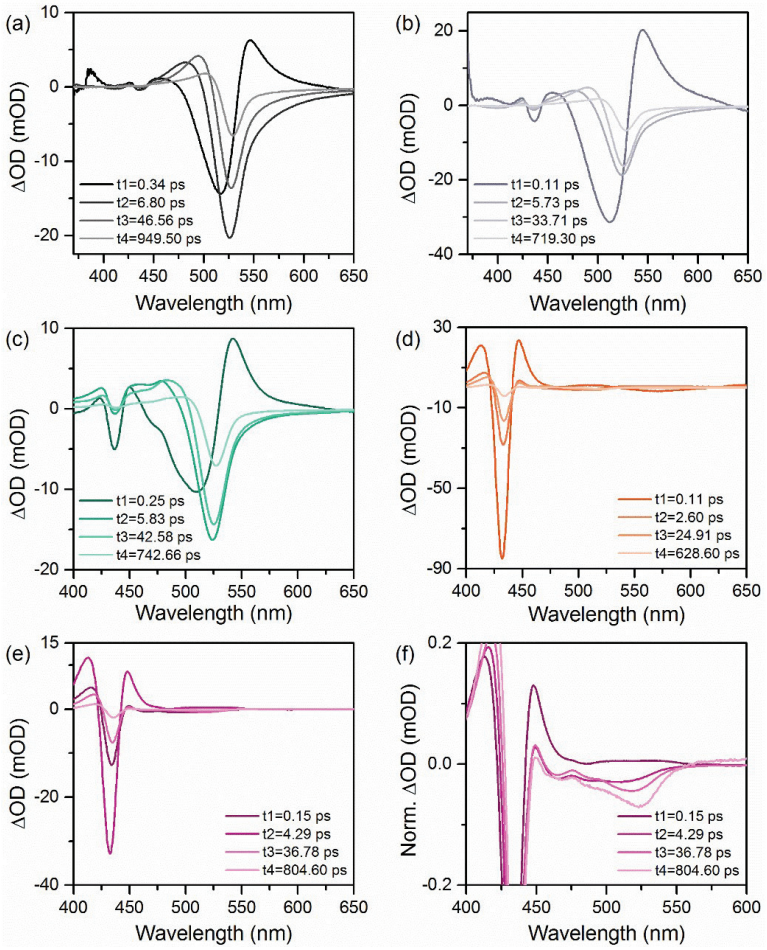

Fig. S21 TA spectra global fitting. (a-e) Spectral contribution at the characteristic decay times, obtained by the global fitting procedure for samples prepared with OA:$PbBr_2$ ratios of 3:1, 4:1, 5:1, 7:1, and 10:1, respectively. (f) is a zoom of (e) to highlight the photobleaching contribution at ca. 525 nm. A tabulated decay times for the global fitting result is also shown in Table S9.

Fig. S22-S24: Cathodoluminescence and time-resolved PL

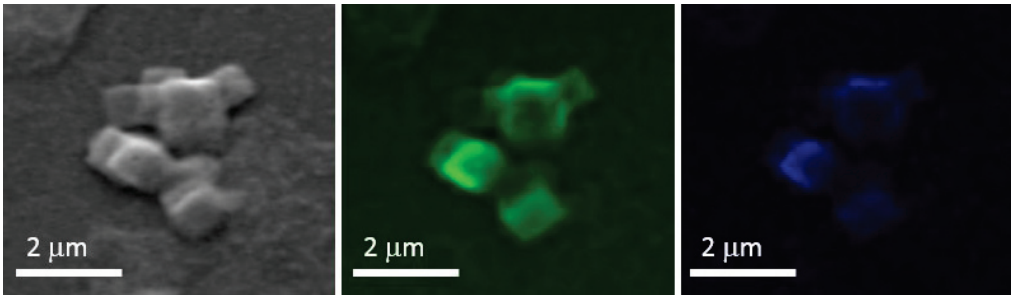

Fig. S22 Cathodoluminescence images of a spin-coated NC film (5:1 of OA: $PbBr_2$) on a silicon substrate. Images are taken using an electron beam of 5 keV energy, current of ~11nA, and exposure time of 10 ms. The CL images of middle and right panel are obtained by mapping with emission wavelength at 525 nm and 440 nm, respectively.

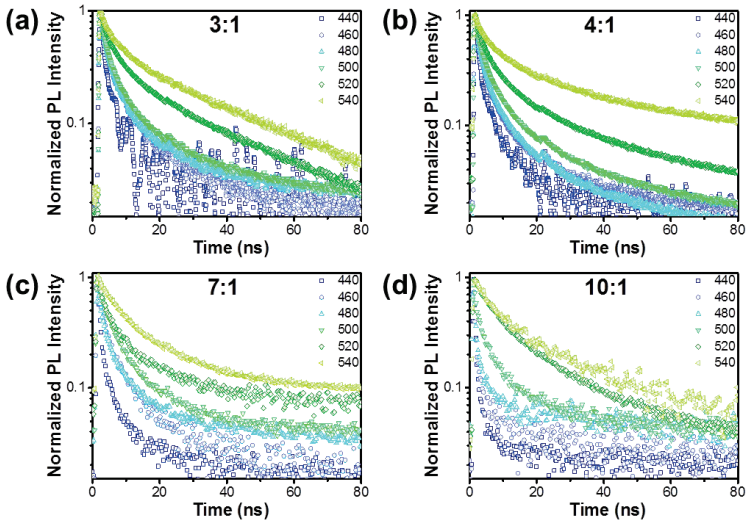

Fig. S23 Time-resolved photoluminescence dynamics of NC thin films with different OA:$PbBr_2$ ratios. (a-d) PL dynamics of NCs 3:1 (a), 4:1 (b), 7:1 (c), and 10:1 (d) with excitation wavelength 405 nm. The legend indicates the emission wavelength in nm. The resulting decay components and the relative weights are reported in Table S10-S14.

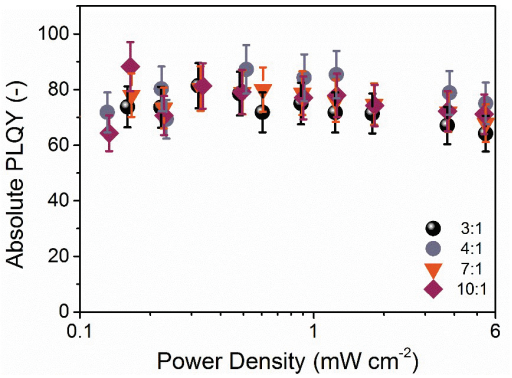

Fig. S24 Normalized photoluminescence quantum yield (PLQY) of nanocrystal thin film as a function of the excitation fluence for different OA:$PbBr_2$ ratios. The measurement error is approximately 5-10%.

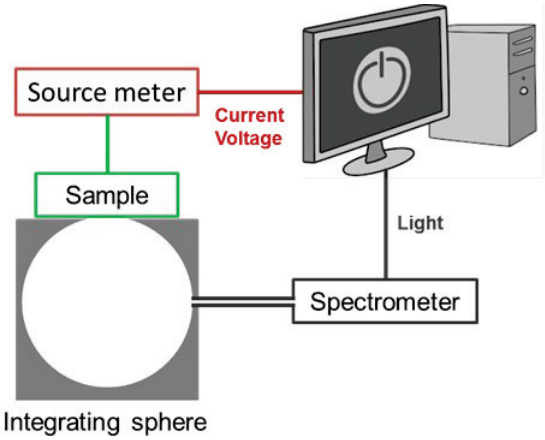

Fig. S25 Experimental setup for LEDs characterization. A Keithley 2612B was used to obtain the current-voltage characteristics of the LED devices. The emission from LEDs was collected by an integrating sphere (OceanOptics FOIS-1) coupled to a calibrated spectrophotometer (OceanOptics QEPro). An OceanOptics HL-3 Plus vis-NIR light source, calibrated using a procedure and documentation patterned after the ISO 17025, IEC Guide 115 and JCGM100:2008 (GUM) protocols, is used to calibrate the absolute irradiance measurement of the spectrometer. As LED devices are placed on the outside the integrating sphere, only forward emission is captured while the edge emission contribution is loss outside the integrating sphere.

Table S1 Overview of selected representative results of light-emission from organic-inorganic and all-inorganic halide perovskite in LEDs.

Perovskite Emitter[a]	Morphology	Device Architecture[b][c]	EQE	CE	L_{max}	V_T	Publication Date
			[%]	[cd A^{-1}]	[cd m^{-2}]	[V]	[-]
$CH_3NH_3PbBr_3$[25]	Thin film	ITO/PEDOT:PSS/Pe/F8/Ca/Ag	0.1	0.3	364	3.3	2014-08
$CH_3NH_3PbBr_3$[9]	Thin film	ITO/Buf-HIL/Pe/TPBI/LiF/Al	0.125	0.57	417	~4	2014-11
$CH_3NH_3PbBr_3$[39]	Thin film	ITO/PEDOT:PSS/Pe/ZnO/Ca/Ag	n.r.[d]	~21	~550	2	2015-01
$CH_3NH_3PbBr_3$[40]	Thin film	ITO/PEDOT:PSS/Pe-PIP/F8/Ca/Ag	1.2	n.r.	~200	n.r.	2015-02
$CH_3NH_3PbBr_3$[10]	Thin film	ITO/ZnO-PEI/Pe/TFB/MoO_x/Au	0.8	n.r.	~20,000	2.8	2015-04
$CH_3NH_3PbBr_3$[41]	Thin film	ITO/PEDOT:PSS/Pe/SPB-02T/LiF/Ag	0.1	0.43	3,490	~2.4	2015-11
$CH_3NH_3PbBr_3$[42]	NPLs	ITO/PEDOT:PSS/Pe/PVK:PBD/BCP/LiF/Al	0.48	n.r.	10,590	3.8	2015-11
$CH_3NH_3PbBr_3$[26]	Thin film	Glass/SOCP/Pe/TPBI/LiF-Al	8.53	**42.9**	~15,000	~4	2015-12
$CH_3NH_3PbBr_3$[11]	Thin film (printed)	ITO/Pe-PEO/Ag NWs	1.1	4.91	21,014	2.6	2015-12
$CH_3NH_3PbBr_3$[17]	Nanoparticle	ITO/PEDOT:PSS/Pe/TPBI/Cs_2CO_3/Al	3.8	11.5	11,830	2.8	2016-06
$CsPbBr_3$[13]	Thin Film	ITO/PEDOT:PSS/Pe-PEO/TPBI/LiF/Al	4.26	15.67	53,525	2.6	2016-08
$CsPbBr_3$[28]	Nanoparticle	ITO/PEDOT:PSS/PVK/Pe/TPBI/LiF/Al	3	8	330	3	2016-08
$CH_3NH_3PbBr_3$[12]	Thin film	ITO/NiO_x/Pe/TPBi/LiF/Al	n.r.	15.9	~70,000	~3.5	2016-08
$CsPbBr_3$[14]	Thin film	ITO/Pe-polymer/In-Ga	5.7	21.5	**591,197**	2.2	2016-09
$CsPbBr_3$[18]	Nanoparticle	ITO/PEDOT:PSS/PolyTPD/Pe/TPBI/LiF/Al	6.27	13.3	15185	3.4	2016-11
$CH(NH_2)_2PbBr_3$[43]	Thin film	ITO/ZnO/Pe/PolyTPD/MoO_3/Al	1.16	2.65	13,062	**1.9**	2016-11
$CH(NH_2)_2PbBr_3$[44]	Nanoparticle	ITO/PEDOT:PSS/Pe/TPBI/Cs_2CO_3/Al	n.r.	6.4	2,714	2.8	2016-11
$CH_3NH_3PbBr_3(C_4H_{10}BrNH_2)$[27]	Thin film	ITO/PVK/Pe/TPBI/LiF/Al	9.3	17.1	~8000	~3.5	2017-01
$Cs_{10}(MA_{0.17}FA_{0.83})_{90}PbBr_3$[32]	Thin film	ITO/ZnO/Pe/NPD/MoO_3/Al	7.3	23.7	19,420	2.4	2017-02
$CH_3NH_3PbBr_3$[33]	Thin film	ITO/PEDOT:PSS/Pe/TPBI/LiF/Al	8.21	34.46	6950	~3.5	2017-03
$CsPbBr_3$[45]	Thin film	ITO/PEDOT:PSS/Pe/TPBI/LiF/Al	4.76	21.38	51,890	2.6	2017-05
$CH(NH_2)_2PbBr_3$[46]	Nanoparticle	ITO/Buf-HIL/Pe/TPBI/LiF/Al	2.05	9.16	~700	~3	2017-05
$CH_3NH_3PbBr_3$[34]	Nanoparticle	ITO/Buf-HIL/Pe/TPBI/LiF/Al	5.09	15.5	~1000	~3	2017-06
$Cs_{0.87}MA_{0.13}PbBr_3$[35]	Thin film	ZnO/PVP/Pe/CBP/MoO_3/Al	**10.4**	33.9	91,000	2.9	2017-06
$CH(NH_2)_2PbBr_3$[47]	Nanoparticle	ITO/PEDOT:PSS/PolyTPD/Pe-PMMA/3TPYMB/LiF/Al	3.04	13.02	2939	2.75	2017-08
$CH(NH_2)_2PbBr_3$ (this work)	**Nanoparticle**	**ITO/PEDOT:PSS/Pe/PO-T2T/Ca/Al**	**13.4**	**57.6**	**>56,000**	**2.2**	**2017-11**

[a] All perovskites display green emission unless stated differently.

[b] Pe = perovskite.

[c] **ITO** = In-doped SnO_2; **PEDOT:PSS** = poly(3,4-ethylenedioxythiophene):polystyrene sulfonate; **F8** = poly(9,9-dioctylfluorene); **Buff-HIL** = buffered hole-injection layer; **TPBI** = 2,2',2''-(1,3,5-benzinetriyl)-tris(1-phenyl-1-H-benzimidazole); **TPD** = *N*,*N*'-bis(3-methylphenyl)-*N*,*N*'-diphenylbenzidine); **PIP** = poly(imide) polymer; **PEI** = poly(ethylenimine), **TFB** = poly(9,9-dioctyl-fluorene-co-*N*-(4-butylphenyl)diphenylamine); **EA** = ethanolamine; **SPB-02T** = blue copolymer, Merck Co.; **BCP** = bathocuproine; **PEO** = poly(ethyleneoxide); **PVK** = poly(9-vinlycarbazole); **PVK:PBD** = (poly(9-vinylcarbazole):2-(4-biphenylyl)-5-phenyl-1,3,4-oxadiazole), **PolyTPD** = poly[N,N'-bis(4-butylphenyl)-N,N'-bisphenylbenzidine]; **CBP** = 4,40-Bis(N-carbazolyl)-1,10-biphenyl; **3TPYMB** = Tris[2,4,6-trimethyl-3-(pyridin-3-yl)phenyl]borane; and **PO-T2T** = 2,4,6-Tris[3-(diphenylphosphinyl)phenyl]-1,3,5-triazine

[d] Not reported.

Table S2 Device performance at various luminances. The table summarizes the voltage applied, EQE, current efficiency, and luminous power efficiency at 100 and 1000 cd m^{-2} as shown in Fig. 1 and S2. The maximum values are listed, while the bracketed values show the average and standard deviation values. Data is not available for 10: 1 NC device since the maximum luminance does not reach 100 cd m^{-2}.

$OA:PbBr_2$ Ratio	No. of Devices	Voltage [V]		EQE [%]		Current Efficiency [cd A^{-1}]		Luminous Power Efficiency [lm W^{-1}]	
		@ 100 cd m^{-2}	@ 1000 cd m^{-2}	@ 100 cd m^{-2}	@ 1000 cd m^{-2}	@ 100 cd m^{-2}	@ 1000 cd m^{-2}	@ 100 cd m^{-2}	@ 1000 cd m^{-2}
3:1	20	3.0 (2.9±0.1)	3.7 (3.5±0.1)	9.9 (5.1±2.8)	11.9 (7.4±2.9)	42.3 (21.8±12.5)	51.2 (31.0±12.9)	45.8 (23.7±13.5)	44.2 (27.4±10.9)
4:1	49	2.9 (2.7±0.2)	3.6 (3.3±0.3)	10.9 (9.4±0.9)	12.9 (12.1±0.4)	47.0 (40.2±4.0)	55.3 (51.7±1.9)	52.8 (46.8±4.0)	58.1 (49.5±4.3)
5:1	34	3.6 (3.0±0.3)	4.8 (3.9±0.4)	11.6 (9.7±1.2)	13.4 (11.9±0.6)	49.9 (42.0±5.0)	57.6 (51.6±2.5)	51.0 (43.5±4.7)	48.4 (42.5±4.1)
7:1	23	3.7 (3.2±0.3)	5.5 (4.4±0.5)	9.7 (9.2±0.3)	9.4 (7.8±1.2)	41.7 (39.6±1.5)	40.2 (33.1±5.2)	45.2 (39.2±3.4)	32.4 (24.5±6.2)
10:1	14	N.A.	N.A.	N.A.	N.A.	N.A.	N.A.	N.A.	N.A.

Table S3. Summary of the device parameters of LED devices used for constant current test as shown in Fig. S7. The devices were measured by sweeping voltage biases up to 2.9 V before the constant current stability test.

Device Nr.	Maximum Luminance [cd m^{-2}]	Maximum Current Efficiency [cd A^{-1}]	Maximum Luminous Power Efficiency [lm W^{-1}]	Maximum EQE [%]
1	227	35.8	38.8	8.3
2	223	33.8	36.6	7.8
3	268	33.5	36.3	7.5

Table S4. Table summarizes the LED device characteristics with different electron transporting layers as shown in Fig. S4. The emissive layer consists of perovskite NCs synthesized with $OA:PbBr_2$ is 4:1.

Electron Transporting Layer	Turn-on Voltage [V]	Maximum Luminance [cd m^{-2}]	Maximum Current Efficiency [cd A^{-1}]	Maximum Luminous Power Efficiency [lm W^{-1}]	Maximum EQE [%]
B3PYMPM	2.7	14957	35.1	30.1	8.1
PO-T2T	2.2	25901	55.3	53.2	12.9

Table S5. Device characteristic parameters of flexible devices. Table summarizes the maximum luminance, current efficiency, luminous power efficiency, and EQE of flexible LED devices as shown in Fig. S10. The emission area is 3mm^2. The emissive layer is the perovskite nanocrystals synthesized with OA:$PbBr_2$ of 4:1.

N_{th} Device	Luminance [cd m^{-2}]	Current Efficiency [cd A^{-1}]	Luminous Power Efficiency [lm W^{-1}]	EQE [%]
1	7637	46.0	39.5	10.5
2	7030	41.6	38.0	9.6
3	6040	47.3	43.1	10.9
4	8611	49.2	42.1	11.3
5	13153	54.1	47.4	12.4
6	10475	51.2	43.5	11.7

Table S6. Device performance of flexible LEDs at various luminances. The table summarizes the voltage applied, EQE, current efficiency, and luminous power efficiency at 100 and 1000 cd m^{-2} as shown in Fig. S10. The emissive layer is the perovskite nanocrystals synthesized with OA:$PbBr_2$ of 4:1.

N_{th} device	Voltage [V]		EQE [%]		Current Efficiency [cd A^{-1}]		Luminous Power Efficiency [lm W^{-1}]	
	@ 100 cd m^{-2}	@ 1000 cd m^{-2}	@ 100 cd m^{-2}	@ 1000 cd m^{-2}	@ 100 cd m^{-2}	@ 1000 cd m^{-2}	@ 100 cd m^{-2}	@ 1000 cd m^{-2}
1	2.9	3.7	7.6	10.4	33.2	45.3	36.0	38.4
2	2.9	3.7	7.7	9.5	33.6	41.6	36.5	35.3
3	2.9	3.7	8.9	10.9	38.5	47.2	41.7	40.1
4	2.9	3.6	8.0	10.9	35.2	47.6	38.1	41.5
5	2.8	3.4	8.5	11.7	37.2	51.0	41.7	47.1
6	2.9	3.6	8.2	11.3	35.6	49.3	38.5	43.0

Table S7. Table summarizes the device characteristics of large area LED devices as shown in Fig. S11. At maximum luminance, LEDs with area > 15.2 mm^2 saturated the spectrometer. The bracketed number showed the characteristic values after corrected for the saturation, by scaling the luminance values linearly according to the spectral regions that does not saturate the spectrometer with the assumption that the spectral shape does not change at any injection density. Note: the largest area device (95.2 mm^2) is larger than the opening of the integrating sphere (78.5 mm^2). The reported values are not corrected for the loss of photons (i.e. the photons not collected by the integrating sphere). The emissive layer is the perovskite nanocrystals synthesized with OA:$PbBr_2$ of 4:1.

Device Area [mm^{-2}]	Luminance [cd m^{-2}]	Current Efficiency [cd A^{-1}]	Luminous Power Efficiency [lm W^{-1}]	EQE [%]
8.97	20577	42.7	39.2	9.9
15.2	19688 (22332)	37.2	34.2	8.6
35.4	12438 (20016)	30.9	24.3	7.2
95.2	6106 (13658)	22.8 (24.5)	18.7	5.3 (5.7)

Table S8. Device performance of large area LEDs at various luminances as shown in Fig. S11. The table summarizes the voltage applied, EQE, current efficiency, and luminous power efficiency at 100 and 1000 cd m^{-2}.

Device Area [mm^2]	Voltage [V]		EQE [%]		Current Efficiency [cd A^{-1}]		Luminous Power Efficiency [lm W^{-1}]	
	@ 100 cd m^{-2}	@ 1000 cd m^{-2}	@ 100 cd m^{-2}	@ 1000 cd m^{-2}	@ 100 cd m^{-2}	@ 1000 cd m^{-2}	@ 100 cd m^{-2}	@ 1000 cd m^{-2}
8.97	2.7	3.2	5.8	9.2	25.3	39.9	29.4	39.2
15.2	2.7	3.2	5.1	8.1	21.9	34.9	25.5	34.2
35.4	2.9	3.9	3.3	6.1	14.4	26.1	15.6	21.0
95.2	3.4	3.9	3.2	5.3	13.8	22.8	12.8	18.4

Table S9. Tabulated decay times for the global fitting result shown in Fig. S21.

	OA:$PbBr_2$ [-]				
	3:1[#]	4:1[#]	5:1*	7:1[#]	10:1*
t_1 [ps]	0.34 ± 0.01	0.11 ± 0.01	0.25 ± 0.01	0.11 ± 0.003	0.15 ± 0.01
t_2 [ps]	6.80 ± 0.11	5.73 ± 0.13	5.83 ± 0.08	2.60 ± 0.04	4.287 ± 0.05
t_3 [ps]	46.56 ± 1.36	33.71 ± 3.24	42.58 ± 0.31	24.91 ± 0.36	36.78 ± 2.27
t_4 [ps]	949.5 ± 23.1	719.3 ± 14.4	742.7 ± 5.6	628.6 ± 18.2	804.6 ± 18.6

[#] Averaged 6 times

* Averaged 18 times

Table S10. Characteristic fluorescence lifetimes for OA:$PbBr_2$ = 3:1, after 405 nm excitation and signal collection at different emission wavelengths as shown in Fig. S23(a).

Emission Wavelength	A_1	τ_1	A_2	τ_2	τ_{av}
[nm]	[-]	[ns]	[-]	[ns]	[ns]
440	0.79	0.8	0.21	7.0	2.1
460	0.71	1.4	0.29	9.3	3.7
480	0.71	1.5	0.29	8.9	3.7
500	0.72	1.7	0.28	11.3	4.3
520	0.61	2.6	0.39	20.8	9.6
540	0.52	3.2	0.48	27.7	15.1

Table S11. Characteristic fluorescence lifetimes for OA:$PbBr_2$ = 4:1, after 405 nm excitation and signal collection at different emission wavelengths as shown in Fig. S23(b).

Emission Wavelength	A_1	τ_1	A_2	τ_2	τ_{av}
[nm]	[-]	[ns]	[-]	[ns]	[ns]
440	0.79	1.0	0.21	7.8	2.4
460	0.74	1.3	0.26	8.9	3.3
480	0.72	1.6	0.28	10.0	3.9
500	0.65	1.9	0.35	12.5	5.6
520	0.63	2.5	0.37	17.6	8.1
540	0.52	3.1	0.48	23.9	13.2

Table S12. Characteristic fluorescence lifetimes for OA:$PbBr_2$ = 5:1, after 405 nm excitation and signal collection at different emission wavelengths as shown in Fig. 6(b).

Emission Wavelength	A_1	τ_1	A_2	τ_2	τ_{av}
[nm]	[-]	[ns]	[-]	[ns]	[ns]
440	0.95	0.6	0.05	4.4	0.8
460	0.60	1.3	0.40	8.7	4.3
480	0.58	1.7	0.42	9.5	4.9
500	0.56	2.3	0.44	11.2	6.2
520	0.52	4.3	0.48	16.8	10.3
540	0.42	4.3	0.58	18.1	12.1

Table S13. Characteristic fluorescence lifetimes for OA:$PbBr_2$ = 7:1, after 405 nm excitation and signal collection at different emission wavelengths as shown in Fig. S23(c).

Emission Wavelength	A_1	τ_1	A_2	τ_2	τ_{av}
[nm]	[-]	[ns]	[-]	[ns]	[ns]
440	0.84	0.7	0.16	5.6	1.5
460	0.72	1.5	0.28	9.5	3.7
480	0.65	1.7	0.35	10.0	4.6
500	0.64	2.3	0.36	9.9	5.0
520	0.64	2.3	0.36	13.2	6.2
540	0.50	16.3	0.50	4.1	10.2

Table S14. Characteristic fluorescence lifetimes for OA:$PbBr_2$ = 10:1, after 405 nm excitation and signal collection at different emission wavelengths as shown in Fig. S23(d).

Emission Wavelength	A_1	τ_1	A_2	τ_2	τ_{av}
[nm]	[-]	[ns]	[-]	[ns]	[ns]
440	0.95	0.5	0.05	5.3	0.7
460	0.90	0.5	0.10	7.2	1.2
480	0.89	0.6	0.11	8.7	1.5
500	0.67	1.0	0.33	8.2	3.3
520	0.51	4.3	0.49	18.6	11.3
540	0.48	4.2	0.52	21.9	13.4

References:

1. Y. Cao, I. D. Parker, G. Yu, C. Zhang and A. J. Heeger, *Nature*, 1999, **397**, 414-417.
2. X. Dai, Z. Zhang, Y. Jin, Y. Niu, H. Cao, X. Liang, L. Chen, J. Wang and X. Peng, *Nature*, 2014, **515**, 96-99.
3. B. R. Pauw, J. S. Pedersen, S. Tardif, M. Takata and B. B. Iversen, *J Appl Crystallogr*, 2013, **46**, 365-371.
4. G. Xing, B. Wu, X. Wu, M. Li, B. Du, Q. Wei, J. Guo, E. K. L. Yeow, T. C. Sum and W. Huang, *Nat. Commun.*, 2017, **8**, 14558.
5. M. E. F. Bouduban, A. Burgos-Caminal, R. Ossola, J. Teuscher and J.-E. Moser, *Chem Sci*, 2017, **8**, 4371-4380.
6. Y. Shirasaki, G. J. Supran, M. G. Bawendi and V. Bulović, *Nat. Photon.*, 2012, **7**, 13.
7. H. H. Chou and C. H. Cheng, *Adv. Mater.*, 2010, **22**, 2468-2471.
8. J. Kwak, W. K. Bae, D. Lee, I. Park, J. Lim, M. Park, H. Cho, H. Woo, D. Y. Yoon and K. Char, *Nano Lett.*, 2012, **12**, 2362-2366.
9. Y. H. Kim, H. Cho, J. H. Heo, T. S. Kim, N. Myoung, C. L. Lee, S. H. Im and T. W. Lee, *Adv. Mater.*, 2015, **27**, 1248-1254.
10. J. Wang, N. Wang, Y. Jin, J. Si, Z. K. Tan, H. Du, L. Cheng, X. Dai, S. Bai, H. He, Z. Ye, M. L. Lai, R. H. Friend and W. Huang, *Adv. Mater.*, 2015, **27**, 2311-2316.
11. S. G. Bade, J. Li, X. Shan, Y. Ling, Y. Tian, T. Dilbeck, T. Besara, T. Geske, H. Gao, B. Ma, K. Hanson, T. Siegrist, C. Xu and Z. Yu, *ACS Nano*, 2016, **10**, 1795-1801.
12. Y. K. Chih, J. C. Wang, R. T. Yang, C. C. Liu, Y. C. Chang, Y. S. Fu, W. C. Lai, P. Chen, T. C. Wen, Y. C. Huang, C. S. Tsao and T. F. Guo, *Adv. Mater.*, 2016, **28**, 8687-8694.
13. Y. Ling, Y. Tian, X. Wang, J. C. Wang, J. M. Knox, F. Perez-Orive, Y. Du, L. Tan, K. Hanson, B. Ma and H. Gao, *Adv. Mater.*, 2016, **28**, 8983–8989.
14. J. Li, X. Shan, S. G. R. Bade, T. Geske, Q. Jiang, X. Yang and Z. Yu, *J. Phys. Chem. Lett.*, 2016, **7**, 4059-4066.
15. J. Song, J. Li, X. Li, L. Xu, Y. Dong and H. Zeng, *Adv. Mater.*, 2015, **27**, 7162-7167.
16. G. Li, F. W. R. Rivarola, N. J. L. K. Davis, S. Bai, T. C. Jellicoe, F. de la Peña, S. Hou, C. Ducati, F. Gao, R. H. Friend, N. C. Greenham and Z.-K. Tan, *Adv. Mater.*, 2016, **28**, 3528-3534.
17. J. Xing, F. Yan, Y. Zhao, S. Chen, H. Yu, Q. Zhang, R. Zeng, H. V. Demir, X. Sun, A. Huan and Q. Xiong, *ACS Nano*, 2016, **10**, 6623-6630.
18. J. Li, L. Xu, T. Wang, J. Song, J. Chen, J. Xue, Y. Dong, B. Cai, Q. Shan, B. Han and H. Zeng, *Adv. Mater.*, 2017, **29**, 1603885.
19. S. Y. Kim, W. I. Jeong, C. Mayr, Y. S. Park, K. H. Kim, J. H. Lee, C. K. Moon, W. Brütting and J. J. Kim, *Adv. Funct. Mater.*, 2013, **23**, 3896-3900.
20. D. R. Lee, B. S. Kim, C. W. Lee, Y. Im, K. S. Yook, S.-H. Hwang and J. Y. Lee, *ACS Appl. Mater. & Interfaces*, 2015, **7**, 9625-9629.
21. C. Y. Kuei, W. L. Tsai, B. Tong, M. Jiao, W. K. Lee, Y. Chi, C. C. Wu, S. H. Liu, G. H. Lee and P. T. Chou, *Adv. Mater.*, 2016, **28**, 2795-2800.
22. Z. Yan, Y. Wang, J. Wang, Y. Wang, J. Ding and L. Wang, *J. Mater. Chem. C*, 2017, **5**, 10122-10125.

23. J. R. Manders, L. Qian, A. Titov, J. Hyvonen, J. Tokarz‐Scott, K. P. Acharya, Y. Yang, W. Cao, Y. Zheng and J. Xue, *J. Soc. Inf. Disp.*, 2015, **23**, 523-528.
24. H. Zhang, S. Chen and X. W. Sun, *ACS nano*, 2017.
25. Z.-K. Tan, R. S. Moghaddam, M. L. Lai, P. Docampo, R. Higler, F. Deschler, M. Price, A. Sadhanala, L. M. Pazos, D. Credgington, F. Hanusch, T. Bein, H. J. Snaith and R. H. Friend, *Nat. Nano.*, 2014, **9**, 687-692.
26. H. Cho, S.-H. Jeong, M.-H. Park, Y.-H. Kim, C. Wolf, C.-L. Lee, J. H. Heo, A. Sadhanala, N. Myoung, S. Yoo, S. H. Im, R. H. Friend and T.-W. Lee, *Science*, 2015, **350**, 1222-1225.
27. Z. Xiao, R. A. Kerner, L. Zhao, N. L. Tran, K. M. Lee, T.-W. Koh, G. D. Scholes and B. P. Rand, *Nat. Photon.*, 2017, **11**, 108.
28. J. Pan, L. N. Quan, Y. Zhao, W. Peng, B. Murali, S. P. Sarmah, M. Yuan, L. Sinatra, N. M. Alyami, J. Liu, E. Yassitepe, Z. Yang, O. Voznyy, R. Comin, M. N. Hedhili, O. F. Mohammed, Z. H. Lu, D. H. Kim, E. H. Sargent and O. M. Bakr, *Adv. Mater.*, 2016, **28**, 8718-8725.
29. K. Okumoto, H. Kanno, Y. Hamaa, H. Takahashi and K. Shibata, *Appl. Phys. Lett.*, 2006, **89**, 063504.
30. W. K. Bae, J. Kwak, J. W. Park, K. Char, C. Lee and S. Lee, *Adv. Mater.*, 2009, **21**, 1690-1694.
31. K.-H. Lee, J.-H. Lee, H.-D. Kang, B. Park, Y. Kwon, H. Ko, C. Lee, J. Lee and H. Yang, *ACS Nano*, 2014, **8**, 4893-4901.
32. H. P. Kim, J. Kim, B. S. Kim, H.-M. Kim, J. Kim, A. R. b. M. Yusoff, J. Jang and M. K. Nazeeruddin, *Adv. Opt. Mater.*, 2017, **5**, 1600920.
33. J.-W. Lee, Y. J. Choi, J.-M. Yang, S. Ham, S. K. Jeon, J. Y. Lee, Y.-H. Song, E. K. Ji, D.-H. Yoon, S. Seo, H. Shin, G. S. Han, H. S. Jung, D. Kim and N.-G. Park, *ACS Nano*, 2017, **11**, 3311-3319.
34. Y.-H. Kim, C. Wolf, Y.-T. Kim, H. Cho, W. Kwon, S. Do, A. Sadhanala, C. G. Park, S.-W. Rhee, S. H. Im, R. H. Friend and T.-W. Lee, *ACS Nano*, 2017, **11**, 6586-6593.
35. L. Zhang, X. Yang, Q. Jiang, P. Wang, Z. Yin, X. Zhang, H. Tan, Y. Yang, M. Wei, B. R. Sutherland, E. H. Sargent and J. You, *Nat. Commun.*, 2017, **8**, 15640.
36. N. Stribeck, *X-ray scattering of soft matter*, Springer Science & Business Media, 2007.
37. O. Glatter and O. Kratky, *Small angle X-ray scattering*, Academic press, 1982.
38. A. Guiner, G. Fournet and C. Walker, *J. Wiley & Sons, New York*, 1955.
39. R. L. Z. Hoye, M. R. Chua, K. P. Musselman, G. Li, M.-L. Lai, Z.-K. Tan, N. C. Greenham, J. L. MacManus-Driscoll, R. H. Friend and D. Credgington, *Adv. Mater.*, 2015, **27**, 1414-1419.
40. G. Li, Z.-K. Tan, D. Di, M. L. Lai, L. Jiang, J. H.-W. Lim, R. H. Friend and N. C. Greenham, *Nano Lett.*, 2015, **15**, 2640-2644.
41. J. C. Yu, D. B. Kim, E. D. Jung, B. R. Lee and M. H. Song, *Nanoscale*, 2016, **8**, 7036-7042.
42. Y. Ling, Z. Yuan, Y. Tian, X. Wang, J. C. Wang, Y. Xin, K. Hanson, B. Ma and H. Gao, *Adv. Mater.*, 2016, **28**, 305-311.
43. L. Meng, E.-P. Yao, Z. Hong, H. Chen, P. Sun, Z. Yang, G. Li and Y. Yang, *Adv. Mater.*, 2017, **29**, 1603826.

44. A. Perumal, S. Shendre, M. Li, Y. K. E. Tay, V. K. Sharma, S. Chen, Z. Wei, Q. Liu, Y. Gao, P. J. S. Buenconsejo, S. T. Tan, C. L. Gan, Q. Xiong, T. C. Sum and H. V. Demir, *Sci. Rep.*, 2016, **6**, 36733.
45. C. Wu, Y. Zou, T. Wu, M. Ban, V. Pecunia, Y. Han, Q. Liu, T. Song, S. Duhm and B. Sun, *Adv. Funct. Mater.*, 2017, **27**, 1700338.
46. Y.-H. Kim, G.-H. Lee, Y.-T. Kim, C. Wolf, H. J. Yun, W. Kwon, C. G. Park and T. W. Lee, *Nano Energy*, 2017, **38**, 51-58.
47. S. Kumar, J. Jagielski, N. Kallikounis, Y.-H. Kim, C. Wolf, F. Jenny, T. Tian, C. J. Hofer, Y.-C. Chiu, W. J. Stark, T.-W. Lee and C.-J. Shih, *Nano Lett.*, 2017, **17**, 5277-5284.

Chapter 5.

Dry mechanochemical synthesis of highly luminescent, blue and green hybrid perovskite solids

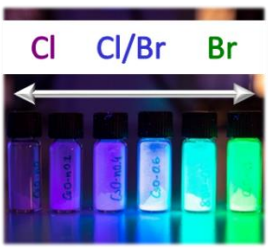

5.1. Motivation, work description and achievement

Dry mechanochemical synthesis is an alternative, solvent-free technique to prepare metal halide perovskites with virtually any composition. It is a simple method which can lead to higher purity due to the absence of processing additives and high boiling point (toxic) solvents.[76,134–140] Mechanochemical synthesis can be used to synthesize multi-component compounds simply by mixing the chemical precursors in the appropriate stoichiometry. Importantly, there is no limitation to the compositional freedom due to solubility of the precursor salts. Moreover, mechanochemically-synthesized perovskites have demonstrated enhanced stability, which has been attributed to a superior purity and crystallinity of the materials in the powder form, resulting in stronger ionic interactions within the crystal lattices.[141,142] Perovskites powders can be processed into thin films using single-source vacuum deposition of pre-synthesized compounds,[143,144] allowing the formation of high-quality perovskite thin films.[145,146]

Mechanochemical synthesis is therefore ideally suited to explore wide bandgap, mixed halide perovskites, where the bandgap can be systematically tuned by substitution of iodide with bromide and chloride.[147–150] Wide bandgap perovskites are particularly interesting for the fabrication of tandem solar cells and for the development of blue light-emitting diodes.[28,151,152] However, producing stable and luminescent wide bandgap perovskites remains challenging, as pure or chloride-rich compounds typically show low PLQY.[149,150,153] Furthermore, mixed halide materials suffer from photoinduced halide segregation,[94,154] which further complicates the preparation of efficient and stable blue-emitting lead halide perovskites. The addition of passivating agents can be beneficial for the enhancement of the PLQY,[155–157] as they can decrease the density of trap states at the grain boundaries and on the surface.

In this chapter, the development of bright photoluminescent wide bandgap mixed halide 3D perovskite powders is reported. The materials are prepared by dry mechanochemical synthesis (ball-milling) starting from the neat binary precursors, and show enhanced photoluminescence upon the addition of an adamantane derivative in the precursor's mixture. It is demonstrated that, by simple stoichiometric control of the halide precursors, the photoluminescence can be finely tuned from the UV to the green part of the visible spectrum.

5.2. Experimental details and methodology

$MA_{0.8}Cs_{0.2}Pb(Br_{0.6}Cl_{0.4})_3$ was prepared by ball-milling; 0.48 mol of CH_3NH_3Br (MABr), 0.32 mol of CH_3NH_3Cl (MACl), 0.12 mol of CsBr and 0.08 mol of CsCl were mixed together with 0.6 mol of $PbBr_2$ and 0.4 mol of $PbCl_2$ in a nitrogen-filled glovebox. The powder mixture was introduced in a 10 mL zirconia ball-mill jar with zirconia beads. Afterwards, ball-milling was performed at a frequency of 30 Hz for 2 hours. The resulting yellowish powder was

characterized in ambient conditions and at RT. The passivated samples were obtained adding increasing amounts (from 0 to 90 mol%) of amantadine hydrochloride (AmCl) to the mixture before ball-milling. For the rest of the $MA_yCs_{1-y}Pb(Br_nCl_{1-n})_3$ samples, MA^+/Cs^+ and Br^-/Cl^- were adjusted accordingly. Cs molar ratio was varied from 0 (pure $MAPb(Br_nCl_{1-n})_3$) to 1 (pure $CsPb(Br_nCl_{1-n})_3$). Br molar ratio was varied from 0 (pure $MA_yCs_{1-y}PbCl_3$) to 1 (pure $MA_yCs_{1-y}PbBr_3$).

The PL spectra were collected using a 375 nm laser as the excitation source and collected with a Hamamatsu C9920-02 spectrometer with a Hamamatsu PMA-11 optical detector. PLQY was measured using a Xe lamp coupled to a monochromator as the excitation source and an integrated sphere coupled to the same spectrometer (Hamamatsu C9920-02 with a Hamamatsu PMA-11 optical detector). UV-visible absorption spectra of the samples were collected in an integrated sphere using a fiber-optics based Avantes Avaspec 2048 spectrophotometer. X-ray diffraction was measured with a Panalytical Empyrean diffractometer equipped with a copper anode (CuKα) operated at 45 kV and 30 mA and a Pixel 1D detector in scanning line mode. Single scans were acquired in the 2 theta = 5° to 50° range in Bragg-Brentano geometry in air. Data analysis was performed with HighScore Plus software.

5.3. Results and discussion

The as-prepared materials, obtained in powder form, were analysed using X-ray diffraction to determine their structure and by optical spectroscopy to determine their optical absorption and luminescence spectral features. The XRD analysis (Figure 5.1a, black line, 0%) suggests the presence of a single mixed halide phase, and its optical absorption (Figure 5.1b, black line, 0%) shows a steep absorption onset at about 500 nm (corresponding to a bandgap energy, E_g, of approximately 2.5 eV), in agreement with previous reports on similar compositions.[158] We were not able to detect any PL, even when the sample was directly irradiated by a UV (375 nm, 100 mW) continuous wave (CW) laser. This is not surprising, as non-passivated, bulk, wide bandgap semiconductors are prone to suffer from non-radiative charge recombination due to a large density of trap states at the surface or grain boundaries.[159] With the aim to reduce the trap states responsible for non-radiative charge recombination, we added amantadine hydrochloride (or 1-adamantanamine hydrochloride, herein after referred to as AmCl) to the precursors of the mechanochemical synthesis.

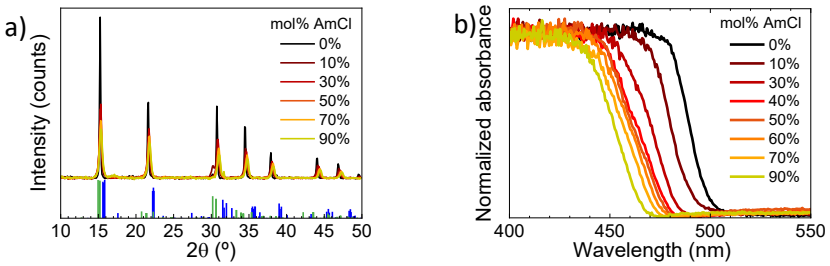

Figure 5.1. a) XRD patterns for $MA_{0.8}Cs_{0.2}Pb(Br_{0.6}Cl_{0.4})_3$ powders with increasing molar concentration of AmCl and reference bulk pattern (bottom) for $MAPbCl_3$ (blue, ICSD collection code 241415) and $MAPbBr_3$ (green, ICSD collection code 158306). b) Absorption spectra for the same series of materials.

While the XRD analysis shows a very similar pattern for the whole series, independently on the concentration of AmCl (Figure 5.1a), the optical absorption onset shifts to shorter wavelengths with increasing amounts of AmCl (Figure 5.1b). This is because the use of the chloride salt AmCl inevitably results in the incorporation of excess of chloride into the material. Importantly, it seems that the addition of AmCl does not lead to the formation or segregation of different phases but to a homogeneous single (mixed halide) perovskite phase. This can be a consequence of the higher reactivity of MAX and CsX towards PbX_2, which are stoichiometrically added in order to obtain the perovskite $MA_{0.8}Cs_{0.2}Pb(Br_{0.6}Cl_{0.4})_3$, precluding the formation of any compound between AmCl and the other reagents. Most likely, AmCl is still present in the synthesis product but it is amorphous and/or distributed at the grain boundaries. Remarkably, for the materials synthesized in the presence of AmCl, we were able to detect photoluminescence even at low excitation density. As observed from the optical absorption, the increased amount of chloride causes a blue-shift in the PL signals (Figure 5.2a), with the PL maxima shifting from 478 nm to 458 nm when the AmCl concentration is increased from 10 mol% to 90 mol%, respectively (an increase in the bandgap of about 0.1 eV). Thanks to the presence of AmCl, the powders show luminescence even when illuminated with a low-intensity UV lamp (Figure 5.2b). The AmCl additive is thus capable to passivate the $MA_{0.8}Cs_{0.2}Pb(Br_{0.6}Cl_{0.4})_3$ bulk material, as the PLQY increased from 0 to 4% for AmCl concentration of 40-50 mol% (Figure 5.2c). This implies that the density of trap states is substantially reduced in the presence of AmCl. For AmCl concentrations > 50 mol%, the PLQY was found to slightly decrease. The PLQY reduction is not yet fully rationalized, but can be ascribed to a diminished crystallinity (as revealed by the XRD analysis) and to the wider bandgap of the material, as not-quenching shallow traps become deep traps favouring non-radiative recombination.

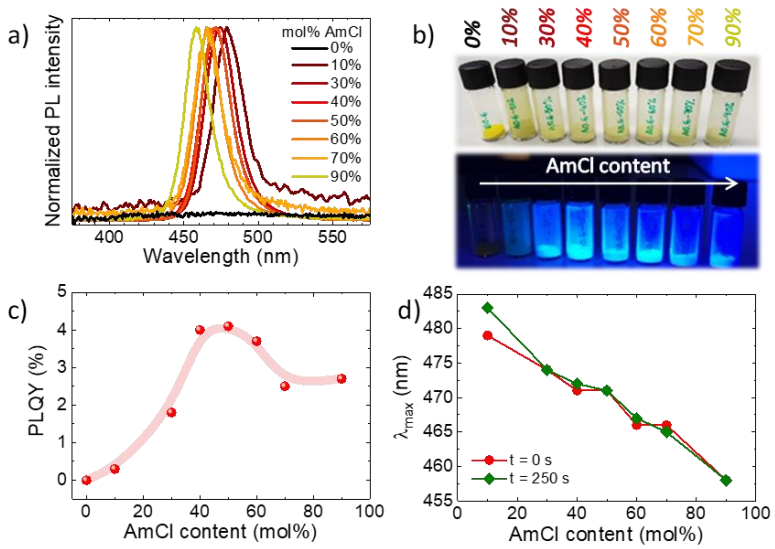

Figure 5.2. a) Photoluminescence spectra (λ_{exc} = 375 nm) of $MA_{0.8}Cs_{0.2}Pb(Br_{0.6}Cl_{0.4})_3$ powders with varying concentration of AmCl passivating agent, from 0 to 90 mol%. b) Photographs taken under ambient (above) and UV light (λ = 365 nm, below), c) PLQY (the line is a guide to the eye) and d) first and last measurements of the photo-stability test of the maximum peaks wavelength plotted as a function of the added mol% of AmCl.

As mentioned before, mixed halide perovskites can undergo halide segregation under illumination.[93][154,155] In this regard, the material photostability was studied by monitoring the PL spectra as a function of time under continuous irradiation. The position of the PL maxima as a function of the AmCl concentration at time 0 and after 250 s is reported in Figure 5.2d. We observed a small shift in the maximum PL intensity only at a low AmCl concentration (10 mol%), while for the rest of the samples no change in the optical properties (sign of halide segregation) was detected.

To study the effect of the composition on the optical properties, the amount of Cs^+ was varied in the mechanochemical synthesis of $MA_{1-y}Cs_yPb(Br_{0.6}Cl_{0.4})_3$ from y = 0 (pure MA^+) to 0.2, 0.4 and 1 (pure Cs^+), maintaining a 50 mol% AmCl concentration. A small deviation in the bandgap of the material was observed upon exchanging MA^+ with Cs^+, as shown by the optical absorption spectra (Figure 5.3a). Also the PL spectra showed a small shift from 467 nm to 472 nm when the caesium content was varied from 0 to 1 (Figure 5.3b). The structural characterization showed again a high degree of conversion and crystallinity for the entire series of compounds (Figure 5.3c), with an expected shift to larger angles upon substitution with the smaller caesium cation. The different intensity of the main diffraction peaks between the hybrid and fully inorganic perovskites (y = 1) agrees with the slightly different orientation of the unit cell.[160] Interestingly, we found the PLQY to scale inversely with the

amount of Cs^+ used in the synthesis of the perovskite $MA_{1-y}Cs_yPb(Br_{0.6}Cl_{0.4})_3$, with the pure MA^+ materials exhibiting blue emission with 7% PLQY (Figure 5.3d). As the caesium content increases, the PLQY progressively decreases to approximately 1% for the pure inorganic compound (y = 1). This behaviour has been previously attributed to the large dipole moment (2.3 D) and rotational freedom of the MA cation, which would respond to the formation of trapped charges reducing non-radiative recombination.[161,162]

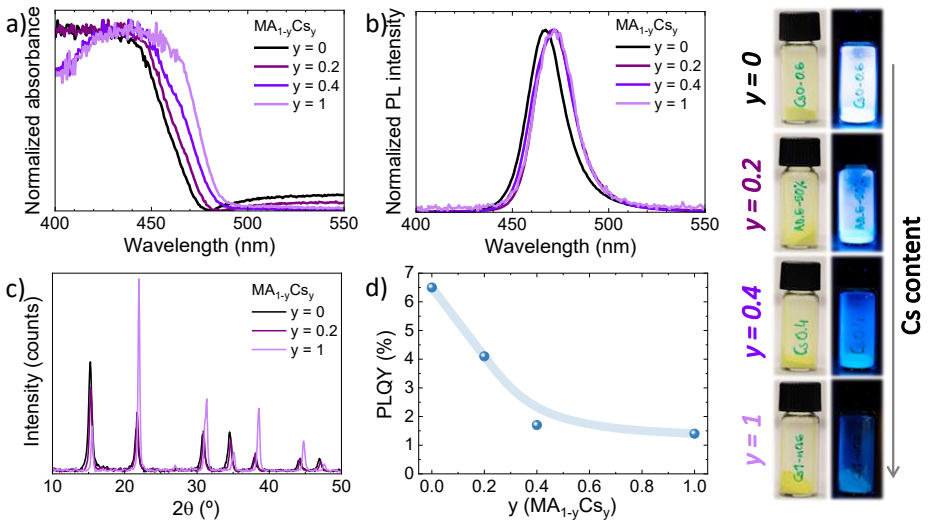

Figure 5.3. a) Absorption and b) photoluminescence spectra for the mechanochemically synthesized $MA_{1-y}Cs_yPb(Br_{0.6}Cl_{0.4})_3$ samples, with y = 0, 0.2, 0.4 and 1. c) XRD patterns for the same compound series and d) PLQY as a function of the Cs^+ content (the line is a guide to the eye). On the right, pictures of the samples with increasing Cs/MA ratio under ambient (left) and UV (right) light.

The effect of the halide exchange on the optical characteristics of the perovskite series was also studied. The bromide content was increased from 0 to 1 in the preparation of 6 different perovskites of the type $MAPb(Br_nCl_{1-n})_3$, keeping constant the concentration of AmCl at 50 mol%. The samples exhibited absorption onsets red-shifting from 410 nm (n = 0, pure chloride compound) to 512 nm (n = 1, pure bromide perovskite) as the bromide content is increased (Figure 5.4a). The corresponding PL maxima follows the same trend, decreasing in energy from 405 nm (violet) to 514 nm (green) for pure chloride and bromide materials, respectively (Figure 5.4b and c). XRD analysis (Figure 5.4d) confirmed the formation of highly crystalline pure chloride and bromide perovskites, as well as for the mixed halide species. The XRD patterns show a displacement of the reflections corresponding to the same planes to smaller angles as the Br/Cl ratio increases.

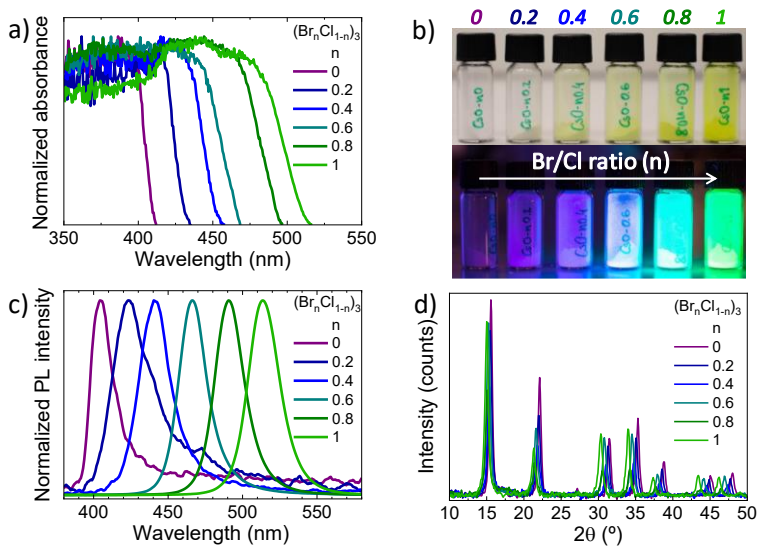

Figure 5.4. a) Optical absorption spectra of the MAPb(Br_nCl_{1-n})$_3$ samples for n = 0, 0.2, 0.4, 0.6, 0.8 and 1. b) Pictures of the samples with varying Br/Cl content under ambient (top) and UV light (λ = 365 nm, bottom). c) PL spectra and d) XRD analysis of all the samples.

As the bandgap narrows, the corresponding PLQY rises from approximately 1% (for 0 ≤ n ≤ 0.4) to 7% (n = 0.6), and up to 15% and 29% for the bromide-rich, green-emitting MAPb(Br_nCl_{1-n})$_3$ (n = 0.8 and 1, respectively). Although we cannot exclude differences in the formation chemistry of the materials, the large increase in PLQY, observed when decreasing the bandgap from blue- (7%) to green-emitting (29%) perovskites, is likely related to the energy and distribution of trap states with respect to the electronic bands of the semiconductors. Deep traps that are quenching in blue perovskites become shallower or fall within the electronic bands when the bandgap is narrower, as discussed previously in the introduction.

5.4. Published work

The publication is reproduced from Wiley-VCH.

DOI: 10.1002/adom.201901494, Adv. Optical Mater., 2019, 1901494.

ADVANCED OPTICAL MATERIALS
www.advopticalmat.de

Dry Mechanochemical Synthesis of Highly Luminescent, Blue and Green Hybrid Perovskite Solids

Laura Martínez-Sarti, Francisco Palazon, Michele Sessolo, and Henk J. Bolink*

A simple method to obtain bright photoluminescent wide bandgap mixed-halide 3D perovskites is reported. The materials are prepared by dry mechanochemical synthesis (ball-milling) starting from neat binary precursors, and show enhanced photoluminescence upon the addition of an adamantane derivative in the precursors' mixture. The structural characterization suggests that the additive does not participate in the crystal structure of the perovskite, which remains unvaried even with high loading of amantadine hydrochloride. By simple stoichiometric control of the halide precursors, the photoluminescence can be finely tuned from the UV to the green part of the visible spectrum. Photoluminescence quantum yields as high as 29% and 5% have been obtained for green- and blue-emitting perovskite solids, even at very low excitation densities.

Metal halide perovskites are being studied for several applications, such as light-emitting diodes, solar cells, photodetectors, lasers, water splitting or memristors.[1–8] This wide application spectrum is enabled by their remarkable optical and electronic properties, such as their high absorption coefficient, defect tolerance, ambipolar and large charge diffusion length, and high rate of radiative recombination.[9–13] Some of the key factors to obtain high quality perovskites are the purity of the perovskite precursors, the choice of the most appropriate synthetic method, and the control over the environmental processing conditions.[14,15] Solution-based techniques are widely adopted to prepare perovskite compounds. Small amounts of additives (if the solubility in common solvents is sufficient) or different chemical precursors are often used.[16–18] Also, high boiling point (toxic) solvents, and multiple processing steps,[19,20] are usually needed to ensure the formation of highly crystalline materials. Solvent-free "dry" mechanochemical synthesis is an alternative technique to prepare perovskites with virtually any composition. It is a simple method which can lead to higher purity due to the absence of processing additives and solvents.[21–28] Mechanochemical synthesis can be used to synthesize multicomponent compounds simply by mixing the chemical precursors in the appropriate stoichiometry. Importantly, there is no limitation to the compositional freedom from the solubility of the precursor salts. Moreover, mechanochemically synthesized perovskites have demonstrated enhanced stability, which has been attributed to superior purity and crystallinity of the materials in the powder form, resulting in stronger ionic interactions within the crystal lattices.[29,30] Additionally, it has been shown that some perovskites can be processed into thin film using single-source vacuum deposition of pre-synthesized compounds,[31,32] allowing the formation of high-quality perovskite layers.[33,34] Other techniques such as aerosol deposition are also being developed.[35]

Mechanochemical synthesis is therefore ideally suited to explore wide bandgap, mixed halide perovskites, where the bandgap can be systematically tuned by substitution of iodide with bromide and chloride.[36–39] Wide bandgap perovskites are particularly interesting for the fabrication of tandem solar cells and for the development of blue light-emitting diodes.[3,40,41] However, producing stable and luminescent wide bandgap perovskites remains challenging, as pure or chloride-rich compounds typically show low photoluminescence (PL) quantum yield (PLQY).[38,39,42] Furthermore, mixed halide materials suffer from photoinduced halide segregation,[43,44] which further complicates the preparation of efficient and stable blue-emitting lead halide perovskites. The addition of passivating agents can be beneficial for the enhancement of the PLQY,[45–47] as they can decrease the density of trap states at the grain boundaries and on the surface.

In this work, we describe the mechanochemical synthesis of stable mixed-cation/mixed-halide perovskites with emission spanning the blue to green region of the visible spectrum. We demonstrate that strong enhancements in the PLQY are obtained by the addition of amantadine hydrochloride to the precursor mix prior to the ball-milling. The effect of this additive is studied as a function of its concentration, and only minor structural changes are observed in the resulting perovskites. Mixed-cation/mixed-halide perovskites, with the general formula $MA_{1-y}Cs_yPb(Br_nCl_{1-n})_3$ (where MA stands for methylammonium) can be easily modified to fine-tune their optical properties. $MA_{0.8}Cs_{0.2}Pb(Br_{0.6}Cl_{0.4})_3$ was chosen as the starting material because this particular halide ratio has a bandgap energy corresponding to the blue region of the electromagnetic spectrum, and the addition of small amounts of Cs brings ambient and structural stability to the perovskite.[48] The precursors, CsBr, CsCl, MABr, MACl, $PbBr_2$, and $PbCl_2$ were

L. Martínez-Sarti, Dr. F. Palazon, Dr. M. Sessolo, Prof. H. J. Bolink
Instituto de Ciencia Molecular
Universidad de Valencia
C/Catedrático José Beltrán 2, 46980 Paterna, Spain
E-mail: michele.sessolo@uv.es

The ORCID identification number(s) for the author(s) of this article can be found under https://doi.org/10.1002/adom.201901494.

DOI: 10.1002/adom.201901494

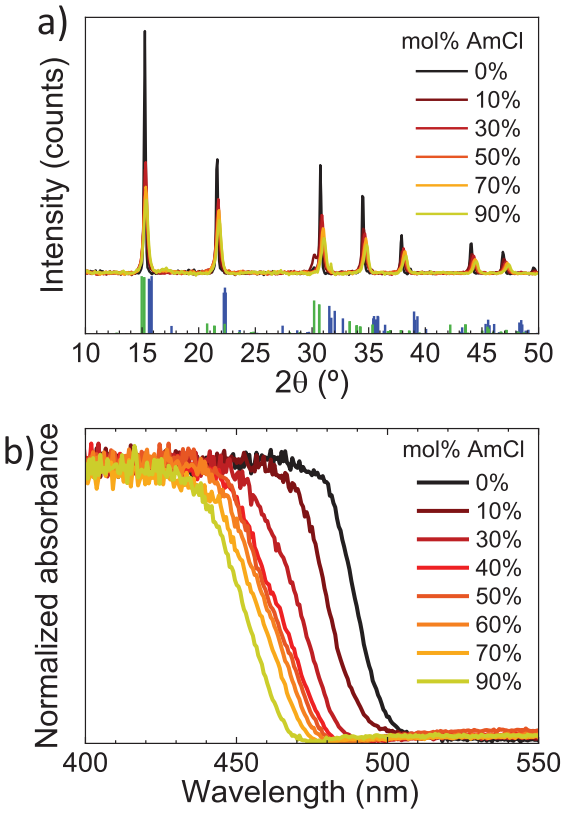

Figure 1. a) XRD patterns for $MA_{0.8}Cs_{0.2}Pb(Br_{0.6}Cl_{0.4})_3$ powders with increasing molar concentration of AmCl and reference bulk pattern (bottom) for $MAPbCl_3$ (blue, ICSD collection code 241415) and $MAPbBr_3$ (green, ICSD collection code 158306). b) Absorption spectra for the same series of materials.

mixed accordingly to the targeted compound's stoichiometry $MA_{0.8}Cs_{0.2}Pb(Br_{0.6}Cl_{0.4})_3$ inside a nitrogen-filled glove box and introduced in a 10 mL zirconia ball-mill jar together with zirconia beads. Afterward, ball-milling was performed at a frequency of 30 Hz for 2 h (see the Experimental Section for details).

The as-prepared materials, obtained in powder form, were analyzed using X-ray diffraction to determine their structure and by optical spectroscopy to determine their optical absorption and luminescence spectral features. The X-ray diffraction (XRD) analysis (**Figure 1**a, black line, 0%) shows intense reflections centered between the reference peaks of pure-bromide $MAPbBr_3$ (ICSD 158306) and pure-chloride $MAPbCl_3$ (ICSD 241415) perovskites, suggesting the presence of a single mixed-halide phase (the presence of 20% Cs^+ also shifts the XRD signal with respect to pure-methylammonium reference patterns, although this shift is less significant). Hence, the structural analysis confirms the formation of the desired compound. Its optical absorption was measured by placing the powder in a quartz Petri dish into an integrating sphere (Figure 1b, black line, 0%). The material presents a steep absorption onset at about 500 nm (corresponding to a bandgap energy, E_g, of ≈2.5 eV), in agreement with previous reports on similar compositions.[49] We were not able to detect any photoluminescence, even when the sample was directly irradiated by a UV (375 nm, 100 mW) continuous wave (CW) laser. This is not surprising, as nonpassivated, bulk, wide bandgap semiconductors are prone to suffer from nonradiative charge recombination due to a large density of trap states at the surface or grain boundaries.[50] With the aim to reduce the trap states responsible for nonradiative charge recombination, we added amantadine hydrochloride (or 1-adamantanamine hydrochloride, herein after referred to as AmCl) to the precursors of the mechanochemical synthesis. We chose this particular compound in view of its steric hindrance, which would not favor the formation of layered perovskite compounds. Similar molecules have been employed previously in the synthesis of perovskites,[51] either to passivate the material[52,53] or for device encapsulation.[48] Here the additive AmCl was introduced in the synthesis in excess with respect to the perovskite precursors, varying its molar ratio (with respect to lead) from 0 to 90 mol%. Importantly, for this specific set of precursors, their solubility in common polar organic solvents is not sufficient to explore the range of compositions allowed by mechanochemical synthesis. It is worth to note that the use of the chloride salt AmCl inevitably results in the incorporation of excess chloride into the material. Indeed, the optical absorption onset shifts to shorter wavelengths (i.e., the bandgap is widened) with increasing amount of AmCl (Figure 1b). At the same time, the XRD analysis shows a very similar pattern for the whole series, independently on the concentration of AmCl (Figure 1a). This means that the addition of AmCl does not lead to the formation or segregation of different phases but maintains a homogeneous single (mixed-halide) perovskite phase. This can be a consequence of the higher reactivity of MAX and CsX toward PbX_2 (where X stands for Cl or Br), which are stoichiometrically added in order to obtain the perovskite $MA_{0.8}Cs_{0.2}Pb(Br_{0.6}Cl_{0.4})_3$, precluding the formation of any compound between AmCl and the other reagents. Beside a small shift to higher angle, caused by the increased incorporation of the smaller chloride anion, when more AmCl is used the intensity of the peaks decreases and their full width at half maximum increases (see also Figure S1, Supporting Information for details). These observations might indicate the formation of smaller crystal domains or in general a reduced crystallinity. From electron microscopy analysis (Figure S2, Supporting Information), however, we could not identify any clear trend of the material crystallinity as a function of the additive content. Most likely, AmCl is still present in the synthesis product but it is amorphous and/or distributed at the grain boundaries. While the XRD analysis confirms that AmCl is not incorporated within the perovskite structure, additional experiments show that the additive can indeed react with Pb(II). When only AmCl and $PbCl_2$ are ball-milled in a 2:1 molar ratio, the XRD of the resulting powders does not present any of the $PbCl_2$ characteristic diffraction peaks, while new signals centered at 2θ = 10.3°, 15.4°, 17.1° appear (Figure S3, Supporting Information). No reference XRD pattern was found for this new material, but most likely it is an octahedral polymeric structure similar to others reported in the literature for lead halide coordination compounds.[54]

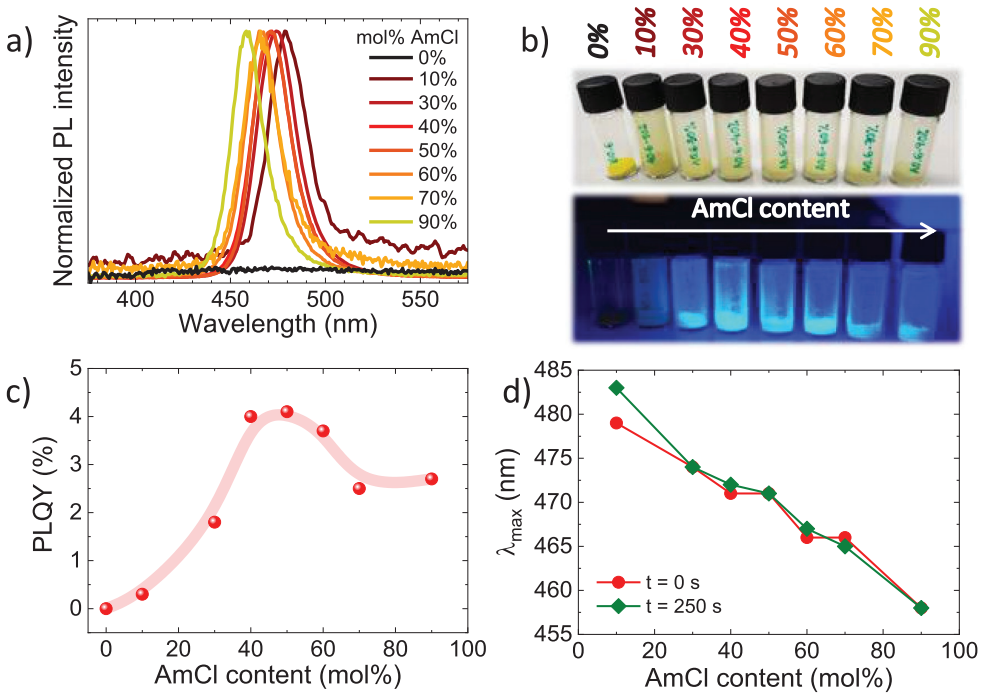

Figure 2. a) Photoluminescence spectra (λ_{exc} = 375 nm) of $MA_{0.8}Cs_{0.2}Pb(Br_{0.6}Cl_{0.4})_3$ powders with varying concentration of AmCl passivating agent, from 0 to 90 mol%. b) Photographs under ambient (above) and UV light (λ = 365 nm, below), c) PLQY (the line is a guide to the eye) and d) first and last measurements of the photostability test of the maximum peaks' wavelength plotted as a function of the added mol% of AmCl.

The fact that AmCl does not participate into the crystal structure of $MA_{0.8}Cs_{0.2}Pb(Br_{0.6}Cl_{0.4})_3$ while it can form complexes with Pb(II), suggests that AmCl can indeed interact with the perovskite to passivate surface traps. As a matter of fact, we were able to detect photoluminescence from the perovskite, when synthesized in the presence of AmCl. As observed from the optical absorption, the increasing amount of chloride causes a blue-shift in the PL signals (**Figure 2**a), with the PL maxima shifting from 478 to 458 nm when the AmCl concentration is increased from 10 to 90 mol%, respectively (an increase in the bandgap of about 0.1 eV). Thanks to the presence of AmCl, the powders show luminescence even when illuminated with a low-intensity UV lamp (Figure 2b). The AmCl additive is thus capable to passivate the $MA_{0.8}Cs_{0.2}Pb(Br_{0.6}Cl_{0.4})_3$ bulk material, as the PLQY increased from 0 to 4% for AmCl concentration of 40–50 mol% (Figure 2c). It is worth to note that the PLQY was measured in an integrating sphere using a Xe lamp coupled to a monochromator as the excitation source, resulting in a very low photogenerated carrier concentration. This implies that the density of trap states is substantially reduced in the presence of AmCl. The origin of the enhanced optical properties in the presence of AmCl is not completely clear, but we exclude an effect of the chloride anion as its incorporation via other ammonium cations does not lead to any appreciable increase in photoluminescence (Figure S4, Supporting information). For AmCl concentrations >50 mol%, the PLQY was found to slightly decrease. The PLQY reduction is not yet fully rationalized, but can be ascribed to a diminished crystallinity (as revealed by the XRD analysis) and to the wider bandgap of the material, i.e., not-quenching shallow traps become deep traps favoring nonradiative recombination. $MA_{0.8}Cs_{0.2}Pb(Br_{0.6}Cl_{0.4})_3$ powders containing 50 mol% AmCl were further analyzed by X-ray photoelectron spectroscopy (XPS) in order to investigate the elemental composition (Figure S5, Supporting Information). The elemental analysis was found to be in good agreement with the compound stoichiometry (Cs = 0.3, Pb = 1, Br = 1.8, and Cl = 1.5), taking into account the amount of AmCl used.

As mentioned before, mixed halide perovskites can undergo halide segregation under illumination.[44,45,55] In this regard, the material photostability was studied by monitoring the PL spectra as a function of time, under continuous irradiation. The position of the PL maxima as a function of the AmCl concentration at time 0 and after 250 s is reported in Figure 2d (see Figure S6, Supporting Information, for further details). We observed a small shift in the maximum PL intensity only at low AmCl concentration (10 mol%), while for the rest of the samples no change in the optical properties (sign of halide segregation) was detected.

We further studied the effect of the composition on the optical properties of the perovskite by exchanging the A-site cation and the X-site anion. The amount of Cs^+ was varied in the mechanochemical synthesis of $MA_{1-y}Cs_yPb(Br_{0.6}Cl_{0.4})_3$ from

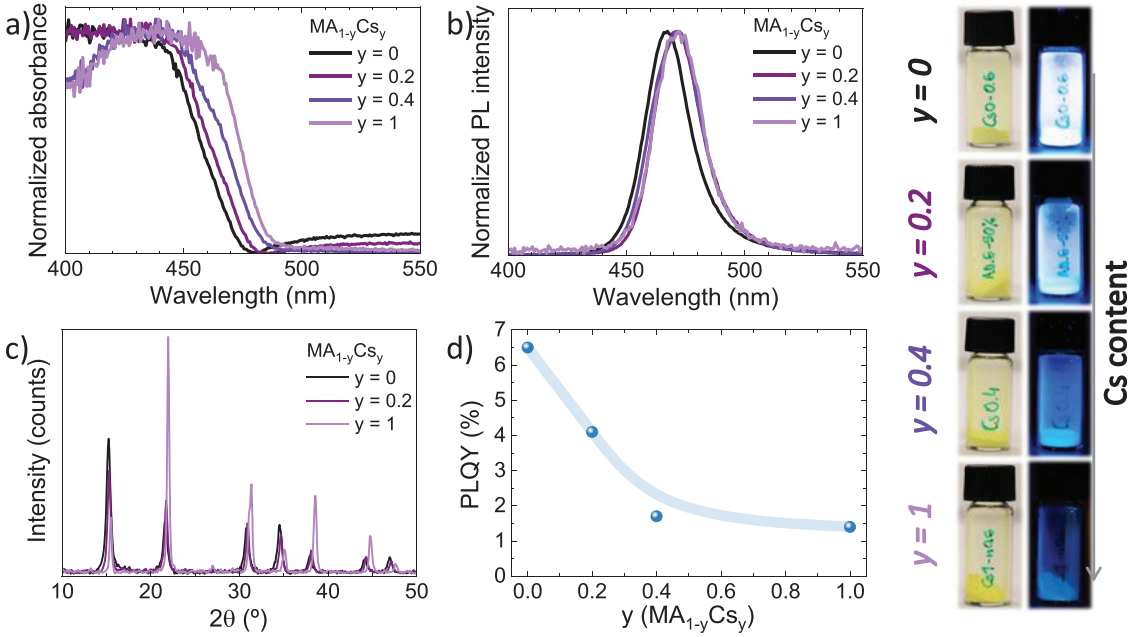

Figure 3. a) Absorption and b) photoluminescence spectra for the mechanochemically synthesized $MA_{1-y}Cs_yPb(Br_{0.6}Cl_{0.4})_3$ samples, with $y = 0$, 0.2, 0.4, and 1. c) XRD patterns for the same compound series and d) PLQY as a function of the Cs^+ content (the line is a guide to the eye). On the right, pictures of the samples with increasing Cs/MA ratio under ambient (left) and UV (right) light.

$y = 0$ (pure MA) to 0.2, 0.4, and 1 (pure Cs^+), maintaining a 50 mol% AmCl concentration. A small deviation in the bandgap of the material was observed upon exchanging MA with Cs^+, as evidenced by the optical absorption spectra (**Figure 3**a), with the hybrid perovskites having larger bandgap as compared to the inorganic one. Also the PL spectra showed a small shift from 467 nm to 472 nm when y was varied from 0 to 1 (Figure 3b). The structural characterization (Figure 3c) showed again a high degree of conversion and crystallinity for the entire series of compounds, with an expected shift to larger angles upon substitution with the smaller cesium cation. The different intensity of the main diffraction peaks between hybrid and fully inorganic perovskites ($y = 1$) agrees with the slightly different orientation of the unit cell.[56] The concentration of Cs^+ in this perovskite series was confirmed by XPS (Figure S7 and Table S1, Supporting Information). Interestingly, we found the PLQY to scale inversely with the amount of Cs^+ used in the synthesis of the perovskite $MA_{1-y}Cs_yPb(Br_{0.6}Cl_{0.4})_3$, with the pure MA materials exhibiting blue emission with 7% PLQY (Figure 3d). As the cesium content increases, the PLQY progressively decreases to ≈1% for the pure inorganic compound ($y = 1$). This behavior has been previously attributed to the large dipole moment (2.3 D) and rotational freedom of the MA cation, which would respond to the formation of trapped charges reducing non-radiative recombination.[57,58]

The mechanochemical synthesis is ideal for the preparation of complex perovskite compositions, hence we also studied the effect of the halide exchange on the optical characteristics of the perovskite series, in particular the relationship between the bandgap and the PLQY. The synthesis was carried out modifying the content of all precursors, adjusting the ratio of both MABr/MACl and $PbBr_2/PbCl_2$, and keeping constant the concentration of AmCl at 50 mol%. The bromide content was increased from 0 to 1 in the preparation of 6 different perovskites of the type $MAPb(Br_nCl_{1-n})_3$. **Figure 4**a,c shows the optical absorption and PL spectra, respectively, for the entire sample series. The samples exhibited absorption onsets red-shifting from 410 nm ($n = 0$, pure chloride compound) to 512 nm ($n = 1$, pure bromide perovskite) as the bromide content is increased. The corresponding PL maxima follow the same trend, decreasing in energy from 405 nm (violet) to 514 nm (green) for pure chloride and bromide materials, respectively. The CIE coordinates calculated from the PL spectra of the different samples are reported in Figure S8 (Supporting Information). XRD analysis (Figure 4d) confirmed the formation of highly crystalline pure chloride and bromide perovskites, as well as for the mixed halide species. The XRD patterns (Figure 4d) show a displacement of the signals corresponding to the same planes to smaller angles as the Br/Cl ratio increases (a more detailed comparison of the diffractogram can be found in Figure S9, Supporting Information). As the bandgap narrows, the corresponding PLQY rises from ≈1% (for $0 \le n \le 0.4$) to 7% ($n = 0.6$), and up to 15% and 29% for the bromide-rich, green-emitting $MAPb(Br_nCl_{1-n})_3$ ($n = 0.8$ and 1, respectively). We also performed the mechanochemical synthesis of the same series of materials, but substituting 20% of MA with Cs^+. The structural and optical characterization (Figure S10, Supporting Information), are

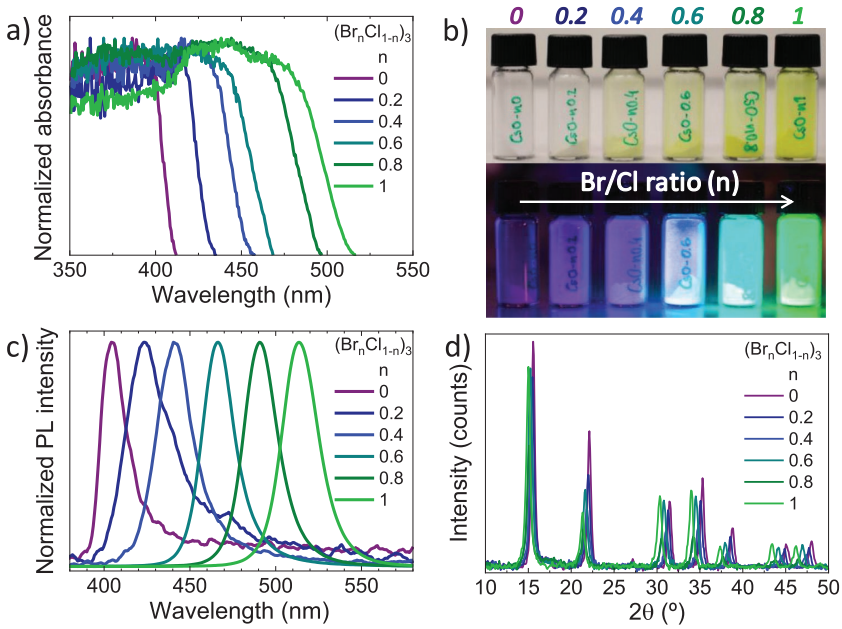

Figure 4. a) Optical absorption spectra of the $MAPb(Br_nCl_{1-n})_3$ samples for $n = 0$, 0.2, 0.4, 0.6, 0.8, and 1. b) Pictures of the samples with varying Br/Cl content under ambient (top) and UV light ($\lambda = 365$ nm, bottom). c) PL spectra and d) XRD analysis of all samples.

very similar to those presented in Figure 4, and we observed slightly lower PLQY (1% and 25% for the pure chloride and pure bromide compounds, respectively), which is consistent with the trend observed for materials with higher cesium content (Figure 3). Although we cannot exclude differences in the formation chemistry of the materials, the large increase in PLQY, observed when decreasing the bandgap from blue (7%) to green-emitting (29%) perovskites, is likely related to the energy and distribution of trap states with respect to the electronic bands of the semiconductors. Quenching, deep traps in blue perovskites become shallower or fall within the electronic bands when the bandgap is narrower, as discussed previously.

In summary, we have prepared a series of highly luminescent lead halide perovskite powders leveraging the benefits of mechanochemical synthesis. Mechanochemical synthesis is a simple, solvent-free method, useful to prepare perovskites with virtually any composition. Importantly, mechanochemical synthesis is a valuable tool to investigate complex materials and the direct effect of additives on their properties, without the limitation in terms of solubility and crystallization kinetics which are unavoidable in solution-processed perovskites. We have synthesized compounds whose emission color can be tuned from the violet to the green, and with enhanced photoluminescence efficiency thanks to the use of the additive AmCl. The amount of AmCl was varied and a 50 mol% loading was found to lead to the highest photoluminescence quantum yield for these specific compounds and with the experimental conditions used. The use of the passivating molecule leads to a decrease of the nonradiative recombination pathways without modifying the structure of the synthesized materials, resulting in an increase of the quantum yield from 0 to 7% in the blue, and up to 29% for green-emitting bulk perovskites.

Experimental Section

Mechanochemical Synthesis: $MA_{0.8}Cs_{0.2}Pb(Br_{0.6}Cl_{0.4})_3$ was prepared by ball-milling; 0.48 mol of CH_3NH_3Br (MABr), 0.32 mol of CH_3NH_3Cl (MACl), 0.12 mol of CsBr, and 0.08 mol of CsCl were mixed together with 0.6 mol of $PbBr_2$ and 0.4 mol of $PbCl_2$ inside a nitrogen-filled glove box. The powder mixture was then introduced in a 10 mL zirconia ball-mill jar with zirconia beads. Afterward, ball-milling was performed at a frequency of 30 Hz for 2 h. The resulting yellowish powder was then studied as obtained in ambient conditions and at room temperature. The passivated samples were obtained adding increasing amounts (from 0 to 90 mol%) of AmCl to the mixture before ball-milling. For the rest of the $MA_yCs_{1-y}Pb(Br_nCl_{1-n})_3$ samples, MAX/CsX and Br^-/Cl^- were adjusted accordingly. Cs molar ratio was varied from 0 (pure $MAPb(Br_nCl_{1-n})_3$) to 1 (pure $CsPb(Br_nCl_{1-n})_3$). Br molar ratio was varied from 0 (pure $MA_yCs_{1-y}PbCl_3$) to 1 (pure $MA_yCs_{1-y}PbBr_3$). See Tables S2–S4 (Supporting Information) for the precursor quantities of the different samples.

Characterization: The PL spectra were collected using a 375 nm laser excitation source and a spectrometer (Hamamatsu C9920-02 with a Hamamatsu PMA-11 optical detector). PLQY values were obtained using a Xe lamp coupled to a monochromator as the excitation source and an integrated sphere coupled to a spectrometer (Hamamatsu C9920-02 with a Hamamatsu PMA-11 optical detector). The instrumental error is ≈1%. UV–visible absorption spectra of the films were collected in an integrated sphere using a fiber-optics based Avantes Avaspec2048 spectrophotometer. X-ray diffraction was measured with a Panalytical Empyrean diffractometer equipped with a copper anode (CuKα) operated at 45 kV and 30 mA and a Pixel 1D detector in scanning line mode. Single scans were acquired in the $2\theta = 5°$–$50°$ range in

Bragg–Brentano geometry in air. Data analysis was performed with HighScore Plus software.

Supporting Information

Supporting Information is available from the Wiley Online Library or from the author.

Acknowledgements

The research leading to these results received funding from the European Union Programme for Research and Innovation Horizon 2020 (2014–2020) under the Marie Skłodowska-Curie Grant Agreement PerovSAMs No. 747599 and the Spanish Ministry of Economy and Competitiveness (MINECO) via the Unidad de Excelencia María de Maeztu MDM-2015-0538, MAT2017-88821-R, PCIN-2015-255, PCIN-2017-014, and the Generalitat Valenciana (Prometeo/2016/135). M.S. acknowledges the MINECO for his RyC contract.

Conflict of Interest

The authors declare no conflict of interest.

Keywords

blue-emitting perovskites, mechanochemical synthesis, passivation, perovskites, photoluminescence

Received: September 4, 2019
Revised: October 22, 2019
Published online:

[1] L. N. Quan, B. P. Rand, R. H. Friend, S. G. Mhaisalkar, T.-W. Lee, E. H. Sargent, *Chem. Rev.* **2019**, *119*, 7444.
[2] A. K. Jena, A. Kulkarni, T. Miyasaka, *Chem. Rev.* **2019**, *119*, 3036.
[3] T. Leijtens, K. A. Bush, R. Prasanna, M. D. McGehee, *Nat. Energy* **2018**, *3*, 828.
[4] F. P. García de Arquer, A. Armin, P. Meredith, E. H. Sargent, *Nat. Rev. Mater.* **2017**, *2*, 16100.
[5] H. Wei, J. Huang, *Nat. Commun.* **2019**, *10*, 1066.
[6] Gurudayal, J. Ager, N. Mathews, in *Halide Perovskites* (Eds: T.-C. Sum, N. Mathews), Wiley-VCH Verlag GmbH & Co. KGaA, Weinheim, Germany **2018**, pp. 273–292.
[7] X. Zhao, H. Xu, Z. Wang, Y. Lin, Y. Liu, *InfoMat* **2019**, *1*, 183.
[8] R. A. John, N. Yantara, Y. F. Ng, G. Narasimman, E. Mosconi, D. Meggiolaro, M. R. Kulkarni, P. K. Gopalakrishnan, C. A. Nguyen, F. De Angelis, S. G. Mhaisalkar, A. Basu, N. Mathews, *Adv. Mater.* **2018**, *30*, 1805454.
[9] W. Li, Z. Wang, F. Deschler, S. Gao, R. H. Friend, A. K. Cheetham, *Nat. Rev. Mater.* **2017**, *2*, 16099.
[10] J. Huang, Y. Yuan, Y. Shao, Y. Yan, *Nat. Rev. Mater.* **2017**, *2*, 17042.
[11] J. M. Ball, A. Petrozza, *Nat. Energy* **2016**, *1*, 16149.
[12] B. R. Sutherland, E. H. Sargent, *Nat. Photonics* **2016**, *10*, 295.
[13] T. M. Brenner, D. A. Egger, L. Kronik, G. Hodes, D. Cahen, *Nat. Rev. Mater.* **2016**, *1*, 15007.
[14] R. Swartwout, M. T. Hoerantner, V. Bulović, *Energy Environ. Mater.* **2019**, *2*, 119.
[15] Z. Li, T. R. Klein, D. H. Kim, M. Yang, J. J. Berry, M. F. A. M. van Hest, K. Zhu, *Nat. Rev. Mater.* **2018**, *3*, 18017.
[16] W. Zhang, M. Saliba, D. T. Moore, S. K. Pathak, M. T. Hörantner, T. Stergiopoulos, S. D. Stranks, G. E. Eperon, J. A. Alexander-Webber, A. Abate, A. Sadhanala, S. Yao, Y. Chen, R. H. Friend, L. A. Estroff, U. Wiesner, H. J. Snaith, *Nat. Commun.* **2015**, *6*, 6142.
[17] N. K. Noel, S. N. Habisreutinger, B. Wenger, M. T. Klug, M. T. Hörantner, M. B. Johnston, R. J. Nicholas, D. T. Moore, H. J. Snaith, *Energy Environ. Sci.* **2017**, *10*, 145.
[18] H. Zhang, M. K. Nazeeruddin, W. C. H. Choy, *Adv. Mater.* **2019**, *31*, 1805702.
[19] P. Wang, Y. Wu, B. Cai, Q. Ma, X. Zheng, W.-H. Zhang, *Adv. Funct. Mater.* **2019**, *29*, 1807661.
[20] M. Jung, S.-G. Ji, G. Kim, S. Il Seok, *Chem. Soc. Rev.* **2019**, *48*, 2011.
[21] Y. Zhang, S. G. Kim, D. K. Lee, N. G. Park, *ChemSusChem* **2018**, *11*, 1813.
[22] D. Prochowicz, P. Yadav, M. Saliba, M. Saski, S. M. Zakeeruddin, J. Lewiński, M. Grätzel, *ACS Appl. Mater. Interfaces* **2017**, *9*, 28418.
[23] Y. El Ajjouri, F. Palazon, M. Sessolo, H. J. Bolink, *Chem. Mater.* **2018**, *30*, 7423.
[24] L. Protesescu, S. Yakunin, O. Nazarenko, D. N. Dirin, M. V. Kovalenko, *ACS Appl. Nano Mater.* **2018**, *1*, 1300.
[25] P. Sadhukhan, S. Kundu, A. Roy, A. Ray, P. Maji, H. Dutta, S. K. Pradhan, S. Das, *Cryst. Growth Des.* **2018**, *18*, 3428.
[26] Z. Hong, D. Tan, R. A. John, Y. K. E. Tay, Y. K. T. Ho, X. Zhao, T. C. Sum, N. Mathews, F. García, H. Sen Soo, *iScience* **2019**, *16*, 312.
[27] S. Yun, A. Kirakosyan, S. G. Yoon, J. Choi, *ACS Sustainable Chem. Eng.* **2018**, *6*, 3733.
[28] F. Palazon, Y. El Ajjouri, H. J. Bolink, *Adv. Energy Mater.* **2019**, https://doi.org/10.1002/aenm.201902499.
[29] N. C. D. Nath, M. Gavindasamy, J. J. Lee, *Nanosci. Nanotechnol. Lett.* **2018**, *10*, 1025.
[30] N. Leupold, K. Schötz, S. Cacovich, I. Bauer, M. Schultz, M. Daubinger, L. Kaiser, A. Rebai, J. Rousset, A. Köhler, P. Schulz, R. Moos, F. Panzer, *ACS Appl. Mater. Interfaces* **2019**, *11*, 30259.
[31] P. Fan, D. Gu, G. X. Liang, J. T. Luo, J. L. Chen, Z. H. Zheng, D. P. Zhang, *Sci. Rep.* **2016**, *6*, 1.
[32] G. Longo, L. Gil-Escrig, M. J. Degen, M. Sessolo, H. J. Bolink, *Chem. Commun.* **2015**, *51*, 7376.
[33] J. Ávila, C. Momblona, P. P. Boix, M. Sessolo, H. J. Bolink, *Joule* **2017**, *1*, 431.
[34] M. J. Crane, D. M. Kroupa, J. Y. Roh, R. T. Anderson, M. D. Smith, D. R. Gamelin, *ACS Appl. Energy Mater.* **2019**, *2*, 4560.
[35] F. Panzer, D. Hanft, T. P. Gujar, F. J. Kahle, M. Thelakkat, A. Köhler, R. Moos, *Materials* **2016**, *9*, 277.
[36] J. H. Noh, S. H. Im, J. H. Heo, T. N. Mandal, S. Il Seok, *Nano Lett.* **2013**, *13*, 1764.
[37] I. Levchuk, A. Osvet, X. Tang, M. Brandl, J. D. Perea, F. Hoegl, G. J. Matt, R. Hock, M. Batentschuk, C. J. Brabec, *Nano Lett.* **2017**, *17*, 2765.
[38] Q. A. Akkerman, V. D'Innocenzo, S. Accornero, A. Scarpellini, A. Petrozza, M. Prato, L. Manna, *J. Am. Chem. Soc.* **2015**, *137*, 10276.
[39] A. Sadhanala, S. Ahmad, B. Zhao, N. Giesbrecht, P. M. Pearce, F. Deschler, R. L. Z. Hoye, K. C. Gödel, T. Bein, P. Docampo, S. E. Dutton, M. F. L. De Volder, R. H. Friend, *Nano Lett.* **2015**, *15*, 6095.
[40] J. Xing, Y. Zhao, M. Askerka, L. N. Quan, X. Gong, W. Zhao, J. Zhao, H. Tan, G. Long, L. Gao, Z. Yang, O. Voznyy, J. Tang, Z.-H. Lu, Q. Xiong, E. H. Sargent, *Nat. Commun.* **2018**, *9*, 3541.
[41] Y. Liu, J. Cui, K. Du, H. Tian, Z. He, Q. Zhou, Z. Yang, Y. Deng, D. Chen, X. Zuo, Y. Ren, L. Wang, H. Zhu, B. Zhao, D. Di, J. Wang, R. H. Friend, Y. Jin, *Nat. Photonics* **2019**, *13*, 760.

[42] S. D. Stranks, V. M. Burlakov, T. Leijtens, J. M. Ball, A. Goriely, H. J. Snaith, *Phys. Rev. Appl.* **2014**, *2*, 034007.
[43] M. C. Brennan, S. Draguta, P. V. Kamat, M. Kuno, *ACS Energy Lett.* **2018**, *3*, 204.
[44] S. J. Yoon, S. Draguta, J. S. Manser, O. Sharia, W. F. Schneider, M. Kuno, P. V. Kamat, *ACS Energy Lett.* **2016**, *1*, 290.
[45] N. K. Noel, A. Abate, S. D. Stranks, E. S. Parrott, V. M. Burlakov, A. Goriely, H. J. Snaith, *ACS Nano* **2014**, *8*, 9815.
[46] D. S. Lee, J. S. Yun, J. Kim, A. M. Soufiani, S. Chen, Y. Cho, X. Deng, J. Seidel, S. Lim, S. Huang, A. W. Y. Ho-Baillie, *ACS Energy Lett.* **2018**, *3*, 647.
[47] X. Li, C. C. Chen, M. Cai, X. Hua, F. Xie, X. Liu, J. Hua, Y. T. Long, H. Tian, L. Han, *Adv. Energy Mater.* **2018**, *8*, 1800715.
[48] J. W. Lee, D. H. Kim, H. S. Kim, S. W. Seo, S. M. Cho, N. G. Park, *Adv. Energy Mater.* **2015**, *5*, 1501310.
[49] D. M. Jang, K. Park, D. H. Kim, J. Park, F. Shojaei, H. S. Kang, J. P. Ahn, J. W. Lee, J. K. Song, *Nano Lett.* **2015**, *15*, 5191.
[50] N. K. Kumawat, X.-K. Liu, D. Kabra, F. Gao, *Nanoscale* **2019**, *11*, 2109.
[51] P. Audebert, G. Clavier, V. Alain-Rizzo, E. Deleporte, S. Zhang, J.-S. Lauret, G. Lanty, C. Boissière, *Chem. Mater.* **2009**, *21*, 210.
[52] Q.-L. Li, W.-X. Lu, N. Wan, S.-N. Ding, *Chem. Commun.* **2016**, *52*, 12342.
[53] M. M. Tavakoli, W. Tress, J. V Milić, D. Kubicki, L. Emsley, M. Grätzel, *Energy Environ. Sci.* **2018**, *11*, 3310.
[54] Y. Cui, J. Ren, G. Chen, W. Yu, Y. Qian, *Acta Crystallogr., Sect. C: Cryst. Struct. Commun.* **2000**, *56*, e552.
[55] E. T. Hoke, D. J. Slotcavage, E. R. Dohner, A. R. Bowring, H. I. Karunadasa, M. D. McGehee, *Chem. Sci.* **2015**, *6*, 613.
[56] M. R. Linaburg, E. T. McClure, J. D. Majher, P. M. Woodward, *Chem. Mater.* **2017**, *29*, 3507.
[57] G. Nan, X. Zhang, M. Abdi-Jalebi, Z. Andaji-Garmaroudi, S. D. Stranks, G. Lu, D. Beljonne, *Adv. Energy Mater.* **2018**, *8*, 1702754.
[58] H. Tan, F. Che, M. Wei, Y. Zhao, M. I. Saidaminov, P. Todorović, D. Broberg, G. Walters, F. Tan, T. Zhuang, B. Sun, Z. Liang, H. Yuan, E. Fron, J. Kim, Z. Yang, O. Voznyy, M. Asta, E. H. Sargent, *Nat. Commun.* **2018**, *9*, 3100.

Supporting Information

Dry mechanochemical synthesis of highly luminescent, blue and green hybrid perovskite solids

Laura Martínez-Sarti, Francisco Palazon, Michele Sessolo* and Henk J. Bolink.

L. Martínez-Sarti, Dr. F. Palazon, Dr. M. Sessolo, Prof. H. J. Bolink
Instituto de Ciencia Molecular, Universidad de Valencia
C/ Catedrático José Beltrán, 2, 46980 Paterna, Spain
E-mail: michele.sessolo@uv.es

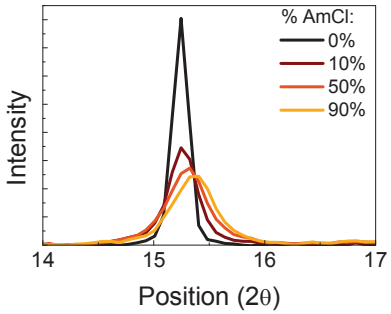

Figure S1. Comparison of the width and intensity of one of the peaks of the XRD patterns of samples with different AmCl quantities added.

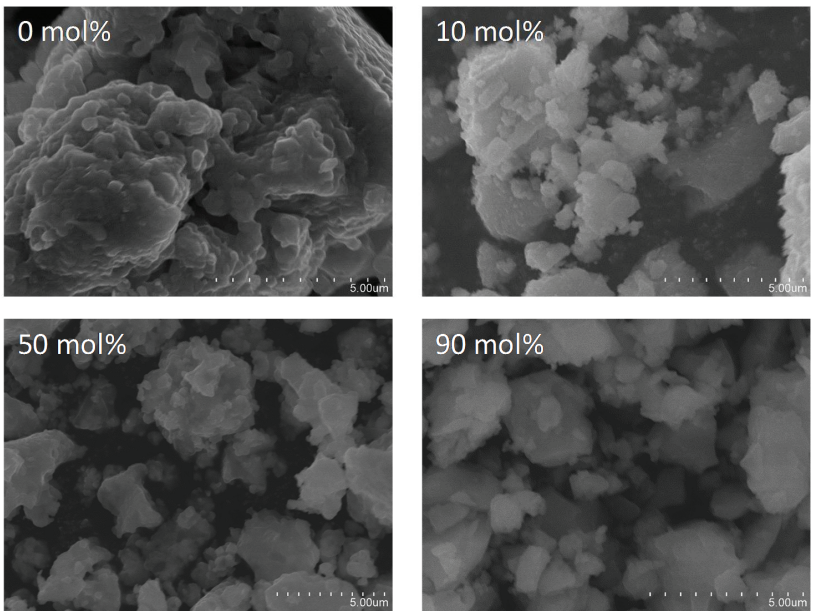

Figure S2. SEM analysis of $MA_{0.8}Cs_{0.2}Pb(Br_{0.6}Cl_{0.4})_3$ powders with increasing AmCl content.

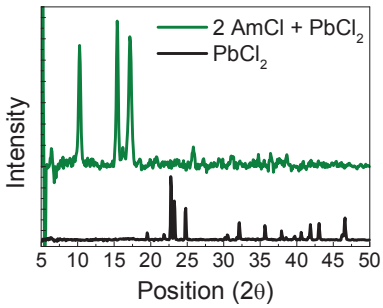

Figure S3. XRD patterns for resulting powders from the AmCl and $PbCl_2$ mixture in a 2:1 ratio and reference bulk pattern of $PbCl_2$.

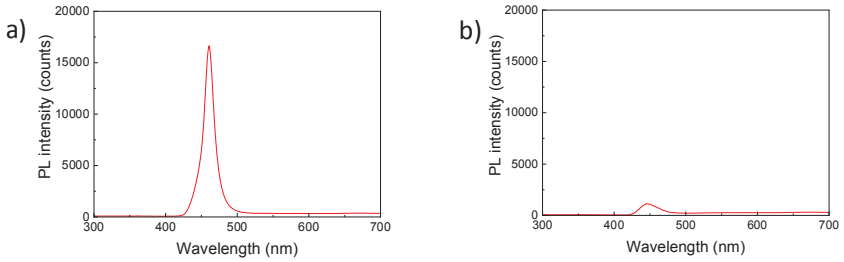

Figure S4. Photoluminescence spectra of $MA_{0.8}Cs_{0.2}Pb(Br_{0.6}Cl_{0.4})_3$ in the presence of 50 mol% a) AmCl and b) 4-fluoro-phenethylammonium chloride.

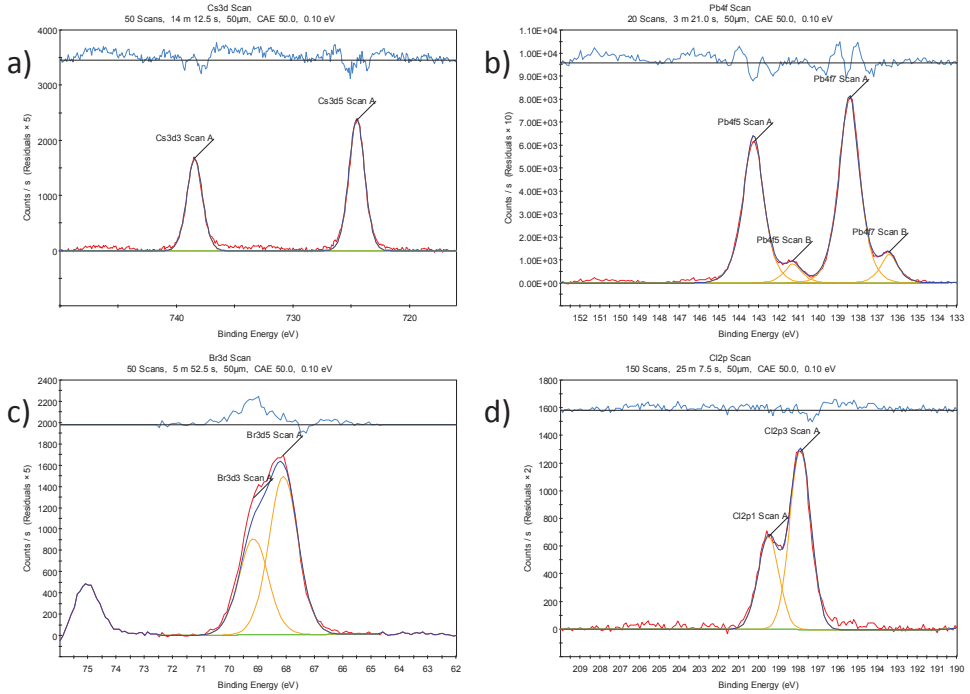

Figure S5. XPS spectra of the a) Cs 3d, b) Pb 4f, c) Br 3d and d) Cl 2p regions for the $MA_{0.8}Cs_{0.2}Pb(Br_{0.6}Cl_{0.4})_3$ powders containing 50 mol% AmCl. The calculated atomic % of the corresponding elements are: Cs = 3.8%, Pb = 12.0%, Br = 21.0%, Cl = 17.4%.

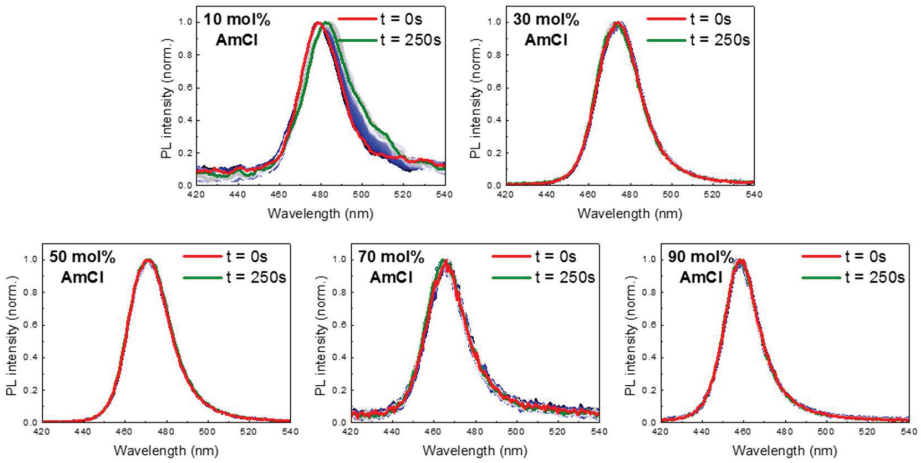

Figure S6. PL spectra of the different samples sample measured over time. First scan (t = 0 s) represented with a red colour line was taken immediately after laser excitation. Last scan (t = 250 s) represented with a green colour line. Scans in the middle go from a dark blue colour to a light blue colour, progressively degrading from the first scan to the last scan.

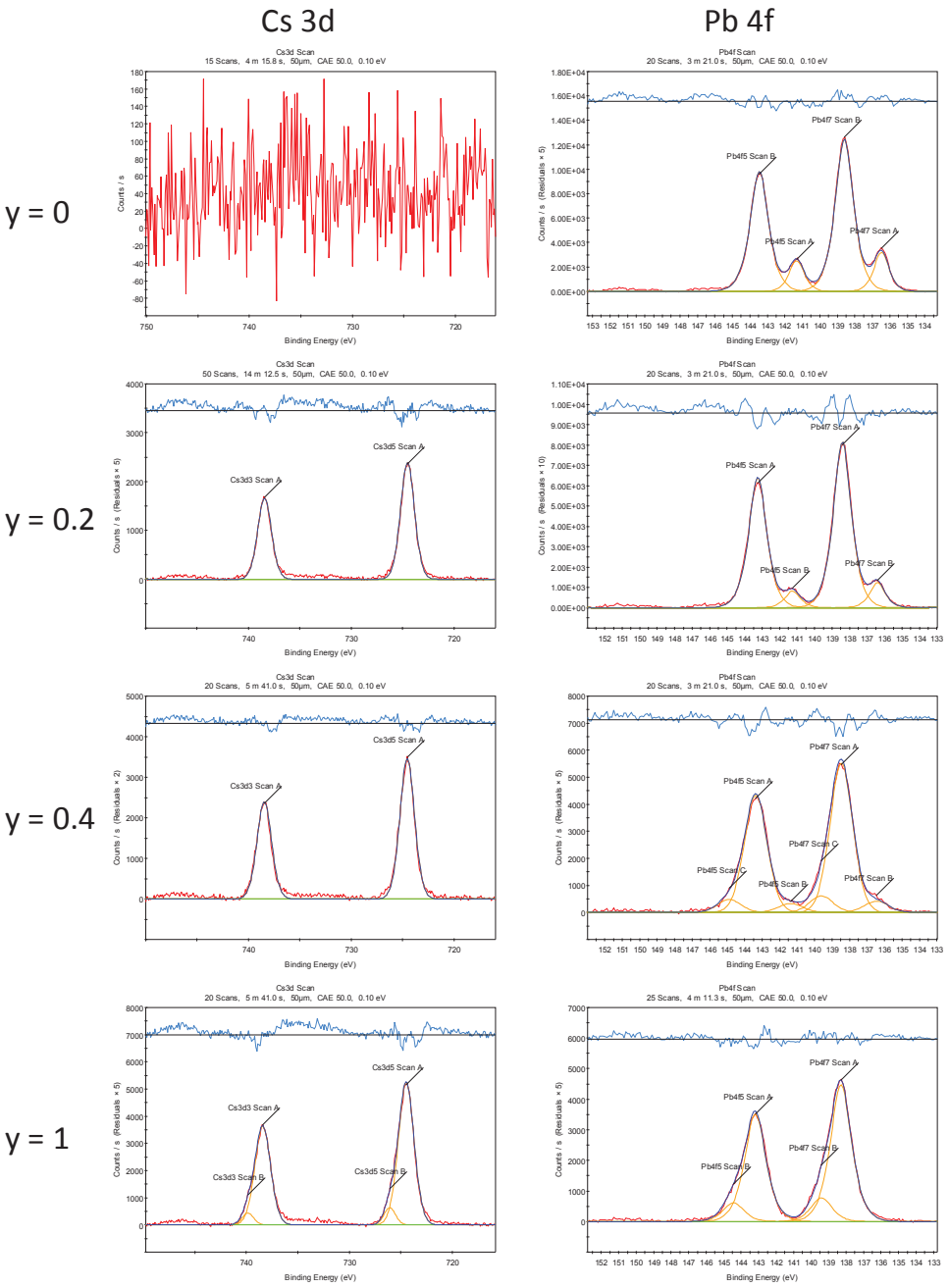

Figure S7. XPS spectra of the Cs 3d and Pb 4f regions for the $MA_{1-y}Cs_yPb(Br_{0.6}Cl_{0.4})_3$ sample series. The corresponding elemental analysis is shown in Table S1.

$(Br_nCl_{1-n})_3$	x	y
n = 0	0.17	0.01
n = 0.2	0.16	0.01
n = 0.4	0.16	0.04
n = 0.6	0.13	0.08
n = 0.8	0.07	0.36
n = 1	0.10	0.73

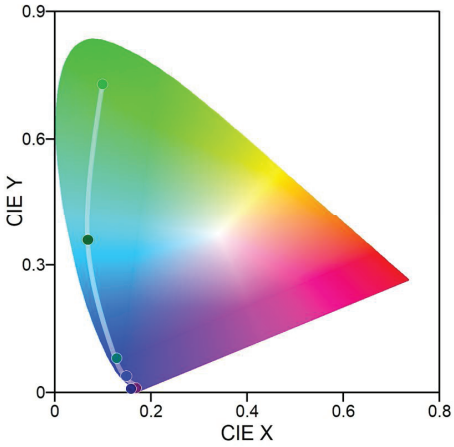

Figure S8. CIE colour coordinates calculated from the photoluminescence spectra of the for the different mixed halides compounds.

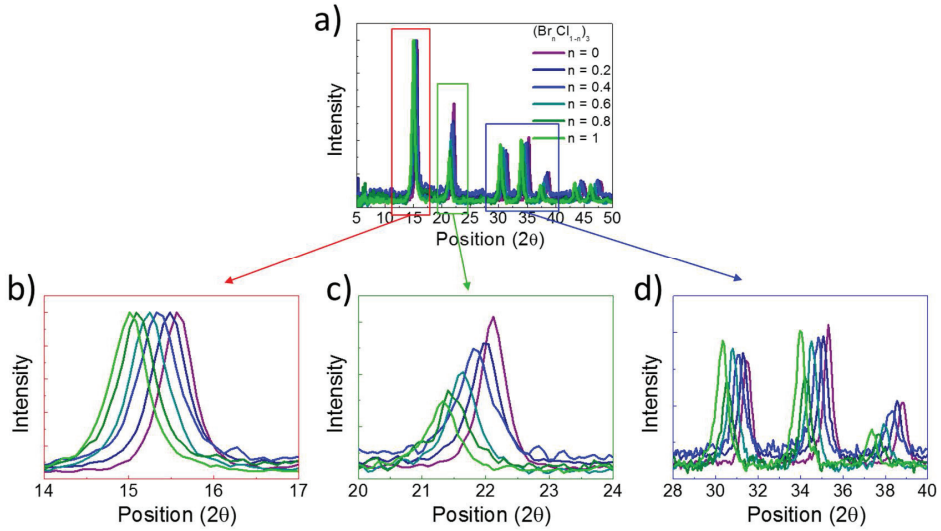

Figure S9. (a) XRD patterns of samples ($MAPb(Br_nCl_{1-n})_3$) n = 0, 0.2, 0.4, 0.6, 0.8 and 1 plotted together for comparison purposes. (b) Closer look for position range going from 2Θ = 14° to 17°, (c) from 2Θ = 20° to 24° and (d) from 2Θ = 28° to 40°.

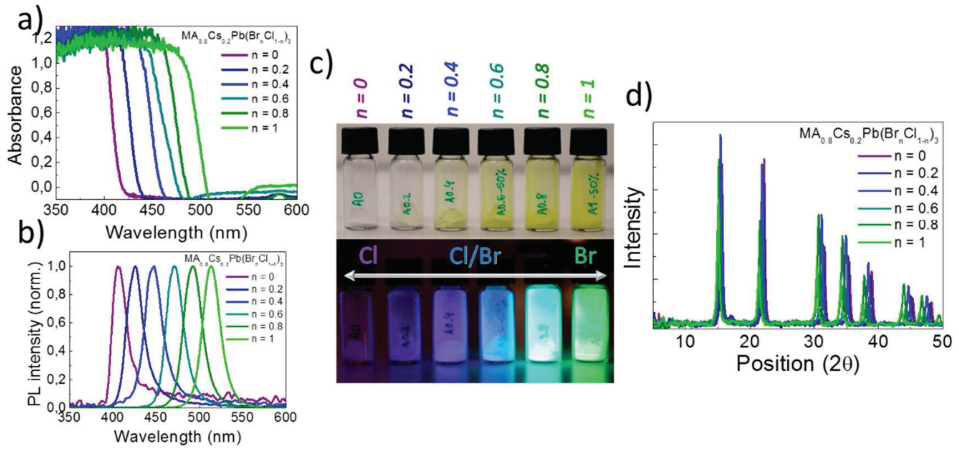

Figure S10. (a) Absorbance and (b) PL characteristics of the $MA_{0.8}Cs_{0.2}Pb(Br_nCl_{1-n})_3$ samples for n = 0, 0.2, 0.4, 0.6, 0.8 and 1. (c) Pictures of the mentioned samples with a varying Br/Cl content under ambient light (top) and UV light (λ = 365 nm) (bottom). (d) XRD analysis of all the samples.

Table S1. XPS elemental analysis of the $MA_{1-y}Cs_yPb(Br_{0.6}Cl_{0.4})_3$ samples.

		Cs 3d	**Pb 4f**
y = 0	*% Atomic*	0	13.1
	Molar ratio	0	1
y = 0.2	*% Atomic*	3.8	12.0
	Molar ratio	0.3	1
y = 0.4	*% Atomic*	7.0	12.2
	Molar ratio	0.6	1
y = 1	*% Atomic*	14.2	11.1
	Molar ratio	1.3	1

Table S2. Precursors quantities for the mechanochemical synthesis of $MA_{1-y}Cs_yPb(Br_{0.6}Cl_{0.4})_3$.

	MABr (mmol)	MACl (mmol)	CsBr (mmol)	CsCl (mmol)	$PbBr_2$ (mmol)	$PbCl_2$ (mmol)	AmCl (mmol)
$MAPb(Br_{0.6}Cl_{0.4})_3$	0.6	0.4	-	-	0.6	0.4	0.5
$MA_{0.8}Cs_{0.2}Pb(Br_{0.6}Cl_{0.4})_3$	0.48	0.32	0.12	0.08	0.6	0.4	0.5
$MA_{0.6}Cs_{0.4}Pb(Br_{0.6}Cl_{0.4})_3$	0.36	0.24	0.24	0.16	0.6	0.4	0.5
$CsPb(Br_{0.6}Cl_{0.4})_3$	-	-	0.6	0.4	0.6	0.4	0.5

Table S3. Precursors quantities for the mechanochemical synthesis of $MAPb(Br_nCl_{1-n})_3$.

	MABr (mmol)	MACl (mmol)	CsBr (mmol)	CsCl (mmol)	$PbBr_2$ (mmol)	$PbCl_2$ (mmol)	AmCl (mmol)
$MAPbCl_3$	-	1	-	-	-	1	0.5
$MAPb(Br_{0.2}Cl_{0.8})_3$	0.2	0.8	-	-	0.2	0.8	0.5
$MAPb(Br_{0.4}Cl_{0.6})_3$	0.4	0.6	-	-	0.4	0.6	0.5
$MAPb(Br_{0.6}Cl_{0.4})_3$	0.6	0.4	-	-	0.6	0.4	0.5
$MAPb(Br_{0.8}Cl_{0.2})_3$	0.8	0.2	-	-	0.8	0.2	0.5
$MAPbBr_3$	1	-	-	-	1	-	0.5

Table S4. Precursors quantities for the mechanochemical synthesis of $MA_{0.8}Cs_{0.2}Pb(Br_nCl_{1-n})_3$.

	MABr (mmol)	MACl (mmol)	CsBr (mmol)	CsCl (mmol)	$PbBr_2$ (mmol)	$PbCl_2$ (mmol)	AmCl (mmol)
$MA_{0.8}Cs_{0.2}PbCl_3$	-	0.8	-	0.2	-	1	0.5
$MA_{0.8}Cs_{0.2}Pb(Br_{0.2}Cl_{0.8})_3$	0.16	0.64	0.04	0.16	0.2	0.8	0.5
$MA_{0.8}Cs_{0.2}Pb(Br_{0.4}Cl_{0.6})_3$	0.32	0.48	0.08	0.12	0.4	0.6	0.5
$MA_{0.8}Cs_{0.2}Pb(Br_{0.6}Cl_{0.4})_3$	0.48	0.32	0.12	0.08	0.6	0.4	0.5
$MA_{0.8}Cs_{0.2}Pb(Br_{0.8}Cl_{0.2})_3$	0.64	0.16	0.16	0.04	0.8	0.2	0.5
$MA_{0.8}Cs_{0.2}PbBr_3$	0.8	-	0.2	-	1	-	0.5

Chapter 6.

General conclusions

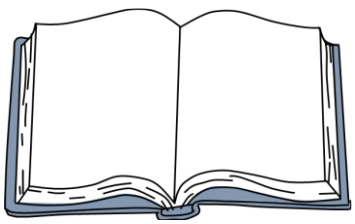

The aim of the thesis was the development of new perovskite materials with high purity, high photoluminescent efficiency and different colours, which is crucial for the development of novel LEDs. In this thesis, efficient, simple and bright materials are developed. Additionally, some of these materials are used in the preparation of efficient light-emitting devices.

In chapter 2, the development of stable and highly photoluminescent red-emitting perovskites is described. The material consisted of hybrid quasi-2D perovskite nanocrystals of the type $(LA)_2(A)_{n-1}Pb_nI_{3n+1}$, where LA is an alkylamine and A is a mixture of MA^+ and Cs^+. The bandgap, and hence the emission wavelength, of these structures could be shifted by varying the chain length of the larger cations employed in the synthesis. Such shift was ascribed to the formation of quasi-2D crystals with different periodicities and different interlayer spacing, which changes the strength of the quantum confinement. Importantly, the addition of butanol in the sample purification led to an improved photoluminescent quantum yield, exceeding 90%. The high luminescence was maintained for more than 500 hours, making these materials especially promising for applications in light-emitting diodes and phosphors.

In chapter 3, the preparation of insoluble films of green luminescent perovskites is reported. For this, a novel bifunctional ligand to synthesize highly luminescent green-emitting perovskite was employed. These materials were then used to develop solution-based multilayer LEDs. The luminescent system consisted in $MAPbBr_3$ nanoparticles with 11-aminoundecanoic acid hydrobromide as a coordinating ligand. Dispersions of nanoparticles with a diameter below 10 nm and a photoluminescent quantum yield of about 80% were readily obtained at RT and in atmospheric conditions. Thanks to the use of the bifunctional ligand, the nanoparticles could be anchored on a variety of electroactive surfaces, such as inorganic semiconductors or conducting polymers. The nanoparticles anchored to ZnO and PEDOT:PSS thin films showed a remarkable photoluminescence quantum yield of approximately 50%. The nanoparticles-sensitized ZnO films could be directly integrated into light-emitting devices, leading to modest but homogeneous light emission. The effective anchoring of semiconducting nanoparticles to the surface opens new paths for the preparation of simple and inexpensive solution-processed multilayer LEDs.

The development of green-emitting LEDs with a remarkable combination of high external quantum efficiency, luminance, power and current efficiency is presented in chapter 4. The electroluminescent compound consisted of low-dimensional octylammonium lead bromide microplatelets and 3D $FAPbBr_3$ nanocrystals, self-assembled into 2D-3D hierarchical composite films with a photoluminescent quantum yield exceeding 80%. The efficient luminescence was ascribed to an energy cascade through the hierarchical self-assembled structures. Upon charge injection, the 2D microplatelets function as a transport layer to balance the electron and hole injection, while passivating the nanocrystals. The charge carriers in the higher bandgap (smaller) nanocrystals rapidly cascade into the lowest bandgap (largest) nanocrystals within the size distribution. In the largest nanocrystals, the carrier densities increase substantially thereby increasing radiative recombination. This approach

led to electroluminescence with a maximum luminance of about 56000 cd m^{-2} with a 13.4% external quantum efficiency.

Chapter 5 reports on the synthesis of bright photoluminescent wide bandgap mixed halide 3D perovskite powders of the type $MA_{1-y}Cs_yPb(Br_nCl_{1-n})_3$, with emission spanning the blue to green region of the visible spectrum using a solvent-free simple method. The materials were prepared by dry mechanochemical synthesis (ball-milling) starting from neat binary precursors. The composition, and thus the emission wavelength, could be easily modified by simple stoichiometric control of the precursors. While no photoluminescence could be measured from the neat perovskite, a strong improvement in the photoluminescent quantum yield was obtained upon addition of amantadine hydrochloride, with almost no structural changes. The enhancement demonstrated the effective passivation of non-radiative states previously present in the neat sample. Photoluminescent quantum yield as high as 7% in the blue (y = 0, n = 0.6) and 29% in the green (y = 0, n = 1) were obtained from 3D perovskite powders.

The strategies and systems investigated and described in the different chapters aim to contribute to the progress of the perovskite optoelectronics field.

Chapter 7.

Summary in Spanish / Resumen en castellano

Índice

Capítulo 1. Introducción

1.1. Visión general

Los diodos emisores de luz (LEDs, por sus siglas en inglés) son dispositivos que emiten luz al aplicar un voltaje a los electrodos, haciendo que electrones y huecos recombinen en un semiconductor liberando energía en forma de fotones. Este fenómeno se denomina electroluminiscencia, y el color de la luz está determinado por la diferencia de energía entre la banda de conducción y la banda de valencia del semiconductor elegido (banda prohibida de energía, E_g).

Las ventajas de los LEDs frente a las fuentes de luz incandescente incluyen un menor consumo de energía, una vida útil más larga, una mayor robustez física y un tamaño más pequeño. En los últimos años, los LEDs se han vuelto omnipresentes y se encuentran en diversas aplicaciones en las industrias aeroespacial y automotriz, así como en publicidad, señales de tráfico, flashes de cámaras, pantallas e iluminación. Debido a su alta eficiencia, los LEDs están siendo ampliamente adoptando como fuentes de luz alternativas a las bombillas incandescentes y los tubos fluorescentes.

Actualmente, los LEDs comerciales de más alta calidad se basan en semiconductores inorgánicos, fabricados a altas temperaturas y a través de complejos procesos de deposición. Es importante destacar que estos LEDs inorgánicos son fuentes de luz puntual, lo que dificulta su implementación en aplicaciones como pantallas flexibles o luminarias de pantalla plana. Los LEDs orgánicos (OLEDs) son más adecuados para estas aplicaciones, ya que son dispositivos planos formados por múltiples capas de semiconductores orgánicos, que pueden procesarse a baja temperatura y por lo tanto en prácticamente cualquier sustrato, incluidos sustratos flexibles. Uno de los principales obstáculos todavía presentes es la fabricación de OLEDs eficientes y estables con emisión de luz azul. Esto se debe a que la alta energía de las transiciones electrónicas necesarias para obtener luz azul conlleva el uso de semiconductores orgánicos con estabilidad electroquímica reducida. Recientemente se ha demostrado que las perovskitas, materiales semiconductores con una banda prohibida directa, pueden ser una alternativa a los actuales semiconductores inorgánicos y orgánicos para aplicaciones en pantallas de colores e iluminación, ya que son económicas y fáciles de fabricar, y pueden además modificarse fácilmente para generar luz de distintos colores.

Según las recomendaciones de la Unión Internacional de Telecomunicaciones (ITU) y la Comisión Internacional de Iluminación (CIE), las tres bandas de emisión primarias aptas para pantallas se centran en 630 nm (rojo), 532 nm (verde) y 467 nm (azul).[1] Gracias a la posibilidad de modificar fácilmente sus propiedades y color de emisión, las perovskitas son particularmente prometedoras para los LEDs, en concreto las perovskitas de haluros metálicos, y especialmente en su forma nanoestructurada, ya que pueden procesarse por

disolución a bajas temperaturas en una amplia gama de sustratos flexibles o rígidos. Además, las perovskitas nanoestructuradas alcanzan eficiencias de fotoluminiscencia elevadas y espectros de emisión muy estrechos (considerando la anchura a media altura, FWHM). Las perovskitas tienen un ancho de banda prohibida que puede modificarse fácilmente desde el ultravioleta (UV) hasta el infrarrojo cercano (NIR), lo que es un factor relevante para una amplia gama de aplicaciones optoelectrónicas.

Para poder ser llevadas al mercado, las perovskitas necesitan todavía mejoras importantes, sobre todo debido a su poca estabilidad ante la exposición prolongada a la luz, la humedad y las altas temperaturas.[2–4] Sin embargo, se están haciendo grandes progresos en este campo, y no hay que descartar que las perovskitas puedan ser utilizadas en un futuro en LEDs de bajo coste y diferente color.

De entre las perovskitas de haluro metálico, los materiales semiconductores más prometedores son las perovskitas de haluro de plomo. Las células solares y los LEDs de perovskita han demostrado ya eficiencias comparables a las de los semiconductores inorgánicos tradicionales.[5,6] Para obtener altas eficiencias de conversión de energía en los dispositivos de perovskita, basta con capas muy delgadas (< 1 µm) del material activo. A pesar de que la cantidad total de Pb por m^2 es muy baja, se están realizando muchos estudios para reducir posibles consecuencias debidas a la toxicidad de las perovskitas de plomo, y en los últimos años se ha avanzado mucho en el desarrollo de encapsulaciones efectivas contra la humedad y el oxígeno,[7,8] e incluso en el reciclaje de perovskitas al final de la vida útil del dispositivo.[9,10] Paralelamente, los investigadores también se están centrando en el desarrollo de perovskitas sin plomo. Aunque se han investigado otras estructuras de perovskitas de metales alternativos como estaño, germanio, paladio, bismuto o antimonio,[11–14] las perovskitas de haluro de plomo tienen propiedades semiconductoras muy superiores a las de todos los demás materiales alternativos.[15] Algunas de las características favorables de las perovskitas de haluro de plomo son:

a. Bajo coste de los precursores, que utilizan elementos abundantes y que pueden reciclarse fácilmente.
b. Reactividad simple y formación favorecida, que permite el procesamiento de capas delgadas a baja temperatura.
c. Alto coeficiente de absorción.
d. Posibilidad de lograr alto rendimiento cuántico de fotoluminiscencia (PLQY).
e. Larga longitud de difusión de los portadores de carga (en comparación con semiconductores orgánicos).

En vista de estas propiedades y de la implementación exitosa de compuestos de perovskita en dispositivos de alta eficiencia, las perovskitas desarrolladas en esta tesis están basadas en haluros de plomo.

1.2. Perovskitas de haluros metálicos

Las perovskitas deben su nombre al mineral titanato de calcio, $CaTiO_3$, conocido como perovskita, que debe su nombre al mineralogista ruso Lev Perovski.[16] Sin embargo, el término perovskita incluye todos los materiales que tienen el mismo tipo de estructura cristalina que el titanato de calcio, e incluso sus derivados. La fórmula general para las perovskitas tridimensionales (3D) es AMX_3, donde A y M son dos cationes de diferentes tamaños y carga y X es un anión. Aunque los compuestos de perovskita más comunes son los óxidos, una subclase de estos materiales consiste en haluros metálicos ternarios, donde A es un catión monovalente orgánico o inorgánico, M es un metal divalente y X es un haluro. Las investigaciones sobre perovskitas de haluro de plomo estaban ya en curso hace décadas, aunque con el objetivo principal de estudiar sus propiedades estructurales y magnéticas.[17,18] Ishihara et al. estudiaron por primera vez las propiedades excitónicas de láminas de perovskita,[19,20] realizando un trabajo transcendental sobre las propiedades optoelectrónicas de los compuestos híbridos de haluro de plomo. Los primeros intentos de fabricar dispositivos emisores de luz utilizando perovskitas de haluro de plomo se realizaron a fines del siglo XX.[21,22] Sin embargo, la electroluminiscencia solo se podía detectar a temperaturas de nitrógeno líquido, excluyendo cualquier aplicación práctica de los dispositivos. No fue hasta 2014 cuando se demostró por primera vez electroluminiscencia infrarroja y visible en perovskitas de haluro de plomo a temperatura ambiente.[23] Desde entonces, la comprensión de las propiedades de la perovskita así como de su cristalización ha avanzado enormemente, contribuyendo al desarrollo de LEDs de perovskita eficientes. En el momento de la preparación de esta tesis, se ha llegado a demostrar dispositivos emisores de luz roja y verde con eficiencias cuánticas externas superiores al 20%,[163] y LEDs de perovskita azules con eficiencias cuánticas externas de hasta el 9,5%.[28]

1.2.1. Composición, estructura cristalina y tamaño

Las perovskitas pueden cristalizar con diferentes estructuras, siendo la más simple la perovskita AMX_3 3D, que ha sido ampliamente estudiada debido a sus excelentes propiedades fotovoltaicas. En la estructura AMX_3, A es un catión monovalente orgánico pequeño, generalmente metilamonio (MA^+, $CH_3NH_3^+$) o formamidinio (FA^+, $CH(NH_2)_2^+$), o un catión inorgánico grande como el cesio (Cs^+), M es un metal divalente con coordinación octaédrica estable, Pb^{2+}, Sn^{2+} o Ge^{2+} y X es un anión haluro o una mezcla de ellos (Cl^-, Br^- o I^-). La estructura de la perovskita 3D consiste en octaedros de $[MX_6]^{-4}$ unidos por los vértices, con cationes A ocupando las cavidades formadas por ocho de estos octaedros adyacentes (Figura 1.2, Página 12). Para conseguir estructuras 3D estables, los cationes A deben caber en la cavidad delimitada por los octaedros inorgánicos. Si los cationes son más grandes, la red 3D ya no puede acomodarlos y en su lugar se forman estructuras de perovskitas de dimensionalidad inferior. Las perovskitas pueden clasificarse en función de su estructura

cristalina (o red inorgánica) y de su tamaño,[31,32] como se encuentra representado en la Figura 1.3 (Página 13).

Estructura cristalina

Las perovskitas se pueden clasificar según la disposición espacial de los cationes A y de la red formada por los octaedros de $[MX_6]^{-4}$, octaedros de $[PbX_6]^{-4}$ en el caso de las perovskitas de haluro de plomo.La estructura general depende en gran medida del impedimento estérico de los cationes A utilizados.[33,34] Cuando el tamaño de los cationes orgánicos no cabe dentro de las cavidades de la red inorgánica, como en el caso de cationes orgánicos de cadena larga, la estructura 3D (Figura 1.3a, e, i, m, Página 13) colapsa formando estructuras cristalinas de menor dimensionalidad. Si solo están presentes cationes grandes (LA), la estructura cristalina que se forma en el caso de los haluros de plomo consiste en capas de octaedros de $[PbX_6]^{-4}$ unidos por los vértices y alternados con capas de estos cationes orgánicos. Estas estructuras bidimensionales (2D) están formuladas por $(LA)_2PbX_4$ (Figura 1.3b, f, j, n, Página 13). Por otra parte, en presencia de ambos cationes, grandes (LA) y pequeños (A), se forma una estructura intermedia conocida como fase cuasi-2D o Ruddlesden-Popper,[35,36] de fórmula genérica $(LA)_2(A)_{n-1}Pb_nX_{3n+1}$. Las perovskitas con una estructura cuasi-2D consisten en un número n de capas de octaedros $[PbX_6]^{-4}$ intercalados con cationes pequeños y separados por capas de cationes de amonio más grandes (Figura 1.4q, Página 14). Si la red de haluros de plomo consiste en octaedros $[PbX_6]^{-4}$ conectados por las esquinas, bordes o caras formando cadenas, la estructura cristalina es monodimensional (1D) (Figura 1.3c, g, k, o, Página 13). La fórmula química de estas estructuras es variable dependiendo de la conectividad entre los octaedros de haluro metálico. Por último, las estructuras cristalinas cero-dimensionales (0D) consisten en octaedros de $[PbX_6]^{-4}$ completamente aislados rodeados por cationes monovalentes grandes, con la fórmula genérica A_4BX_6 (Figura 1.3d, h, l, p, Página 13). Siguiendo esta clasificación, se pueden preparar sólidos de perovskita con diferentes estructuras cristalinas, como por ejemplo perovskitas con cristales de más de 100 nm en las tres dimensiones y con una estructura cristalina 3D,[37] pozos cuánticos 2D,[38–40] hilos/cadenas cuánticas 1D[41,42] o moléculas/grupos 0D[43–45] (Figuras 1.3a, b, c, d, respectivamente, Página 13).

Tamaño

Además de la dimensionalidad de la estructura cristalina, las perovskitas, y en general cualquier material, se pueden clasificar según su tamaño físico. De esta forma, la notación 3D define a sólidos de perovskita con cristales/granos que miden más de 100 nm en sus tres dimensiones. Asimismo, las nomenclaturas 2D, 1D y 0D corresponden a materiales con dimensiones menores de 100 nm en una, dos y tres dimensiones, respectivamente. La nomenclatura más clara para referirse a los diferentes tamaños de perovskita sería *bulk* para

3D (Figura 1.3a, b, c, d, Página 13), nanocapas o nanoláminas para 2D (Figura 1.3e, f, g, h, Página 13), nanohilos para 1D (Figura 1.3i, j, k, l, Página 13) y nanopartículas para 0D (Figura 1.3m, n, o, p, Página 13). Por lo tanto, uno puede encontrar en la literatura ejemplos de perovskitas con la misma estructura cristalina 3D AMX_3 pero con diferentes tamaños, como por ejemplo, perovskita *bulk*,[37] nanoláminas,[46] nanohilos[47–49] y nanopartículas (NPs)[26,50] (Figura 1.3a, e, i, m, Página 13, respectivamente).

La formación de estructuras cristalinas de baja dimensionalidad o perovskitas con un tamaño de cristal/grano pequeño conlleva el control del crecimiento del material, que puede producirse, entre otros, por la presencia de aminas de cadena larga (en la sección 1.2.3 se describirán diferentes métodos de síntesis). Cuando hay cationes grandes presentes en la síntesis, la formación de cristales/granos de tamaño reducido o estructuras cristalinas de baja dimensionalidad depende de factores como la naturaleza química y la proporción de estas moléculas, y puede conducir a menudo a una mezcla de especies. En la síntesis de nanocristales de perovskita, los cationes grandes de coordinación también se conocen comúnmente como ligandos.

1.2.2. Propiedades optoelectrónicas y estructurales

La perovskita de haluro metálico exhibe propiedades ópticas favorables para la preparación de dispositivos optoelectrónicos, como un alto coeficiente de absorción, alto PLQY y un estrecho espectro de fotoluminiscencia (PL), cuya posición puede modificarse desde el UV al NIR cambiando sus elementos constitutivos, tamaño o estructura cristalina. Varios trabajos han demostrado que un intercambio del haluro modifica las propiedades ópticas.[51–53] De hecho, las perovskitas de haluros mixtos también se pueden preparar fácilmente, mostrando propiedades ópticas intermedias en comparación con los haluro puros (Figura 1.5a, Página 16).[52,53]

La mayoría de las características que presenta el material pueden racionalizarse en función de su estructura electrónica. En la Figura 1.5b (Página 16) se muestra un diagrama esquemático de energía.[54] La banda de conducción de las perovskitas de haluro se forma a partir de los orbitales antienlazantes formados por la hibridación entre orbitales *p* del Pb y orbitales s del haluro, y es principalmente tipo *p* debido a la alta densidad de estados del plomo. Por otra parte, la banda de valencia se forma a partir de los orbitales antienlazantes de la hibridación de orbitales *s* del Pb y orbitales *p* del haluro.[54–57] La modificación del haluro conduce a cambios significativos en el ancho de banda prohibida. Como la banda de conducción está influenciada principalmente por la energía de orbitales atómicos *p* del Pb, un cambio de haluro afecta principalmente a la banda de valencia. Los orbitales *p* del haluro que contribuyen a la formación de la banda de valencia cambian de 5*p* a 4*p* y a 3*p* a medida que el haluro se cambia de I a Br y a Cl. La disminución del nivel *p* del X es el factor dominante para determinar la posición de la banda de valencia, lo que resulta en un aumento del ancho

de banda prohibida al pasar de I a Br y a Cl. Por otro lado, el catión del sitio A no participa directamente en el enlace y solo influye indirectamente en la estructura electrónica por una variación del volumen de la red AMX_3 o por introducir una distorsión en la estructura. Aumentar el tamaño del catión A, por ejemplo, al pasar de Cs a MA y FA, generalmente aumenta el volumen o la distorsión de la red, lo que conduce a una disminución en los niveles de M. Esta reducción se debe a la moderación del efecto de confinamiento, es decir, un electrón en un átomo de Pb está menos confinado y su energía disminuye. Variar el catión A conduce a cambios relativamente pequeños en el volumen y la estructura y, en consecuencia, el ancho de banda prohibida solo se ve ligeramente afectada.[54]

Además de por la composición, las propiedades ópticas de las perovskitas de haluro de plomo están fuertemente influenciadas tanto por el tamaño de partícula como por la dimensionalidad de la estructura cristalina (como se muestra en la Figura 1.3, Página 13). Si el confinamiento espacial de los portadores de carga es del mismo orden de magnitud que el radio de Bohr del excitón, las perovskitas exhiben efectos de confinamiento cuántico. En concreto, el ancho de banda prohibida aumenta a medida que aumenta el confinamiento espacial. La forma más directa de lograr el confinamiento cuántico en las perovskitas es la reducción del tamaño de partícula, como en los puntos cuánticos (QDs) de semiconductores tradicionales.[58] Esto corresponde a moverse de arriba a abajo en la Figura 1.3 (Página 13). Alternativamente, las perovskitas pueden mostrar efectos de confinamiento al disminuir la dimensionalidad de su estructura cristalina (moviéndose de izquierda a derecha en la Figura 1.3 (Página 13) y la Figura 1.4 (Página 14)),[59] como por ejemplo pasando de AMX_3 (3D) a $(LA)_2PbX_4$ (2D) o para pequeños valores de n en perovskitas cuasi-2D $(LA)_2(A)_{n-1}Pb_nX_{3n+1}$. En estas perovskitas de baja dimensionalidad, compuestas por capas inorgánicas semiconductoras y capas orgánicas aislantes alternadas, los electrones y los huecos están confinados dentro de las capas inorgánicas, causando efectos de confinamiento cuántico.

Una característica clave de las perovskitas de haluro metálico es la alta tolerancia a los defectos estructurales. Los defectos inducen estados electrónicos localizados que pueden actuar como trampas electrónicas, donde los portadores de carga pueden ser capturados y perdidos. Debido a la naturaleza de la estructura de bandas de las perovskitas de haluro de plomo, los estados energéticos asociados a defectos tienden a ser poco profundos o localizados dentro de las bandas electrónicas, y por lo tanto son esencialmente benignos.[60] Esta característica única permite obtener perovskitas altamente luminiscentes sin el uso de técnicas de procesamiento sofisticadas.[61] De hecho, los nanocristales (NCs) de perovskita generalmente muestran un PLQY muy alto, con valores reportados cercanos a la unidad.[62] El confinamiento espacial de las cargas, junto con una pasivación de la superficie del material, mejora de manera efectiva el PLQY al eliminar virtualmente todas las vías de decaimiento no radiativas (más detalles en la sección 1.3.1). A pesar de que la alta tolerancia a los defectos es una característica común de todas las perovskitas de haluros metálicos, el PLQY generalmente disminuye para los anchos de bandas prohibida mayores. Lo más probable es que, cuanto más ancha es la banda prohibida, más importante es el efecto de los defectos al

poder actuar como centros de recombinación no radiativa. Otra consecuencia de la alta tolerancia a los defectos que poseen las perovskitas de haluro de plomo son sus buenas propiedades de transporte de carga, transporte ambipolar y alta movilidad de portadores, en comparación con los semiconductores orgánicos.[63–66]

1.2.3. Métodos de síntesis coloidal de nanocristales

La formación de capas delgadas de perovskita para la preparación de LEDs a menudo tiene lugar durante la deposición de los precursores sobre un sustrato (ver sección 1.3.3 para más detalles). Sin embargo, en el caso de perovskitas nanoestructuradas, generalmente requiere primero la síntesis de suspensiones coloidales y luego la deposición sobre un sustrato. Los métodos de síntesis de los nanocristales de perovskita de haluro de plomo se pueden clasificar en dos grupos principales: los métodos en disolución y los métodos en estado sólido. Las síntesis en disolución requieren del uso de disolventes para disolver, mezclar y dar lugar a la reacción de los precursores de perovskita para formar los nanocristales coloidales. Los métodos de síntesis basados en sólidos no usan disolventes durante la síntesis o los usan en cantidades muy inferiores. En la Figura 1.6 (Página 18), se puede observar una clasificación de los métodos de síntesis de nanocristales de perovskita más relevantes.

Métodos de síntesis por disolución

La preparación de nanocristales requiere el control del crecimiento del material a escala nanométrica. Esto se puede lograr utilizando un material inerte y preformado (matriz) para confinar espacialmente los cristales de perovskita, o mediante una síntesis directa sin utilizar una estructura externa. Los métodos *asistidos por una matriz* hacen uso de una matriz polimérica,[24] o una estructura porosa de óxido metálico.[25] El principal inconveniente de estas técnicas es la baja conductividad eléctrica de las capas resultantes ya que el confinamiento tiene lugar dentro de una matriz aislante.

Los nanocristales de perovskita también se pueden sintetizar directamente, sin la necesidad de una estructura externa que actúe como plantilla. Esto se puede lograr mediante la nucleación y el crecimiento de los cristales a partir de un cambio en las condiciones de reacción, o mediante una sobresaturación inducida de una disolución que conduce a la precipitación y cristalización de los nanocristales de perovskita.

En el último caso, los métodos más relevantes son la *reprecipitación asistida por ligando*, LARP,[67] y el método de *emulsión*.[69] La síntesis tiene lugar en presencia de surfactantes (ligandos), típicamente moléculas de alquilamonio de cadena larga que limitan el crecimiento de los cristales.

Por otra parte, las técnicas más comunes en las que los NCs de perovskita se sintetizan por nucleación y crecimiento como consecuencia de cambios en las condiciones de reacción, son

el método de *inyección en caliente*,[52] la síntesis *solvotermal*, por *ultrasonidos* o por *irradiación con microondas*.[70–72]

Alternativamente, el crecimiento de NCs de perovskita puede llevarse a cabo comenzando la nucleación a partir de *NCs preformados (semillas coloidales)*, como PbI_2 pre-sintetizado.[73]

Todos los métodos descritos anteriormente se usan para preparar NCs que luego pueden depositarse sobre sustratos para formar capas delgadas para la preparación de LEDs. Sin embargo, es posible también la formación directa de NCs durante la formación de la capa (preparación *in situ*), donde la limitación del crecimiento de los cristales por ligandos tiene lugar durante la evaporación del disolvente y la condensación de los precursores.[74]

Métodos de síntesis en estado sólido

Los NCs de perovskita de haluros metálicos también se pueden sintetizar mediante procedimientos sin disolvente o con cantidades mínimas. Esto se lleva a cabo mediante una síntesis mecanoquímica como el *método de molienda manual* o el *molino de bolas* de alta energía.[75,76]

1.3. Diodos emisores de luz de perovskita

Debido a las buenas propiedades de transporte de las perovskitas, estos materiales pueden actuar como capas de transporte de cargas en los LEDs.[77] Sin embargo, esta sección se centra en LEDs donde la electroluminiscencia tiene lugar en la capa delgada de perovskita.

1.3.1. Principios de funcionamiento

En los semiconductores, los electrones y los huecos pueden ser foto-generados o inyectados eléctricamente. El proceso por el cual los portadores de carga se recombinan y emiten fotones se conoce como recombinación radiativa. Si el proceso tiene lugar sin la emisión de fotones, se denomina recombinación no-radiativa. Para alcanzar una luminiscencia eficiente, la recombinación no-radiativa debe minimizarse, por ejemplo, reduciendo la concentración de defectos. Aunque las perovskitas de haluro metálico tienen una alta tolerancia a defectos estructurales y electrónicos, los estados asociados a esos defectos siguen presentes en las capas delgadas de perovskita, y su densidad depende de las condiciones de procesamiento del material.[78] Desde este punto de vista, la síntesis (sección 1.2.3) así como el método de deposición (sección 1.3.3) son de gran importancia para obtener materiales semiconductores de alta calidad.

En un LED de perovskita, la capa electroluminiscente se intercala entre capas semiconductoras que inyectan y transportan selectivamente electrones y huecos desde los electrodos al material activo. Una vez que los portadores de carga (electrones y huecos) se encuentran en la perovskita, pueden recombinarse en forma de portadores libres o mediante la formación de excitones, liberando fotones en un proceso conocido como electroluminiscencia. Un modelo aproximado para describir el mecanismo de trabajo de un diodo de perovskita es la unión p-i-n, donde la perovskita actúa como material intrínseco entre capas dopadas.[79] Cuando los electrodos externos de un LED están en cortocircuito, los niveles de Fermi de los contactos metálicos se alinean y el potencial (diferencia de potencial, V_{bi}) cae sobre la región intrínseca. Las características de densidad de corriente frente a voltaje (J-V) se componen típicamente por tres regímenes. El primero es el régimen óhmico, donde se observa la corriente de fuga debido a defectos y cargas resistivas (Figura 1.7, parte 1, Página 21). Cuando se aplica un pequeño voltaje positivo al diodo, menor que V_{bi}, los electrones y los huecos difunden hacia la región intrínseca en el llamado régimen de corriente de difusión (Figura 1.7, parte 2, Página 21). Si se aplican voltajes superiores a V_{bi}, los electrones y los huecos se mueven bajo el efecto del voltaje aplicado (corriente de deriva, Figura 1.7, parte 3, Página 21) y la corriente está entonces limitada por inyección o por carga espacial.

Para describir el funcionamiento de un LED hay varias figuras de mérito representativas, como la luminancia (cd/m^2), la densidad de corriente (A/m^2), la eficiencia de corriente (cd/A), la eficiencia energética o luminosa (lm/W) o la eficiencia cuántica externa (EQE_{EL}, %).

Luminancia: Representa la intensidad de luz emitida (expresada en candelas, cd) por el dispositivo por unidad de superficie en una dirección determinada, teniendo en cuenta la curva de sensibilidad del ojo humano. Se expresa en cd/m^2.

Densidad de corriente (J): Corresponde a la corriente eléctrica por unidad de área del dispositivo. Sus unidades son A/m^2.

Eficiencia de corriente: Es la relación de la luminancia con la densidad de corriente correspondiente. Se expresa en cd/A.

Eficiencia de potencia o luminosa (PCE): Es la relación entre el flujo luminoso y la energía eléctrica consumida por la fuente. Sus unidades son lm/W.

Eficiencia cuántica externa (EQE_{EL}): Define el número de fotones emitidos sobre el número de electrones inyectados. Se expresa como un %.

1.3.2. Arquitecturas de dispositivos

La estructura de los LEDs de perovskita es análoga a la de los OLEDs (Figura 1.8a, Página 23). Dicha estructura consiste en dispositivos multicapa donde los procesos de inyección de carga,

transporte y recombinación se llevan a cabo por diferentes materiales, optimizados para cada proceso en particular. En los LEDs de perovskita, la capa emisora de perovskita se intercala entre las capas selectivas de carga, que tienen la tarea de transportar e inyectar huecos o electrones en la perovskita. Estas capas son semiconductores orgánicos u óxidos metálicos, y se denominan respectivamente como capa de transporte de huecos (HTL) y capa de transporte de electrones (ETL). Sus niveles de energía generalmente permiten transportar selectivamente un tipo de cargas (huecos o electrones) y bloquear las cargas opuestas. Por lo tanto, la recombinación de cargas tiene lugar dentro de la capa de perovskita, lo que aumenta la probabilidad de recombinación radiativa. Para igualar la función de trabajo (WF) de los electrodos, a menudo se usan capas de inyección que consisten en semiconductores dopados con alta densidad de portadores. Estas capas se conocen como capa de inyección de huecos (HIL) y capa de inyección de electrones (EIL). El poli(3,4-etilendioxitiofeno) dopado con sulfonato de poliestireno de sodio (PEDOT:PSS) es un polímero conductor ampliamente empleado como HIL, ya que asegura un contacto óhmico con el electrodo. Con el fin de inyectar electrones de manera eficiente, se utilizan ampliamente como EIL compuestos orgánicos dopados u óxidos metálicos de tipo n (como TiO_2, SnO_2 o ZnO, entre otros). Finalmente, el dispositivo se intercala entre dos electrodos, el ánodo (polarizado positivamente, para la inyección de huecos) y el cátodo (polarizado negativamente, para la inyección de electrones), normalmente formados por metales u óxidos conductores transparentes (TCO). Los TCOs son fundamentales para permitir que la luz salga del dispositivo, siendo los más comunes el óxido de indio dopado con estaño (ITO) o el óxido de estaño dopado con flúor (FTO). Los sustratos son generalmente láminas de vidrio o plástico, como el tereftalato de polietileno, PET, sobre las que se depositan el resto de las capas. Si la luz sale del dispositivo a través de este componente, es importante utilizar un material transparente con el índice de refracción correspondiente. Existen dos tipos de arquitecturas de dispositivo según la polaridad del electrodo transparente. Dependiendo de si el TCO se usa como ánodo (normalmente ITO en vidrio) o cátodo, el dispositivo se denomina p-i-n o n-i-p, respectivamente.[80]

Dependiendo del tipo de perovskita, y en particular de la posición absoluta de las bandas electrónicas, los materiales selectivos de cargas deben elegirse cuidadosamente, con un HOMO (orbital molecular ocupado más alto) y/o LUMO (orbital molecular desocupado más bajo) apropiado para minimizar la diferencia energética con las bandas de perovskita. Del mismo modo, los electrodos deben tener la WF adecuada para que esté alineada con el nivel de energía de las capas de transporte/inyección.

Independientemente de los materiales utilizados y la polaridad, los dispositivos p-i-n y n-i-p comparten los mismos principios de funcionamiento. Brevemente, cuando se aplica un voltaje superior a V_{bi} en un LED de perovskita en sus electrodos, se inyectan electrones y huecos en el dispositivo y se transportan al material activo a través de las EIL/HIL y ETL/HTL, respectivamente (Figura 1.8a, Página 23). Una vez en la capa de perovskita, si se recombinan de manera radiativa, el proceso da lugar a la emisión de luz. La Figura 1.8b (Página 23)

muestra un diagrama de energía de banda plana y resalta los diferentes procesos que conducen a la electroluminiscencia que tiene lugar en un LED (las líneas representan el WF de los electrodos, mientras que los rectángulos representan la banda prohibida de los semiconductores, con las líneas superior e inferior correspondientes al HOMO y LUMO o las bandas de valencia y conducción).

1.3.3. Técnicas de deposición

Una de las principales características de las perovskitas es la posibilidad de obtener capas delgadas semiconductoras de alta calidad (tanto óptica como electrónicamente) con métodos de deposición simples.[81–83] Las capas y dispositivos delgados de perovskita se pueden procesar por disolución o por evaporación mediante métodos de vacío. La técnica de procesado debe permitir el control sobre la cristalinidad, el grosor y la pureza, ya que estos influencian tanto el transporte de carga como las propiedades ópticas y, por tanto, el rendimiento del dispositivo. Las perovskitas nanoestructuradas, como nanopartículas o nanoláminas, en general deben sintetizarse con antelación a la deposición en capa delgadas (indicado en la sección 1.2.3). A pesar de que los cristales de perovskita ya están formados en estos materiales, es necesario elegir la técnica de deposición más adecuada para lograr la formación de capas uniformes y homogéneas, que aseguran un buen rendimiento del dispositivo. En el caso de las perovskitas de baja dimensionalidad, las técnicas más comunes para la preparación de capas delgadas a partir de nanopartículas o nanoláminas pre-sintetizadas son las técnicas basadas en disolución.

Los métodos de deposición por disolución son potencialmente económicos y compatibles con la fabricación continua sobre sustratos flexibles, adecuada para la producción a gran escala. Por otro lado, los métodos de deposición por evaporación en vacío tienen la ventaja de un mayor control sobre el espesor, uniformidad y calidad de la capa de perovskita. Los métodos de vacío también son intrínsecamente aditivos, por lo que los dispositivos multicapa pueden obtenerse fácilmente sin la necesidad de usar disolventes ortogonales.

1.4. Motivación y sinopsis de la tesis

Para contribuir al desarrollo de los sistemas electroluminiscentes del futuro, los LEDs de perovskita necesitan demostrar alta eficiencia de corriente y estabilidad, y deben poderse procesar de manera simple y económica. La preparación de materiales emisores de alta calidad con alta pureza, alta eficiencia de PL y diferentes colores de emisión es imprescindible para lograr dispositivos versátiles y altamente eficientes. Los resultados recogidos en esta tesis tienen como objetivo contribuir al progreso de las perovskitas en el campo de la optoelectrónica, mediante el desarrollo de materiales y dispositivos emisores de luz eficientes y potencialmente económicos.

En los diferentes capítulos, se describen y evalúan varios tipos de perovskita con estructura cristalina 3D, tanto nanoestructuradas (Capítulo 2, 3 y 4) como en sólido extendido (*bulk*) (Capítulo 5). Además, se presentan otros tipos de estructuras cristalinas, como las nanoláminas con estructuras 2D (Capítulo 3) e incluso estructuras cuasi-2D (Capítulo 2). Se describe la fotoluminiscencia y electroluminiscencia de materiales de perovskitas que abarcan todo el espectro visible, del rojo al verde y azul.

Capítulo 2. Nanocristales de perovskitas de yodo de baja dimensionalidad con emisión roja eficiente

2.1. Motivación, descripción del trabajo y logro

Obtener fotoluminiscencia roja, estable y eficiente de NCs de perovskita ha sido un desafío durante años. Las perovskitas de yoduro de plomo tienen la banda prohibida más pequeña, y por tanto son la únicas adecuadas para obtener emisiones en el rojo. Sin embargo, las perovskitas *bulk* $MAPbI_3$ y $FAPbI_3$ emiten a una longitud de onda superior a 770 nm, en la región del infrarrojo cercano. Además, la inestabilidad química del $MAPbI_3$ y la inestabilidad estructural a temperatura ambiente del $FAPbI_3$ y $CsPbI_3$ dificultan la obtención de NCs de perovskita a base de yoduro.[87–90] En los últimos años se han realizado varios avances en la estabilización de dichos sistemas,[90–92] pero a pesar de ello, todavía no se ha logrado un sistema con luminiscencia roja pura (aprox. 630-650 nm), estable y eficiente. Una alternativa para lograr esta emisión a partir de estas perovskitas es usar sistemas mixtos de haluro de Br/I.[93] Sin embargo, estos sistemas generalmente sufren segregación de fase, y por lo tanto no son adecuados para aplicaciones optoelectrónicas reales.[94]

En este capítulo se describe la síntesis de NCs de perovskita cuasi-2D con una luminiscencia eficiente en el rojo y alta estabilidad, obtenidas mediante el uso de un método simple de reprecipitación asistida por ligando a temperatura ambiente. Se ha estudiado además la posibilidad de controlar el ancho de banda prohibida modificando la longitud de la cadena de los ligandos de alquilamonio, lo que conlleva una variación de la dimensionalidad de las nanoestructuras.

2.2. Detalles experimentales y metodología

Para la preparación de nanocristales de perovskita 3D de yodo se planteó una estequiometria inicial de $MA_{0,8}Cs_{0,2}PbI_3$.[98] Se mezclaron $PbBr_2$, 1-octadecene (ODE), oleylamina (o posteriormente decilamina, octilamina y hexilamina) y ácido oleico (OA) para obtener una disolución nombrada como *disolución Pb*. Paralelamente, se añadió MAI y CsI a una disolución con 1-butanol (1-BuOH), ODE y OA (llamada *disolución MACs*). Ambas disoluciones se calentaron bajo agitación continua para asegurar una completa disolución. Después de enfriarlas, la *disolución Pb* se inyectó gota a gota en la *disolución MACs* bajo agitación vigorosa a temperatura ambiente. Inmediatamente, se observó la formación de un precipitado rojo oscuro, resultado de la formación de los NCs. Posteriormente la dispersión se lavó mediante dos etapas de centrifugación, y el sobrenadante de color rojo brillante se utilizó para la caracterización sin ulterior purificación.

Algunas muestras se modificaron añadiendo un disolvente adicional durante la etapa de purificación. Para estas muestras, la síntesis se realizó siguiendo el mismo procedimiento

pero añadiendo grandes cantidades de 1-BuOH a la dispersión de NCs antes de la primera etapa de centrifugación. Los siguientes pasos se mantuvieron invariables, y el precipitado se recogió y se redispersó en tolueno.

2.3. Resultados y discusión

La síntesis condujo a la formación de NCs de perovskita híbrida cuasi-2D, $(LA)_2(A)_{n-1}Pb_nI_{3n+1}$, siendo LA un catión alquilamonio y A una mezcla de MA^+ y Cs^+. En estructuras cristalinas cuasi-2D, el ancho de banda prohibida, y por lo tanto la longitud de onda de emisión, dependen del valor n, que pueden modularse variando la longitud de la cadena de los ligandos empleados. Al reemplazar la oleylamina utilizada en primera instancia por alquilaminas saturadas con longitudes de cadena decrecientes, decilamina, octilamina y hexilamina, se produjo un desplazamiento progresivo del máximo de PL hacia el azul. Este efecto se atribuye a una mayor velocidad de difusión de los iones de amonio de cadena más corta, lo que lleva a la formación de cristales cuasi-2D con menores valores de n y una menor distancia entre capas de octaedros $[PbX_6]^{-4}$, resultando en un mayor confinamiento cuántico. Además, la adición de 1-BuOH en la primera etapa de lavado condujo a la formación de sistemas con una mayor pureza y un PLQY más alto, superior al 90% en el caso de la decilamina. El alto PLQY se mantuvo durante más de 500 horas, lo que hace que estos materiales sean especialmente prometedores para aplicaciones en diodos emisores de luz y como fósforos.

2.4. Trabajo publicado

El trabajo se llevó a cabo en colaboración con PNEL, el grupo de investigación del Prof. Tae-Woo Lee en la Seoul National University en Corea del Sur. El tema de investigación se inició durante una estancia en Seul en 2018, en estrecha colaboración con el Dr. Young-Hoon Kim y Seung Hyeon Jo. El trabajo continuó en el Instituto de Ciencia Molecular de la Universidad de Valencia.

La publicación mostrada en la página 35 está reproducida con el permiso de The Royal Society of Chemistry. DOI: 10.1039/C9NR04520A, Nanoscale, 2019, 11, 12793-12797.

Capítulo 3. Capas delgadas fotoluminiscentes con alta eficiencia basadas en nanopartículas de perovskita híbrida ancladas

3.1. Motivación, descripción del trabajo y logro

Para la preparación de LEDs multicapa, varias capas del mismo o diferentes materiales tienen que depositarse una encima de la otra, lo que puede llevar a una redisolución parcial o a un entremezclado entre las capas adyacentes. Una posible solución a este problema es el uso de agentes reticulantes, que se encargan de fijar el material mediante la formación de enlaces químicos covalentes. Desafortunadamente, los agentes reticulantes no son químicamente compatibles con todos los materiales y pueden introducir estados de trampa debido a restos sin reaccionar.

En este capítulo se describe por primera vez el uso de un ligando bifuncional para la síntesis de NPs de $MAPbBr_3$ altamente fotoluminiscentes, con emisión en el verde. El ligando permite que las nanoestructuras se anclen en la superficie de una variedad de polímeros conductores y semiconductores inorgánicos, que pueden usarse para la preparación de LEDs multicapa.

3.2. Detalles experimentales y metodología

Para la fabricación de NPs de $MAPbBr_3$, el ácido 11-aminoundecanoico se convirtió inicialmente en su sal de amonio mediante la reacción con exceso de HBr, con el fin de mejorar su solubilidad en DMF (dimetilformamida). Las NPs se prepararon mediante una síntesis LARP (reprecipitación asistida por ligando), aprovechando la interacción entre un disolvente polar (DMF, capaz de solubilizar los precursores de perovskita) y uno no polar (tolueno), descrito anteriormente.[26,113]

Se disolvieron $PbBr_2$ y ácido oleico en DMF, formando la *disolución A*. A continuación, se añadió un volumen de esta disolución a una *disolución B*, que consistía en MABr en DMF y cantidades variables de $Br^-NH_3^+$-C_{10}-COOH. La disolución resultante (A + B) se inyectó rápidamente en tolueno bajo agitación, a temperatura ambiente o a 60 ^oC. Inmediatamente se observó la formación de una suspensión amarillo-verdosa, consecuencia de la formación de las NPs. La suspensión se centrifugó para eliminar los agregados más grandes, obteniendo una suspensión luminiscente del sobrenadante.

Las capas de ZnO se depositaron por spin-coating a partir de disoluciones de nanopartículas comerciales en etanol (tamaño de partícula promedio de 35 nm), usando un GYRSET® (tecnología de deposición de cubierta cerrada). Las capas así formadas fueron sometidas a un tratamiento térmico de 30 min a 450 ^oC. Para la preparación de capas de ZnO/NPs $MAPbBr_3$, los sustratos recubiertos con ZnO se sumergieron en la suspensión de NPs durante 12 horas y posteriormente se enjuagaron con tolueno.

3.3. Resultados y discusión

En la síntesis de NCs, la elección del ligando debe hacerse en función de las propiedades deseadas. Estos materiales tienen una gran relación superficie-volumen y, por lo tanto, la superficie es el factor dominante en muchos procesos físicos y químicos.[114] En colaboración con el grupo del Prof. Mhaisalkar en Singapur, se experimentó con la síntesis de NPs de $MAPbBr_3$ utilizando $Br^-NH_3^+$-C_{10}-COOH como ligando, en contraposición con los cationes amonio o aminas de cadena larga comúnmente utilizados en la síntesis de nanopartículas de perovskita, como el haluro de oleilamonio o el haluro de octilamonio, entre otros.[67,105,115] El ligando elegido tiene dos funcionalidades diferentes. Por un lado, el catión de amonio posibilita una interacción fuerte con la superficie de las NPs de perovskita, mientras que el grupo carboxilo permite el anclaje de las NPs en superficies funcionales, como las de semiconductores inorgánicos o polímeros conductores. Este ligando permitió la preparación de NPs a temperatura ambiente y en condiciones atmosféricas. La caracterización de la dispersión de NPs resultante mostró la presencia de partículas con un diámetro inferior a 10 nm y un PLQY de aproximadamente 80%. Para probar las propiedades de adhesión de las NPs funcionalizadas con el ligando, sustratos de vidrios recubiertos con ZnO y PEDOT:PSS se sumergieron en la suspensión de NPs durante 12 horas y luego se enjuagaron con tolueno. Las NPs se anclaron de forma eficiente a las capas delgadas de ZnO y PEDOT:PSS, ya que mostraron un PLQY de más del 50% incluso después de enjuagarlas con tolueno. Las capas de ZnO funcionalizadas con NPs se integraron en dispositivos emisores de luz, con una emisión de luz modesta pero homogénea. El anclaje efectivo de NPs semiconductoras a superficies con diferentes naturalezas químicas abre nuevos caminos para la preparación de LEDs multicapa simples y económicos.

3.4. Trabajo publicado

El trabajo se realizó en colaboración con ERI@N, un instituto de investigación de la Nanyang Technological University de Singapur dirigido por el Prof. Subodh Mhaisalkar. El trabajo de investigación se inició durante una estancia allí en 2015, en estrecha colaboración con el Dr. Koh Teck Ming, y continuó en el Instituto de Ciencias Moleculares de la Universidad de Valencia.

 DOI: 10.1039/C6CC05549D, Chem. Commun., 2016, 52, 11351-11354.

Capítulo 4. Nanoestructuras jerárquicas de perovskita autoensambladas para LEDs de alta eficiencia mediante transferencia de energía en cascada

4.1. Motivación, descripción del trabajo y logro

Como se destacó en la introducción, las perovskitas de haluro metálico exhiben propiedades que son interesantes para aplicaciones en sistemas de iluminación y pantallas planas. Sin embargo, los métodos de preparación necesarios para obtener materiales altamente luminiscentes son complejos y a menudo difíciles de reproducir, limitando el progreso hacia sus aplicaciones.

En este capítulo se describe la preparación y caracterización de capas luminiscentes formadas por estructuras jerárquicas autoensambladas de baja dimensionalidad. Estas estructuras forman capas con un PLQY de más del 80%, y muestran un mecanismo de transferencia de energía en cascada que conduce a LEDs con eficiencias electroluminiscentes muy altas, con una combinación de EQE, luminancia, eficiencia de corriente y eficiencia de potencia superior a otros LEDs de perovskita con emisión en el verde.

4.2. Detalles experimentales y metodología

Para sintetizar los NCs de $FAPbBr_3$, se usó el método LARP (reprecipitación asistida por ligando) a temperatura ambiente. Se preparó una disolución precursora mezclando FABr y $PbBr_2$ en DMF. A continuación, la disolución resultante se añadió gota a gota en una disolución de tolueno bajo agitación vigorosa que contenía ácido oleico, n-butanol y cantidades variables de n-octilamina para lograr relaciones de OA:$PbBr_2$ desde 3:1 hasta 10:1. Inmediatamente se formó una disolución amarillenta, indicando la formación de los NCs. Una vez completada la reacción, la dispersión coloidal de NCs se lavó en dos etapas de centrifugación. En la primera, la disolución de NCs se centrifugó a 13400 revoluciones por minuto (rpm), y el precipitado se redispersó en tolueno. Luego, los NCs redispersados se centrifugaron a 4400 rpm. El sobrenadante resultante (concentración estimada de aproximadamente 8-10 mg mL^{-1}) se usó para la fabricación del LED.

Para la fabricación de dispositivos se usaron sustratos de vidrio recubiertos con ITO. La capa inyectora de huecos, PEDOT:PSS, se depositó por spin-coating sobre el ITO. A continuación, los sustratos se transfirieron a una caja de guantes con atmósfera de nitrógeno, donde la dispersión coloidal de NCs se depositó sobre las capas de PEDOT:PSS. Antes de iniciar la rotación, la suspensión se dejó en reposo durante 5 minutos para permitir la lenta evaporación del disolvente (y el inicio del autoensamblaje). Posteriormente, se depositó por sublimación en vacío la capa transportadora de electrones (POT2T, 2,4,6-Tris[3-(difenilfosfinil)fenil]-1,3,5-triazina, o B3PYMPM, 4,6-Bis(3,5-di(piridin-3-il)fenil)-2-

metilpirimidina) en una cámara de alto vacío. Finalmente, Ba (7 nm) y Al (80 nm) se evaporaron térmicamente delimitando el área del dispositivo mediante una máscara metálica. Para la fabricación de dispositivos flexibles se siguió un protocolo similar, pero utilizando sustratos flexibles PET/ITO. En este caso, se depositaron capas PEDOT:PSS más gruesas para compensar la rugosidad de la superficie de ITO sobre el sustrato de PET flexible.

4.3. Resultados y discusión

La síntesis tipo LARP (reprecipitación asistida por ligando) permitió la formación de NCs 3D de $FAPbBr_3$, con un diámetro de entre 5 a 30 nm, y MPLs cuasi-2D de bromuro de plomo y octilamonio, con una longitud de entre 0,5 a 2 µm. Es importante destacar como la relación entre los MPLs y los NCs podía modularse fácilmente variando la relación OA:$PbBr_2$. Cuando se depositaron sobre sustratos, se formaron capas compuestas por estructuras jerárquicas autoensambladas muy planas (rugosidad RMS ± 1 nm), una característica fundamental para lograr dispositivos de alta calidad. Las capas con las diferentes proporciones OA:$PbBr_2$ exhibieron PLQY altos, con valores que oscilaban entre 75% y 89%. Estos sistemas permitieron la preparación de LEDs con un rendimiento inusitado, que se atribuyó a una transferencia de energía en cascada entre las estructuras jerárquicas 2D-3D autoensambladas. Cuando los dispositivos están en funcionamiento, las microláminas 2D actúan como capa de transporte y como intermediario para equilibrar la inyección de electrones y huecos, pasivando a la vez los nanocristales. A continuación, se produce una rápida transferencia en cascada de cargas desde los NCs con un ancho de banda prohibida mayor (los NCs más pequeños) a los nanocristales con un ancho de banda prohibida menor (los más grandes). Al aumentar sustancialmente la densidad de cargas en los NCs más grandes, se incrementa la proporción de recombinación radiativa. Gracias a este mecanismo, los LEDs presentaron emisión en el verde con un valor de máximo de luminancia de aproximadamente 56000 cd m^{-2}, eficiencia de corriente de ~58 cd A^{-1}, eficiencia de potencia de ~58 cd A^{-1} y EQE de 13,4%.

4.4. Trabajo publicado

El trabajo se realizó en estrecha colaboración con ERI@N, un instituto de investigación de la Nanyang Technological University de Singapur dirigido por el Prof. Subodh Mhaisalkar.

La publicación mostrada en la página 73 está reproducida con el permiso de The Royal Society of Chemistry. DOI: 10.1039/C8EE00293B, Energy Environ. Sci., 2018, 11, 1770-1778.

Capítulo 5. Síntesis mecanoquímica de sólidos de perovskita híbrida altamente luminiscentes, azules y verdes

5.1. Motivación, descripción del trabajo y logro

La síntesis mecanoquímica "seca" es una técnica alternativa a los procesos de síntesis por disolución de las perovskitas. Es un método simple que permite preparar perovskitas con prácticamente cualquier composición, sin limitaciones de solubilidad ni posible presencia de aditivos de procesamiento o disolventes (tóxicos) en el material final.[76,134–140] Además, las perovskitas sintetizadas por mecanoquímica han demostrado una mayor estabilidad debido a la alta pureza y cristalinidad superior de los materiales en forma de polvo, que resulta en interacciones más fuertes dentro de las redes cristalinas.[141,142]

La producción de perovskitas estables y luminiscentes con un gran ancho de banda prohibida (> 2.5 eV) sigue siendo un desafío, ya que las sales precursoras (cloruros metálicos) tienen baja solubilidad y las perovskitas suelen mostrar bajo PLQY.[149,150,153] Además, las perovskitas de haluros mixtos a menudo sufren segregación fotoinducida de los haluros,[94,154] lo que complica aún más la preparación de perovskitas con emisión en el azul eficientes y estables.

En este capítulo se describe un método simple para obtener perovskitas 3D con un ancho de banda prohibida amplio, de tipo $MA_{1-y}Cs_yPb(Br_nCl_{1-n})_3$. Los materiales se preparan mediante síntesis mecanoquímica en seco (molienda de bolas) a partir de precursores puros, y muestran fotoluminiscencia mejorada tras la adición de un derivado de adamantano en la mezcla de precursores. La caracterización estructural sugiere que el aditivo no participa en la estructura cristalina de la perovskita. Ajustando la estequiometría de los precursores, la fotoluminiscencia puede modularse desde el UV a la parte verde del espectro visible.

5.2. Detalles experimentales y metodología

La perovskita $MA_{0,8}Cs_{0,2}Pb(Br_{0,6}Cl_{0,4})_3$ se preparó mediante molienda de bolas, mezclando 0,48 mol de MABr; 0,32 mol de MACl; 0,12 mol de CsBr y 0,08 mol de CsCl con 0,6 mol de $PbBr_2$ y 0,4 mol de $PbCl_2$, dentro de una caja seca con atmósfera de nitrógeno. La mezcla de polvos precursores se introdujo luego en un recipiente de zirconia de 10 mL, junto con bolas de zirconia. Posteriormente, se llevó a cabo el proceso de molienda a una frecuencia de 30 Hz durante 2 horas. El polvo amarillento resultante se estudió tal cual se obtuvo, en condiciones ambientales. Las muestras pasivadas se obtuvieron agregando una cantidad creciente (de 0 a 90% molar) de hidrocloruro de amantadina (o clorhidrato de 1-adamantanamina, AmCl) a la mezcla antes de la molienda. Para el resto de las muestras de $MA_yCs_{1-y}Pb(Br_nCl_{1-n})_3$, las proporciones de precursores se ajustaron en consecuencia, modificando la relación molar Cs^+/MA^+ de 0 ($MAPb(Br_nCl_{1-n})_3$ puro) a 1 ($CsPb(Br_nCl_{1-n})_3$ puro) o la relación molar Br^-/Cl^- de 0 ($MA_yCs_{1-y}PbCl_3$ puro) a 1 ($MA_yCs_{1-y}PbBr_3$ puro).

5.3. Resultados y discusión

El análisis de la perovskita $MA_{0,8}Cs_{0,2}Pb(Br_{0,6}Cl_{0,4})_3$ mediante difracción de rayos-X y absorción óptica mostró la presencia de una sola fase de haluro mixto, con una absorción óptica intensa a partir de aproximadamente los 500 nm. Sin embargo, no se pudo detectar ninguna señal de PL. Para intentar reducir los estados electrónicos responsables de la recombinación no radiativa, se agregó AmCl a los precursores de la síntesis mecanoquímica y se estudió su efecto variando la concentración de 10 a 90 mol%. La caracterización de los materiales resultantes mostró que la adición de AmCl no conducía a la formación o segregación de diferentes fases, sino que mantenía una única fase homogénea de perovskita (haluro mixto). En presencia de AmCl, el material bulk $MA_{0,8}Cs_{0,2}Pb(Br_{0,6}Cl_{0,4})_3$ aumentó el PLQY de 0 a 4% para una concentración de AmCl de 40-50 mol%, indicando que el aditivo AmCl es capaz de pasivar la perovskita.

Para estudiar el efecto de la composición del material sobre las propiedades ópticas, se modificó la cantidad de Cs^+ en la síntesis mecanoquímica de $MA_{1-y}Cs_yPb(Br_{0,6}Cl_{0,4})_3$ de y = 0 a 0,2; 0,4 y 1, manteniendo una concentración de AmCl del 50 mol%. La caracterización estructural mostró un alto grado de conversión y cristalinidad para la serie de compuestos, con el mismo patrón de difracción pero con un pequeño desplazamiento a ángulos más grandes a medida que se sustituía el MA^+ por el catión cesio más pequeño. También se observó un ligero cambio del máximo de emisión PL a longitudes de onda más bajas. Al aumentar el contenido de Cs en la síntesis, el PLQY disminuyó de un máximo de 7% (y = 0) a aproximadamente 1% (compuesto inorgánico puro, y = 1). Este comportamiento se atribuyó al mayor momento dipolar (2,3 D) y libertad de rotación del catión MA^+, que puede compensar la formación de estados electrónicos responsables de la recombinación no-radiativa.[161,162]

También se estudió el efecto del intercambio de haluro sobre las características ópticas de la perovskita. Para ello, el contenido de bromuro se aumentó de forma gradual de 0 a 1 en la preparación de 6 perovskitas diferentes del tipo $MAPb(Br_nCl_{1-n})_3$, manteniendo constante la concentración de AmCl a 50 mol%. El análisis de difracción de rayos X confirmó la formación de perovskitas de cloruro y bromuro altamente cristalinas, así como de las especies de haluros mixtos. Los patrones de difracción mostraron un desplazamiento de las señales correspondientes a los mismos planos a ángulos más pequeños a medida que aumentaba la relación Br^-/Cl^-. Los resultados de la caracterización óptica mostraron una disminución del ancho de banda prohibida y un desplazamiento del máximo de emisión hacia longitudes de onda menores a medida que se aumentaba el contenido de bromuro. A medida que disminuía el ancho de banda prohibida, el PLQY asociado aumentaba de aproximadamente 1% (para $0 \leq n \leq 0,4$) a 7% (n = 0,6), y hasta 15% y 29% para el $MAPb(Br_nCl_{1-n})_3$ con n = 0,8 y 1, respectivamente. El aumento del PLQY al disminuir el ancho de banda de las perovskitas podría estar relacionado con la energía y la distribución de los estados electrónico responsables de recombinación no radiativa con respecto a las bandas electrónicas de los semiconductores. Los estados electrónicos de trampa, profundos en las perovskitas azules,

se acercan o caen dentro de las bandas electrónicas cuando disminuye el ancho de banda prohibida.

5.4. Trabajo publicado

La publicación mostrada en la página 131 está reproducida desde Wiley-VCH. DOI: 10.1002/adom.201901494, Adv. Optical Mater., 2019, 1901494.

Capítulo 6. Conclusiones generales

El objetivo de la tesis ha sido la preparación de materiales de perovskita de alta calidad, con alta pureza, alta eficiencia de PL y color variable, para el desarrollo de LEDs de futura generación. En esta tesis, se describe algunos materiales luminiscentes, eficientes y económicos, y dispositivos emisores de luz.

El Capítulo 2 se centra en la preparación de perovskita con emisión en el rojo, estable y muy luminiscente. El sistema consiste en nanocristales de perovskita híbrida cuasi-2D de tipo $(LA)_2(A)_{n-1}Pb_nI_{3n+1}$, donde LA es un catión alquilamonio y A una mezcla de MA^+ y Cs^+. El ancho de banda prohibida de estas estructuras, y por lo tanto la longitud de onda de emisión, puede modificarse variando la longitud de la cadena de los ligados empleados en la síntesis. Este efecto se debe a la formación de cristales cuasi-2D con diferentes periodicidades y diferente espaciado entre capas, lo que supone un cambio del confinamiento cuántico. Sorprendentemente, la adición de butanol en la purificación del material aumenta la pureza y el rendimiento cuántico fotoluminiscente, superior al 90%. El alto rendimiento cuántico fotoluminiscente se mantiene durante más de 500 horas, lo que hace que estos materiales sean especialmente prometedores para aplicaciones en diodos emisores de luz y fósforos.

El Capítulo 3 describe el uso novedoso de un ligando bifuncional para la síntesis de perovskita altamente fotoluminiscentes con emisión en el verde, y la preparación de LEDs multicapa por disolución. El sistema consiste en nanopartículas de $MAPbBr_3$ con bromhidrato de ácido 11-aminoundecanoico como ligando de coordinación, con un diámetro inferior a 10 nm y un rendimiento cuántico fotoluminiscente de aproximadamente el 80%, obtenidas fácilmente a temperatura ambiente y en condiciones atmosféricas. Gracias al uso del ligando bifuncional $Br^-NH_3^+$-C_{10}-COOH, las nanopartículas se pueden anclar en diferentes superficies electroactivas, como semiconductores inorgánicos o polímeros conductores. Las nanopartículas ancladas a capas delgadas de ZnO y PEDOT:PSS muestran un notable rendimiento cuántico de fotoluminiscencia de aproximadamente 50%, y pueden integrarse directamente en dispositivos emisores de luz. El anclaje de nanopartículas semiconductoras a distintas superficies abre nuevos caminos para la preparación de LEDs multicapa simples y económicos.

El Capítulo 4 describe la preparación de LEDs emisores en el verde con una combinación de alta eficiencia cuántica externa, luminancia, potencia y eficiencia de corriente. El sistema consiste en microláminas de bromuro de plomo y octilamonio de baja dimensionalidad y nanocristales de $FAPbBr_3$ 3D, que forman capas compuestas por estructuras jerárquicas 2D-3D autoensambladas con un rendimiento cuántico fotoluminiscente superior al 80%. El alto rendimiento se debe a una transferencia de energía en cascada entre las estructuras jerárquicas autoensambladas. En dispositivos, las microláminas 2D funcionan como capa de transporte y como intermediario para equilibrar la inyección de electrones y huecos,

mientras pasivan los nanocristales. Los portadores de carga se generan en los nanocristales con mayores anchos de banda prohibida (los nanocristales más pequeños) y rápidamente se transfieren a los nanocristales con menores anchos de banda prohibida (los más grandes). En los nanocristales más grandes, la densidad de portadores de carga aumenta sustancialmente, reduciendo las posibilidades de recombinación no radiativa. Este mecanismo es responsable de una luminancia máxima de aproximadamente 56000 cd m^{-2}, ~58 cd A^{-1} de eficiencia de corriente, ~58 cd A^{-1} de eficiencia energética y 13,4% de eficiencia cuántica externa.

En el Capítulo 5 se describe un método simple para obtener materiales fotoluminiscentes de perovskita 3D de haluro mixto del tipo $MA_{1-y}Cs_yPb(Br_nCl_{1-n})_3$ con un amplio ancho de banda prohibida y con una emisión que abarca desde la región azul a la verde del espectro visible. Los materiales se preparan mediante una síntesis mecanoquímica en seco (molienda de bolas) a partir de precursores binarios puros, y su composición, y por lo tanto la longitud de onda de emisión, se puede modificar fácilmente simplemente controlando la estequiometría de los precursores. Mientras que no se puede detectar fotoluminiscencia de la muestra de perovskita pura, la adición de clorhidrato de amantadina en la mezcla de precursores permite obtener un importante aumento en el rendimiento cuántico fotoluminiscente, casi sin cambios estructurales. Ente incremento indica la pasivación de centros de recombinación no radiativa que estaban presentes en la muestra sin aditivos. La estrategia descrita permite obtener polvos de perovskita 3D con valores de eficiencia fotoluminiscente de hasta 7% en el rango de emisión azul (y = 0; n = 0,6) y 29% en el rango de emisión verde (y = 0; n = 1).

Las estrategias y sistemas investigados y descritos en los diferentes capítulos tienen como objetivo contribuir al progreso de la optoelectrónica de perovskita.

Bibliography

[1] R. Zhu, Z. Luo, H. Chen, Y. Dong, S.-T. Wu, *Opt. Express* **2015**, *23*, 23680.

[2] Q. Fu, X. Tang, B. Huang, T. Hu, L. Tan, L. Chen, Y. Chen, *Adv. Sci.* **2018**, *5*, 1700387.

[3] N. H. Tiep, Z. Ku, H. J. Fan, *Adv. Energy Mater.* **2016**, *6*, 1.

[4] G. Niu, X. Guo, L. Wang, *J. Mater. Chem. A* **2015**, *3*, 8970.

[5] Best Research-Cell Efficiency Chart, https://www.nrel.gov/pv/cell-efficiency.html.

[6] Y. Miao, Y. Ke, N. Wang, W. Zou, M. Xu, Y. Cao, Y. Sun, R. Yang, Y. Wang, Y. Tong, W. Xu, L. Zhang, R. Li, J. Li, H. He, Y. Jin, F. Gao, W. Huang, J. Wang, *Nat. Commun.* **2019**, *10*, 1.

[7] H. C. Weerasinghe, Y. Dkhissi, A. D. Scully, R. A. Caruso, Y.-B. Cheng, *Nano Energy* **2015**, *18*, 118.

[8] Y. Wei, X. Deng, Z. Xie, X. Cai, S. Liang, P. Ma, Z. Hou, Z. Cheng, J. Lin, *Adv. Funct. Mater.* **2017**, *27*, 1.

[9] A. Binek, M. L. Petrus, N. Huber, H. Bristow, Y. Hu, T. Bein, P. Docampo, *ACS Appl. Mater. Interfaces* **2016**, *8*, 12881.

[10] J. M. Kadro, N. Pellet, F. Giordano, A. Ulianov, O. Müntener, J. Maier, M. Grätzel, A. Hagfeldt, *Energy Environ. Sci.* **2016**, *9*, 3172.

[11] J.-T. Lin, C.-C. Liao, C.-S. Hsu, D.-G. Chen, H.-M. Chen, M.-K. Tsai, P.-T. Chou, C.-W. Chiu, *J. Am. Chem. Soc.* **2019**, *141*, 10324.

[12] X. Chang, D. Marongiu, V. Sarritzu, N. Sestu, Q. Wang, S. Lai, A. Mattoni, A. Filippetti, F. Congiu, A. G. Lehmann, F. Quochi, M. Saba, A. Mura, G. Bongiovanni, *Adv. Funct. Mater.* **2019**, *29*, 1903528.

[13] C. Lan, G. Liang, S. Zhao, H. Lan, H. Peng, D. Zhang, H. Sun, J. Luo, P. Fan, *Sol. Energy* **2019**, *177*, 501.

[14] A. Singh, N.-C. Chiu, K. M. Boopathi, Y.-J. Lu, A. Mohapatra, G. Li, Y.-F. Chen, T.-F. Guo, C.-W. Chu, *ACS Appl. Mater. Interfaces* **2019**, *11*, 35088.

[15] Q. Zhang, F. Hao, J. Li, Y. Zhou, Y. Wei, H. Lin, *Sci. Technol. Adv. Mater.* **2018**, *19*, 425.

[16] P. Paufler, *Acta Crystallogr. Sect. A Found. Crystallogr.* **2012**, *68*, 523.

[17] J. Koppen, R. Hamersma, J. V. Lebesque, A. R. Miedema, *Phys. Lett. A* **1967**, *25*, 376.

[18] E. R. Peterson, R. D. Willett, *J. Chem. Phys.* **1972**, *56*, 1879.

[19] T. Ishihara, J. Takahashi, T. Goto, *Solid State Commun.* **1989**, *69*, 933.

[20] T. Ishihara, J. Takahashi, T. Goto, *Phys. Rev. B* **1990**, *42*, 11099.

[21] M. Era, S. Morimoto, T. Tsutsui, S. Saito, *Appl. Phys. Lett.* **1994**, *65*, 676.

[22] T. Hattori, T. Taira, M. Era, T. Tsutsui, S. Saito, *Chem. Phys. Lett.* **1996**, *254*, 103.

[23] Z. K. Tan, R. S. Moghaddam, M. L. Lai, P. Docampo, R. Higler, F. Deschler, M. Price, A. Sadhanala, L. M. Pazos, D. Credgington, F. Hanusch, T. Bein, H. J. Snaith, R. H. Friend, *Nat. Nanotechnol.* **2014**, *9*, 687.

[24] N. Kitazawa, *J. Mater. Sci.* **1998**, *33*, 1441.

[25] A. Kojima, M. Ikegami, K. Teshima, T. Miyasaka, *Chem. Lett.* **2012**, *41*, 397.

[26] L. C. Schmidt, A. Pertegás, S. González-Carrero, O. Malinkiewicz, S. Agouram, G. Mínguez Espallargas, H. J. Bolink, R. E. Galian, J. Pérez-Prieto, *J. Am. Chem. Soc.* **2014**, *136*, 850.

[27] K. Lin, J. Xing, L. N. Quan, F. P. G. de Arquer, X. Gong, J. Lu, L. Xie, W. Zhao, D. Zhang, C. Yan, W. Li, X. Liu, Y. Lu, J. Kirman, E. H. Sargent, Q. Xiong, Z. Wei, *Nature* **2018**, *562*, 245.

[28] Y. Liu, J. Cui, K. Du, H. Tian, Z. He, Q. Zhou, Z. Yang, Y. Deng, D. Chen, X. Zuo, Y. Ren, L. Wang, H. Zhu, B. Zhao, D. Di, J. Wang, R. H. Friend, Y. Jin, *Nat. Photonics* **2019**, *13*, 760.

[29] V. M. Goldschmidt, *Berichte Der Dtsch. Chem. Gesellschaft* **1927**, *60*, 1263.

[30] C. Li, X. Lu, W. Ding, L. Feng, Y. Gao, Z. Guo, *Acta Crystallogr. Sect. B Struct. Sci.* **2008**, *64*, 702.

[31] H. Lin, C. Zhou, Y. Tian, T. Siegrist, B. Ma, *ACS Energy Lett.* **2018**, *3*, 54.

[32] S. González-Carrero, R. E. Galian, J. Pérez-Prieto, *Part. Part. Syst. Charact.* **2015**, *32*, 709.

[33] B. Saparov, D. B. Mitzi, *Chem. Rev.* **2016**, *116*, 4558.

[34] Y. Fu, M. P. Hautzinger, Z. Luo, F. Wang, D. Pan, M. M. Aristov, I. A. Guzei, A. Pan, X. Zhu, S. Jin, *ACS Cent. Sci.* **2019**, *5*, 1377.

[35] Z. Wang, Q. Lin, F. P. Chmiel, N. Sakai, L. M. Herz, H. J. Snaith, *Nat. Energy* **2017**, *2*, 17135.

[36] C. C. Stoumpos, D. H. Cao, D. J. Clark, J. Young, J. M. Rondinelli, J. I. Jang, J. T. Hupp, M. G. Kanatzidis, *Chem. Mater.* **2016**, *28*, 2852.

[37] L. Zhang, X. Yang, Q. Jiang, P. Wang, Z. Yin, X. Zhang, H. Tan, Y. M. Yang, M. Wei, B. R. Sutherland, E. H. Sargent, J. You, *Nat. Commun.* **2017**, *8*, 15640.

[38] L. N. Quan, M. Yuan, R. Comin, O. Voznyy, E. M. Beauregard, S. Hoogland, A. Buin, A. R. Kirmani, K. Zhao, A. Amassian, D. H. Kim, E. H. Sargent, *J. Am. Chem. Soc.* **2016**, *138*, 2649.

[39] E. R. Dohner, E. T. Hoke, H. I. Karunadasa, *J. Am. Chem. Soc.* **2014**, *136*, 1718.

[40] E. R. Dohner, A. Jaffe, L. R. Bradshaw, H. I. Karunadasa, *J. Am. Chem. Soc.* **2014**, *136*, 13154.

[41] H. Lin, C. Zhou, Y. Tian, T. Besara, J. Neu, T. Siegrist, Y. Zhou, J. Bullock, K. S. Schanze, W. Ming, M. H. Du, B. Ma, *Chem. Sci.* **2017**, *8*, 8400.

[42] Z. Yuan, C. Zhou, Y. Tian, Y. Shu, J. Messier, J. C. Wang, L. J. Van De Burgt, K. Kountouriotis, Y. Xin, E. Holt, K. Schanze, R. Clark, T. Siegrist, B. Ma, *Nat. Commun.* **2017**, *8*, 1.

[43] Y. Li, G. Zheng, C. Lin, J. Lin, *Solid State Sci.* **2007**, *9*, 855.

[44] M. De Bastiani, I. Dursun, Y. Zhang, B. A. Alshankiti, X. H. Miao, J. Yin, E. Yengel, E. Alarousu, B. Turedi, J. M. Almutlaq, M. I. Saidaminov, S. Mitra, I. Gereige, A. Alsaggaf, Y. Zhu, Y. Han, I. S. Roqan, J. L. Bredas, O. F. Mohammed, O. M. Bakr, *Chem. Mater.*

2017, *29*, 7108.

[45] C. Zhou, H. Lin, Y. Tian, Z. Yuan, R. Clark, B. Chen, L. J. Van De Burgt, J. C. Wang, Y. Zhou, K. Hanson, Q. J. Meisner, J. Neu, T. Besara, T. Siegrist, E. Lambers, P. Djurovich, B. Ma, *Chem. Sci.* **2018**, *9*, 586.

[46] Q. A. Akkerman, S. G. Motti, A. R. Srimath Kandada, E. Mosconi, V. D'Innocenzo, G. Bertoni, S. Marras, B. A. Kamino, L. Miranda, F. De Angelis, A. Petrozza, M. Prato, L. Manna, *J. Am. Chem. Soc.* **2016**, *138*, 1010.

[47] D. Zhang, Y. Yu, Y. Bekenstein, A. B. Wong, A. P. Alivisatos, P. Yang, *J. Am. Chem. Soc.* **2016**, *138*, 13155.

[48] Z. Wen, W. Zhai, C. Liu, J. Lin, C. Yu, Y. Huang, J. Zhang, C. Tang, *RSC Adv.* **2019**, *9*, 24928.

[49] M. J. Ashley, M. N. O'Brien, K. R. Hedderick, J. A. Mason, M. B. Ross, C. A. Mirkin, *J. Am. Chem. Soc.* **2016**, *138*, 10096.

[50] J. Shamsi, A. S. Urban, M. Imran, L. De Trizio, L. Manna, *Chem. Rev.* **2019**, *119*, 3296.

[51] K. Tanaka, T. Takahashi, T. Ban, T. Kondo, K. Uchida, N. Miura, *Solid State Commun.* **2003**, *127*, 619.

[52] L. Protesescu, S. Yakunin, M. I. Bodnarchuk, F. Krieg, R. Caputo, C. H. Hendon, R. X. Yang, A. Walsh, M. V. Kovalenko, *Nano Lett.* **2015**, *15*, 3692.

[53] G. E. Eperon, S. D. Stranks, C. Menelaou, M. B. Johnston, L. M. Herz, H. J. Snaith, *Energy Environ. Sci.* **2014**, *7*, 982.

[54] S. Tao, I. Schmidt, G. Brocks, J. Jiang, I. Tranca, K. Meerholz, S. Olthof, *Nat. Commun.* **2019**, *10*, 1.

[55] T. Umebayashi, K. Asai, T. Kondo, A. Nakao, *Phys. Rev. B - Condens. Matter Mater. Phys.* **2003**, *67*, 155405.

[56] Y. H. Chang, C. H. Park, K. Matsuishi, *J. Korean Phys. Soc.* **2004**, *44*, 889.

[57] F. Brivio, A. B. Walker, A. Walsh, *APL Mater.* **2013**, *1*, 042111.

[58] D. Di, K. P. Musselman, G. Li, A. Sadhanala, Y. Ievskaya, Q. Song, Z. K. Tan, M. L. Lai, J. L. MacManus-Driscoll, N. C. Greenham, R. H. Friend, *J. Phys. Chem. Lett.* **2015**, *6*, 446.

[59] J. A. Sichert, Y. Tong, N. Mutz, M. Vollmer, S. Fischer, K. Z. Milowska, R. García Cortadella, B. Nickel, C. Cardenas-Daw, J. K. Stolarczyk, A. S. Urban, J. Feldmann, N. Mutz, Y. Tong, C. Cardenas-Daw, J. K. Stolarczyk, M. Vollmer, S. Fischer, A. S. Urban, J. A. Sichert, K. Z. Milowska, B. Nickel, R. García Cortadella, Y. Tong, N. Mutz, M. Vollmer, S. Fischer, K. Z. Milowska, R. García Cortadella, B. Nickel, C. Cardenas-Daw, J. K. Stolarczyk, A. S. Urban, J. Feldmann, *Nano Lett.* **2015**, *15*, 6521.

[60] C. Ran, J. Xu, W. Gao, C. Huang, S. Dou, *Chem. Soc. Rev.* **2018**, *47*, 4581.

[61] J. Kang, L. W. Wang, *J. Phys. Chem. Lett.* **2017**, *8*, 489.

[62] F. Liu, Y. Zhang, C. Ding, S. Kobayashi, T. Izuishi, N. Nakazawa, T. Toyoda, T. Ohta, S. Hayase, T. Minemoto, K. Yoshino, S. Dai, Q. Shen, *ACS Nano* **2017**, *11*, 10373.

[63] A. Kojima, K. Teshima, Y. Shirai, T. Miyasaka, *J. Am. Chem. Soc.* **2009**, *131*, 6050.

[64] S. D. Stranks, G. E. Eperon, G. Grancini, C. Menelaou, M. J. P. Alcocer, T. Leijtens, L. M. Herz, A. Petrozza, H. J. Snaith, *Science* **2013**, *342*, 341.

[65] Q. Dong, Y. Fang, Y. Shao, P. Mulligan, J. Qiu, L. Cao, J. Huang, *Science* **2015**, *347*, 967.

[66] C. S. Ponseca, T. J. Savenije, M. Abdellah, K. Zheng, A. Yartsev, T. Pascher, T. Harlang, P. Chabera, T. Pullerits, A. Stepanov, J. P. Wolf, V. Sundström, *J. Am. Chem. Soc.* **2014**, *136*, 5189.

[67] F. Zhang, H. Zhong, C. Chen, X. G. Wu, X. Hu, H. Huang, J. Han, B. Zou, Y. Dong, *ACS Nano* **2015**, *9*, 4533.

[68] S. Gonzalez-Carrero, L. C. Schmidt, I. Rosa-Pardo, L. Martínez-Sarti, M. Sessolo, R. E. Galian, J. Pérez-Prieto, *ACS Omega* **2018**, *3*, 1298.

[69] H. Huang, F. Zhao, L. Liu, F. Zhang, X. G. Wu, L. Shi, B. Zou, Q. Pei, H. Zhong, *ACS Appl. Mater. Interfaces* **2015**, *7*, 28128.

[70] M. Chen, Y. Zou, L. Wu, Q. Pan, D. Yang, H. Hu, Y. Tan, Q. Zhong, Y. Xu, H. Liu, B. Sun, Q. Zhang, *Adv. Funct. Mater.* **2017**, *27*, 1701121.

[71] Y. Tong, E. Bladt, M. F. Aygüler, A. Manzi, K. Z. Milowska, V. A. Hintermayr, P. Docampo, S. Bals, A. S. Urban, L. Polavarapu, J. Feldmann, *Angew. Chemie - Int. Ed.* **2016**, *55*, 13887.

[72] H. Liu, Z. Wu, H. Gao, J. Shao, H. Zou, D. Yao, Y. Liu, H. Zhang, B. Yang, *ACS Appl. Mater. Interfaces* **2017**, *9*, 42919.

[73] Y. Hassan, Y. Song, R. D. Pensack, A. I. Abdelrahman, Y. Kobayashi, M. A. Winnik, G. D. Scholes, *Adv. Mater.* **2016**, *28*, 566.

[74] L. Zhao, Y. W. Yeh, N. L. Tran, F. Wu, Z. Xiao, R. A. Kerner, Y. L. Lin, G. D. Scholes, N. Yao, B. P. Rand, *ACS Nano* **2017**, *11*, 3957.

[75] D. Chen, J. Li, X. Chen, J. Chen, J. Zhong, *ACS Appl. Mater. Interfaces* **2019**, *11*, 10059.

[76] L. Protesescu, S. Yakunin, O. Nazarenko, D. N. Dirin, M. V. Kovalenko, *ACS Appl. Nano Mater.* **2018**, *1*, 1300.

[77] T. Matsushima, F. Bencheikh, T. Komino, M. R. Leyden, A. S. D. Sandanayaka, C. Qin, C. Adachi, *Nature* **2019**, *572*, 502.

[78] S. Heo, G. Seo, Y. Lee, D. Lee, M. Seol, J. Lee, J. B. Park, K. Kim, D. J. Yun, Y. S. Kim, J. K. Shin, T. K. Ahn, M. K. Nazeeruddin, *Energy Environ. Sci.* **2017**, *10*, 1128.

[79] X. Sun, R. Asadpour, W. Nie, A. D. Mohite, M. A. Alam, *IEEE J. Photovoltaics* **2015**, *5*, 1389.

[80] C. Momblona, L. Gil-Escrig, E. Bandiello, E. M. Hutter, M. Sessolo, K. Lederer, J. Blochwitz-Nimoth, H. J. Bolink, *Energy Environ. Sci.* **2016**, *9*, 3456.

[81] J. W. Lee, N. G. Park, *MRS Bull.* **2015**, *40*, 654.

[82] M. Sessolo, C. Momblona, L. Gil-Escrig, H. J. Bolink, *MRS Bull.* **2015**, *40*, 660.

[83] H. Zhou, Q. Chen, Y. Yang, *MRS Bull.* **2015**, *40*, 667.

[84] M. Liu, M. B. Johnston, H. J. Snaith, *Nature* **2013**, *501*, 395.

[85] O. Malinkiewicz, A. Yella, Y. H. Lee, G. M. Espallargas, M. Graetzel, M. K. Nazeeruddin, H. J. Bolink, *Nat. Photonics* **2014**, *8*, 128.

[86] M. Era, T. Hattori, T. Taira, T. Tsutsui, *Chem. Mater.* **1997**, *9*, 8.

[87] B. Conings, J. Drijkoningen, N. Gauquelin, A. Babayigit, J. D'Haen, L. D'Olieslaeger, A.

Ethirajan, J. Verbeeck, J. Manca, E. Mosconi, F. De Angelis, H. G. Boyen, *Adv. Energy Mater.* **2015**, *5*, 1.

[88] D. M. Trots, S. V. Myagkota, *J. Phys. Chem. Solids* **2008**, *69*, 2520.

[89] H. Huang, M. I. Bodnarchuk, S. V. Kershaw, M. V. Kovalenko, A. L. Rogach, *ACS Energy Lett.* **2017**, *2*, 2071.

[90] L. Protesescu, S. Yakunin, S. Kumar, J. Bär, F. Bertolotti, N. Masciocchi, A. Guagliardi, M. Grotevent, I. Shorubalko, M. I. Bodnarchuk, C. J. Shih, M. V. Kovalenko, *ACS Nano* **2017**, *11*, 3119.

[91] C. Wang, A. S. R. Chesman, J. J. Jasieniak, *Chem. Commun.* **2017**, *53*, 232.

[92] J. Pan, Y. Shang, J. Yin, M. De Bastiani, W. Peng, I. Dursun, L. Sinatra, A. M. El-Zohry, M. N. Hedhili, A. H. Emwas, O. F. Mohammed, Z. Ning, O. M. Bakr, *J. Am. Chem. Soc.* **2018**, *140*, 562.

[93] E. T. Hoke, D. J. Slotcavage, E. R. Dohner, A. R. Bowring, H. I. Karunadasa, M. D. McGehee, *Chem. Sci.* **2015**, *6*, 613.

[94] M. C. Brennan, S. Draguta, P. V. Kamat, M. Kuno, *ACS Energy Lett.* **2018**, *3*, 204.

[95] J. W. Lee, D. H. Kim, H. S. Kim, S. W. Seo, S. M. Cho, N. G. Park, *Adv. Energy Mater.* **2015**, *5*, 1501310.

[96] G. Niu, W. Li, J. Li, X. Liang, L. Wang, *RSC Adv.* **2017**, *7*, 17473.

[97] X. Liu, Z. Yang, C. C. Chueh, A. Rajagopal, S. T. Williams, Y. Sun, A. K. Y. Jen, *J. Mater. Chem. A* **2016**, *4*, 17939.

[98] X. Liang, R. W. Baker, K. Wu, W. Deng, D. Ferdani, P. S. Kubiak, F. Marken, L. Torrente-Murciano, P. J. Cameron, *React. Chem. Eng.* **2018**, *3*, 640.

[99] J. Cho, Y. H. Choi, T. E. O'Loughlin, L. De Jesus, S. Banerjee, *Chem. Mater.* **2016**, *28*, 6909.

[100] D. H. Cao, C. C. Stoumpos, O. K. Farha, J. T. Hupp, M. G. Kanatzidis, *J. Am. Chem. Soc.* **2015**, *137*, 7843.

[101] Y. H. Chang, J. C. Lin, Y. C. Chen, T. R. Kuo, D. Y. Wang, *Nanoscale Res. Lett.* **2018**, *13*, 247.

[102] J. V. Milić, J. H. Im, D. J. Kubicki, A. Ummadisingu, J. Y. Seo, Y. Li, M. A. Ruiz-Preciado, M. I. Dar, S. M. Zakeeruddin, L. Emsley, M. Grätzel, *Adv. Energy Mater.* **2019**, *9*, 1.

[103] X. X. Zhang, C. Wang, Y. Zhang, X. X. Zhang, S. Wang, M. Lu, H. Cui, S. V. Kershaw, W. W. Yu, A. L. Rogach, *ACS Energy Lett.* **2019**, *4*, 242.

[104] S. Ahmad, C. Hanmandlu, P. K. Kanaujia, G. V. Prakash, *Opt. Mater. Express* **2014**, *4*, 1313.

[105] S. Sun, D. Yuan, Y. Xu, A. Wang, Z. Deng, *ACS Nano* **2016**, *10*, 3648.

[106] A. Pan, B. He, X. Fan, Z. Liu, P. Alivisatos, L. He, Y. Liu, J. J. Urban, A. P. Alivisatos, L. He, Y. Liu, *ACS Nano* **2016**, *10*, 7943.

[107] N. Pradhan, D. Reifsnyder, R. Xie, J. Aldana, X. Peng, *J. Am. Chem. Soc.* **2007**, *129*, 9500.

[108] L. Yuan, R. Patterson, X. Wen, Z. Zhang, G. Conibeer, S. Huang, *J. Colloid Interface Sci.* **2017**, *504*, 586.

[109] Y. Takeoka, K. Asai, M. Rikukawa, K. Sanui, *Bull. Chem. Soc. Jpn.* **2006**, *79*, 1607.

[110] S. Gonzalez-Carrero, G. M. Espallargas, R. E. Galian, J. Pérez-Prieto, *J. Mater. Chem. A* **2015**, *3*, 14039.

[111] J. Yan, W. Qiu, G. Wu, P. Heremans, H. Chen, *J. Mater. Chem. A* **2018**, *6*, 11063.

[112] Y. Tian, M. Peter, E. Unger, M. Abdellah, K. Zheng, T. Pullerits, A. Yartsev, V. Sundström, I. G. Scheblykin, *Phys. Chem. Chem. Phys.* **2015**, *17*, 24978.

[113] H. Huang, A. S. Susha, S. V. Kershaw, T. F. Hung, A. L. Rogach, *Adv. Sci.* **2015**, *2*, 1.

[114] M. A. Boles, D. Ling, T. Hyeon, D. V. Talapin, *Nat. Mater.* **2016**, *15*, 141.

[115] L. Protesescu, S. Yakunin, M. I. Bodnarchuk, F. Bertolotti, N. Masciocchi, A. Guagliardi, M. V. Kovalenko, *J. Am. Chem. Soc.* **2016**, *138*, 14202.

[116] E. Galoppini, *Coord. Chem. Rev.* **2004**, *248*, 1283.

[117] D. B. Mitzi, K. Chondroudis, C. R. Kagan, *IBM J. Res. Dev.* **2001**, *45*, 29.

[118] D. Sapori, M. Kepenekian, L. Pedesseau, C. Katan, J. Even, *Nanoscale* **2016**, *8*, 6369.

[119] S. Bhaumik, S. A. Veldhuis, Y. F. Ng, M. Li, S. K. Muduli, T. C. Sum, B. Damodaran, S. Mhaisalkar, N. Mathews, *Chem. Commun.* **2016**, *52*, 7118.

[120] P. Tyagi, S. M. Arveson, W. A. Tisdale, *J. Phys. Chem. Lett.* **2015**, *6*, 1911.

[121] Z. Dang, J. Shamsi, F. Palazon, M. Imran, Q. A. Akkerman, S. Park, G. Bertoni, M. Prato, R. Brescia, L. Manna, *ACS Nano* **2017**, *11*, 2124.

[122] M. Sessolo, H. J. Bolink, *Adv. Mater.* **2011**, *23*, 1829.

[123] P. Audebert, G. Clavier, V. Alain-Rizzo, E. Deleporte, S. Zhang, J.-S. S. Lauret, G. Lanty, C. Boissière, *Chem. Mater.* **2009**, *21*, 210.

[124] Z. Yuan, Y. Shu, Y. Tian, Y. Xin, B. Ma, *Chem. Commun.* **2015**, *51*, 16385.

[125] S. Gonzalez-Carrero, R. E. Galian, J. Pérez-Prieto, *J. Mater. Chem. A* **2015**, *3*, 9187.

[126] H. Bin Kim, I. Im, Y. Yoon, S. Do Sung, E. Kim, J. Kim, W. I. Lee, *J. Mater. Chem. A* **2015**, *3*, 9264.

[127] Y. Athanassov, F. P. Rotzinger, P. Péchy, M. Grätzel, *J. Phys. Chem. B* **1997**, *101*, 2558.

[128] S. Coe, W. K. Woo, M. Bawendi, V. Bulović, *Nature* **2002**, *420*, 800.

[129] M. Yuan, L. N. Quan, R. Comin, G. Walters, R. Sabatini, O. Voznyy, S. Hoogland, Y. Zhao, E. M. Beauregard, P. Kanjanaboos, Z. Lu, D. H. Kim, E. H. Sargent, *Nat. Nanotechnol.* **2016**, *11*, 872.

[130] N. Wang, L. Cheng, R. Ge, S. Zhang, Y. Miao, W. Zou, C. Yi, Y. Sun, Y. Cao, R. Yang, Y. Wei, Q. Guo, Y. Ke, M. Yu, Y. Jin, Y. Liu, Q. Ding, D. Di, L. Yang, G. Xing, H. Tian, C. Jin, F. Gao, R. H. Friend, J. Wang, W. Huang, *Nat. Photonics* **2016**, *10*, 699.

[131] L. N. Quan, Y. Zhao, F. P. García De Arquer, R. Sabatini, G. Walters, O. Voznyy, R. Comin, Y. Li, J. Z. Fan, H. Tan, J. Pan, M. Yuan, O. M. Bakr, Z. Lu, D. H. Kim, E. H. Sargent, *Nano Lett.* **2017**, *17*, 3701.

[132] W. Y. Hung, G. C. Fang, S. W. Lin, S. H. Cheng, K. T. Wong, T. Y. Kuo, P. T. Chou, *Sci. Rep.* **2014**, *4*, 4.

[133] J. H. Lee, S. H. Cheng, S. J. Yoo, H. Shin, J. H. Chang, C. I. Wu, K. T. Wong, J. J. Kim, *Adv. Funct. Mater.* **2015**, *25*, 361.

[134] Y. Zhang, S. G. Kim, D. K. Lee, N. G. Park, *ChemSusChem* **2018**, *11*, 1813.

[135] D. Prochowicz, P. Yadav, M. Saliba, M. Saski, S. M. Zakeeruddin, J. Lewiński, M. Grätzel, *ACS Appl. Mater. Interfaces* **2017**, *9*, 28418.

[136] Y. El Ajjouri, F. Palazon, M. Sessolo, H. J. Bolink, *Chem. Mater.* **2018**, *30*, 7423.

[137] P. Sadhukhan, S. Kundu, A. Roy, A. Ray, P. Maji, H. Dutta, S. K. Pradhan, S. Das, *Cryst. Growth Des.* **2018**, *18*, 3428.

[138] Z. Hong, D. Tan, R. A. John, Y. K. E. Tay, Y. K. T. Ho, X. Zhao, T. C. Sum, N. Mathews, F. García, H. Sen Soo, *iScience* **2019**, *16*, 312.

[139] S. Yun, A. Kirakosyan, S. G. Yoon, J. Choi, *ACS Sustain. Chem. Eng.* **2018**, *6*, 3733.

[140] F. Palazon, Y. El Ajjouri, H. J. Bolink, *Adv. Energy Mater.* **2019**, *1902499*, 1.

[141] J.-J. Nath, Narayan Chandra Deb; Murugadoss, Gavindasamy; Lee, *Nanosci. Nanotechnol. Lett.* **2018**, *10*, 1025.

[142] N. Leupold, K. Schötz, S. Cacovich, I. Bauer, M. Schultz, M. Daubinger, L. Kaiser, A. Rebai, J. Rousset, A. Köhler, P. Schulz, R. Moos, F. Panzer, *ACS Appl. Mater. Interfaces* **2019**, *11*, 30259.

[143] P. Fan, D. Gu, G. X. Liang, J. T. Luo, J. L. Chen, Z. H. Zheng, D. P. Zhang, *Sci. Rep.* **2016**, *6*, 1.

[144] G. Longo, L. Gil-Escrig, M. J. Degen, M. Sessolo, H. J. Bolink, *Chem. Commun.* **2015**, *51*, 7376.

[145] J. Ávila, C. Momblona, P. P. Boix, M. Sessolo, H. J. Bolink, *Joule* **2017**, *1*, 431.

[146] M. J. Crane, D. M. Kroupa, J. Y. Roh, R. T. Anderson, M. D. Smith, D. R. Gamelin, *ACS Appl. Energy Mater.* **2019**, *2*, 4560.

[147] J. H. Noh, S. H. Im, J. H. Heo, T. N. Mandal, S. Il Seok, *Nano Lett.* **2013**, *13*, 1764.

[148] I. Levchuk, A. Osvet, X. Tang, M. Brandl, J. D. Perea, F. Hoegl, G. J. Matt, R. Hock, M. Batentschuk, C. J. Brabec, *Nano Lett.* **2017**, *17*, 2765.

[149] Q. A. Akkerman, V. D'Innocenzo, S. Accornero, A. Scarpellini, A. Petrozza, M. Prato, L. Manna, *J. Am. Chem. Soc.* **2015**, *137*, 10276.

[150] A. Sadhanala, S. Ahmad, B. Zhao, N. Giesbrecht, P. M. Pearce, F. Deschler, R. L. Z. Hoye, K. C. Gödel, T. Bein, P. Docampo, S. E. Dutton, M. F. L. De Volder, R. H. Friend, *Nano Lett.* **2015**, *15*, 6095.

[151] J. Xing, Y. Zhao, M. Askerka, L. N. Quan, X. Gong, W. Zhao, J. Zhao, H. Tan, G. Long, L. Gao, Z. Yang, O. Voznyy, J. Tang, Z.-H. Lu, Q. Xiong, E. H. Sargent, *Nat. Commun.* **2018**, *9*, 3541.

[152] T. Leijtens, K. A. Bush, R. Prasanna, M. D. McGehee, *Nat. Energy* **2018**, *3*, 828.

[153] S. D. Stranks, V. M. Burlakov, T. Leijtens, J. M. Ball, A. Goriely, H. J. Snaith, *Phys. Rev. Appl.* **2014**, *2*, 1.

[154] S. J. Yoon, S. Draguta, J. S. Manser, O. Sharia, W. F. Schneider, M. Kuno, P. V. Kamat, *ACS Energy Lett.* **2016**, *1*, 290.

[155] N. K. Noel, A. Abate, S. D. Stranks, E. S. Parrott, V. M. Burlakov, A. Goriely, H. J. Snaith, *ACS Nano* **2014**, *8*, 9815.

[156] D. S. Lee, J. S. Yun, J. Kim, A. M. Soufiani, S. Chen, Y. Cho, X. Deng, J. Seidel, S. Lim, S. Huang, A. W. Y. Ho-Baillie, *ACS Energy Lett.* **2018**, *3*, 647.

[157] X. Li, C. C. Chen, M. Cai, X. Hua, F. Xie, X. Liu, J. Hua, Y. T. Long, H. Tian, L. Han, *Adv. Energy Mater.* **2018**, *8*, 1.

[158] D. M. Jang, K. Park, D. H. Kim, J. Park, F. Shojaei, H. S. Kang, J. P. Ahn, J. W. Lee, J. K. Song, *Nano Lett.* **2015**, *15*, 5191.

[159] N. K. Kumawat, X.-K. Liu, D. Kabra, F. Gao, *Nanoscale* **2019**, *11*, 2109.

[160] M. R. Linaburg, E. T. McClure, J. D. Majher, P. M. Woodward, *Chem. Mater.* **2017**, *29*, 3507.

[161] G. Nan, X. Zhang, M. Abdi-Jalebi, Z. Andaji-Garmaroudi, S. D. Stranks, G. Lu, D. Beljonne, *Adv. Energy Mater.* **2018**, *8*, 1702754.

[162] H. Tan, F. Che, M. Wei, Y. Zhao, M. I. Saidaminov, P. Todorović, D. Broberg, G. Walters, F. Tan, T. Zhuang, B. Sun, Z. Liang, H. Yuan, E. Fron, J. Kim, Z. Yang, O. Voznyy, M. Asta, E. H. Sargent, *Nat. Commun.* **2018**, *9*, 3100.

[163] K. Lin, J. Xing, L. N. Quan, F. P. García de Arquer, X. Gong, J. Lu, L. Xie, W. Zhao, D. Zhang, C. Yan, W. Li, X. Liu, Y. Lu, J. Kirman, E. H. Sargent, Q. Xiong, Z. Wei, F. P. G. de Arquer, X. Gong, J. Lu, L. Xie, W. Zhao, D. Zhang, C. Yan, W. Li, X. Liu, Y. Lu, J. Kirman, E. H. Sargent, Q. Xiong, Z. Wei, *Nature* **2018**, *562*, 245.

List of abbreviations

0D	Zero-dimensional / Cero-dimensional
1D	One-dimensional / Monodimensional
2D	Two-dimensional / Bidimensional
3D	Three-dimensional / Tridimensional
AFM	Atomic-Force Microscopy / Microscopía de fuerza atómica
AmCl	Amantadine hydrochloride / Hidrocloruro de amantadina
BuOH	Butanol
CBP	4,4'-Bis(N-carbazolyl)-1,1'-biphenyl / 4,4'-Bis(N-carbazolil)-1,1'-bifenilo
cd	Candela
CW	Continuous wave / Onda continua
DecylA	Decylamine / Decilamina
DMF	Dimethylformamide / Dimetilformamida
DMSO	Dimethylsulfoxide / Dimetilsulfóxido
EIL	Electron Injection Layer / Capa de inyección de electrones
EL	Electroluminescence / Electroluminiscencia
EQE	External Quantum Efficiency / Eficiencia cuántica externa
ETL	Electron Transport Layer / Capa de transporte de electrones
FA	Formamidinium / Formamidinio
FTO	Fluorine-doped Tin Oxide / Óxido de estaño dopado con fluor
FWHM	Full Width at Half Maximum / Ancho total a mitad de máximo
GBL	γ-Butyrolactone / γ-Butirolactona
HexylA	Hexylamine / Hexilamina
HIL	Hole Injection Layer / Capa de inyección de huecos
HOMO	Highest Occupied Molecular Orbital / Orbital molecular ocupado más alto
HTL	Hole Transport Layer / Capa de transporte de huecos
ITO	Indium Tin-doped Oxide / Óxido de indio dopado con estaño
LARP	Ligand Assisted Re-Precipitation / Reprecipitación asistida por ligandos
LED	Light-Emitting Diode / Diodo emisor de luz
LUMO	Lowest Unoccupied Molecular Orbital / Orbital molecular desocupado más bajo

MA	Methylammonium / Metilamonio
MPL	Microplatelet / Microlámina
NC	Nanocrystal / Nanocristal
NIR	Near Infrared / Infrarrojo cercano
NMP	N-methyl Pyrrolidone / N-metil-2-pirrolidona
norm.	Normalized / Normalizado
NP	Nanoparticle / Nanopartícula
OA	Oleic acid / Ácido oleico
OctylA	Octylamine / Octilamina
ODE	Octadecene / Octadeceno
OLED	Organic Light-Emitting Diode / Diodo emisor de luz orgánico
OleylA	Oleylamine / Oleilamina
PEDOT:PSS	Poly(3,4-ethylenedioxythiophene) doped with Polystyrene Sulfonate / Poli(3,4-etilendioxitiofeno) dopado con poli(estireno sulfonato)
PET	Polyethylene terephthalate / Tereftalato de polietileno
PL	Photoluminescence / Fotoluminiscencia
PLQY	Photoluminescence Quantum Yield / Rendimiento cuántico fotoluminescente
PMMA	Poly(methyl methacrylate) / Poli(metil metacrilato)
PVP	Poly(vinyl pyrrolidone) / Poli(vinil pirrolidona)
QD	Quantum Dot / Punto cuántico o partícula cuántica
rpm	Revolutions Per Minute / Revoluciones por minuto
RT	Room Temperature / Temperatura ambiente
SEM	Scanning Electron Microscopy / Microscopía electrónica de barrido
TEM	Transmission Electron Microscopy / Microscopía electrónica de transmisión
TCO	Transparent Conductive Oxide / Óxido conductor transparente
UV	Ultraviolet / Ultravioleta
WF	Work Function / Función de trabajo
XPS	X-ray photoelectron spectroscopy / Espectroscopía de fotoelectrones emitidos por rayos X.
XRD	X-ray Diffraction / Difracción de rayos X

Publications

Included in the thesis:

L. Martínez-Sarti, F. Palazon, M. Sessolo and H. J. Bolink, **Dry mechanochemical synthesis of highly luminescent, blue and green hybrid perovskite solids**. *Adv. Opt. Mater.*, **2019**, 1901494.

L. Martínez-Sarti, S. H. Jo, Y.-H. Kim, M. Sessolo, F. Palazon, T.-W. Lee and H. J. Bolink, **Low-dimensional iodide perovskite nanocrystals enable efficient red emission**. *Nanoscale*, **2019**, 11, 12793-12797.

X. Y. Chin, A. Perumal, A. Bruno, N. Yantara, S. A. Veldhuis, **L. Martínez-Sarti**, B. Chandran, V. Chirvony, A. Shu-Zee Lo, J. So, C. Soci, M. Grätzel, H. J. Bolink, N. Mathews and S. G. Mhaisalkar, **Self-assembled Hierarchical Nanostructured Perovskites Enable Highly Efficient LEDs via Energy Cascade**. *Energy Environ. Sci.*, **2018**, 11, 1770-1778.

L. Martínez-Sarti, T. M. Koh, M.-G. La-Placa, P. P. Boix, M. Sessolo, S. G. Mhaisalkar and H. J. Bolink, **Efficient photoluminescent thin films consisting of anchored hybrid perovskite nanoparticles**. *Chem. Commun.*, **2016**, 52 (76), 11351-11354.

Other publications:

A. Jiménez-Solano, **L. Martinez-Sarti**, A. Pertegás, G. Lozano, H. Bolink and H. Míguez, **Dipole reorientation and local density of optical states influence the emission of light-emitting electrochemical cells**. *Phys. Chem. Chem. Phys.*, **2020**, Just accepted.

M. Sessolo, M.-G. La-Placa, **L. Martínez-Sarti** and H. J. Bolink, **Perovskite Light-Emitting Devices - Fundamentals and Working Principles: Photovoltaics, Light Emitting Devices, and Beyond**. Book, **2019**, chapter 3.1, Halide Perovskites: Photovoltaics, Light Emitting Devices, and Beyond.

Q. A. Akkerman, **L. Martínez-Sarti**, L. Goldoni, M. Imran, D. Baranov, H. J. Bolink, F. Palazon and L. Manna, **Molecular Iodine for a General Synthesis of Binary and Ternary Inorganic and Hybrid Organic–Inorganic Iodide Nanocrystals**. *Chem. Mater.*, **2018**, 30 (19), 6915–6921.

S. González-Carrero, **L. Martínez-Sarti**, M. Sessolo, R. E. Galian and J. Pérez-Prieto, **Highly photoluminescent, dense solid films from organic-capped $CH_3NH_3PbBr_3$ perovskite colloids**. *J. Mater. Chem. C*, **2018**, 6, 6771-6777.

A. Babaei, K. Rakstys, S. Guelen, V. Fallah Hamidabadi, M.-G. La-Placa, **L. Martínez-Sarti**, M. Sessolo, H. Aron Joel, O. P. M. Gaudin, V. Schanen, M. K. Nazeeruddin and H. J. Bolink, **Solution processed organic light-emitting diodes using a triazatruxene crosslinkable hole transporting material**. *RSC Adv.*, **2018**, 8, 35719-35723.

S. Gonzalez-Carrero, L. C. Schmidt, I. Rosa-Pardo, **L. Martínez-Sarti**, M. Sessolo, R. E. Galian and J. Pérez-Prieto, **Colloids of Naked $CH_3NH_3PbBr_3$ Perovskite Nanoparticles: Synthesis, Stability, and Thin Solid Film Deposition**. *ACS Omega*, **2018**, 3, 1298-1303.

M. Alkan-Zambada, S. Keller, **L. Martínez-Sarti**, A. Prescimone, J. M. Junquera-Hernández, E. C. Constable, H. J. Bolink, M. Sessolo, E. Ortí and C. E. Housecroft, **[Cu(P^P)(N^N)][PF_6] compounds with bis(phosphane) and 6-alkoxy, 6-alkylthio, 6-phenyloxy and 6-phenylthio-substituted 2,2'-bipyridine ligands for light-emitting electrochemical cells**. *J. Mater. Chem. C*, **2018**, 6, 8460-8471.

S. Keller, A. Prescimone, H. Bolink, M. Sessolo, G. Longo, **L. Martínez-Sarti**, J. M. Junquera-Hernández, E. C. Constable, E. Ortí and C. E. Housecroft, **Luminescent copper(I) complexes with bisphosphane and halogen-substituted 2,2'-bipyridine ligands**. *Dalton Trans.*, **2018**, 47, 14263-14276.

M. G. La-Placa, G. Longo, A. Babaei, **L. Martínez-Sarti**, M. Sessolo and H. J. Bolink, **Photoluminescence quantum yield exceeding 80% in low dimensional perovskite thin-films via passivation control**. *Chem. Commun.*, **2017**, 53, 8707-8710.

S. Keller, A. Pertegás, G. Longo, **L. Martínez**, J. Cerdá, J. M. Junquera-Hernández, A. Prescimone, E. C. Constable, C. E. Housecroft, E. Ortí and H. J. Bolink, **Shine bright or live long: substituent effects in $[Cu(N^N)(P^P)]^+$-based light-emitting electrochemical cells where N^N is a 6-substituted 2,2'-bipyridine**. *J. Mater. Chem. C*, **2016**, 4, 3857-3871.

L. Martínez-Sarti, A. Pertegás, M. Monrabal-Capilla, E. Gilshteyn, I. Varjos, E. I. Kauppinen, A. G. Nasibulin, M. Sessolo and H. J. Bolink, **Flexible light-emitting electrochemical cells with single-walled carbon nanotube anodes**. *Organic Electronics*, **2016**, 30, 36-39.

F. Brunner, **L. Martínez-Sarti**, S. Keller, A. Pertegás, A. Prescimone, E. C. Constable, H. J. Bolink and C. E. Housecroft, **Peripheral halo-functionalization in $[Cu(N^N)(P^P)]^+$ emitters: influence on the performances of light-emitting electrochemical cells**. *Dalton Trans.*, **2016**, 45, 15180-15192.

D. Rota Martir, A. K. Bansal, V. Di Mascio, D. Bradford Cordes, A. F. Henwood, A. Slawin, P. Kamer, **L. Martinez-Sarti**, A. Pertegás, H. J. Bolink, I. Samuel and E. Zysman-Colman, **Enhancing the Photoluminescence Quantum Yields of Blue-Emitting Cationic Iridium(III) Complexes Bearing Bisphosphine Ligands**. *Inorg. Chem. Front.*, **2016**, 3(2), 218-235.

Prior to PhD:

G. Longo, A. Pertegás, **L. Martínez-Sarti**, M. Sessolo and H. J. Bolink, **Highly luminescent perovskite–aluminum oxide composites**. *J. Mater. Chem. C*, **2015**, 3, 11286-11289.

D. Cortizo-Lacalle, A. Pertegás, **L. Martínez-Sarti**, M. Melle-Franco, H. J. Bolink and A. Mateo-Alonso, **Twisted hexaazatrianthrylene: synthesis, optoelectronic properties and near-infrared electroluminescent heterojunctions thereof**. *J. Mater. Chem. C*, **2015**, 3: 9170-9174.

L. Martínez-Sarti and S. Díez-González, **On the unique reactivity of $Pd(OAc)_2$ with organic azides: Expedient synthesis of nitriles and imines.** *ChemCatChem*, **2013**, 5: 1722-1724.

Acknowledgements

My deep gratitude goes first to my supervisors, Henk Bolink and Michele Sessolo, for guiding and teaching me many things through all this process. For their advices and their availability to attend us despite the many appointments they have. To Henk, thanks for giving the opportunity to me at the beginning and for all the good experiences I was allowed to live. Thanks for caring about all your students, both personally and their development and needs as scientific researchers. For trying to make the workplace a comfortable and enjoyable place to stay in. And many thanks for trusting and valuing me along these years. Y a Michele, gracias por tu capacidad de comprensión y tu trabajo duro. Por la sensibilidad y empatía que tanto empeño pones en ocultar de tu carácter. Por repartir marrones a diestro y siniestro con una sonrisa. Por escucharnos, por estar siempre dispuesto a atendernos y por tu gran esfuerzo.

My appreciation also extends to my laboratory colleagues. Thanks to everyone who have shared moments and emotions with me during this process. A Lidón, gracias por haber estado ahí y haber sido un apoyo de principio a fin. Por ser una máquina, en el trabajo y en la vida. Por haber estado siempre dispuesta a unirte a los retos personales y de trabajo, por las charlas, las reflexiones y las risas en la pecera. También a Dani, por tu humor y por los buenos momentos vividos dentro y fuera del laboratorio. Por currarte los regalos y estar dispuesto a ofrecerme tu ayuda cuando la he necesitado. ¡Gracias por haberme ayudado con las fotos y con la portada! A Jorge, por las risas, los viajes y los buenos ratos de ahora, y sobre todo de antaño. A Toni, por haber sido mi mentor en el laboratorio y haberme enseñado tanto y con tanta paciencia. A Cristian, por tu apoyo constante y por tu paciencia. Por cuidarme y por intentar comprenderme siempre. Y por todos los buenos momentos. Also to M. Cristina, Maria Grazia, Giulia, Vaheed, Benni, Ángel... together with each and every one of you who are or have been teaching me, collaborating, helping, as well as laughing, travelling, partying and enjoying life with me: Chris, Jorge F., Azin, Kassio, Ana, Paco, Pablo, María, Paula, Alejandra, David, Jose, Isidora, Paz, Enrico, Yous, Marteen, Wiria, Lorenzo, Bas, Sang, Vicente, Beom, Xavi, Cihan, Miguel, Abhi, Nathan, Vladimir... and to the one I have forgotten, you are also included. My gratitude as well to the people with whom I share and have shared the office, for the good atmosphere and the complicity (Lidón, M. Cristina, Ana, Víctor, Mario, Javi C...), along with the people in the Master, for all the anecdotes we lived together (Jorge, Ramón, Javi L., Javi C., Mario, Jesús, Garin...). Many many thanks, because working with these colleagues and in this great atmosphere is a pleasure.

I do not want to forget each one of the people who was there in my research stays. First of all, I would like to express my gratitude to the professors who accepted me in their research groups: Prof. Subodh Mhaisalkar, Prof. Tae-Woo Lee and Prof. Liberato Manna. Not everyone has the opportunity to live such enriching experiences. I would like to show my thanks to the many different and awesome people I have met during those periods. Special thanks to Daymond (Koh Teck Ming) and Yanfong for my days in Singapore, Young Hoon and Tito for

my days in South Korea, and Cansu, Lea, Mengji and Luca for taking me in when I was in Italy. I would like to extend my gratitude also to the people with who I had the opportunity to collaborate in other projects, and from which I have learned a lot: Enrique Ortí, Raquel Galián, Sora, Nacho, Xin Yu Chin, Dmitry, Quinten, Diego, Murat, Fabian, Sarah Keller...

Y sin ninguna duda, a mi familia, por cuidarme, guiarme e intentar hacérmelo todo más fácil. A mi hermano y a Bea, por los divertidos momentos y vuestros ánimos en este largo proceso. A mis padres, por vuestro apoyo incondicional y toda la ayuda que siempre estabais y estáis dispuestos a prestarme. Porque ellos están ya ahí antes de que se lo pidas :P. Gracias por tanto.